Interactions of slow multiply charged ions with large, free radiosensitizing metallic nanoparticles

Arkadiusz Mika

Normandie Université

THESE

Pour obtenir le diplôme de doctorat

Spécialité Physique

Préparée au sein de l'Université de Caen Normandie

Interactions of slow multiply charged ions with large, free radiosensitizing metallic nanoparticles

Présentée et soutenue par
Arkadiusz MIKA

Thèse soutenue publiquement le 19 Décembre 2017 devant le jury composé de		
M. Paul-Antoine HERVIEUX	Professeur des universités, Strasbourg	Rapporteur
M. Bruno MANIL	Professeur des universités, Paris 13	Rapporteur
Mme Paola BOLOGNESI	Maître de conférences, Consiglio Nazionale delle Ricerche, Rome, Italie	Examinateur
M. Philippe RONCIN	Directeur de recherche, Université Paris Sud	Examinateur
M. Patrick ROUSSEAU	Maître de conférences, HDR, Université Caen Normandie	Directeur de thèse
M. Bernd A. HUBER	Ingénieur de recherche, CEA, HDR, Ganil, Caen	Examinateur

Thèse dirigée par Patrick ROUSSEAU, laboratoire CIMAP/GANIL

UNIVERSITÉ CAEN NORMANDIE

ED PSIME

CIMAP

Interactions of slow multiply charged ions with large, free radiosensitizing metallic nanoparticles

Arkadiusz Piotr MIKA

1er février 2018

Acknowledgements

To begin my acknowledgements I would like to say that the last 3 years and several months of my life were incredibly intense and enriching, much beyond any expectations I could have had. This was a great personal and scientific journey, which wouldn't have been possible without the people I had a chance to meet and work with on the way and to whom I would like to express my overall gratitude below.

With the first words, I feel grateful to the members of my jury present during the defense and who accepted the evaluation of the quality of my work, providing important remarks and advice. I thank both of the rapporteurs, Paul-Antoine Hervieux and Bruno Manil, as well as the president of the jury Philippe Roncin and jury member Paola Bolognesi.

At this point, I would like to express my gratitude and greatest acknowledgements to Bernd "Le Chef" Huber - for the best physics lessons I have ever experienced. His guidance through the whole process, numerous discussions and the positive approach were sources of inspiration to "make things work" and do things correctly, with a great dose of humour, sometimes on the way to the local shop or car mechanic. I wish everyone such quality supervision during their doctoral work.

Equally indebted I feel towards my supervisory duo : Patrick Rousseau and Alicja Domaracka, who took care of me on an everyday basis both personally and scientifically, sometimes seriously "a bit like parents" and sometimes in a more entertaining way "a bit like wiser siblings" (and I am sure both cases were necessary !). Their constant support and willingness to provide help in any possible situation allowed me to reach my final goal in the great and friendly atmospheres of Caen and the barbecue of Biéville-Beuville !

I would also like to express my gratitude to Violaine Vizcaino, who introduced me to the straight into the world of ion trajectory simulations in a great pedagogical manner and always supported me with her positive attitude and clear explanations of experimental devices, as well as showing me how a proper Normandy karaoke birthday party should look.

I am thankful as well to both Jaroslav Kocisek and Rudi Delaunay, with whom I worked at the beginning of my thesis on the COLIMACON Setup and from whom I had a chance to learn the most important aspects of proper collision experiments.

Warm wishes and acknowledgements I would like to express to "always in a good mood" Jimmy Rangama, whose assistance and help together with Omar Kamalou concerning proper maintenance of the cluster source were of a great help for the final success of my experiments.

Many warm thanks as well to Jean-Christophe Poully as a great office buddy and Alain Mery and Matthieu Lalande - who together form the strong but always smiling core of the PIBALE Team.

I feel significantly indebted to the "beam team" : Ville Toivanen and Laurent Maunoury, who operated and maintained the ion source for numerous hours during my experiments. Gratitude also to surface specialists team : Florant Moisy and Hichem ben Ammar - my AFM teachers, Jean-Gabriel Matei, Isabelle Monnet for great TEM images and Serge Bouffard, Henning Loebius, Emmanuel Balanzat, Marcel Toulemonde, Philippe Boduch and Hermann "..IIIYYO sound" Rothard for their discussions and help with samples.

Next, I feel I must mention here Lucas Schwob and Coralie Ledroff who both gave me many great lessons in the french language, culture, and how not to drink embuscade, and who showed me that there are many joys in Normandy and Bretagne, even if it is raining.

Equally thankful I feel to the great nuclear physicist Denis Wilmsen, "the buddy" and "brother-in-arms" for all the discussions about the most crazy topics we had and all the funny moments we shared, from french classes even up to (not the most successful) kayaking attempts. As well at this point I cannot forget about Pascale Randriantiana, for her great companionship and particularly for her help with some bureaucratic struggles I went through in Caen from which she "rescued" me. Monsieur Vishant aka "Siva" Kumar and Aditya "the Fire" Agnihotri to whom I feel grateful for indian style food and fruitful cheering conversations.

Many thanks go to those people who helped me enormously in establishing a working experimental setup, connecting all pieces together and building a new detection device. These great specialists of their fields are Jean-Marc Ramillon, Claire Feierstein-Plancq, Thierry Been, Fabian Noury, Jean-Marc Fontbonne and David Etasse.

I feel thankful as well to the extraordinary people I have met in general during these 3 years, both locally and through international collaborations : Amine Cassimi, Jean-Yves Chesnel, Stéphane Guillouis, Yannick Saintigny, Basile Auge, Clara Grygiel, Linda de Baeremaker, Francois Chevalier, Lucie Bercker, Christiane Malot, Delphine Hasley, Philippe Boduch, Alexis Ribet, Matthieu Babo, Bartholomé Cauchois, Pierre Chauveau, Saba Ansari and the great quantum "chemist-soon-to-be-fitness-trainer" Dariusz Piekarski... I have met many more great people during the time of this project and there are numerous who have stayed by me since much much longer, so please forgive me if I didn't mention all and hereby below I thank those as well.

Sometimes we feel that we can be a part of something bigger and this can also bring us into many unexpected situations, both exciting but also challenging. Indeed, I feel like I was a part of such a "something bigger", being the European Commission ITN Marie Curie Project named ARGENT, and it was one of the greatest, long lasting and unique events in my life. However, the uniqueness of this program came entirely from the amazing group of people I have befriended and with whom I shared great moments in Orsay, Paris, Boppard, Genova, Obergurgl, Belfast... and in many other occasions. From the very first meeting in Orsay in 2014 to very last meeting in 2018, again in Orsay, seeing the happy faces of the ARGENTers was

an incredible motivation and source of inspiration for many life aspects for me. I am sure I will feel still this way in future if there will appear any occassion to unite us all again (for which I really hope), no matter if professionally or privately. Thank You all, guys. Thanks to Ali, Soraia, Kaspar, Vladimir, Vivek, Sophie, Alexey, Pablo, Vu Long, Marta, Daria and Lily ! Thanks to all the people who were involved in ARGENT activities - from coordinators, managers through early stage researchers to their supervisors and even beyond. I wish You all the best in Your lives and that You will be a part of "something bigger" as often as possible.

There is also a group of people who have surrounded me with their cheerfulness and great friendship since many years and who I cannot omit here. I have experienced from them the best one can experience in the matter of real friendship. Great and Greater (and I think still too small) Thanks to Tomasz "Tomas" Olbrycht, Michał "Studniar" Studniarek, Michał "Ziomal" Maciejak, Wojciech Szewc, Filip "Filu" Schleicher, Beata Taudul, Aleksandra Czmiel, Antonina Lewandowska, Arkadiusz "Kwiatek" Kwieciński, Łukasz "Zawo" Zawodnik, Marcin "Cinek" and Piotr "Piter" Szelerscy, Szymek Florianowicz, Stasiu Domaradzki and to the greatest of mechanical minds in Olesnica, Monsieur Przemysław "Kuban Turbo-Lord" Kubik.

The most important dedication and acknowledgement I left for those who are for me the most important and without whom nothing would be possible : My Parents and my brother Kacper. For the whole effort You made to raise me properly, for Your encouragement, for all those sacrifices You had to go through over the last 29 years and for Your love. Thank You very much.

Contents

Introduction | 1

1.1 Short scientific and historical note

The interaction of ionizing radiation in the form of energetic ions and photons with matter is an object of very broad interest. The aim is the understanding of the most basic mechanisms and their potential applications in everyday's use. First studies were initiated in 1896 by Becquerel [1], and although initially mainly motivated by scientific curiosity, with time they found their way into today's modern economy.

Since the beginning, the impact of radiation had a profound effect on the surrounding matter. For example, the discovery of ultraviolet light and its chemical effects on silver chloride lead to first precurssors of photography. High energy photon radiation, discovered by Wilhelm Roentgen [2] by the observation of fluorescence on coated glass, was soon used as one of the main diagnostic tools which revolutionized medicine. First natural radioactivity was observed by Henri Becquerel and further developed by his doctoral student Marie Sklodowska-Curie, who was a leading person in its further applications into the treatment of neoplasms . The discovery of different penetration depths of alpha and beta particles by Rutherford allowed to differentiate them and it was one of first experiments concerning the interaction of ionized particles with matter in general. All of the most important discoveries concerning different types of ionizing radiation took place in the late XIX and early XX century, along with discovery of positrons, muons, pions up to the 30's in XX century and further progress was based mostly on the development of powerful particle accelerators.

On the other hand, the second half of the XXth century is characterized by more and more dynamical developments of ion-based irradiation therapies (hadrontherapy), which is non-invasive and is characterized by an ultrahigh level of precision in targeting unhealthy tissues. Combined with other treatments (like chemotherapy) or enhanced by introduction of radio-sensitizing agents in the region of interest becomes more and more effective in the treatment of difficult deap-seated tumors. Furthermore, this might improve future possibilities of an efficient treatment of radioresistant cancers by enhancing strongly local doses due to radiosensitiziation effects induced by advanced, highly selective drugs activated by radiation.

As it is seen, each discovery leads to interesting and beneficial applications, shifting civilization in a step-wise manner ahead. For example today, in the world based on the internet technology, computers, lasers, sensors, ultrafast communication, not many people realize that production of the smallest electronic chips demands modification of the material properties on the micro and nanoscale, for which ionizing radiation is inevitable.

The online etymological dicitionary http://www.etymonline.com states, that the word radiation takes its origin from Latin or Old French, where rai or $radius$ meant the spoke of a wheel, gush or spurt and it is not surprising that it brings into imagination the association of propagation of energy from one point to another in space.

Depending on the nature of such "energy carrier" one can introduce various types of classifications. For the present context the most important aspect is the propagation of an ion - charged atom - in space, which can be in vacuum or matter. Concerning the propagation of ions inside or in the vicinity of matter one can introduce further specifications, but in the most basic view a propagating ion is a carrier of charge, mass and energy when passing through matter it passes through a system composed of positively charged, heavier nuclei and negatively charged lighter electrons moving in the potential formed by nuclei. Naturally, Coulombic forces, acting between different charges as well as the particle-character of ion-atom collisions lead to a disturbation of the equilibrium states of electrons and atoms - changing their velocities and positions, thus modifying irradiated system inducing chemical and structural changes.

1.2 Motivation

The main objective of this work was the instrumental development of an experimental setup and the investigation of the interaction between small (below 10 nm) metallic clusters and multiply charged ions in the 10s to 100s keV total kinetic energy regime.

Why one would be interested in this research in general? There are two main motivations for such studies, one being more practical and another purely scientific. The former one concerns the improvement of modern radiotherapy protocols enhanced by novel type of radiosensitizing drugs, that are based on metallic nanoparticles. Especially, in the framework of a modern type of radiotherapy - nanoparticle enhanced hadrontherapy - the understanding of possible interaction mechanisms is crucial for an effective treatment of patients. Hadrontherapy differs from standard type of radiation therapies, because instead of photons, one uses the beam of energetic ions (from here the prefix - HADRON) profiting from their advantages in terms of their energy deposition while penetrating the matter compared to photons and the strong localization of the dose delivery. Below, in the Context chapter - "Radiobiology part"- we will present to the Reader the conceptual synthesis of information about the general description of the damage on molecular and cellular scale, induced by radiation and assisted by the presence of radiosensitizers. The ITN Marie Curie-Sklodowska Research Program ARGENT funded by the European Commission, is exactly dedicated to the above mentioned challenges, and here my work as its important element will be described as well.

From the purely scientific point of view, clusters of atoms or molecules are many-body objects. A detailed quantum mechanical description in terms of stability, phase-transitions, fragmentation, electronic properties (like elementary excitations, electron and photon emis-

sion/absorption) etc. is extremely difficult, if not impossible today. Depending on the property one would like to describe theoretically, some assumptions and models have to be used, however, their application neglects numerous other important effects. That's why the experiments are both the inspiration and source of new information stimulating developments of more and more complete theoretical models, as well as the ways to verify their validity. In the Scientific context part we summarize the state-of-the art of the research work done on mostly metallic clusters and their interaction with ions.

1.3 Marie Curie-Skłodowska ITN ARGENT Project

The Marie Curie-Skłodowska „ARGENT"(„Advanced Radiotherapy, Generated by Exploiting Nanoprocesses and Technologies") Program is the Initial Training Network project, currently ongoing and supported by the European Commission.

Within its framework, world-leading researchers from various fields (physics, chemistry, biology, pharmacy) are brought together with the aim to train a cohort of 13 Early Stage Researchers (ESRs) representing multidisciplinary fields. These ESRs gain skills allowing them to perform research activities for a better understanding and exploiting the nanoscale processes that drive physical, chemical, and biological effects induced by ionizing radiation in the presence of radiosensitizing nanoparticles.

This activity is at the frontline of current practices and its main advantage stems from its multidisciplinary and intersectorial character. There are 3 main workpackages as main research objectives.

The first workpackage -„Nanodosimetry"- is devoted for the advancements of the understanding of physico-chemical processes initiated by the interaction between biological matter and radiation in order to predict and control the effects of new treatments accompanied by the application of nanoparticle-based drugs. It combines experimental and computational techniques in answering the most fundamental questions of radiation induced nanoscale damage and its object of interest are biomolecules and their clusters (also solvated in water) as well as the nanoagents.

The second workpackage - „Therapeutic Nanoagents"- aims to develop a new class of nanodrugs to combine the effects of radiation and diagonostic - so-called theranostic approach, as well as the characterization of nanodrug behavior in a cellular environment in the context of cellular uptake, localization and toxicity effects in presence or without of radiation.

The last workpackage - "Preclinical evaluation" - aims to bring the research much closer to clinical practice and to improve existing and develop new tools in the treatment protocols for better patient outcome. Combination of advanced experimental and theoretical tools allows for the investigation of nanoscale interactions for preclinical testing, veryfing their clinical applicability.

1.3.1 Physics of radiation and hadron-therapies

1.3.1.1 Dose deposition and concept of radiosensitization mechanisms

In the standard radiotherapy treatment, when high energy photons are used as a source of the ionizing radiation, the deposition of the energy inside the matter follows a characteristic curve: initially the dose deposition rises up to the maximum point, where electron equilibrium is reached and after that point it decreases exponentially (fast neutrons and photons have such an exponential dependence of dose absorption). In fig.1.1 the dose deposition of 6 MeV X-Ray photons as a function of depth in the body is shown with a pink curve.

Normally in such a case the placement of the target should be as close as possible to the maximum of the dose deposition. In the case of MeV photons this lies in the very first few centimeters of the irradiated tissue. As it is clearly seen a large amount of dose is deposited in surrounding tissues. Especially, in the case of deep-seated tumors, the threshold of a minimum dose, that has to be delivered into the cancerous region, demands multiple irradiations, also from different angles. This means many healthy regions are prone to large quantities of the unnecessary energy delivered from radiation and it increases strongly the risk of the development of secondary tumors.

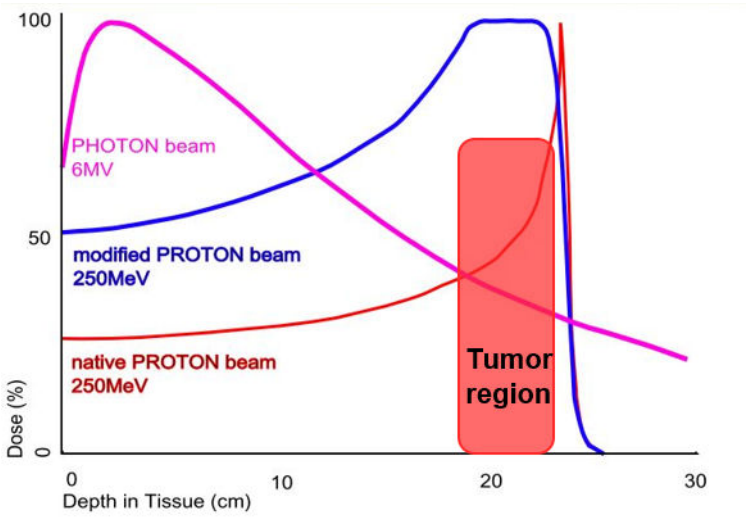

Figure 1.1 *The dose deposited as a function of the depth in the tissue for three different treatment situations: irradiation with 6 MeV photon beam (pink curve), native beam of proton with energy of 250 MeV(red curve) and modified proton beam with initial energy of 250 MeV. Graph taken from the website of University College London (https://www.hep.ucl.ac.uk/pbt/).*

In case of an atomic ion, the energy is deposited inversly proportionally to the square of its

velocity, according to the Bethe-Bloch formula (in non-relativistic approximation):

$$-\frac{dE}{dx} = \frac{4\pi n z^2}{m_e v^2} \cdot (\frac{e^2}{4\pi\epsilon_0})^2 \cdot [ln(\frac{2m_e v^2}{I})] \quad (1)$$

where E- particle energy , z- particle charge, x-distance of travel, n-electron density of the material,I-mean excitation potential and v-particle velocity. The slower the particle gets during the penetration, the larger the probability of the ionization and the excitation of surrounding atoms and molecules. At the point, where the accumulation of ionization events is maximal, the appearance of a dose peak known as „Bragg peak", is observed. This behavior can be seen in fig.1.1 following red curve, representing a proton beam with an energy of 250 MeV . In this case the Bragg peak is localized deep (range of ∼25 cm) inside the tissue. After the Bragg peak, the particle strongly reduces its kinetic energy and a drastic drop in dose is observed. The position of that peak is proportional to initial energy of the particle.

Due to the strong localization of the Bragg Peak an effective irradiation of the tumor demands multiple irradiations with variation of the initial energy in order to cover the whole selected volume. Such overlap of many Bragg-peaks is known as so called Spread-Out Bragg Peak (SOBP). In fig.1.1 SOBP is marked as blue line for the case of a modified proton beam at initial energy of 250 MeV and below. Unfortunately, this method results also in an elevated accumulation of the dose in healthy parts

Fig.1.2 shows an example from the realization in a clinical environment of the meningioma. It represent the case of dose depositions for the case of three types of radiation methods used- A: photon IMRT (Intensity Modulated Radiation Therapy), B: Carbon ion beam and C: proton treatment planning, after [3].

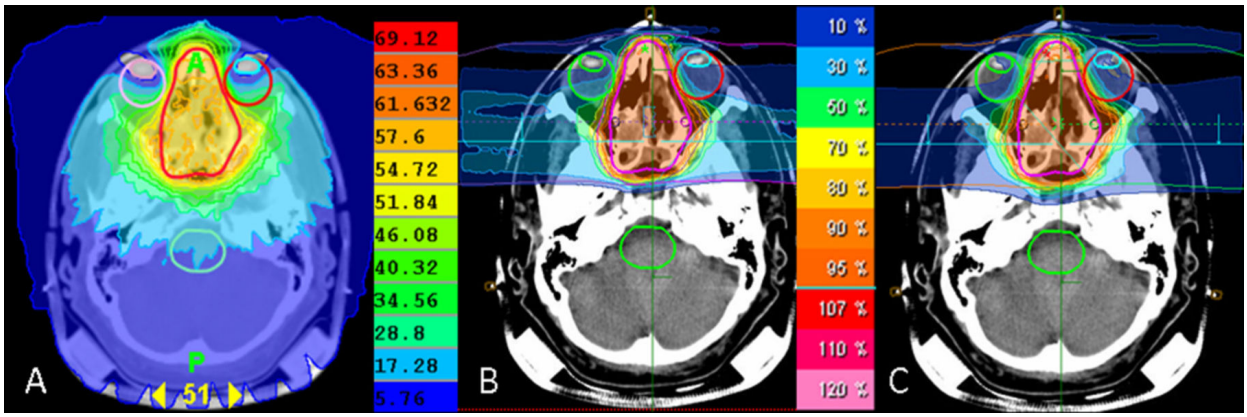

Figure 1.2 *Dose distribution in transverse plane for (A) photon IMRT, (B) carbon ion and (C) proton treatment planning techniques. The same beam arrangements were used for carbon ion and proton plans. These plans consisted of two lateral beams and one cranial beam. Figure taken from Katsur et al. [3].*

The disease region, marked fully with red contour line and localized close to the sinus, is a very sensitive part due to the presence of important body organs: eyes and optical nerve.

The color represents the amount of the dose deposited: blue the lowest and red the largest. In case of the photon treatment (A) one can clearly observe that practically the whole volume of the skull would be irradiated, delivering even more than ∼20 % of the dose to the healthy tissue. On the other hand in two other cases (B,C) when carbon and proton beams are used strong majority of the healthy region is completely spared from any irradiation. Additionally, in the vicinity of the tumor itself the relative amount of the dose is more concentrated on the unhealthy part compared to the previous case, with the border between cancerous and non-cancerous tissue defined in greater detail. This example shows a strong improvement in terms of the treatment and reduced risk of the appearance of secondary radiation induced side-effects.

As it was mentioned above, although a large improvement in dose deposition of a charged particle based therapy compared to a photon based radiotherapy is obtained, the necessity to cover the whole volume of the tumor still results in unwanted irradiation of healthy regions. Therefore, the main question that is arising is the following: would it be possible to increase the sensitivity of the targeted cancer tissue (for example by injecting a specific type of a drug) in a way that less irradiation procedures will result in the same observed biological effect as in the normal case without sensitization, as it is shown in fig.1.3? The answer is positive and such type of substances are known as radiosensitizers or radio-enhancers.

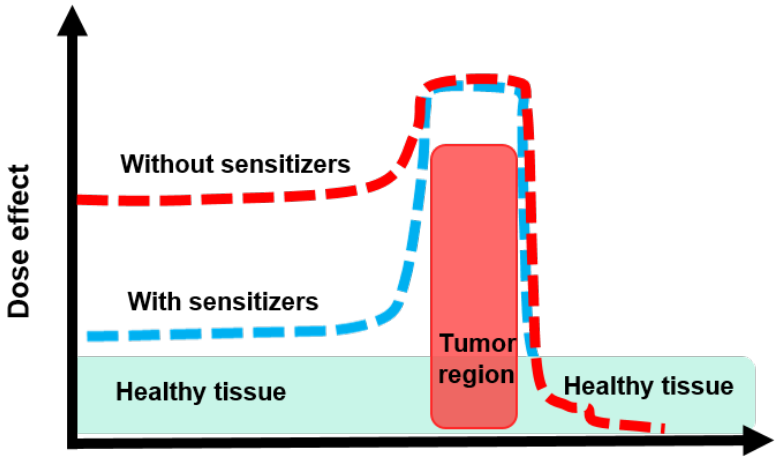

Figure 1.3 *Red dashed line corresponds to the dose effect without the radiosensitizer, while the blue dashed line shows the dose effect with radiosensitizing agent present in the tumor tissue.*

There are different mechanisms of actions of conventional radiosensitizers, which are chemotherapeutic agents. There are multiple types of such chemoradiotherapeutics. In case of fluoropyrimidines the main mechanism of the action relies on the dysregulation of the cellular cycle S-phase (moment when DNA material is undergoing replication). Another drug, gemcitabine is similar in action, causing the disrepair of the radiation-damaged DNA. In case of platinum analogs, like cisplatin the inhibition of DNA repair due to radiation by cross-linking of DNA

strands takes place. The oxygen itself is a potent radiosensitizer because radiation induces formation of oxygen-derived free radicals which damage DNA and the lack of oxygen in the tumor cells (known as hypoxia conditions) makes the tumor radioresistant. For this hypoxic cells radiosensitizers as misonidazoles and metronidazoles are applied.

In the framework of my thesis and in the framework of the ARGENT Project, the main interest lies on the new generation of radiosensitizers based on nanoparticles which so far have been reported to be effective like i.e noble metal nanoparticles and other metallic nanoparticles [4, 5].

1.3.1.2 Damage on the cellular and molecular scale

Before describing the potential effectiveness of metallic nanoparticles combined with ion irradiation it is useful to discuss the concept of nanoscale damage. In case of ions propagating in living matter, the projectiles pass through a large number of cells, however, from the ion point of view it is simply a large ensemble of molecules, where 70 % is water and remaining part are biomolecules forming cells and their composition varies according to the type of the cell.

Therefore, different types of damage exist. From the biological point of view the most important one is targeting of nuclear DNA. However, also the damage of cellular and nuclear membranes as well as that of cellular organella (for example mitochondria or mitochondrial DNA) exists, although these are classified as less dangerous to the cell survival. Other damage mechanisms are related to longterm cell signalling (for example by the bystander effect, where the release of specific signalling proteins due to initial damage may alter the chemical environment of other surrounding cells and induce cell death).

Going by one step further, one arrives at the damage occuring on the molecular scale. The mechanisms at the molecular level are governed by physico-chemical laws. In the case of previously mentioned DNA destruction, one can distinguish two mechanisms causing damage: a) direct ionization of the DNA and b) indirect ionization, caused by free radicals formed in the micro-environment of DNA and being related to water radiolysis. The DNA can be damaged in a few ways, for example by the damage of base pairs (base injury, deletion, cross-linkage - easily repairable by cellular repair mechanisms) or single and double strand breaking. In case of single strand breaks, the sugar-phosphate rail of the DNA undergoes ionization and it can be repaired rather fast, however the repair is not fully free of errors and it is repairable only up to some extent. The most important damage is the breakage of both strands of the DNA in close proximity, as this type of damage is difficult to repaire and prone to errors. The occurence probability is increasing in case of high doses and high LET type of radiation (in medical physics community its termed as Linear Energy Transfer,in non-medical community known as stopping power as well).

During the passage an ion through the molecular environment, initially it has the energy of several 10s of MeV and during its propagation the energy is lost due to processes like ionization,

excitation, nuclear fragmentation (for heavier nuclei) etc. Therefore the kinetic energy of the ion is transferred to the surrounding tissue and the dose (understood as density of deposited locally energy) is the indicator for the damage [6]. Because the ion encounters on its path directly only small fraction of biomolecules, it is commonly understood that the majority of the dose is related to ionizations and excitations produced by secondary electrons and the formation of radicals from the medium (the most important ones are $\cdot OH$,$NO\cdot$,$H\cdot$,H_2O_2). Secondary electrons are produced in very short time scale of 10^{-18} s having in majority energies below 50 eV, which allows them to propagate on the average distances up to 10nm. Their propagation takes place in the range of 10^{-16}-10^{-15}s and determines another time scale of the nanodamage. The elastic electrons initially ionize the medium and finally, after loosing the majority of their energy in ionization events get bound to molecules or form solvated electrons. This leads to another process of biomolecular damage, the so-called Dissociative Electron Attachement (DEA) of molecules. Here the electron bound to the molecule induces a final bond breaking of such molecular ion. The process of electron-phonon coupling, participating in the relaxation of the energy by transfer of the energy from electronic degrees of freedom to motion of atoms takes place within a 1-1.5 nm wide cylinder leading to rapid heating of the medium and to a rise of pressure by a factor of 10^3 compared to standard pressure surrounding hot region [6]. The time scale of this phenomenon is in the range of 10^{-14}-10^{-13}s and leads to the formation of a shock wave which propagates further for a few hundreds of picoseconds [7]. It is possible that if DNA molecule is close to the ion path its strands can be broken by such a thermal heat-pressure wave. Furthermore, the transport of hydroxyl radicals and solvated electron is strongly enhanced radially even to a few nm out of the original ion path, which influences strongly dose effects and biodamage.

Summarizing, in the nanoscale damage the most important processes are primary ionizations, production of secondary electrons and photons (high and low energies) and due to their branching, the formation of radicals and excited species (electronic and vibrational), molecular fragmentations, the dissociative electron attachement, as well as local heating with heat transfer resulting in the formation of ion-induced shock-waves. These phenomena occur at time scales of approximately 10^{-18}-10^{-7} s and on the space scale between a single Angstrom up to tens of nanometers. Therefore it spans approximately 10 orders of magnitude in time and 3 orders of magnitude in space, which clearly emphasizes the multiscale character of biodamage.

1.3.1.3 Metal nanoparticles as potential radiosensitizers.

For the applications of metal nanoparticles as potential radiosensitizers there are a few aspects in their development that have to be considered, like their shape, size, material, coating of the surface, structure and their net charge. These properties influnce biological mechanisms of the cell regarding the uptake or toxicity. But in general, the understanding of their interaction with radiation is important.

Promising demonstrations of radiosensitizing properties were shown both in vitro and in-

vivo [8–12]. For the case of gold nanoparticles, there are several advantages concerning their biocompatibility, easy surface modification, synthesis and surface functionalization by ligand attachement (this allows for the selectivity of cancerous cells over healthy ones). The enhancement of the dose with AuNP in tumor cells was shown by Zhang et al. [13] by Monte Carlo simulation studies. They relied on the Geant4 Monte Carlo simulation toolkit calibrated with a high-dose-rate Ir-192 brachytherapy source. In the case of gold nanoparticles their studies corresponded to rather large objects, with radius of 50 nm, uniformly distributed in 1 cm^3 volume with a concentration of 9.7% gold nanosphere solution in a water phantom environment. Their findings showed that a radiation dose enhancement of clinically relevant magnitude, up to 28%, occurs.

Another work of Heinfeld et al. [8], based on studies with mices, used two different concentrations (2.7 g and 1.35 g per kg of body weight) of 2 nm AuNP in water solutions intravenously injected into EMT-6 mammary carcinomas combined with the irradiation of 250 kV X-Rays. The results on mice have shown 1-year survival rates of 86% (larger concentration), 50% (lower concentration) and 20% (no NPs).

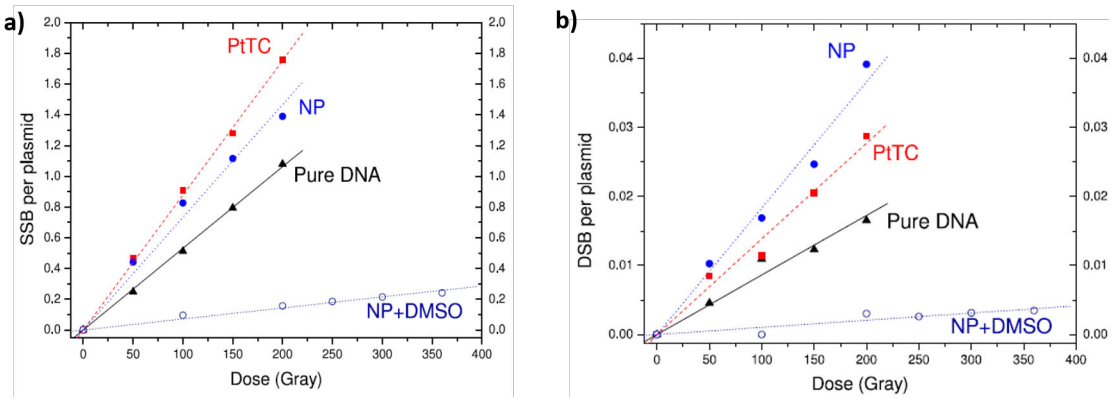

Figure 1.4 *a)The average number of single strand breaks (SSBs) and b) double strand breaks (DBSs) per plasmid versus the dose for pure DNA (black triangles), DNA in the presence of PtTC (dark squares), DNA in the presence of PtNP coated with PAA (dark spheres), and the same as the latter case with DMSO added in the solution (open spheres). The samples were irradiated by ions C^{6+} 276 MeV/amu (LET = 13.4 keV/mm) [14].*

Nanoparticles of high-Z elements are considered to enhance processes of radiosensitization by two mechanisms - increased emission of secondary electrons that can ionize biomolecules leading to bond breaking, and enhanced production of previously mentioned radicals close to metal surface [14, 15]. In fig.1.4 the assesment of biodamage based on the number of single and double strand breaks of DNA induced by irradiation with C^{6+} ions at 276 MeV/amu with Pt-based nanoparticles is presented. It is clear that for increasing dose the number of SSBs and DSBs is linearly increasing. The lowest slope is observed in the case of a solution of NPs with

DMSO, as DMSO works as the scavenger of hydroxyl radicals. The largest damage for SSB formation is observed when combined PtTC (Platinum chloro-terpyrydine) and irradiation is performed, followed by combined PtNPs and irradiation. On the other hand, a more interesting result is shown for the case of double strand breaks, where the presence of PtNPs increases the amount of damage by factor of more than 2 (for 200 Grays) if compared with the irradiation of pure DNA without any sensitizer, and by factor of ∼130% compared to PtTC sensitizer.

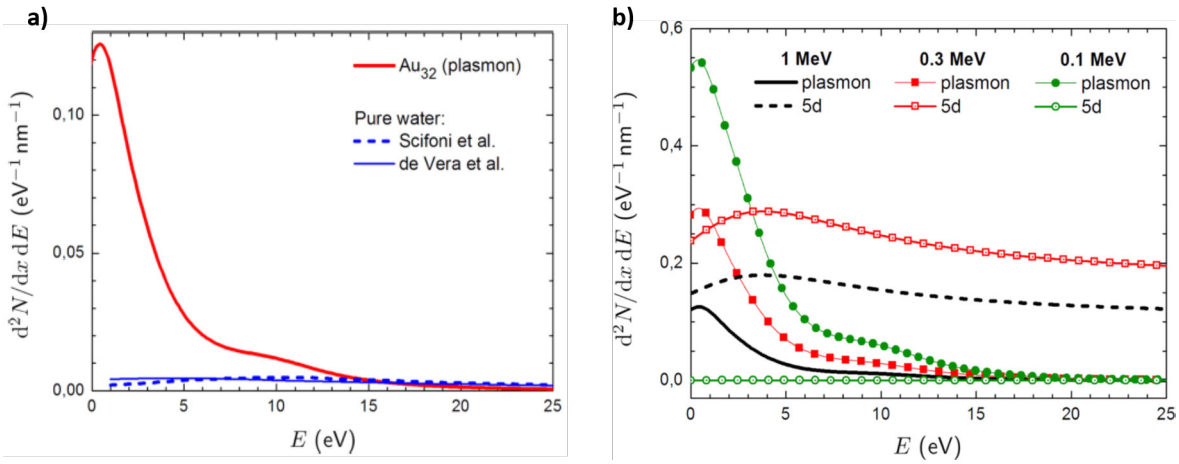

Figure 1.5 *a) Number of electrons per unit length per unit energy emitted via the plasmon excitation mechanism from the Au_{32} cluster irradiated by a 1 MeV proton (red curve) and the number of electrons generated from an equivalent volume of pure water (blue curve); b)number of electrons per unit length per unit energy produced via the plasmon and the 5d excitation mechanisms in the Au_{32} cluster irradiated by a proton of different kinetic energies [15].*

Calculations performed by the group of A. Solov'yov [15] show the effect of the plasmon excitations as one of the key mechanisms leading to enhanced low-energy electron emission from small gold clusters, along the excitations of large resonances of 5d orbitals of single atoms composing the Au cluster. In fig.1.5 a) the comparison of electron production by Au_{32} cluster (red curve) and by water (blue dashed and solid lines) with equivalent volume when irradiated with 1 MeV energy protons is shown. A striking difference of around 1 order of magnitude in favor of gold cluster is observed.

Fig.1.5 b) presents the production of electrons both due to plasmon and 5d excitations from Au_{32} clusters in different kinematic conditions.The case of 0.3 MeV protons corresponds to the Bragg peak (shown with green data points). As the production of electrons due to the giant resonances is dominant with respect to plasmon excitations for higher kinetic energies of projectile, their ratio is changing in favor of plasmon mechanisms when going to lower projectile energies close to 0.1 MeV. Here plasmon excitation is estimated to be about 3 orders of magnitude more efficient.

Element	Resistivity (Ω*m)	Element	Resistivity (Ω*m)
Bi	$1{,}29 \times 10^{-6}$	**Pt**	$1{,}06 \times 10^{-7}$
Au	$2{,}44 \times 10^{-8}$	**Hg**	$9{,}8 \times 10^{-7}$
Cu	$1{,}68 \times 10^{-8}$	**GaAs**	$1{,}0 \times 10^{-3}$ $\leftrightarrow 1{,}0 \times 10^{8}$
Ag	$1{,}59 \times 10^{-8}$	**Diamond**	$1{,}0 \times 10^{12}$

Table 1 *The comparison of electrical resistivity of Bismuth with other elements.*

1.3.2 Silver and bismuth as radiosensitizing precursors

As metallic model systems, that were used in the present experiments, silver and bismuth were chosen. Silver is a noble metal, known especially as antibacterial agent having therapeutic properties in the nanoscale due to its oxidative properties. In terms of the electronic structure, the silver atom is similar to the gold atom as the valence electrons have a similar configuration shifted by one principal quantum number n: Ag:[Kr]$4d^{10}5s^{1}$, Au:[Xe]$5d^{10}6s^{1}$. Noble metals (especially silver and gold and their combinations) are known as potential precursors for the production of nanoparticles and drugs for nanomedicine, especially for the treatment of cancer. They exhibit optical properties, that can be tuned for the desired wavelengths according to their shape (e.g., nanoparticles, nanoshells, nanorods etc.), size (e.g., 1 to 100 nm), and composition (e.g., core/shell or alloy noble metals), enabling imaging, photothermal and radiotherapy related applications. These NPs can also be functionalized with various moieties, like antibodies, peptides, and/or DNA/RNA to be more selective for cancerous tissues [16]. The mechanism of the radiosensitization of the AgNPs is not fully understood, however its anti-tumor capability was proven and initially attributed to the initiation of the apoptosis by activating the oxidative stress and influencing the fluidity of membranes. One of the proposed mechanisms is the release of silver Ag^{+} cation, which has the ability to capture the electron from the environment working as oxidative agent [10].
The second system collided with highly charged ions are clusters of bismuth. Bismuth is a material with very interesting and particular properties. From the pure materialistic point of view it is a brittle, crystalline metal that occurs in solid state under normal conditions. Among all the metals, bismuth is the most diamagnetic one. It has as well very low thermal conductivity compared to other metals and a large resistivity, around 80 times larger than that of silver and copper. A comparison of resitivities for Bi with various materials is given in table 1.

Bismuth undergoes a phase transition when the size of the system decreases. In case of thin layers Hoffman et al. confirmed the long-standing theoretical prediction that quantum confinement should convert Bi from a semimetal to a semiconductor at a critical thickness of the order of 300 Å [17].
There are two main reasons for choosing the bismuth metal as a second system for the inves-

tigation of the interaction of highly charged ions with clusters.

Firstly, bismuth is considered as rather non-toxic heavy metal, and it has been widely used in biomedical industries. Recently, bismuth nanoparticles have drawn great attention for application in biological sciences such as bio-imaging,-sensing, biomolecular detection, and X-ray radiosensitizing. In recent works, Hossain et al. [18] shows higher dose enhancements for Bi than Au and platinum nanoparticles for a given nanoparticle size, concentration, and location. At 350 mg/g, with bismuth nanoparticles 1.25 and 1.29 times higher dose enhancement is obtained if compared with GNPs and platinum nanoparticles respectively (irradiation by a 50 kVp source). Correspondingly, Auger electrons from bismuth nanoparticles provided 2 to 2.4 times higher enhancement than the other two kinds of nanoparticles.

1.4 Collisions of ions with clusters and nanoparticles

Clusters have become a field of very broad research in multiple contexts. This is partly due to the fact that there are many types of clusters, differing in their bonding type, their chemical composition and structure. For example a classification according to main types of bonding can be made:

1. ionic clusters like $(NaCl)_n$ with strong ionic bonds in the range of 2$\sim$4 eV;
2. covalent clusters like C_{60} or S_n with bond strength between 1 and 4 eV;
3. metal clusters like Na_n,Al_n,Ag_n with bond strength between 0.5$\sim$3 eV;
4. Van der Waals clusters like rare gas clusters Ar_n, Xe_n characterized by very weak bond energies below 300 meV;

As it was mentioned previously, the main interest of our studies concerns metal clusters as those were classified as good potential radiosensitizing precursors (although this statement does not exclude such properties for other clusters). In this part I would like to review some results known from previous studies concerning properties of metal clusters in the context of the interaction with ion irradiation.

Nearly all excitations of clusters involve electromagnetic interactions that couple directly the cluster electrons and ions. Such excitations can be static in slowly varying electric or magnetic fields or dynamic like in the electric field of a laser pulse. In case of dynamic excitations the process of measurement is often destructive and in the measurement process one concentrates on emitted products, like photons, electrons and fragments (neutral and charged).

1.4.1 Clusters in collisions with ions

Experimental studies of ion collisions with free metallic clusters are rare. The most examined system involves clusters of sodium with investigations starting in the 1990's. Sodium clusters were treated theoretically as a finite size prototypes with long range forces that can undergo

Coulomb dissociation if multiply charged. Because they create finite fermionic systems of delocalized electrons already for small cluster sizes (n$\sim$10), there were numerous questions about their behavior: the influence of electronic effects like shell structure, their stability in case of excess charges, similarities and differences to classicaly charged liquid droplets or atomic nuclei. Especially last point is very interesting, as in the case of nuclei one has to deal with the Coulombic repulsion of charges uniformly distributed within the nuclei and short-range nuclear forces, whereas for metal clusters the competition between Coulomb repulsive forces from the charge on the surface and cohesive surface forces plays a major role. This naturally affects the fissility of a cluster (tendency to undergo a fission process) which in case of metal clusters is the emission of small charged fragments.

Critical sizes against Coulomb dissociation for sodium clusters were examined in 1995 by [19] using beams of protons, O^{5+} and Ar^{8+} ions (in low energy regimes - 10's to 100's of keV of total kinetic energy). In this experiment, a beam of sodium clusters was prepared by a thermal gas aggregation source. At the time, the collision of cluster with ion beam was shown to be an alternative method to produce multiply charged metal cluster, as previously laser beams were used, which were characterized by pulse durations in the range of nanoseconds. The application of ion beams was advantageuos as the electric pulse exciting and ionizing the ion was in the range of femtoseconds (velocity close to Fermi velocity of electrons), allowing to produce distribution of internal energies (temperature) from cold to warm clusters depending on the collision parameter (for peripheric collisions the electron capture being the main mechanism of ionization, for central collisions high electronic excitations and ionizations are probable).It was shown that experimental appearance sizes depend on the cluster temperature.

Fig.1.6a) shows the increase of the experimentally observed appearance size of 4-times charged sodium clusters, ionized in collisions with O^{5+} projectiles, with the initial cluster temperature. For the lowest value of 80 K, the appearance size is estimated to be n_{app}=90. If the temperature is increased above 300 K, the appearance size increases to n_{app}=120. The increased temperature and hence the increased internal energy of the cluster helps to overcome the fission barrier; thus, more atoms are required to stabilize the charged system. For a comparison, the figure shows also for a given cluster temperature of 80 K that the appearance size varies in a wide range when sodium clusters are ionized in collisions with projectiles in different charge states, yielding the largest value for the case of proton collisions (and laser ionization) (n_{app} $\sim$120) and the lowest one for Xe^{28+} ions ($n_{app}\sim$70). This indicates that the energy transfer, related to the 4-fold ionization, depends on the projectile charge. The amount of the energy which is transferred during collisions of projectiles in different charge states with sodium clusters ionizing them 5 times is shown in Fig. 1.6b). For the highest projectile charge (q=28) the minimum energy transferred to the ionized cluster is about 1.5 eV. Decreasing the charge state to q=5, this energy slowly rises but it is still low (in the range up to $\sim$8 eV). However, for projectile charges below q=5 the situation changes. A 5-fold ionization requires for low charge state of projectile, a much closer approach between cluster and projectile, leading to a much larger transfer of energy. For case of q=3 and less (as well as the case of ionization by

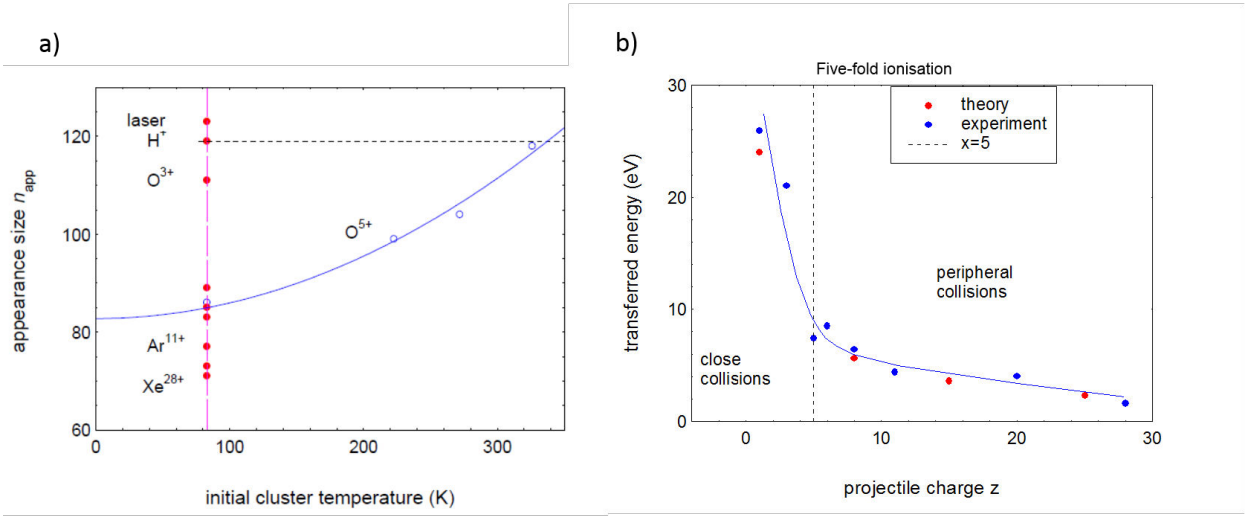

Figure 1.6 *The appearance size of 4-times charged metal cluster (Na) a) plotted as a function of the internal energy, represented by the temperature of the cluster (80 K), ionized by O^{5+} projectile (open circles, blue line); b) the appearance size for lowest experimental temperature obttained for different projectile charge states.*

laser) the cluster receives more than 20 eV, increasing internal energy strongly. The projectile charge state q=5 separates the regimes of penetrating and peripheral collisions. Therefore, the most effective way to observe the lowest possible appearance size for a multiply charged cluster, is to use projectiles in the highest possible charge state q and where capture occurs at large internuclear distances

Some theoretical ab initio approaches concerning the dynamics of fragmentation of small sodium clusters, highly charged above the fissility of X=1, were performed as well, for example by Blaise et al. [20] using the formalism of TDDFT calculations. In fig.1.7 the fragmentation of Na_{24}^{q+} cluster, charged above its X=1 fissility limit, is shown for q=4 to 7. For example for q=4 (also q=3) authors state that mainly sequential emission of Na_3^+ is observed on a 1ps time scale. Very seldom the emission of Na^+ is found. This process lasts long as the remaining residue, which develops a fission barrier becomes too cool to undergo a deformation leading to the emission of other fragments (at least at the scale of 5 ps). If the initial charge q increase to q=5 and above, the contribution of the emission of Na^+ is dominant, but all possible fragments up to hexamer are visible in fragmentation spectra.

1.4.2 Ion collisions with clusters of biomolecules in a water environment

In the effort of studying more realistic scenarios of fragmentation of biomolecules, the realization of experiments with biomolecules embedded into water clusters is of high interest.

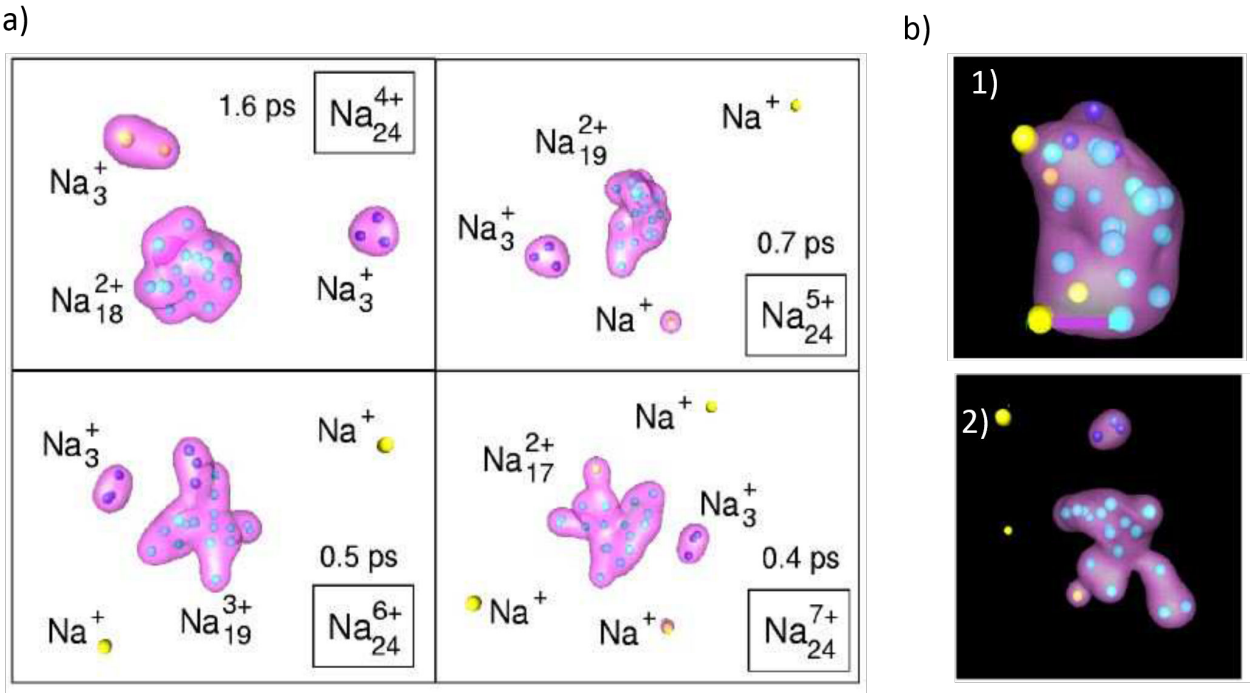

Figure 1.7 *a) Snapshots of the Coulomb fission of Na_{24} with different initial charges Q^+=4-7 and an initial temperature T_{in} = 800 K in the time scale of 1st picosecond of the fragmentation process; b) snapshots of the fragmentation of Na_{24}^{7+} cluster after 0.1 ps (1) and 0.45 ps (2), purple color representing valence electron density, while the yellow are sodium cations. Figures from [20].*

The environment can interact with the molecule undergoing energy relaxation processes and leading to fragmentation channels, which are not observed in single-molecule. Furthermore different redistribution of charge and energy (for example proton transfer inside the cluster) may occur.

Thymine is an example where different fragmentation channels are observed in the case of isolated biomolecules and in pure clusters of this molecule [21]. The authors observe the decrease of relative intensities of some of the fragments normally produced in the isolated molecule fragmentation as well as the appearance of new fragmentation channels in case of clusters, which are the loss of NH_2CH and OH molecules.

Regarding the issue of the energy and charge redistribution, in early studies with single molecules of C_{60} and clusters of $(C_{60})_n$ the evaporation of C_2 fragment observed in single ionization of single C_{60} molecule has a much lower yield when experiments with clusters were performed under identical conditions [22]. The explanation of such a finding is, that the energy transferred during the collisional process is redistributed among all degrees of freedom of the cluster system, meaning that less energy is deposited locally, decreasing efficiently the fragmentation yield and bond cleavage observed in the molecular case.

The most realistic experimental scenarios (like the ion passage inside the cellular environment) are investigations of biomolecules hydrated in a water environment. The radiolysis of water is a rather well understood phenomena and its description can be found in many radiation chemistry textbooks. Research of the ionization of water clusters $(H_2O)_n$ demonstrates that protonated water clusters $H^+(H_2O)_{n-1}$ are produced as well as the realease of OH radicals. Such water clusters have potential to emit also low-energy secondary electrons in the process of intermolecular coulombic decay processes [23, 24]. Also, from investigations with ions like Xe^{20+} at 300 keV by Maissony [25] it was shown that the emission of energetic cations takes place - for example of larger clusters of $(H_2O)_{8,9,10}H^+$ with kinetic energy of 2 eV and protons with energies as high as 15 eV.

Mixed clusters (nanosolvated biomolecules) can mimic the conditions in biological tissues to large extent. One of the first experiments of this type was the collision of adenosine 5-monophoshphate with neutral atoms of Neon and Sodium [26] (cooperation of groups from Aarhus and Caen). It was performed by an electrospray ion source at a collision energy of 50 keV. The applied CID method allows to prepare ions of AMP with a variable number of attached water molecules, which gives the possibility for the comparison of fragmenation channels depending on the solvation degree. By comparison of spectra of isolated molecule and the molecule solvated in H_2O , it was seen that when number of water molecules surrounding the AMP molecule was larger than 13, the dissociation of the biomolecule is not anymore observed as the excess of the energy was taken for the loss of loosely bound water molecules, proving the protective effect of the chemical environment.

A similar study was done for the case of isolated and nano-hydrated uracil clusters in collision with C^{4+} at 36 keV, [27]. Normally, intense fragments HCNH and CO are observed for the isolated uracil case. In case of uracil surrounded with water shells for the first time hydrated and protonated fragments were observed, which was not seen for case of other hydrated nucleobases like adenine and thymine [28, 29]. This finding is very interesting, because it indicates a strong interaction between uracil and water molecules which is due to hydrophilic sites in Uracil. The presence of smaller water clusters bound to the observed molecular fragments with simulatneous survival of hydrogen bonds during fragmentation of the overall ensemble is observed.

1.4.3 Noble metal nanoparticles embedded in matrix and irradiated

Regarding the interaction of large deposited silver nanoparticles (3 nm and more) with ions, some investigations were done at GANIL(Caen) and ARAMIS(Orsay). For both cases the nanoparticles were chemically synthesized and confined between two silica layers [30]. There were three classes of monodisperse metallic NPs: pure Au, pure Ag and $Au_{0.5}Ag_{0.5}$. The samples underwent the irradiation in the nuclear stopping and electronic stopping regimes, using 4-MeV Au ions (in order to create small „satellites") and 74-MeV Kr ions. The morphological investigations were performed with transmission electron microscopy.

The TEM images of the irradiation of large Au nanoparticles ($>$10 nm) are shown in fig.1.8.

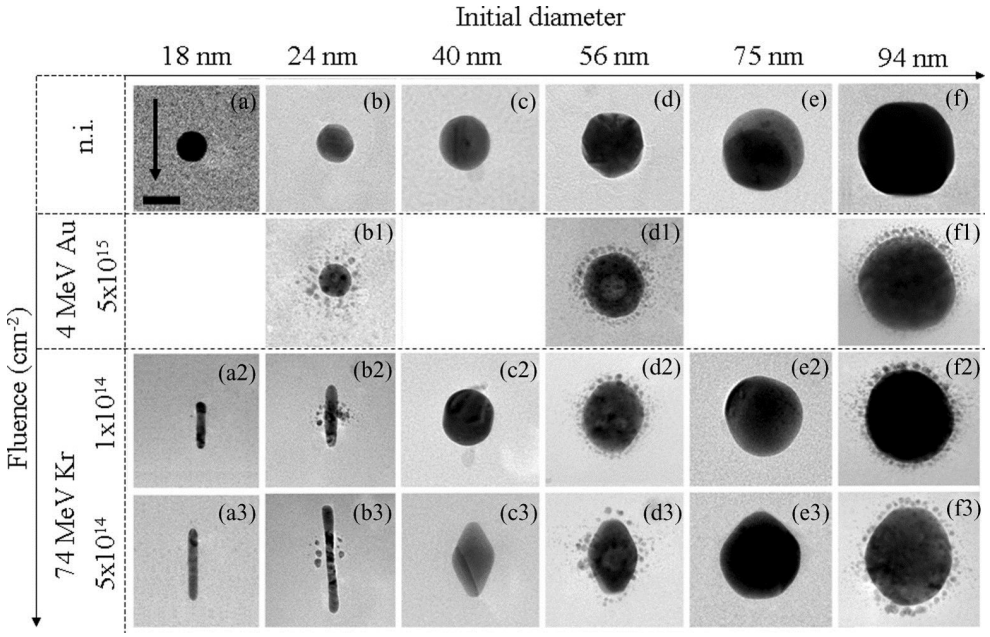

Figure 1.8 *The diagram showing the morphological changes of Au NPs for increasing initial size (x axis) and irradiation fluence (y axis). The ion-beam direction is indicated by the arrow. Samples (b1), (d1), and (f1) have been preirradiated with 4-MeV Au ions, resulting in the halo of satellites around the central NPs (a2) to (f3). Afterwards, all the samples have been irradiated 74-MeV Kr ions. Adapted from [30].*

It is clear that a correlation between the size of the NP and the final morphology exists. The largest objects are not deformed even at the highest irradiation fluence. For cases between 30 and 70 nm a slight deformation is observed for lower fluence, while in higher fluence clear deformation becomes observable (for case of NP of 75 nm elongation towards direction of the ion beam is clearly visible). For objects with size of around 40 nm the elongation is observed on both sides of the NPs along passage of an ion. NPs with diameter from 10 to 30 nm are transformed continously into nanorods and nanowires.

A more detailed investigation of very small gold NPs was performed by Rizza et al. [31], showing that irradiation of NPs of gold embedded in a silica matrix with sizes close to ∼10-20 nm can result in a total dissolution of the original object into much smaller clusters of diameter close to ∼2 nm or less. It is called the „halo" of smaller clusters which surround the original object. In fig.1.9a) the original non-irradiated NP is shown and f) is the original size distribution of NPs as synthesized, with centroid at around 16 nm. Images from b) to e) are examples of the evolution of the object as a function of the irradiation flunce with associated size distributions in the images marked f) to j). While increasing the irradiation fluence, the average size of larger NPs is shifting gradually towards smaller sizes, more and more dissolution is observed until the final complete dissolution into numerous small precipitated metal clusters occurs with size close to 2nm at largest fluence.

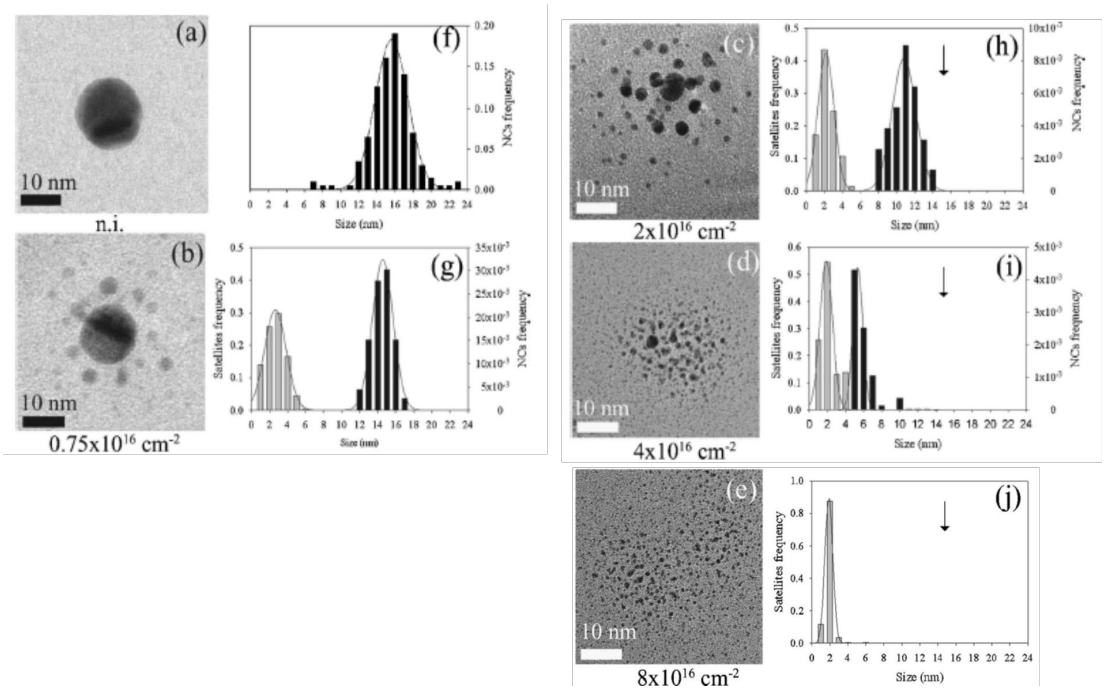

Figure 1.9 *The TEM micrographs of the evolution of gold nanoparticles under 4 MeV Au irradiation at temperature of 300 K. The samples were irradiated at increasing fluences up 8·10^{16} cm^{-2}. The corresponding size distributions of NP and satellites are shown on the right part of TEM images. Adapted from [31].*

1.4.4 Summary

I would like to emphasize that the investigation of clusters is a very broad discipline and it is beyond the scope of this introduction to review all interesting aspects. The main goal was to show that important motivation stems from the possible applications of metal clusters in future hadrontherapy treatments (radiobiological context) and because of that more detailed understanding of their behavior is necessary. The realization of molecular beams of nm-sized metal cluster/nanoparticle colliding with ions, is one important step in the strategy to create realistic target imitating the situation in hadrotnherapy, namely: nanoparticles with possible molecular coating (as it is introduced into the organism), solvated in water environment with possible other biomolecules (or their clusters) present.

The behavior of isolated (bio)molecules, pure water clusters and water-solvated biomolecules in collision with ions was already investigated and is known for some specific cases. In terms of pure metal clusters several studies on sodium clusters have been performed. So far no systematic studies on other types of metal clusters, especially noble metals like silver or gold as well as large nanoparticles containing a few thousands of atoms are performed. This thesis is devoted to contribute to our understanding of the above mentioned issue with the final aim to create a perfect target by the combination of the metal particle solvated in water and decorated by other biomolecules and ligands.

The novel experimental set-up : COLIMACON DUO | 2

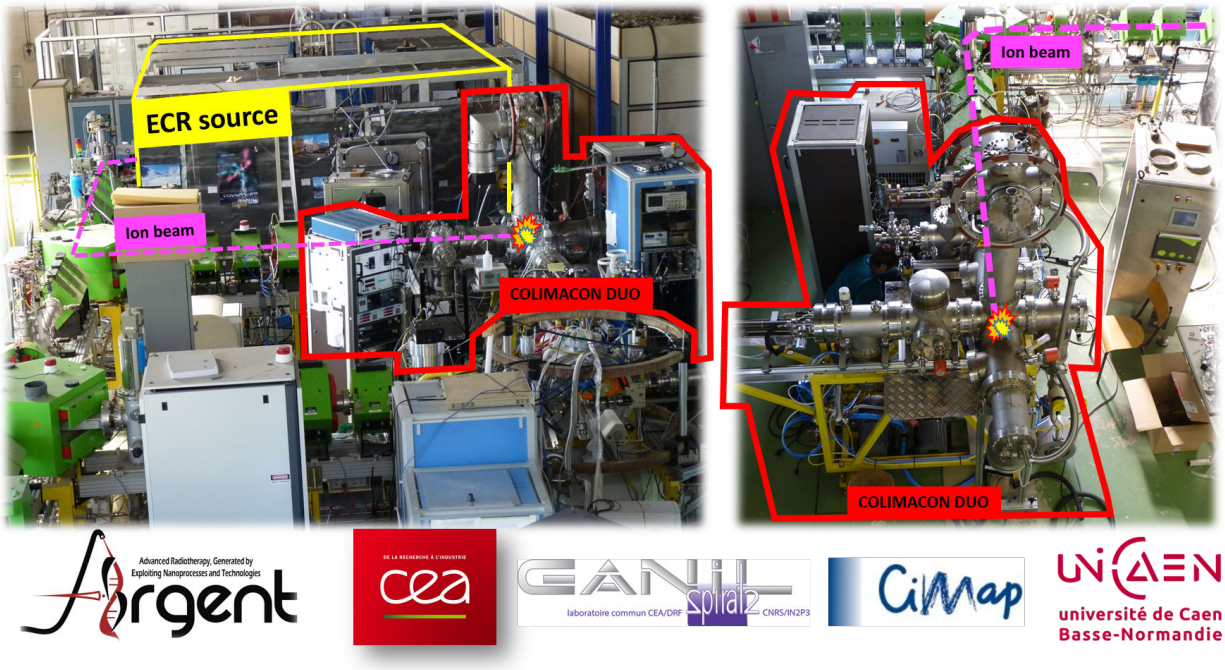

General views (side view on the left, top view on the right) of the COLIMACON DUO set-up (red frame), its installation in the ARIBE facility and its connection to the ECR ion source (yellow frame) where multiply charged ions are produced. The purple line shows the beam transport from the ion source to the experiment.

The main objective of the work described in the following is the design, the construction and the validation of a new experimental set-up and the performance of collision experiments between ions and large, free metallic nanoparticles in the gas-phase. This development is a necessary step for improving our understanding of the complexity and mechanisms governing the interaction of ions with free nano-objects in general (the studies are not limited to metallic nanoparticles only, but allow also for the creation of molecular beams of clusters from semiconductors and isolators).

The quantitative description of the interaction of nanoparticles with ions is of interest and beneficial for many reasons. From the physical point of view the evolution after the energy deposition in a nanoparticle, representing a many-body system, is too difficult to be calculated using a precise ab-initio approach and experimental data deliver the necessary validation for theoretical assumptions and simulations. On the other side, in practical applications ions are used to modify various properties, especialy on the nanoscale in today's opto/nanoelectronic industries as well as in biomedicine for example in ion beam-based therapies. Here, fundamental studies have the potential to improve the material properties and to develop more efficient methods as for example in the nanoparticle enhanced ion beam cancer treatment.

The basic idea to realize such a collision experiment is to use a crossed beams device where an accelerated beam of multiply charged ions crosses a slow beam of neutral nanoparticles and where the positively charged products of the interaction are detected and analysed using time-of-flight mass spectroscopy.

This chapter provides the description of the main components of the experimental set-up called COLIMACON DUO which was further developed on the basis of the previously existing COLIMACON set-up, which stands for COLlision entre des Ions et des Molécules ou des Agrégats COmplexes Neutres (eng. Collision between Ions and Molecules or complex neutral clusters). The essential modifications and new developments concern the production of a beam of neutral, large, metallic nanoparticles and clusters, a purification chamber for producing a clean neutral cluster beam and a characterization chamber where nanoparticles are deposited at low energies on a substrate allowing for size-analysis with the aid of AFM or TEM microscopy. From the existing COLIMACON device only the ion beam guiding system as well as the interaction region and the time-of-flight device have been used.

2.1 General set-up description and short historical note

The present experiment is based on the interaction of two collimated beams: a continuous dense molecular beam of neutral nanoparticles is crossed under 90° in the interaction zone with a pulsed beam of multiply charged ions. The interaction occurs under high vacuum conditions with a base pressure of $\leq 10^{-9}$ mbar; with operating cluster source the pressure in the interaction zone increases to $\approx 10^{-7}$ mbar due to the Ar gas flow which is required in the cluster source for sputtering and particle transport. In fig.2.1 the main components of

the setup are presented: the magnetron based cluster source, the differential chamber (where removal of charged clusters produced by the source takes place), the interaction zone where beams of clusters and projectiles cross and the installation of the additional Ar ion gun with beam bending system for test measurements.

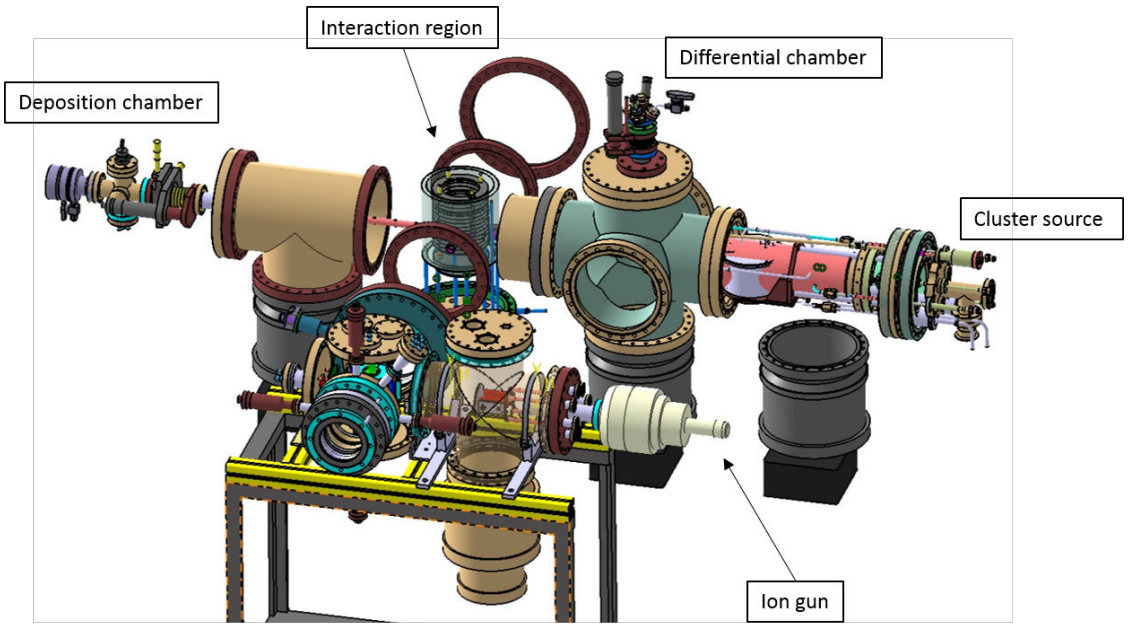

Figure 2.1 *Design of the COLIMACON DUO set-up with its main components: New cluster source based on a magnetron discharge, differential chamber for preparing an intense neutral beam, Interaction zone where both beams cross, deposition chamber for characterizing neutral particles; additional Ar ion gun and beam bender for test measurements. The ToF system which is mounted vertically above the interaction zone is not shown,(created with CATIA Software).*

Positively charged ions produced in such collisions are extracted by a pulsed electric field applied in the interaction region guiding them towards a high-resolving time-of-flight mass spectrometer. Finally they are post-accelerated to high voltages (19 kV) and are recorded as a function of their mass/charge ratio.

For the success of the experiment it is important to form a well defined and very intense beam of neutral nanoparticles. Earlier studies of cluster formation in gas aggregation sources have shown that the size distribution of neutral clusters follows a log-normal distribution where the position of the maximum depends on the source condition: vapor pressure and character of the material to be aggregated, density of the aggregation-supporting gas (He or Ar), cooling conditions and aggregation length.

With the existing COLIMACON device several types of ion cluster interactions have been studied based on the use of a gas aggregation source and an oven device. This concerns clusters of fullerenes or PAHs (polycyclic aromatic hydrocarbons), of nucleic acids and amino

acids and radiosensitizers and smaller sodium clusters. (references to be given) In all cases the cluster material was evaporated in an oven device at temperatures below ∼300°C (exception C_{60}: ∼600°C) and the corresponding cluster masses have been below ∼5 kD. In contrast, in the present device much larger systems, up to ∼100 kD, are investigated, requiring longer times for particle analysis leading to lower repetition and signal rates (see discussion further below). Thus, the demand for a high density of the neutral target is of crucial importance.

In our laboratory large clusters of copper, silver and bismuth have been produced in a separate set-up using a magnetron discharge. However, the obtained intensity or beam quality was never sufficient to perform ion-cluster collisions in the gas phase successfully.

Concerning the projectile, the ion beam is provided by an ECR ion source and guided towards the experimental area with the aid of a set of dipole and quadrupole magnets as well as beam steering units. The ECR source can produce multiply charged ions in charge states up to 30 (Xe^{30+}) at energies up to 15 kV/charge from gas-phase precursors. As the ECR source has a limited time availability, the COLIMACON DUO set-up has been equipped with an additional ion gun and beam bender in order to provide on a daily basis singly charged ions with energies up to 5 keV (project HYDRASE).

2.2 ECR ion source

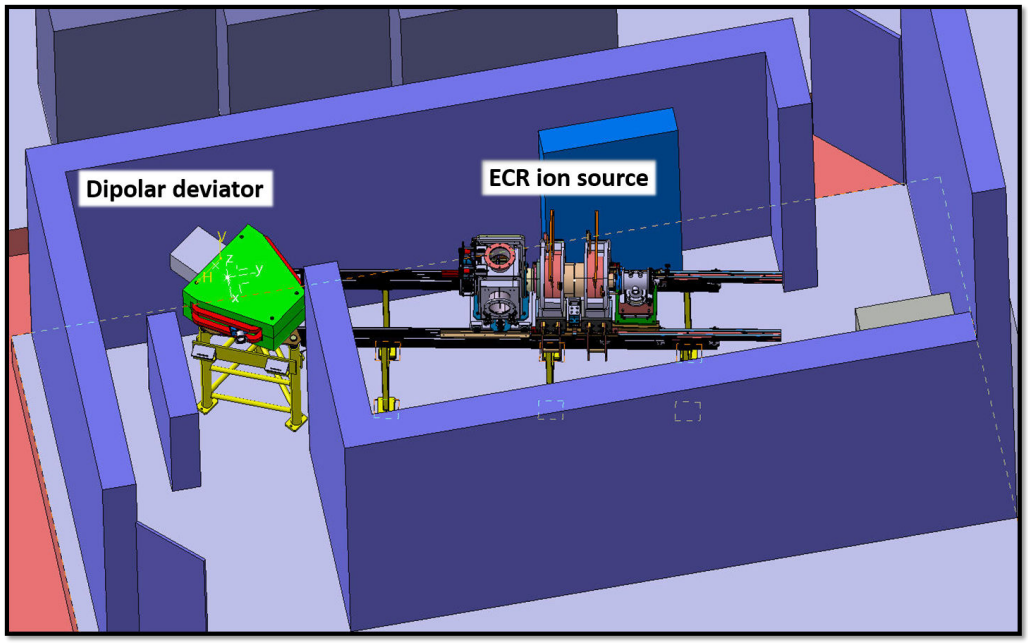

Figure 2.2 *3D design of the GTS ion source housed inside a special protection cage made of walls of lead.*

2.2.1 Mechanisms for the production of highly charged ions

The use of ECR (electron cyclotron resonance) ion sources is a very common way to generate intense high quality beams of multiply charged ions for basic research (nuclear, atomic and molecular physics), for industry (semiconductor, metal processing technologies) and for medicine and radiobiology (ion beam based cancer therapies), where the design of the source may strongly be tied to its application. The performance of ECR ion sources changed strongly over the last 40 years, showing an increase of the extracted ion current intensity by a factor of more than 100 comparing machines built today to those built in the 1980s [32, 33].

The improved generation of multiply charged ions in such sources became possible due to more powerful magnets and microwave generators giving stronger magnetic fields and higher frequencies. These sources are widely used by the accelerator community due to their ability to produce continuous high intensity beams from any element. Additionally, the discharge inside the source is created without electrodes consuming only the injected material (gas or metal vapor), thus, allowing for a long operation time.

In fig.2.2 the 3D design of the GTS Source installed in the ARIBE Facility is illustrated. The whole setup is placed inside the radio-protective shielding cage. Fig.2.3 shows the cross-sectional cut through the main part of the ion source, specifying the crucial stages for the creation of multiply charged ions, which are the gas injection and microwave entrance, the main discharge chamber surrounded by the magnetic mirror device and containing the hexapole magnets for creating a magnetically confined plasma . Furthermore, the extraction part, where the extraction electrodes are localized, is shown.

In the 1980ths, the first ECR on sources were characterized by a low ion confinement time inside the plasma being of the order of 10^{-4} seconds. Under these conditions the charge state distributions of the extracted ions showed a maximum at q=2+ for nitrogen or argon, [34, 35]. Important improvements of the magnetic fields configuration using an additional hexapole field and the injection of a pre-formed plasma allowed for a more efficient ion production. These methods resulted in much longer ion confinement times (by a factor of about 100) which shifted the charge state distributions to higher charge states. Such a topology of the magnetic field connected to an axial extraction system is found in all modern designs of ECR ion sources.

2.2.2 Working principle

In ECR ion sources the magnetic confinement and the heating by electron cyclotron resonance are used to produce a plasma of energetic electrons and rather cold ions. The electrons in the plasma are represented by two populations: a cold one with temperatures corresponding to around 20 eV and a high energy tail reaching energies of about 100 keV. The ions have energies of a few eVs and their charge state is produced by sequential ionization by electron impact. An important parameter in this process is the size of the electron impact ionization cross section, which strongly decreases with the charge state of the initial ion as shown in

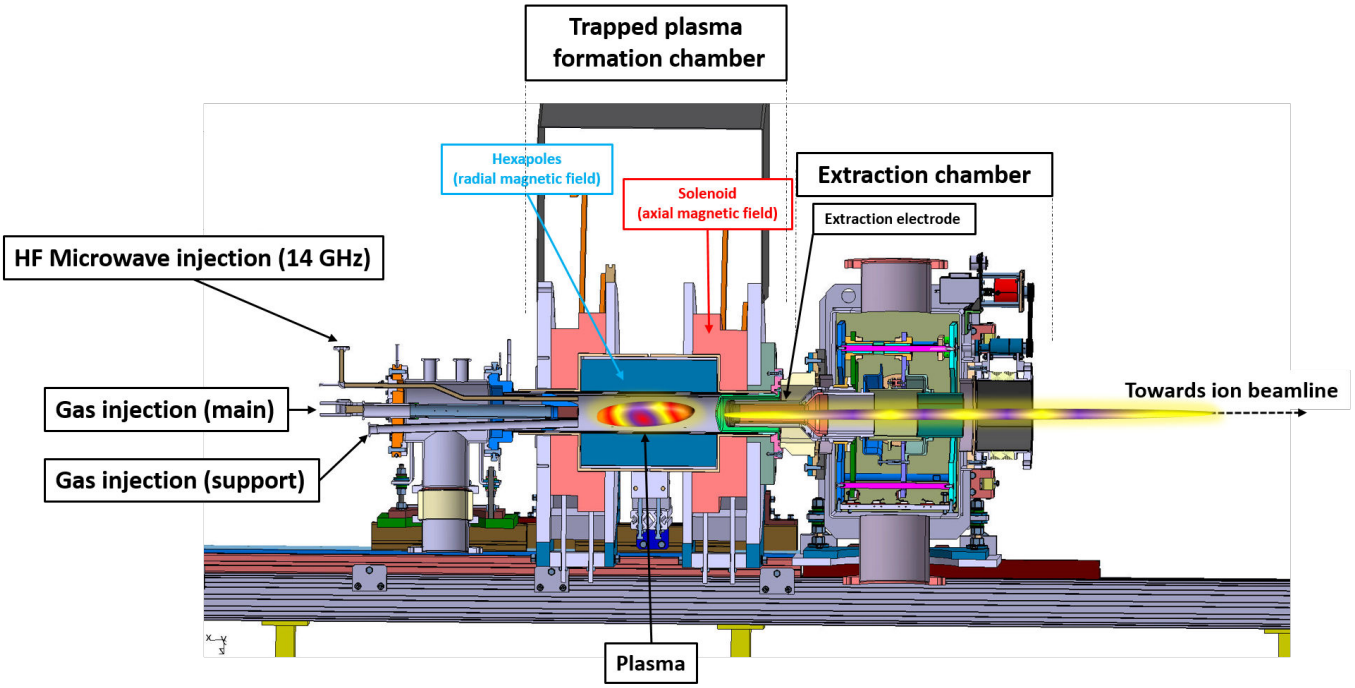

Figure 2.3 *Cross-sectional view through the GTS ion source with stages of magnetically confined plasma formation and extraction.*

fig.2.4 for the case of Ar ions. Compared to the single ionization cross section for a neutral Ar atom, the maximum cross section for producing Ar^{16+} ions starting from Ar^{15+} is lower by a factor of about 3×10^3, depending on the electron energy.

These processes require a finite time, for example for the production of ions in higher charge states about 10^{-2} s are typical, underlining the importance of long plasma confinement times. The confinement of particles inside ECR sources is very complex phenomenon and interested readers may find a more detailed description of this phenomenon elsewhere [36, 37]. It is worth to note shortly, that in the ECR plasma the temperatures for ions and electrons differ strongly, especially electrons having populations of cold, of warm and of hot distributions. As the confinement time depends on the temperature, it is necessary to optimize the plasma parameters and the device configuration. For example by the inclusion of a hexapole device the radial confinement is improved and electrons pass many times "back and forth" crossing the resonance zone, where the magnetic field strength yields a cyclotron resonance frequency which corresponds to the injected HF-frequency. Here the stochastic heating of the electrons occurs. The loss of slow electrons [38] can be counterbalanced by the injection of slow electrons from a separate electron gun, by including a metallic disk close to the plasma or a well chosen material of the plasma chamber (for example Al) in order to increase the production of secondary electrons.

Another important parameter is the neutral particle density of the plasma, which is for

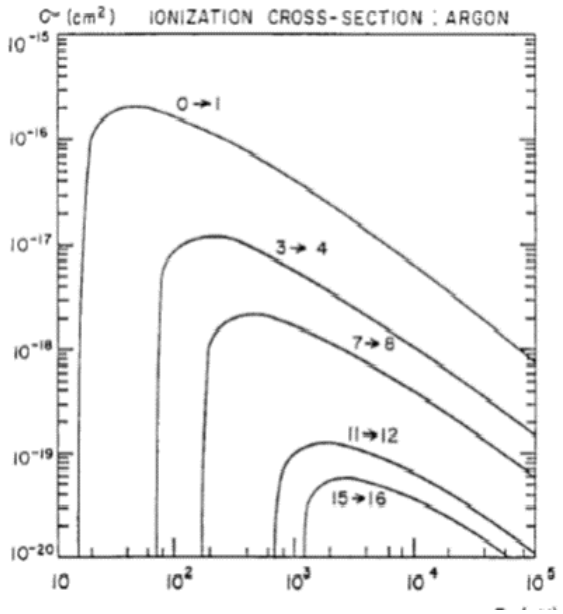

Figure 2.4 *Cross section for subsequent ionization of argon atom with electron impact as a function of electron energy using the formula of Mueller-Salzborn, [39, 40].*

low-density plasmas of the order of 10^{11} cm^{-3} and for high-density plasmas more than 10^{12} cm^{-3}. For high densities, apart from the loss of confinement, another process occurs, which has a strong impact on the loss of ions in high charge states. This is the charge exchange process between ions and neutral atoms. The corresponding cross section for charge exchange is given by the semi-empirical formula [39, 40]:

$$\sigma_{q,q-1} = 1.43 \times 10^{-12}\ q^{1.17}\ V_{0,1}^{2.76}\ (cm^2) \tag{1}$$

where $V_{0,1}$ is the first ionization potential in eV and q is the charge state of ionized atom.

For higher charge states these values are typically larger than the corresponding electron impact ionization cross sections by 3 or 4 orders of magnitude. In order to reduce this loss process the pressure inside the plasma chamber is kept below 10^{-6} mbar.

The performance of the ion source concerning the production of highly charged ions can be improved by the so-called gas-mixing effect. In this case a second gas which is lighter than the working gas is introduced into the plasma chamber. For example for producing Xe^{25+} ions, the gas oxygen may be used as a support gas which can only be ionized up to charge state 8. Thus, the charge state balance in the plasma changes and ion losses are reduced. The accepted explanation of this effect is that there is the energy trasnfer in collisions between the lighter mixing gas and the ions (heavier). Additionally, the average charge of the plasma is lowered by lighter ions increasing plasma confinement times [41].

The plasma chamber is polarized by an electrostatic potential (several kV) which assures

the acceleration of the ions out of the plasma chamber into the grounded beam transport system and thus defines the kinetic energy of the ion beam.

2.2.3 Performance of the GTS Ion Source at ARIBE

The source GTS (Grenoble Test Source) is kept at a voltage V_{source}; therefore, the kinetic energy of the produced ions in charge state q arriving at the grounded interaction region of the experimental set-up is given by E_{kin} (2) :

$$E = q \times V_{source} \tag{2}$$

The charge distribution of the ions produced in the GTS source depends on the conditions of the plasma, so both on the user-set operation parameters as well as the physical properties of the ionized atoms. Ions in all charge states are extracted from the source, however, a selection of the charge of interest takes place in the magnetic dipole stage localized at the exit of the source. The magnetic field vector is perpendicular to the vector of the velocity of the incoming ions, thus the central Lorentz force deflects the ions according to the equation :

$$F_{Lorentz} = -q \cdot \vec{v} \times \vec{B} \tag{3}$$

and the resulting curvature radius for trajectory bending is given by :

$$r = \frac{mv}{qB} \tag{4}$$

where m,v,q stand for mass, velocity and charge of the ion, respecitvely. B is the magnitude of the magnetic induction. This radius has to correspond to the geometrical radius defined by the exit slit of the magnetic device. i.e. for a given ion mass, ion velocity and and charge state, the magnetic flux has to be adjusted correspondingly to separate individual ion masses.

2.2.3.1 Beam transport

Once the beam of ions is properly extracted from the ion source one needs to be able to successfully transport the beam from the source to the interaction region of the experimental set-up. Guiding and shaping of the ion beam is possible due to the use of a combination of electromagnetic multipole units imposing the Lorentz Force on the passing ions. Particularly for the beam deflection, one uses dipolar magnetic fields or electrostatic fields, while for the focusing or defocusing it is the combination of quadrupole units, that act as focusing lenses. Hexapoles allow for the corrections of the chromatic abberations. Additionally the set of 2 perpendicular (horizontal and vertical) slit systems for beam profiling is installed at the first part of the beam transport system. In the following the ion beam is deflected with a large dipole to enter the final beam line leading directly to the COLIMACON setup, presented in fig.2.5. Before entering the experiment, the beam passes through a pin-hole with a variable radius (1 to 10mm). Along the line there are further additional elements for beam control and its characterization, like Faraday cups, profilers and gate-valves.

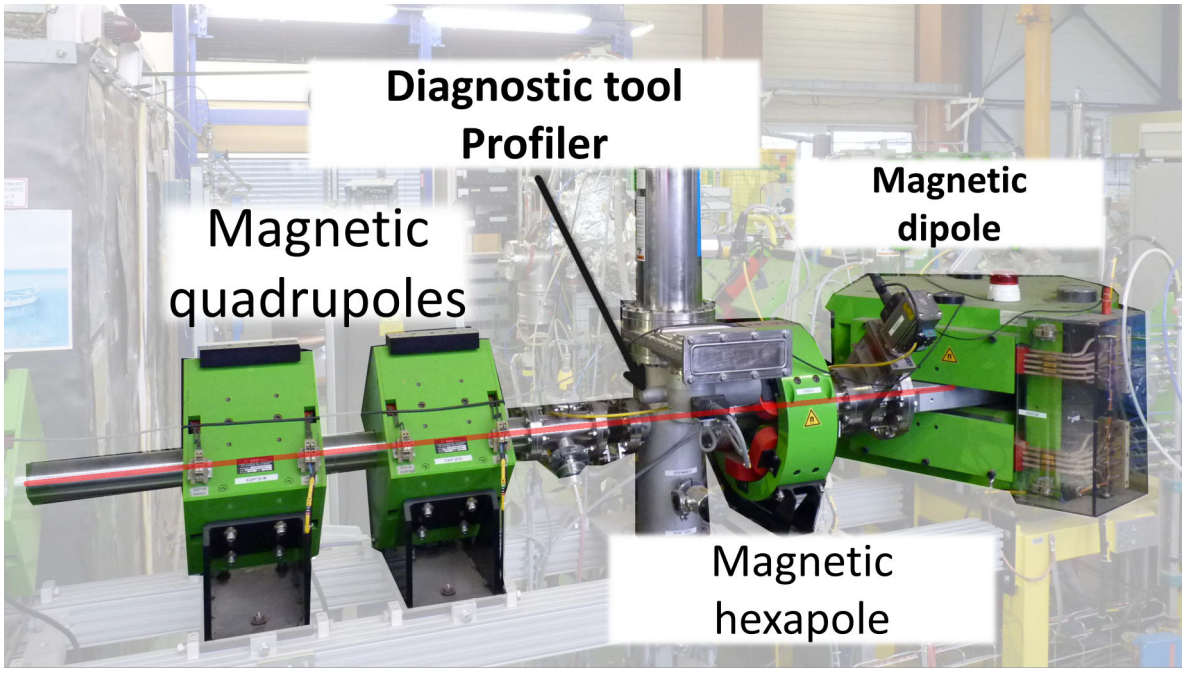

Figure 2.5 *Photo presenting the ion beam transport system between COLIMACON Setup and ECR Ion source with its most important elements : bending dipole, set of quadrupoles, hexapole and diagnostic tool for verification of the beam profile.*

2.2.3.2 ECR GTS source characteristics

The ion source in ARIBE works with the HF frequency of 14.5 GHz and an HF power of 1000W, producing ions from He^{+} up to Xe^{30+}. As the extraction voltage can be varied from 5 to 15 kV (currently the source is upgraded to allow for the application of 30 kV), the energy of the ions can reach from 5 up to 450 keV (900 keV soon), depending on the type of the ion. For convenient conversion from the energy of the ion to the velocity one can use formula

$$v(\frac{m}{s}) = \sqrt{\frac{2E_{kin}}{m}} \tag{5}$$

where E_{kin} - energy of the ion in Joules and m - mass of the ion in kg. If expressed in atomic units it has the following form:

$$v(uma) \simeq 0.2\sqrt{\frac{E_{kin}(eV)}{m(uma)}} \tag{6}$$

Exemplary spectrum of the charge distribution of produced ions for the example of oxygen is shown in fig.2.6. with two images of horizontal and vertical cuts through ion beam showing its profile.

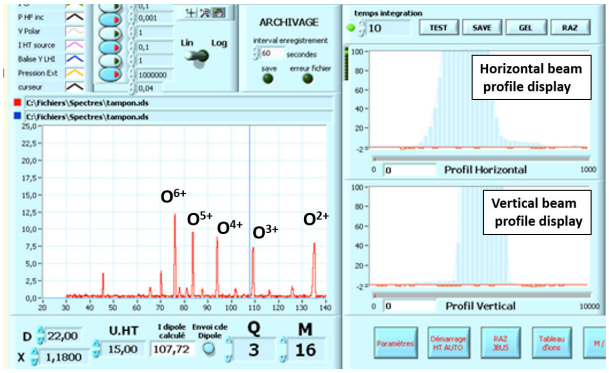

Figure 2.6 *Print-screen of the control unit of the ECR ion source with charge distribution spectrum of the oxygen ions and the ion beam profiles (vertical and horizontal).*

2.2.4 Ion gun

As mentioned previously, the availability of ion beams from the ECR ion source is very limited, mostly restricted to experimental campaigns which were granted in the application process. To account for this limitation a separate ion gun was installed and connected to the experimental set-up capable to deliver singly charged ions for testing purposes. During the experiments two different models were exploited : the model IS40E1 produced by the PREVAC company (fig.2.7 a) and the model 04-303 (fig.2.7 b) constructed by Perkin Elmer (currently RBD Instruments).

Both sources differ in their technical and design properties, however the main principle of operation and the optimum beam parameters are almost identical. The Ion guns provide singly charged ion beams mainly from noble gases like argon, neon or helium with low kinetic energies (from 1 up to 5 keV). Beams of other highly reactive gasses like O^+ can be obtained using a special type of filament.

The main principle of positive ion formation inside the ion gun is based on the ionization of atoms due to the electron impact. The gas (i.e. argon) is injected inside the ionizer, which is shown in fig.2.8. The cathode is a resistively heated wire made of tungsten. Its potential $V_{cathode}$ is kept 120 V below that of the anode V_{anode}, which is represented by the metallic cylindrical grid. In this region the ions are formed.

During the operation the pressure is kept in the range of $P_{ion\,gun}$=10^{-6} mbar. The 1st ionization potential of argon is I_{1st}=15.76 eV and the cross-section for electron impact ionization has its maximum at around E_{kin}=37 eV (see fig.2.4).

Following fig.2.8, the formed Ar^+ ions are accelerated from the repeller towards the centering ring which is grounded and they have kinetic energies between 1 and 5 keV. After leaving the repeller stage they pass through exctraction plate with potential $V_{extraction}$ which is usually a fraction (from 60 up to 95%) of the repeller potential and in combination with the exit ring it creates the electric field determining the trajectory of the outgoing ions allowing for a better

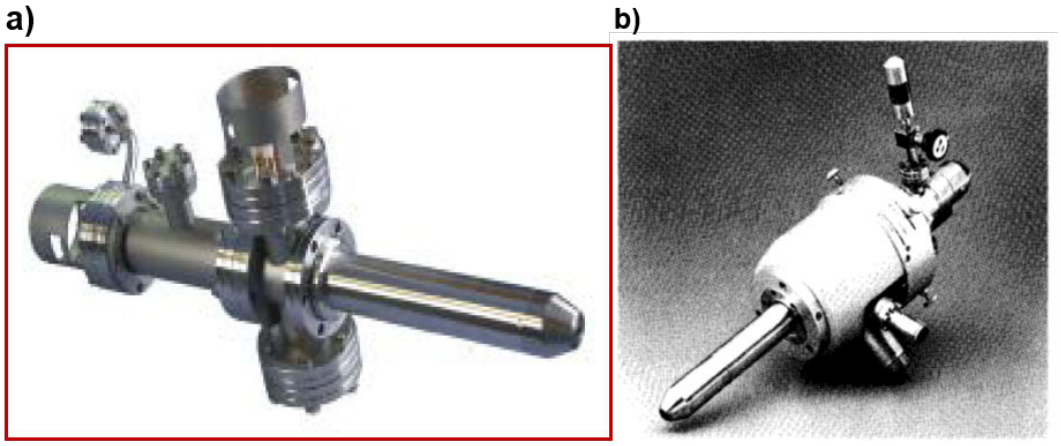

Figure 2.7 *Ion gun models that are available for the experiments at the COLIMACON DUO Setup: a)model IS40E1 from PREVAC and b) model PHI C04-303 by Perkin Elmer (nowadays RBD Instruments).*

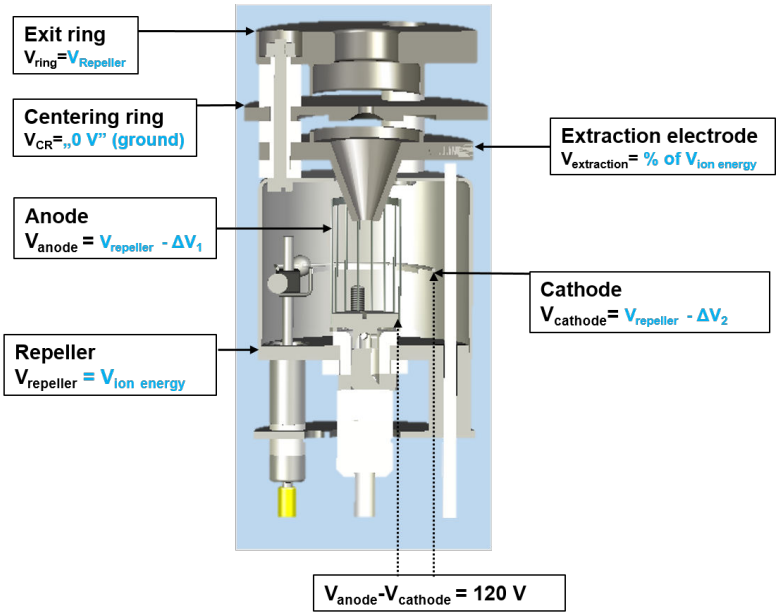

Figure 2.8 *Schematic view of the ionization head (ionizer) of the ion gun showing the main construction elements with their respective potentials.*

focalization/defocalization of the beam before it enters the „pulsation stage". The intensity of the ion beam is measured with a faraday cup localized inside of the adjacent „bender" chamber (see fig.2.9).

As shown in Fig.2.9, it was necessary to modify the beam guiding system in order to allow for the separate supply of the experimental set-up with beams of the ECR and from the Ar ion gun. In fig.2.9 the ECR ion beam comes from the left side and can after passing the inactivated

beam bender unit on a straight line the interaction region. The beam of the Ar ion gun (coming from below as shown in fig.2.9) is bent in the activated beam bender unit by 90° in order to reach the experiment. The pulsed beam of the Ar ions from the ion gun can be produced in a deflection stage, where voltages at deflection plates are switched between V_{defl}=300 V and ground potential with a kHz frequency. The beam "bender" is formed of four electrodes coupled into pairs creating quadrupole-type electric field. Both pairs are polarized with negative and positive potentials ($+V_{bender}$,-V_{bender} respectively) corresponding to the energy of the passing ions: for example for a kinetic energy of the ion of E_{ion}=3 keV an equal potential of V_{bender}=3 kV is required.

It is worth to note that obviously the output current from the ion gun is much lower than that from the ECR ions source. This disadvantage can be partially improved by increasing the length of the ion pulse. However, it has a significant influence on the mass resolution of the recorded particles, as longer ion pulses allow the cationic products to travel freely due to their inital velocities and therefore spreading spatially into a much larger volume.

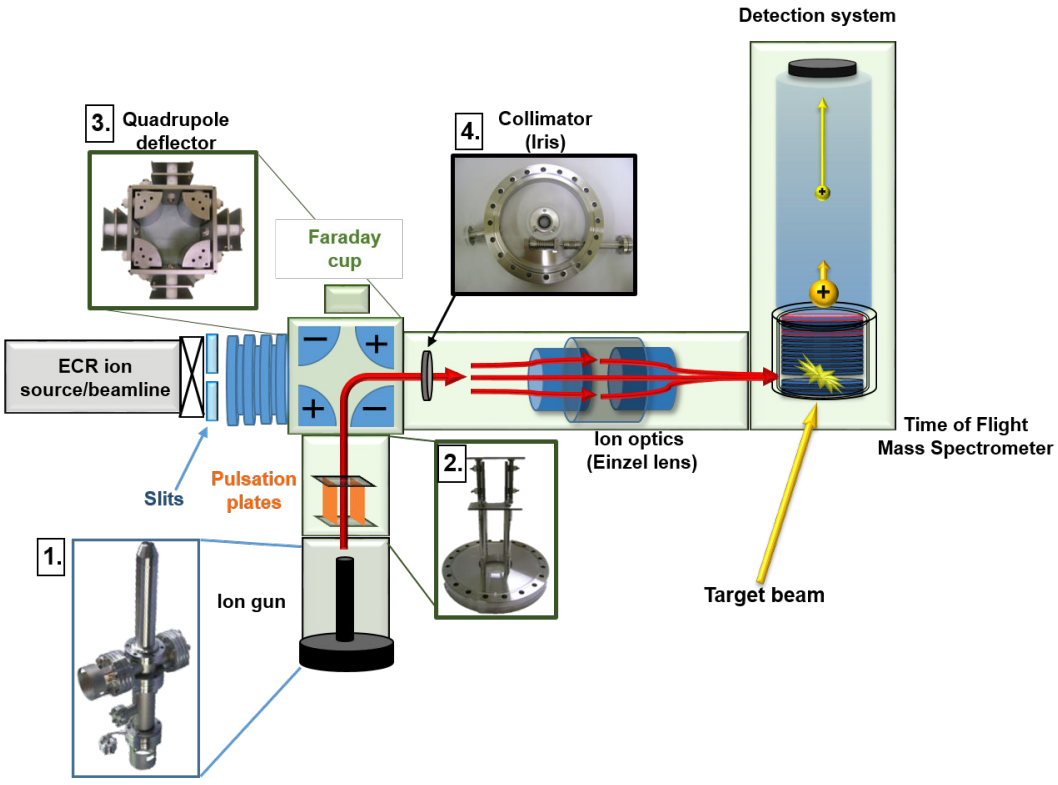

Figure 2.9 *Schematics of the installation of the ion gun in the COLIMACON DUO Set-up with crucial stages related to ion beam transport into the interaction region : 1-ion gun, 2-pulser stage, 3- quadrupole deflection stage and 4-collimator for beam diameter control.*

2.3 Production of clusters and nanoparticles

2.3.1 Short historical note - development of production methods

The production of clusters in form of molecular beams is an already well established field and its first concepts reach back to the 1950's where first clusters were produced from 19 gaseous elements; for their detection they have been ionized by electron impact. These early experiments allowed to obtain ionization energies for electron impact and to analyze relative size distributions, [42, 43]. Further developments, especially the construction of aggregation cluster sources, allowed in addition to large rare gas clusters also the production of semiconductor and metal cluster beams with their first application in implantation techniques and the deposition of thin metal films and hetero-structures, [38]. This was an important step in the development of cluster sources when laser ablation methods were used for the first time, as it extended the production of clusters to practically any type of material, even the ones with high melting point, which in consequence allowed Kroto to discover ultrastable forms of carbon clusters - fullerens [44]. In the 1990's new sources, based on ion or magetron sputtering, arc discharge, sprays, were introduced in parallel with more optimized methods for beam control, [45].

2.3.2 Fundamental aspects of cluster formation

Spontaneous cluster formation is a process of very low probability, therefore, for their efficient production one will require conditions of thermodynamic non-equilibrium, which are existing in specially designed cluster sources. There are many types of cluster sources, however, the steps of cluster formation are common to all of them.

In the first step a vapor pressure of the cluster material of sufficiently high density has to be produced in the gas phase. In this step the vapor of atoms/molecules and first nucleation seeds are formed. The second step corresponds to aggregate growth, i.e. atoms/molecules are attached to cluster seeds and form larger clusters. Furthermore so formed clusters can coalesce together, as well as some evaporation of atoms can also accompany the overall process.

Stable formation of dimers takes place when the gas temperature of the vapor is low, so that the kinetic energy of the atoms becomes lower than the binding energy of the dimer formation. In order to support this formation process a cold buffer gas (He or Ar) is added leading to three body collisions. For very small systems the presence of the third atom is necessary for the fulfillment of the conservation of momentum and energy according to the equation:

$$A + A + G_{buffer\,cold} \rightarrow A_2 + G_{buffer\,hot} \tag{7}$$

On the other hand, the third atom of the buffer gas G is taking the formation energy of the cluster away and thus efficiently cools the formed cluster system. Initially clusters are considered as being warm, as the addition of each atom contributes to the total internal energy, as cluster growth is an exothermic process. The internal energy increases due to the heat of

condensation of the added atoms. Since the formed clusters are hot, there is a competition between their growth (adding an atom) and decay loss of an atom by the evaporative cooling. This competition may lead to a so-called bottle-neck in the growth process. For small systems the coalescence energy can be distributed only among a small number of degrees of freedom and hence the typical time for evaporation is short. For large systems this energy can be distributed among many degrees of freedom and hence the lifetime of the excited system becomes much longer.

To overcome this bottle-neck, the cooling rate must be sufficiently high to favor the cluster growth. Different techniques for cooling are applied, either by cooling the buffer gas to low temperatures (liquid nitrogen temperatures) or by adiabatic expansion and similar techniques. Small clusters are formed simply by successive attachment of one atom at a time, whereas larger clusters can also be formed by collisions between already formed small/medium clusters due to their coalescence.

2.3.3 Gas aggregation and surface erosion methods

There are many types of cluster sources as mentioned previously. These can be divided into three main classes :

1. Supersonic jets - in which the expansion of the gas is kept under high-pressure and where the gas passes through a tiny hole, reducing the relative velocity of the atoms leading to formation of clusters.

2. Gas aggregation sources -where atoms or molecules are transported into a "buffer" of inert gases, which slows them down and accommodates their energy due to collisions leading to clustering (also known as smoke/cloud sources).

3. Surface sources - here a surface of the cluster material is heated by the impulse and energy of photons or the momentum of ions (sputtering) which remove atoms and small clusters from the solid. In electrospray sources a droplet is formed from the surface of liquid material under high potential which after strong evaporation leads to the formation of clusters. This type of source is also classified as surface source.

Below I describe shortly the methods that were used during my work to create beams of molecules as well as molecular and metallic clusters.

2.3.3.1 Gas aggregation molecular cluster source

Numerous experiments have been performed concerning collisions of ions with beams of single molecules or atoms. However, in nature molecules and atoms are mainly present in some molecular and chemical environment which influences their properties. Going one step further in the experimental studies towards complexity and more realistic systems it is advised to analyze the interaction of ions with cluster-ensembles containing 2 up to thousands of precursor elements, bonded by van der Waals, ionic, covalent or metallic bonding. The creation of such

targets in form of molecular beams is realized with the aid of a so-called "gas-aggregation cluster source" which was developed in the CIMAP laboratory to study collisional processes with clusters of sodium atoms and biological molecules and clusters [22, 46, 47].

As it is shown in fig.2.10 this type of source is simply the combination of an oven device placed inside the aggregation chamber, where the exit channel („condensation channel") is usually cooled down to -170°C due to the flow of liquid nitrogen in a double wall container. Additionally, several other injection channels are installed in order to introduce buffer gas like helium or argon. Due to the heating of the oven, precursors are evaporated and collide with cold buffer gas (due to condensation channel cooling) being at the same time transported by the gas stream resulting from the pressure difference. When the thermal kinetic energy of the precursors is low enough and the local density saturation is obtained, atoms/molecules tend to aggregate. Further, they are transported through a small size skimmer (ϕ=2mm) versus a differential pumping stage towards the interaction region. The molecular beam is composed of helium atoms and the produced clusters.

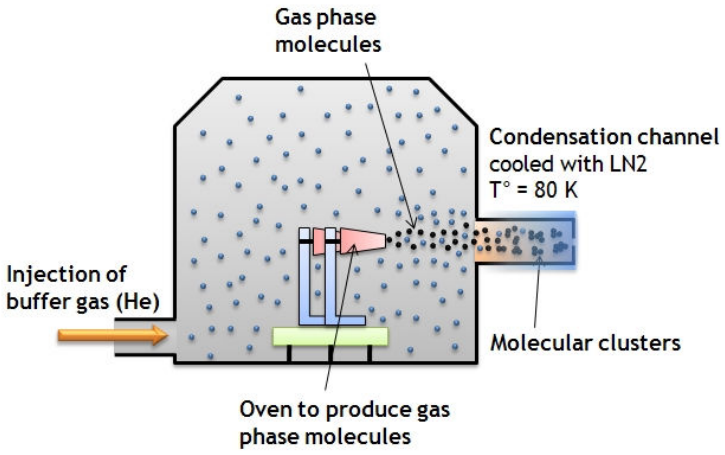

Figure 2.10 *Design of the gas aggregation cluster source with marked important construction elements. The realization is a modified version of the cluster source developed by C. Bréchignac et al. [48].*

There are several parameters that influence the original size distribution of clusters corresponding to a change in the thermodynamic conditions of the clustering process. The most significant parameter is the temperature of the condensation channel, which can be well controlled. However, the experiments were performed with the maximum cooling rate obtainable by a constant flow of liquid nitrogen, resulting in the temperature of the condensation channel $T_{cond.\,channel}$ of about -170°C.

Another parameter is the pressure inside of the condensation chamber, which is governed by a flow controller, allowing for flows between 0 and 600 ml/min. This yields an internal pressure of up to a few mbars. However, at that stage the main limitation for the pressure is due to operational limit of the Turbomolecular DRAG Pump, which can operate with a pre-vacuum up

to 1 mbar to avoid any mechanical damage risk. Thus, standard values of the flow of around 200 ml/min for case of He gas where used, resulting in the internal pressure range of around 0.1 mbar.

The temperature of the heated oven is another important factor as it determines the vapor density in the aggregation source. The evaporation is observed as exponential increase of the pressure inside the chamber. The increase of the oven temperature leads to an enhanced cluster production (higher intensities) which in consequence also leads to a shift of the size distribution towards larger cluster sizes. However, there is the upper limit, in particular for molecular clusters, as thermal decomposition of the precursor may occur already in the oven. In the case of the GABA biomolecule essential evaporation starts at around 90°C and its thermal decomposition occurs at around 150°C. In contrary a fullerene powder requires temperatures of 450°C to 600°C in order to obtain a sufficiently dense vapor pressure, still remaining thermally stable.

On the technical side, problems due to the clogging of the oven or the exit skimmer of the condensation channel can appear disturbing the stable operation of the experiment. Clogging of the skimmer is not as problematic as it can be easily cleaned with a rigid wire from the side of the differential pumping chamber. However, in case of hydrated clusters, large ice cubes can be formed easily, which is dangerous for the pumping system and stops the experiment. The gas aggregation cluster source installed in the COLIMACON Setup was inspired by the device developed by the group of C. Bréchignac et el. from the Laboratory Aimé Cotton, [49].

The Gas Aggregation Source based on thermal heating applied for the production of molecular or atomic precursor vapors is very efficient for high vapor pressure and low evaporation temperature materials. However, considering heavier elements like silver or copper, much more energy has to be supplied to obtain vapor pressures sufficient enough to allow the formation of intense cluster beams.

In general, during the operation of gas aggregation cluster source the vapor pressure of the precurssor is kept at the range $P_{vapor} = 0.01$ up to few mbars, depending on the expected final size distribution of produced clusters (the larger partial pressure the larger clusters), which can be controlled by the temperature of the oven).

In fig.2.11 the dependency of the vapor pressure is shown as a function of the temperature for some selected metal elements : silver, gadolinum, berylium, aluminum, copper, iron and platinum, calculated based on empirical data [50–52]. Among these elements, silver is characterized with the highest values of vapor pressure but anyway one needs to be able to heat an oven device up to at least T=1000°C in order to be at the range of P_{vapor}= 0.01 mbar. For other metals this minimum temperature is shifted to even higher values (T∼1400°C). Naturally, this poses huge technological challenges regarding the construction of the cluster source that is usually cooled down using liquid nitrogen down to temperatures T_{source}=-170°C. As the whole system is placed inside the high vacuum conditions it poses serious technological problems due to the large temperature gradients in small volumes and the very high probability of damage due to thermo-mechanical endurance of materials.

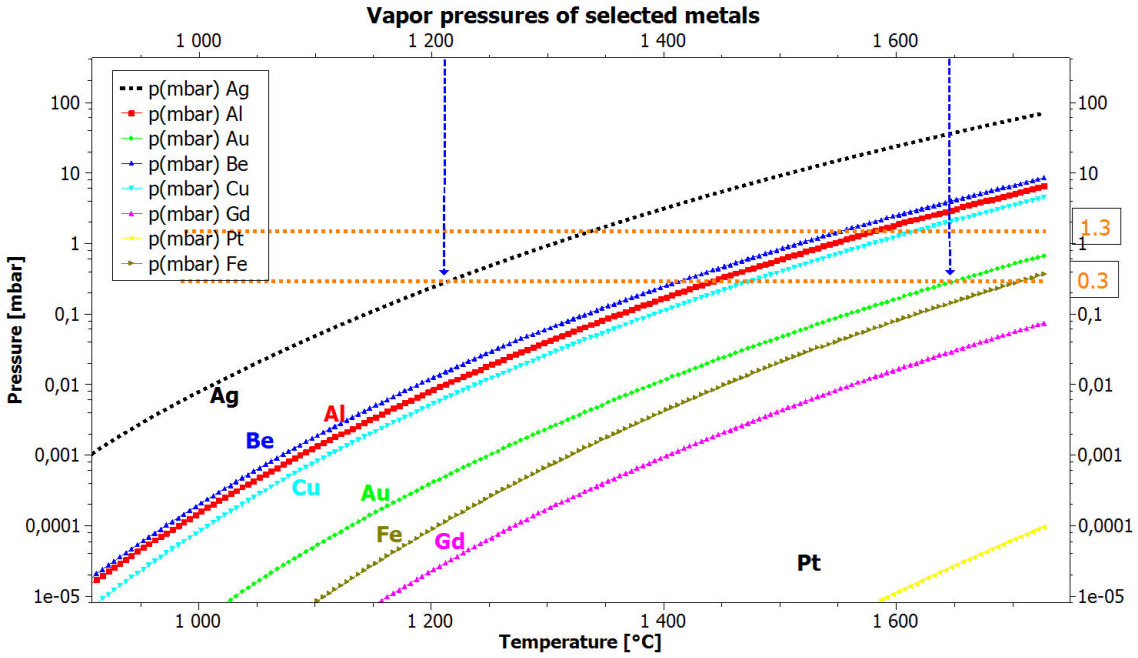

Figure 2.11 *The diagram of vapor pressures for selected metals as a function of the temperature*

This is the main motivation to use for the production of clusters with high melting points other cluster sources working in much less extreme thermal conditions. Here the vapor of the precursor material is produced by the erosion of surfaces induced by some energetic process. This process can be an intense pulsed electrical discharge (so called PACIS - Pulsed-Arc Cluster Source) [53], which generates large intensity of clusters in a single pulse with a fraction of around 10 % being charged.

One can use as well the irradiation of a surface by laser pulses combined with a pulsed cold buffer gas injection, a method that was introduced by the group of Smalley [44]. The intensity of the laser light is of the order of 10^7 W/cm^2. Usually UV Nd :YAG or excimer lasers are used. The size distributions of clusters generated by lasers irradiation range from small up to medium-size clusters (containing up to a few hundred atoms) and the generated clusters are neutral and charged, both negatively and positively.

Another way to erode surfaces is based on the bombardment with energetic inert gas ions, which results in efficient sputtering of high-melting materials. Ions that bombard the surface can come from external ion sources (typically Kr or Xe ions with kinetic energies of 10s of keV and currents on the order of 10 mA). However, one can also create ions close to the target surface by means of a dc or rf induced plasma discharge in the atmosphere of Ar (see the above mentioned PACIS source). In order to be more efficient and to increase the sputter yield, the discharge can be realized in a magnetic field the so-called magnetron configuration. The combination of magnetron sputtering and gas aggregation results in an efficient and stable generation of clusters over a broad range of size distributions (clusters may contain more than

50 000 atoms), [54]. We have developed this type of source and installed it in the COLIMACON DUO setup. Its working principle is described in more detail in the next subsection.

2.3.3.2 Towards metallic clusters - Magnetron sputtering cluster source

A magnetron based discharge cluster source (schematically shown in fig.2.12) was chosen to overcome technological problems mentioned above concerning the production of stable, intense beams of metallic clusters. This source is a combination of the magnetron sputtering device assisted by a magnetic field and a cylindrical gas aggregation chamber (a similar device is used by the group of Haberland [54]).

The cathode of the discharge is a metallic disk of dimensions of 0.250 inch in thickness and 2 inches in diameter. It is sputtered by energetic argon ions produced in a continuous plasma discharge. The assisting magnetic field is produced by a set of two concentric rings. The condensation chamber has double walls and can be cooled down to temperature of liquid nitrogen. Produced clusters are neutral and charged, where in the latter case, mass and size size-selection can be obtained with proper ion optics although strongly reducing the intensity of the cluster beam [55].

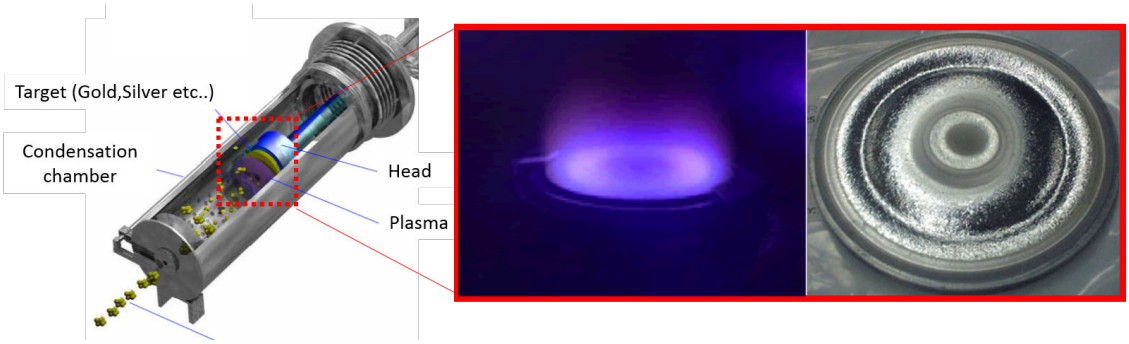

Figure 2.12 *Schematic presentation of the magnetron cluster source (left) overall assembly, magnetron head with discharge (centre, adapted from website of Semicore company) and typical form of the target with eroded sputtering ring after being used.*

2.3.3.3 Sputtering

In order to better understand the working conditions of the source the main mechanisms and characteristics of the magnetron system are described here. Such technique is very common in industrial processing of materials, for example for producing thin high-quality films for opto- or micro-electronic devices. The principle of sputtering can be simple if a neutral inactive buffer gas is used, like Ar in the present work, or more complex when reactive gases like O_2 or N_2 are used. Concerning the targets they can be composed of single or many elements, being metallic, semiconductors or even isolators.

The mechanism of sputtering is based on the bombardment of a surface by Ar^+ ions with sufficiently high kinetic energies inducing cascade processes in the first atomic layers. This leads to the emission of mostly neutral atoms or small clusters from the surface.

The Ar^+ ions are produced inside the plasma by collisions with plasma electrons. Initially "freely" existing electrons are accelerated over certain "non-collisional" distance until the first collision with atoms, which can be elastic (conversion of electron kinetic energy to atom kinetic energy) or inelastic (where the kinetic energy gained by the electron is transferred into ionization or internal excitations of neutral atoms/molecules). Processes of ionization liberate another electron from atomic orbitals which is again accelerated, creating a kind of avalanche ionization leading to the formation of a stable plasma. The Ar^+ ions are guided by the magnetic field and hit the cathode plate with kinetic energies of several hundreds of eV.

Sputtering performance

The efficiency of sputtering is described by the so-called sputtering yield S(E) (E- projectile energy), which is the number of sputtered particles N_{sputt} divided by the number of incident ions N_{inc} :

$$S(E) = \frac{N_{sputt}}{N_{inc}} \tag{8}$$

The sputtering yield theory has been developed by Sigmund for two different energy regimes, [56]. The sputtering yield for ions with energies E$\leq$1 keV can be described by

$$S(E) = \frac{3\lambda\alpha E}{4\pi^2 U_0} \tag{9}$$

where λ=$4M_iM_t/(M_i + M_c)^2$ is the fraction of the maximum energy transferred from the incident atom M_i to the target atom M_t during elastic collisions, α is a non-dimensional quantity depending on the ratio M_t/M_i and U_0 is the cohesive energy (sublimation energy).

Fig.2.13 a) shows the sputtering yield for a copper target as a function of the kinetic energy of the different rare gas projectiles and nitrogen. The yield is strongly dependent on the atomic number and hence the mass of the projectile. The larger the projectile mass the larger the sputtering yield in the whole range of energies, thus being the highest for Xenon projectiles. In the present experiments the gas Ar was used, in some cases mixed with a small fraction of helium.

Fig.2.13 b) is the sputtering yield for a copper target as a function of the kinetic energy of argon projectiles in greater detail, [58]. It is divided into 5 distinct regions which correspond to slightly different mechanisms governing the sputtering process. In region I the kinetic energy of the projectile is too low to induce any ejection of surface atoms. Region II represents a threshold region where sputtering becomes possible and where a very small increase of the kinetic energy results in a drastic increase of the sputtering yield. In regions III and IV one observes the constant increase of the sputtering yield as a function of the energy, however in region IV the sputtering is already significant as a single ion can induce the ejections of several

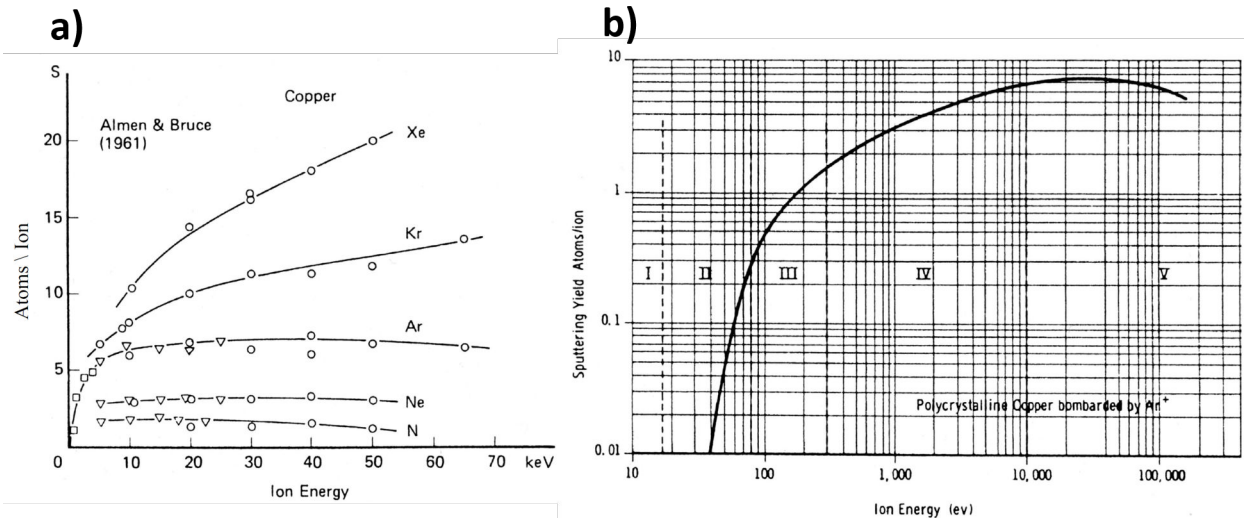

Figure 2.13 *a) Sputtering yield of polycrystalline copper as function of ion energy for nitrogen,neon,argon,krypton and xenon; b) the detailed sputtering yield of polycrystalline copper as function of the ion energy in case of the argon as a projectile, [57, 58].*

surface atoms. The maximum of sputtering is reached at around E_{kin} =20-30 keV. For higher energies the yield drops down again. This is due to the fact that in collision cascades atoms that are sputtered are the ones which originate from the first top layers. At very high projectile energies, the ions penetrate the matter more profoundly so that cascade atoms cannot reach the surface and loose their energy in lattice layers, leading to displacements and heating of the material instead of ejection. In our experiments the potential of the cathode and hence the ion energy varied between 200 and 400 Volts, which corresponds to regions III and IV.

The composition of the target has naturally a very strong influence on the sputtering yield, as shown in fig.2.14, based on the experiments of Laegreid et al. [59] for argon ion projectiles with an energy of E_{kin}=400 eV. The most efficiently sputtered matter is silver which is followed by gold, palladium and copper. In general the sputtering yield follows the filling of the sub-orbital d^{12}.

Magnetron cluster source installed at COLIMACON DUO

The magnetron based cluster source that was installed in the COLIMACON DUO was initially part of an another experimental setup developed in CIMAP laboratory by Jimmy Rangama, Omar Kamalou and Arkadiusz Ławicki. It was developed with the aim to mass select positively charged metal clusters using a specially designed ion extraction-time-of-flight device and results of the production of clusters of copper and bismuth with this source are given in the thesis of O.Kamalou [60]. The overall schematics of this home-made cluster source, adapted into COLIMACON DUO Setup is shown in fig.2.15.

In the middle the schematic cut of the cluster source of the most important elements is shown: magnetron head with target and clustering chamber with variable iris size. Above and

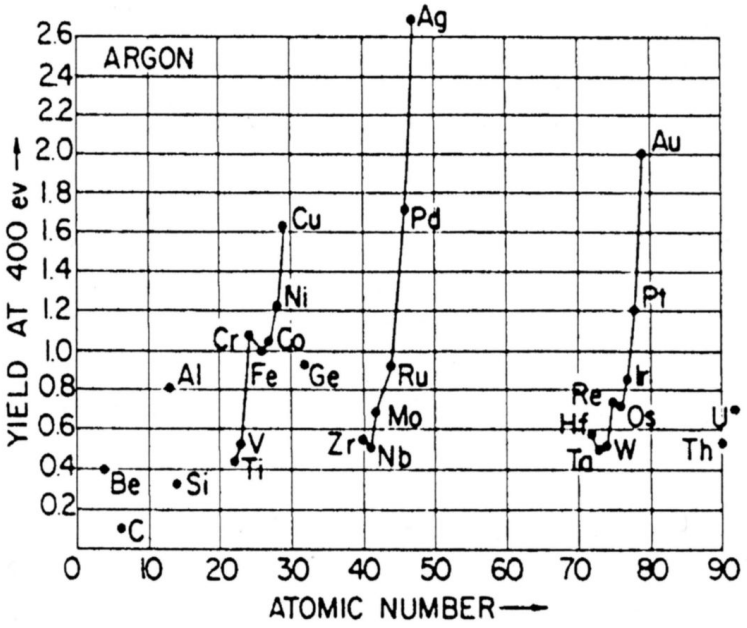

Figure 2.14 *The graph shows the sputtering yield for different target materials as a function of their atomic number. Irradiation by Argon ions at 400 eV [59].*

below the schematics, photos of corresponding elements are presented during the process of the overall assembly. The magnetron head is installed on the long metal tube allowing for the transport of the buffer gas as well as water cooling flow, with constant temperature set at 18 degrees Celsius. The water flow turns out to be very important due to two main reasons: when the magnetron is operational, the resulting plasma heats up the target and therefore a transfer of the heat from the target to the magnet assembly can result in overheating of magnets leading to their destruction. On the other hand, when the cluster source is cooled with liquid nitrogen, the effective heat transfer may result in cooling down the magnetron head to temperatures below -50 $^{\circ}$ C. In consequence this leads to the deformation of the Viton joint inside and as a final result a very large water leak in the cluster source can be observed (rapid raise of the pressure inside, potentially leading to the destruction of the turbomolecular pumps).

The assembly of the magnetron head, where the sputtered target is installed is placed inside the "clustering chamber" which is a long chamber of around 50 cm in length. The double walls are cooled when liquid is injected, terminated with a "funnel-like" copper element in order to improve the transport towards the central part, where a size-controllable Iris (from 1 up to 10 mm) is installed. After the exit from the cluster chamber nanoparticles pass through the small (2 mm of diameter) grounded nozzle. In addition this element is extremely important as the cluster source working in optimal conditions produces intense beams of clusters, which may lead to effective blocking of the nozzle as well as deposition of metallic clusters around leading to short-cuts (nozzle is then effectively "grounded"). Few important modifications of the design were made in order to keep the nozzle clean and isolated from over-deposition of

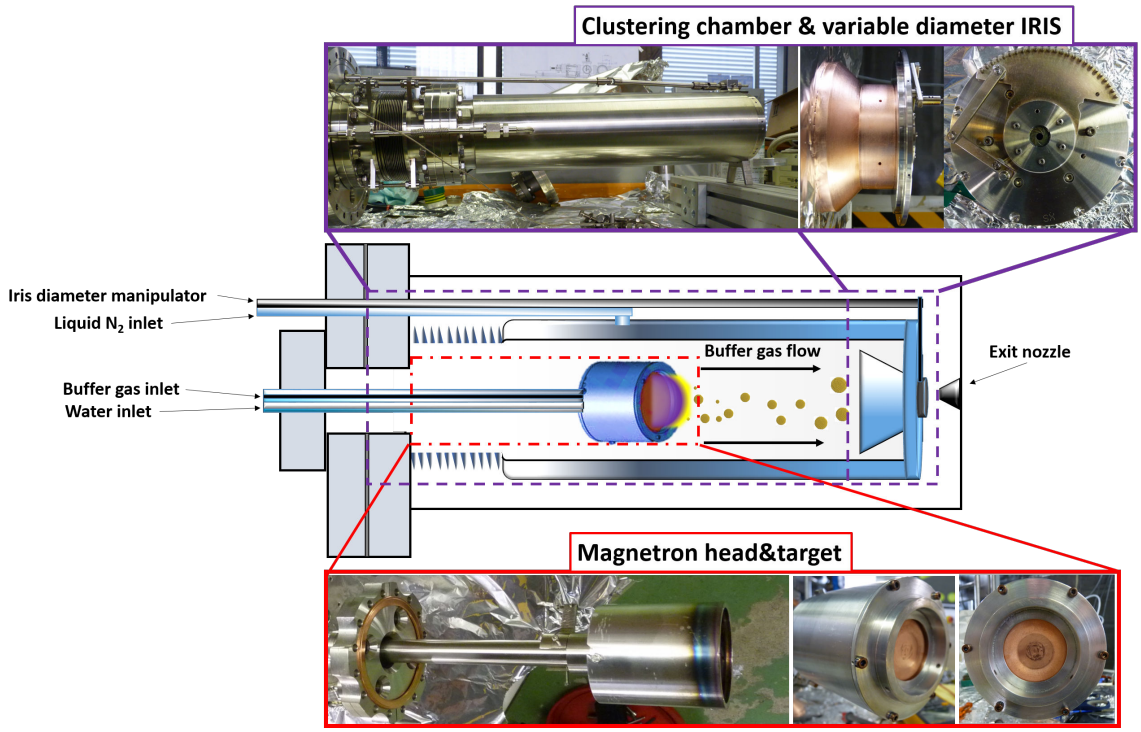

Figure 2.15 *The schematic cut through the magnetron cluster source adapted into the developed experimental setup COLIMACON DUO with photo images of the most important elements - magnetron head and parts of the condensation chamber.*

clusters.

On the photos of magnetron head close to edges one can clearly observe characteristic change of metallic color into mix of darker hues which is a sign that inside the magnetron the plasma discharge also takes place and increases temperature locally, which leads to the change of color.

2.4 Beam transport

Clusters, formed inside the magnetron source, exit this region through an iris with a controllable diameter between 1 and 10 mm. They are further transported through a first skimmer with a diameter of 2 mm, leaving the first chamber (see fig. 2.16). A molecular beam is formed due to the pressure gradient between the interior of the cluster source $p_{cluster}$=0.1 mbar and the pressure inside the differential pumping chamber (p_{diff}=10^{-6} mbar).

As the main interest is the study of the interaction of ions with neutral nanoparticles, charged clusters have to be removed from the molecular beam. This is done by applying an electrostatic potential on the skimmer and on the set of two rectangular plates localized inside the differential pumping chamber. Depending on the potential configuration one can

stop effectively all charged clusters and let pass only neutral systems. A variation of this potential allows to determine the kinetic energy distribution of positive clusters, which provides information about the average velocity of clusters which is important for the analysis by the time-of-flight system (see below).

The cluster beam is further transported to the interaction and extraction region or the deposition chamber through a second skimmer spaced by 40 cm with a diameter of 5 mm. Such geometry determines the diameter of around 7 mm of the cluster beam in the center of the interaction region, where collisions with the ion beam take place.

It is also possible to install a so-called "pick-up" cell, which is a specially designed heated oven, combined with an injection tube, which allows for the attachment of evaporated molecules to the surface of the clusters (cluster decoration).

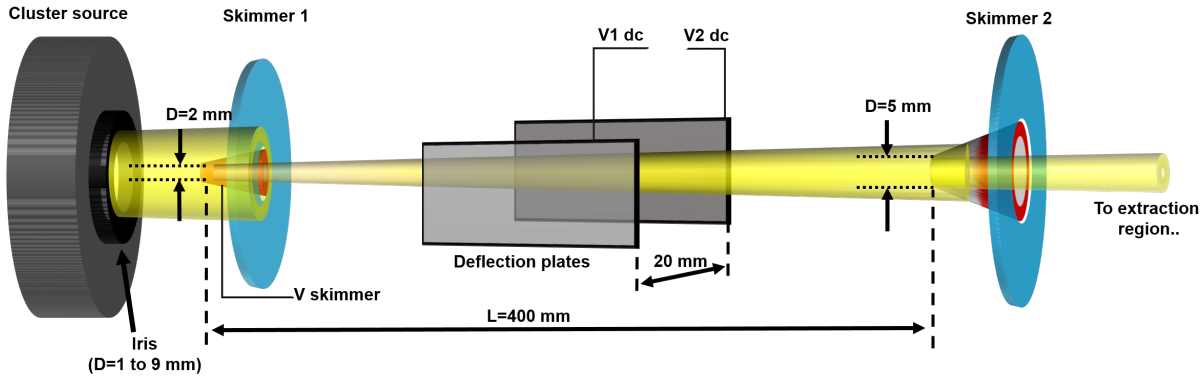

Figure 2.16 *Schematic drawing showing the main components of the transport system for the molecular beam from the cluster source through differential pumping chamber towards the extraction region, where collisions with projectile ions take place.*

2.5 Wiley McLaren Time of Flight Mass Spectrometer

After the interaction of ions with slow clusters a part of the collision products is charged positively. These can be extracted by a pulsed electric field in a specific direction - perpendicular to the beam of the ion projectiles and as well as to the cluster beam target. A general view of the Wiley-McLaren Time-of-Flight (ToF) Mass Spectrometer is shown in fig.2.17. The spectrometer is divided into 4 main regions :

1.The „extraction" region - where the interaction of projectile ions with the target takes place , **2.The „acceleration" region**- where positive products of the interaction are accelerated to a specific kinetic energy, **3- The „free-flight" region**- where no electric field is present and where spatial mass separation occurs due to the initially gained kinetic energy. The last **4.The detection region**- houses the detection device for the charged particles.

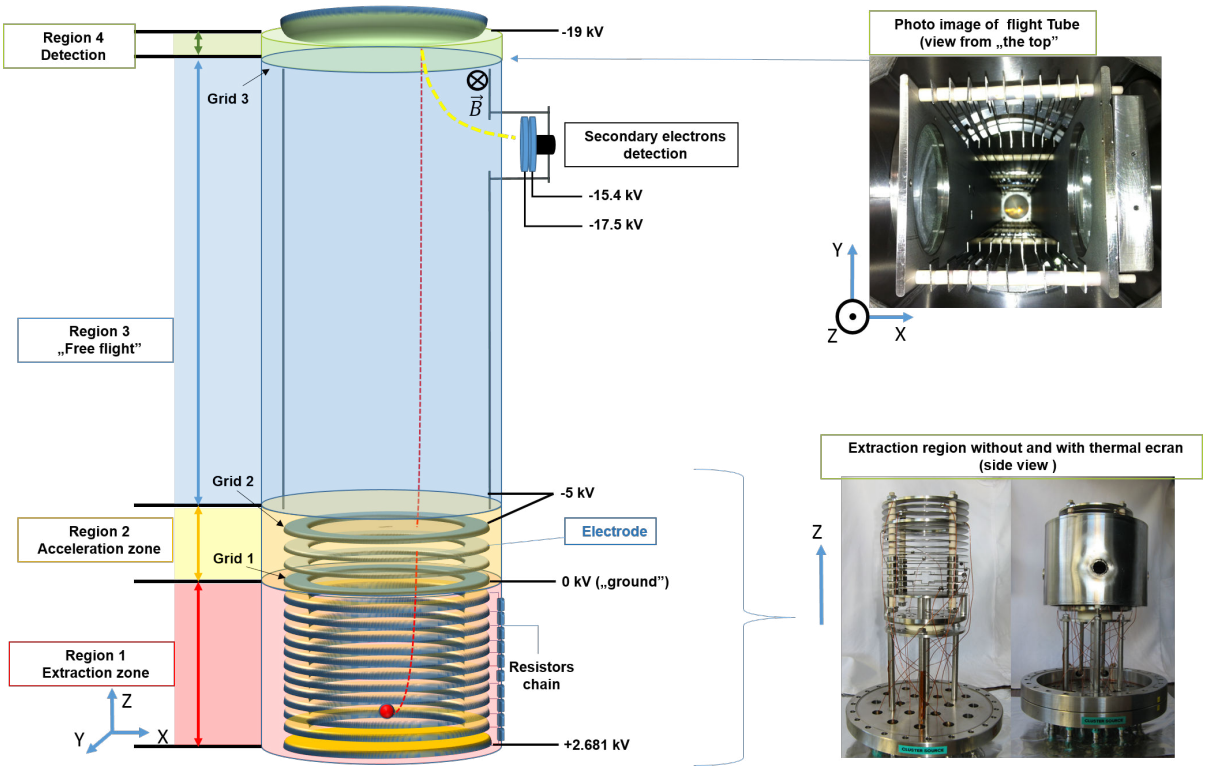

Figure 2.17 *Schematics of Wiley-McLaren ToF Mass Spectrometer (left) depicting the main regions of the flight of the extracted ion and photo of the time-of-flight tube (up and right) as well as a side view of the exctraction region (right, bottom)*

2.5.1 Extraction zone

This is the region where the interaction between the beam of projectiles and the cluster beam occurs. Collisions products that are positively charged can be extracted towards the ToF-system. It is composed of 15 circular symmetry electrodes, that guarantee a very homogeneous electric field, subdivided into two sub-regions based on the Wiley-MacLaren principle [47], so called extraction and acceleration region.

The extraction region (1) is constructed on a circular „bottom" plate which is kept at a potential V_{extr}=2.681 kV and which is followed by 11 ring-like shaped circular electrodes spaced by 1 cm. The total length of this part is 11 cm, the beams enter the system 2.5 cm above the base plate. The rings have an external vs. internal diameter of 13 vs 9 cm and are equidistant by 9 mm with a thickness of 1 mm each. As the last 11th ring is placed on ground potential, the total potential difference is 2.681 kV in the extraction region.

To maintain the field homogeneous as good as possible, the grounded electrode ring is replaced by a grid with 85 % transmission efficiency. An equal distribution of the potential of each of the rings is assured by a set of 2.2 kOhm resistors, which in consequence create a homogenous electrostatic field of $E_1 = 244$ V/cm. The resistor chain is mounted in a box outside of the vacuum to avoid thermal heat load and their connection is maintained by vacuum

feedthroughs.

The acceleration zone is a set of only 4 electrodes, starting with the one kept at the ground potential and with the last one, being in fact again a grid with transmission of 85 %, kept at V=-5 kV. The total length is 3 cm, as dimensions of the electrodes are the same as in the first "acceleration" zone. However, the potential gradient is much larger, providing the field of $\vec{E}_2$ = 1667 V/cm. Under these conditions a spatial focusing of the TOF spectrometer is obtained.

The combination of the electric fields of both zones $\vec{E}_1$ and $\vec{E}_2$ yields for a q-times charged fragment ion a kinetic energy of $E_{kin,total}$= $E_{kin,1}$+$E_{kin,2}$ = 7074× q eV, where $E_{kin,1}$= 8.5cm×244 V/cm×q and $E_{kin,2}$=3cm×1667 V/cm ×q.

During the operation the electric field in the zone 1 is pulsed in timely correlation with the pulsed ion beam, whereas the field in zone 2, is kept constant. As discussed further below, this pulse will be used as a start signal for the time-of-flight measurement.

The whole assembly of the extraction and acceleration zones is placed inside a thermally cooled cylinder. During the experiments the flow of liquid nitrogen cools down the walls, thus, improving the vacuum conditions due to the sticking of residual gas molecules (water, nitrogen, oxygen, carbon dioxide or other molecules remaining from previous experiments) and yielding a base pressure of 10^{-10} to several 10^{-9} mbar (10^{-8} when buffer gas is present).

2.5.2 "Free flight" zone

Positively charged particles (having the same kinetic energy per charge) enter a „free-flight" region. This is housed in a l00 cm long tube, containing two main metallic rectangular plates, both kept at the potential of the last electrode of the acceleration zone, namely at V_{TOF}= -5 kV. To avoid any electric stray fields on the sides between two main "border" plates, smaller 1 mm thick "lamellar" plates were placed (1cm equidistantly) along the whole length of the TOF tube. The free-flight region is terminated by a grid with 94% transmission.

The velocity v of particle with mass m and charge q, entering the zone of free flight, does not increase anymore due to lack of electric fields. It is given by:

$$V_{particle} = \sqrt{\frac{2E_{kin}}{m}} = \sqrt{\frac{2qV}{m}} \tag{10}$$

where E_{kin} is the total kinetic energy acquired in the exctraction zone, determined by experienced potential difference V.

For fragments with different masses the velocities are different which allows for a spatio-temporal separation of fragments inside the TOF tube. Equation 11 gives the value of the time-of-flight T_{flight} necessary to pass through the TOF tube with the length L :

$$T_{flight} = \frac{L}{v_{particle}} = L\sqrt{\frac{m}{2q \times V}} \tag{11}$$

The configuration of the TOF tube allows to independently apply voltages between the two main plates, creating a small difference in the potential in lateral direction. By this means

the initial velocity of the cluster beam and hence the cluster fragments can be compensated avoiding that these fragments touch the TOF walls before they reach the detector.

2.6 Detection and post-acceleration

After the mass/charge analysis the charged particle created during the interaction of the ions with a specific target have to be detected. At the end of the TOF tube they leave the "free-flight" zone and enter a detection unit. They pass a short post-acceleration zone, to increase their velocity to values sufficiently high for an effective detection. In particular for large and heavy particles this is important as the probability to emit a secondary electron from the bombarded surface decreases with decreasing impact velocity and one has to overcome some specific threshold value.

The experiments in the COLIMACON set-up have been performed with two types of detectors: a Daly type detector where the conversion plate is kept at -19 kV and a Position Sensitive Detector (PSD) which can be polarized up to -10kV. In the present work we decided to use the Daly type detector, because we expect a higher detection efficiency in particular for larger and hence slower particles.

2.6.1 Daly type detector

In this type of detection technique [47, 61], positively charged particles are detected indirectly via secondary electrons produced during the collision of high-energy clusters with a metallic surface (conversion plate). The emitted secondary electrons are accelerated by the post-acceleration field towards the TOF-system and are guided by a magnetic field produced by two Helmholtz coils towards an assembly of 3 microchannel plates increasing the number of electrons by a factor of 10^7-10^8.

The conversion plate, kept at a potential of V_{plate}=-19 kV, is made of stainless steel and has a radius of 15 cm with well-rounded edges to avoid any discharges. The difference of the potential between the grid electrode at the top of TOF tube and the conversion plate separated by 2.8 cm is 14 kV, that creates a field of $\vec{E_4} = 5$kV cm^{-1}. This allows to accelerate "slow" heavier particles to velocities assuring their effective detection. Secondary electrons produced due to ion impact are initially accelerated due to the same $\vec{E_4}$ field and further their trajectory is bent by the magnetic field $\vec{B}$ created by Helmholtz coils. Detector bias is formed by applying potentials of -17.5 to the front and -15.4 kV to the end plate, forming difference of 733 Volts per single mirochannel plate. Thus, the electrons arriving from the conversion plate do have a kinetic energy of 1.5 kV.

Detailed studies of the efficiency of secondary electron production by impact of particles were performed [62, 63]. The work performed by Winter's group (fig.2.18) shows that yields

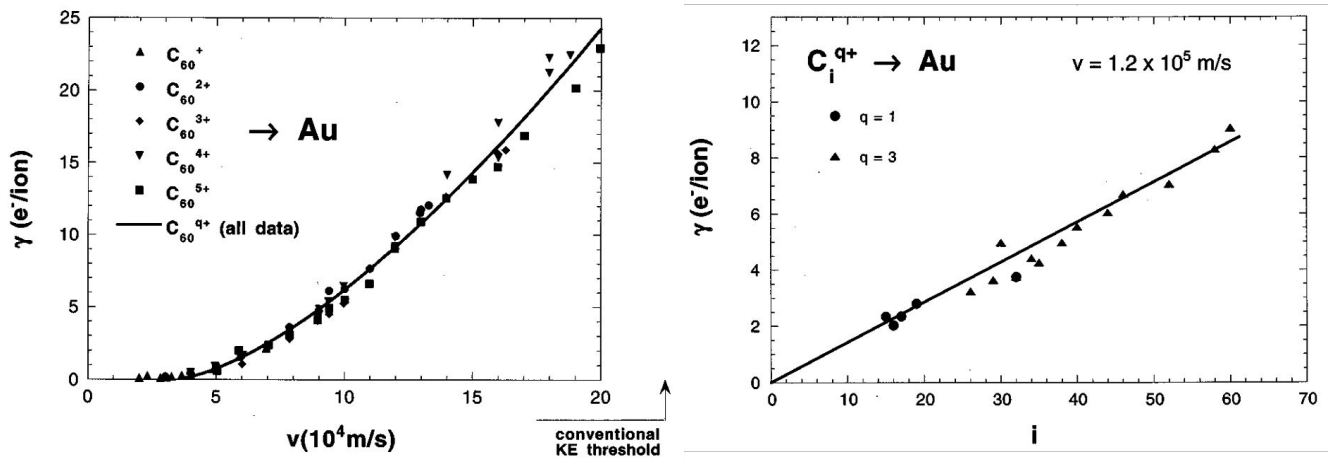

Figure 2.18 *On the left: the yield for the production of secondary electrons produced by impact of singly and multiply charged C^q_{60+} (for q=1 to 5) fullerenes on a gold surface as a function of their velocity. On the right: the yield of produced secondary electrons as a function of the fullerene cluster size and charge state (C_i^{q+} for i=15 to 60 and q=1 and for a given velocity of a projectile , [62].*

induced by impact of carbon clusters (C_i^{q+}, with i=15 to 60 and q=1 to 5) depend only on the velocity of the impinging particle, and do not depend on the charge. Additionally, well above the threshold velocity, the potential emission of secondary electrons from polycrystalline gold surfaces increases linearly with the velocity of the projectile, while a threshold value was estimated to be $v = 3 \times 10^4$ m/s (fig.2.18 left). It is also shown that for given velocity ($v = 1.2 \times 10^5$ m/s, fig.2.18 right) and for two different charge states (q=1 and 3) the yield is a linear function of the size of the particle (carbon clusters).

In order to emit a single electron, the velocity of the incoming C_{60} ion has to be in the range of 50 km/s. Such speed is acquired in the COLIMACON setup (when the conversion plate is set on the potential of $V_{plate} = -19kV$) for clusters with masses below $m_{cluster} \sim 2000$ amu, which corresponds to Ag_{20} or Cu_{30}.

On the other hand, a similar study [63] with vanadium clusters hitting surface of stainless steel was performed. In fig. 2.19 the electron emission yield per impinging atom is shown. One observes a similar linear dependence of the yield as a function of velocity, with threshold velocity $v_{th} = 50$ km/s, which is larger than for fullerene clusters. There is no very detailed data for velocities close to the threshold value, but it is important to note that even if the yield for lower velocities is very small for example in the range of 0.001, a cluster containing 1000 atoms can still be detected with reasonable efficiency.

Fig. 2.20 (left) shows the schema of the assembly of the conversion plate and the multi-channel plate detector (Z - stack, 40 mm diameter with a gain of more than 10^7, produced by Hamammatsu). The MCP is made of semiconducting material with specific internal structure.

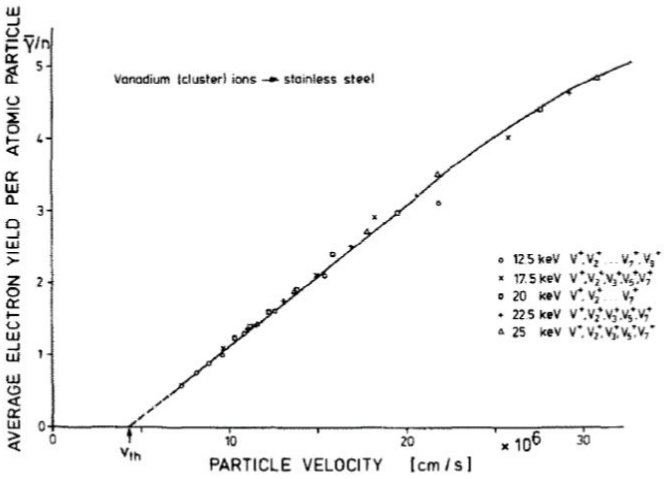

Figure 2.19 *The average electron yield induced by the impact of energetic vanadium clusters V_n^+ (n=1 to 9) on stainless steel with kinetic energies E_{kin} from 12.5 keV to 25 keV, [63].*

In each slab there are numerous small cylindrical holes that cover more than 50 % of the total surface. The surface ratio determines the maximum efficiency of MCP detector. The primary electron entering a small hole in the detector initiates a cascade of secondary electrons, which are all finally collected at the conical copper anode leading to the charge build-up and its conversion into an electrical pulse. The pulse is further amplified in a pre-amplifier stage and sent to the corresponding electronic system for signal detection. The detection efficiency for the

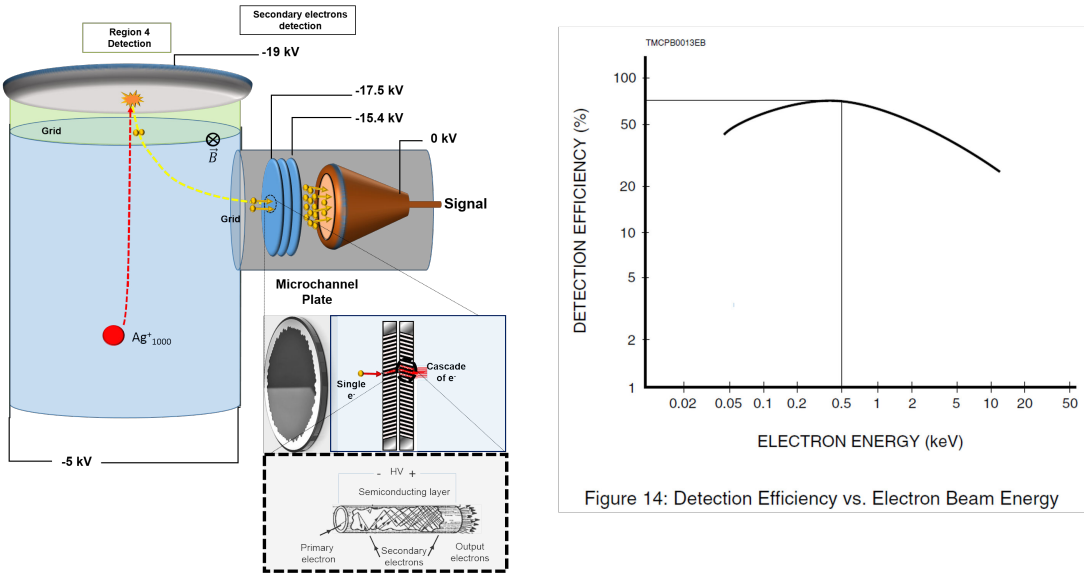

Figure 2.20 *On the left, the schematic trajectories within the Daly type detector. A cross-sectional view through multichannel plate detector is shown, illustrating the electron cascade due to primary electron impact. On the right, the dependence of the detection efficiency of MCP on the energy of the impinging primary electron is shown.*

electrons depends in addition on their kinetic energy and estimates above 60% for electrons with E_{kin}=0.2-2 keV (fig. 2.20 right (data from Hamamatsu documentation sheet website). The potential difference between the conversion plate and the front plate of the MCP detector is kept at ΔV=1.5 kV which yields an impact energy of E_{kin}=1.5 keV.

2.7 Acquisition system

In this part I am presenting the electronic chain for signal acquisition and signal processing which allows to obtain the time of flight and mass spectrum after detection of charged particles.

2.7.1 Electronic chain

The different steps of signal processing are described in the following and are shown in fig.2.21. The input signal is negative and stems from electrons which have passed the MCP device. Its amplitude is of the order of 50 to 100 mV with a half width FWHM of around 1.5 nanoseconds (both depending on the gain of the detector and the number of electrons produced in the cascade).The signal is further amplified by a preamplifier ORTEC VT110, which delivers a signal of about -1 V. The signal is further treated by a discriminator unit "Phillips Scientific Quad 300 Mhz NIM Model 704", where a threshold value can be adjusted (usually set at -170 mV). The threshold allows to remove all signals with amplitudes below the specific threshold value, thus, strongly suppressing low-amplitude background noise. The pulse form is transformed into the standard NIM form (amplitude - 0.8 V) and its timely width can be increased to $\sim$20-40 ns in order to avoid the influence of signal reflections. However, hereby the dead time of the data acquisition is increased as well. From the output of the discriminator the signal is sent to an acquisition card (FAST ComTec P7888) converting the analog signal to a numerical one by a Time to Digital Converter (TDC). This card is integrated in a computer system allowing with a dedicated software package to display and store time of flight spectra in an event-by-event mode (see below).

2.7.2 Electric field pulsing and control

As the mass/charge of reaction products is analyzed by a time-of-flight method, the system has to provide a „start" and the „stop" signal characterizing the drift time. This implies that the ion beam has to be pulsed by deflection plates in order to form a "bunch" of ions, furthermore, the extraction field has to pulsed as well in a synchronized manner. The application of the extraction field delivers the required „start" signal for the TOF measurement corresponding to the drift time τ=0.

The timing of the experiment is controlled by a pulse generator which determines the base frequency of the measurement and which delivers 4 output signals with variable amplitudes, widths and relative delays (see fig.2.21).

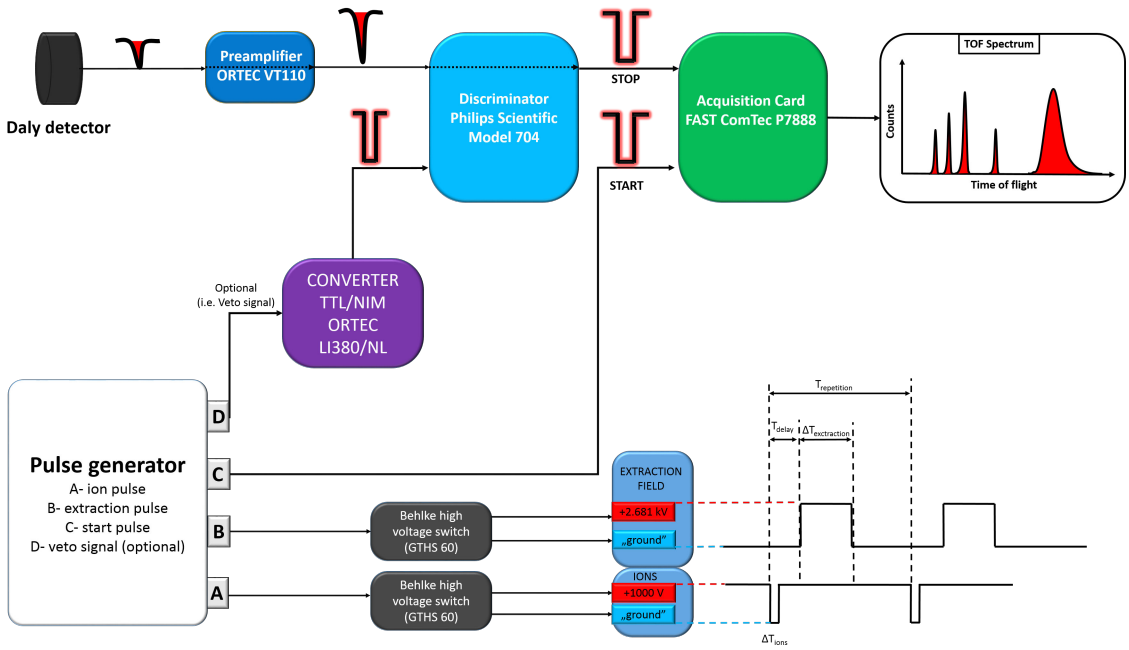

Figure 2.21 *Simplified schema of the electronic signal generation and spectrum acquisition chain with temporal synchronization structure of the extraction and ion pulses.*

The first pulse (Channel A from the generator), is related to T_0 time and controls the ion beam packet. It is connected to a high voltage switch ("Behlke GTHS 60": marked as dark grey rectangle in the picture), which applies a voltage between 0 and 1 kV to deflector plates which are installed right after the ion source. The length of the pulse ΔT determines the length of the ion packet. The typical duration of ion pulses is between 1 and 10 microseconds, however, in an early stage of experiments, values as high as 50 microseconds were used, in order to increase the ion beam current.

The channel B is used to control the electric field in the extraction region. The pulse is sent (similarly to the case the of ion beam packet) to another Behlke switch (the same model Behlke GTHS 60) and allows to define the starting pulse for the time of flight. The pulse is delayed with respect to the first pulse (channel A) by T_{delay}, as the ions require some time to arrive at and to pass the interaction region. The necessary delay time is related to the length of the beam line and the width of the ion pulse. Taking as an example $^{40}Ar^{11+}$ with a kinetic energy of E_{kin}= 165 keV and a width of 1 microsecond one obtains a typical value of

$$T_{delay} = \Delta T_{ions} + \frac{L_{line}}{v} = 1 + L_{line} \times \sqrt{\frac{2E_{kin.\,ion}}{m}} = 12.3\,\mu sec \qquad (12)$$

The values of the voltage applied to the extraction plates are V_{extr}=2.680 kV when the potential of the time of flight tube is V_{TOF}=-5 kV or V_{extr}= 1.340 kV with V_{TOF}=-2.5 kV. The length of the extraction pulse is related to the mass of the system, the larger the mass the longer the extraction pulse should be chosen. A detailed discussion concerning the required length of the extraction pulse will be described in chapter 4 (Characterization of nanoparticles). In general

they vary between $\Delta T_{extraction}$=20 μs used to effectively extract„small cluster" (like Ag_{20}^{+}) up to even 1 ms when observing clusters that contain a number of atoms even above n=20000. As an increase of the extraction width also induce a larger pulsed current through the voltage divider chain, a limitation is given by the power supply which in part can be compensated by a reduction of the base frequency (inverse of $T_{repetition}$) of the experiment.

Channel C is sending a short (50ns long) time signal, coincident in time with the start of extraction, to the acquisition card, which works as a reference point of the START signal. Starting from this moment, any charged particle arriving at the detector produces a STOP signal with its specific time stamp. The time difference between STOP and START is the total time-of-flight of an ion allowing to calculate the m/q ratio. On the other hand, the signal START can be delayed by a fixed amount to avoid the noise due to the extraction pulse or due to the buffer gas.

2.7.3 Spectrum acqusition

The acquisition card records the time of arrival for each detected ion, based on the time stamp from START and STOP signals. The card is multihit-capable, i.e. that all ions arriving after the START up to a preset time window are registered. The spectrum is obtained as a function of a channel number $n_{channel}$, corresponding to the drift time, with a resolution of 1 ns. For the display of the spectrum a channel binning can be performed allowing to follow the evolution of thespectrum more rapidly. The binwidth, usually chosen between 2 and 128 ns/channel, is equivalent to the time of flight of the ion:

$$TOF = binwidth \times n_{channel} \tag{13}$$

The time-of-flight spectrum can be transformed into a m/q spectrum using a calibration based on polynomial fitting. To do this in the very crude approximation, the time of flight can be calculated from the geometrical data and the applied voltages of the system, yielding:

$$T = \alpha\sqrt{\frac{m}{q}} + \beta \; with \; \alpha = 0.144 \; and \; \beta = 0 \; (amu) \tag{14}$$

However, a more precise method is based on a polynomial fitting of well-identified peaks as illustrated for the exemplary spectra shown in fig.2.22, which is a result of collision of O^{6+} ions at E_{kin}=90 keV with molecular beam of argon gas. The graph in fig.2.22 a) represents the spectrum as a function of the channel number, whereas the one in fig. 2.22 b) is the same spectrum in time domain. Knowing a priori, which peaks are dominant and to which m/q they correspond, one can choose several characteristic points (minimum number of points for fitting depends on the polynomial order) to determine the polynomial coefficients, as it is shown in the graph from fig.2.22 c). Finally, the graph in fig.2.22 d) is the mass/charge spectrum and one can clearly associate visible peaks to cations, like singly and multiply ionized Ar atoms, as well as residual gases like nitrogen, oxygen or water and their fragmentation products.

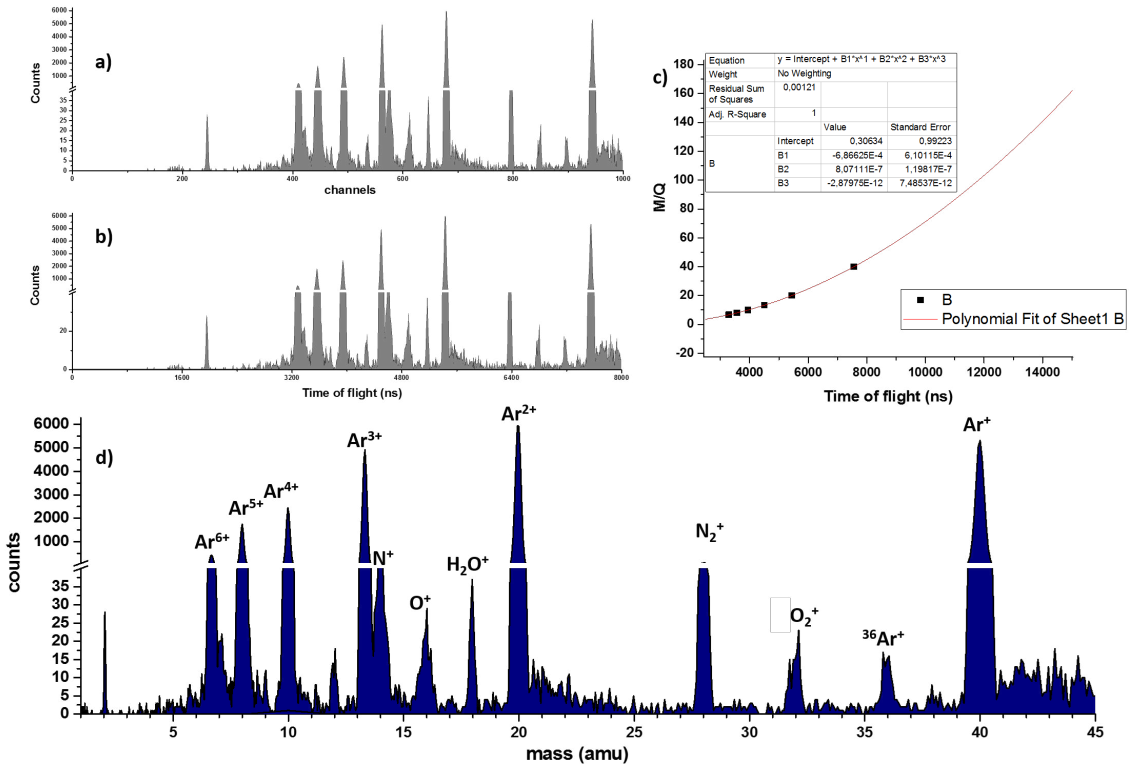

Figure 2.22 *Recorded spectra as a function of a)detector channel and b) time of flight resulting from collision of O^{6+} ions with E_{kin}=90keV with Ar atoms; c) calibration curve for $\frac{m}{q}$ ratio as a function of time-of-flight; d) final mass to charge spectra with peaks associated to recorded cationic products.*

2.7.4 Coincidences and multi-stop spectra

The acquisition system allows to record after a single START signal, corresponding to a single ion bunch, all STOP signals which arrive on the detector in a pre-set analysis time. In the simplest case, one ion interacts with one molecule or cluster, ionizes it and produces one charged secondary ion. In this case, one STOP signal is detected and the collision event is called a single stop event. When the ionization leads to several charged fragments a multi-stop event is produced where several fragment ions are produced in a single event (higher multiplicities). This information is written in a list file as a two dimensional matrix, where each row contains the event number and the time-of-flight values attributed to the different STOP signals. Different events are documented in different rows, thus, allowing for a subsequent event-by-event analysis.

It has to be noted that the detection efficiency is lower than 1 (see discussion below), i.e.

that a fraction of the secondary ions is lost during their time-of-flight analysis and detection. This has to be taken into account for a precise analysis. Furthermore, in order to perform the coincidence measurements and to analyze particle correlations, one has to determine the number of accidental coincidences, which means the probability that within one ion beam pulse more than one ion interacts with the target. In such a case, the observed cationic spectrum and the STOP distribution originate from different events providing false coincidences. To reduce their number the intensity of the ion beam has to be strongly reduced down to the region where the quantity R, defined as ratio of the count rate:

$$R = \frac{C_R}{F} << 1 \tag{15}$$

As an example if we consider that the probability to register one event in a single extraction pulse is around 5 %, than the chance for a second accidental event is 0.25 %. Naturally, if the count rate C_R is very low, one has to take into account very long acquisition times from a few up to even tens of hours in order to obtain a sufficiently good statistics.

The application of the Poisson law allows to estimate the probability for an event to occur in a given time interval based on the count rate. If one considers the count rate C_R (understood as a mean number of counts in a given time interval), defined as

$$C_R = \frac{\mu}{\delta t} \tag{16}$$

then the probability P(k) to observe k counts (k STOPS) in a specific time interval $\delta t'$ is given by

$$P(k) = \frac{\mu^k}{k!} \times e^{-\mu} \tag{17}$$

After substitution of $\mu = C_R \times \delta t$, where δt could be the START-START time interval (inverse of repetition rate R_R), P(k) is equivalent to

$$P(k) = \frac{(C_R \delta t)^k}{k!} \times e^{-C_R \delta t} = \frac{(C_R/R_R)^k}{k!} \times e^{-C_R/R_R} \tag{18}$$

The values of C_R and R_R can be easily obtained by the total number of stops, total number of starts and the time duration of the acquisition.

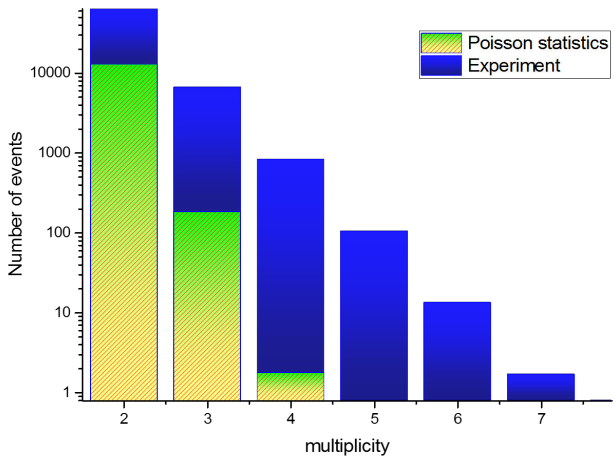

Figure 2.23 *The histrogram representation of the number of experimental (dark blue) and Poisson statistically probable (yellow-green) events as a function of the multiplicity (number of STOPs) resulting from the collisional interactions of Ar^{9+} with E_{kin}=135keV with silver nanoparticles.*

In fig.2.23 the number of events as a function of the multiplicity is shown for Poisson statistics (indicated with green-yellow color histogram) and for the experimental case of Ar^{9+} collisions with silver nanoparticles(blue). The difference between these two histograms gives the number of real events. The number of events for the case of the experiment is larger than that for accidental events and constitutes around 70 % of all 2-stop events. For higher multiplicities accidental events become less important, for the multiplicity k=3, real events constitute more than 95 %.

Coincidence map

As two or more charged fragments can be produced in a single extraction cycle, it is important to analyze the level of correlation between the detected ions. In the most simple case of two detected cations (2STOP spectrum) it is a very convenient way to present the correlation between two products in a 2D map, as shown in the fig.2.24, where the time-of-flight of the slower fragment B^+ is plotted on the Y-axis as a function of the ToF of the faster one A^+ on the X-axis. The plot shows a part of the 2STOP spectrum obtained from collisions of Ne^{6+} ions with large neutral silver nanoparticles (containing more than 2000 atoms).

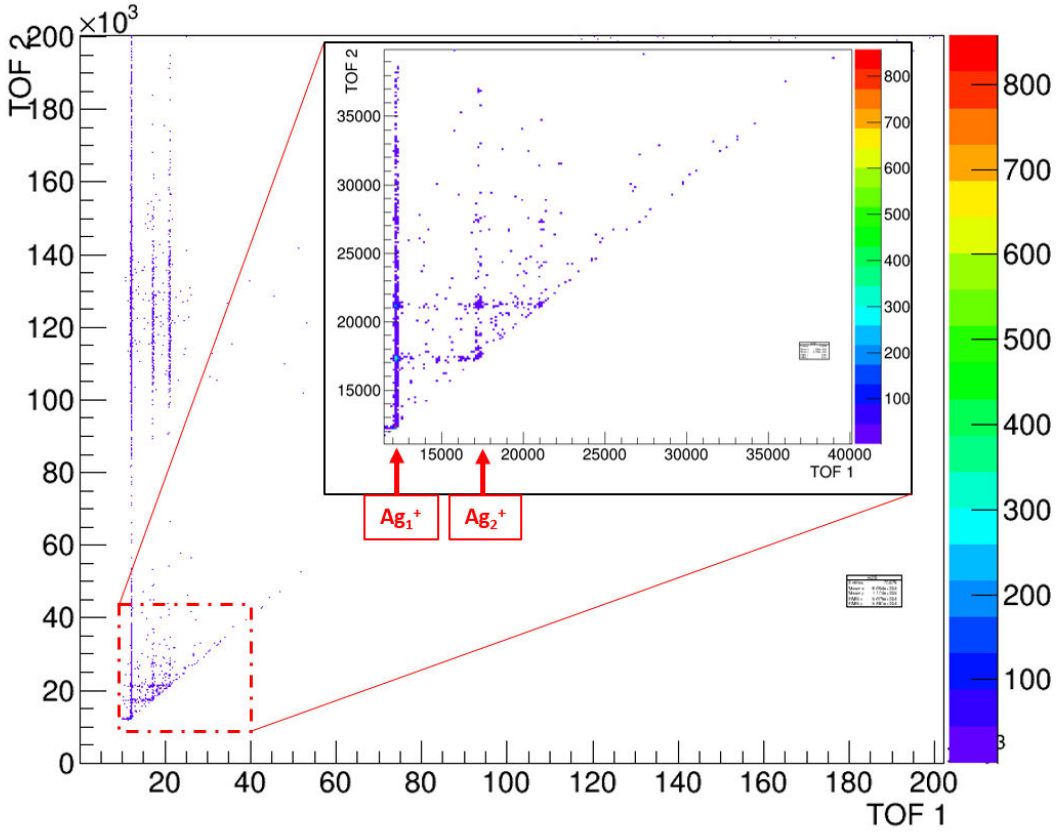

Figure 2.24 *The coincidence map of fragments resulting from collisions of Ne^{6+} ions at $E_{kin} = 90keV$ with Ag_n. The inset in the right upper corner is a zoom into small TOF1 and TOF2 regions showing the characteristic coincidence islands and time of flights of silver monomers or dimers with residues of silver clusters. The color of the map represents the number of counts, and TOF1/TOF2 are given in μs.*

The coincidence map indicates which fragments arrive from the same event providing information about the dynamics of the interaction. On the 2D map one can observe characteristic islands formed by pairs of fragments and by studying their relative intensity one can deduce the importance of different fragmentation or dissociation mechanisms. In addition, from the study of the shape of a single island one can deduce the kinetic energy of the fragments given by the extreme values of the time of flights STOP1 $t_{1,min}$ and $t_{1,max}$ and for STOP2 $t_{2,min}$ and $t_{2,max}$. The δt_X corresponds to the momentum of a fragment and the slope of the island belonging to fragment masses m_A and m_B, and charges q_A and q_B is given by

$$\frac{\delta t_2}{\delta t_1} = -\frac{m_B \cdot v_B}{q_B} \times \frac{q_A}{m_A \cdot m_B} \tag{19}$$

An analysis of the slope shows that for a binary fission process the slope corresponds to -1,

deviations from this value indicate that always a third particle is involved in the fragmentation process.

A coincidence map can be constructed also for a 3STOP spectrum (or a spectrum with higher multiplicity), however, one needs to select the time-of-flight of a specific first fragment and then create a map of the remaining 2STOP events. However, the analysis of the island slope is not anymore sufficient to get information about the dynamics of the fragmentation and different analysis methods have to be used, for example a Dalitz plot in the case of 3 fragments.

2.8 Deposition chamber

In order to be able to characterize neutral nanoparticles it was necessary to build and install in the COLIMACON set-up a particle deposition chamber. It is localized after the extraction region (if looking from the side of the cluster source) along the line of the molecular beam. As it is shown in fig.2.25 the whole chamber consists of a CF 63 cross separated from the main experimental chamber by a vacuum gate valve. Therefore, the removal/exchange of samples/substrate does not require the venting of the whole set-up making replacements more convenient and fast. Inside the chamber the sample (typical size of 8x8 mm) is mounted on

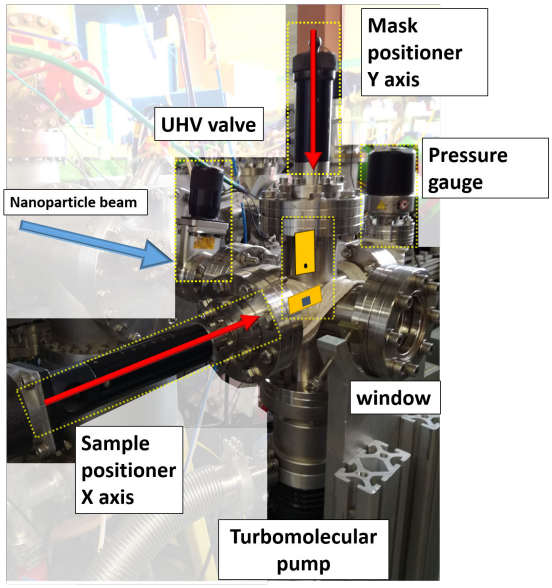

Figure 2.25 *The deposition chamber developed with the aim of metal clusters/nanoparticles deposition for further analysis (i.e. microscopic studies).*

the sample holder movable in the horizontal (X) direction by a vacuum positioner. A metallic mask which is movable in the vertical (Y) direction, contains a 0.6 mm hole and is placed a few millimeters in front of the sample surface. One can perform more than 30 different depositions with the same sample, for example to examine particle size distributions as a function of specific

cluster source parameter.

The whole deposition process occurs under „soft" landing conditions, as the velocity of large clusters inside the molecular beam is in the range of 100 m/s (E_{kin}= 5 eV per cluster composed of few thousand atoms), i.e. impact energies per atom in the meV range.

2.9 Challenges and difficulties

The COLIMACON set-up was initially designed and optimized for the study of the interaction of ions with molecules or small molecular clusters (like biomolecules, fullerenes and PAHs) or small Na clusters. However, the performance of experiments with large metallic nanoparticles is much more challenging due to several aspects. These are linked to their high mass and hence, their low detection efficiency, their limiting trajectories through the TOF spectrometer, and the use of the heavy buffer gas Ar. These points will be discussed in the following.

Case of the buffer gas

A target beam of small molecules is produced by thermal evaporation and subsequent expansion into a region of low pressure. Due to the absence of a buffer gas, the signal to noise ratio is very high in particular when the interaction region is cooled by liquid nitrogen. The situation becomes more demanding when a clusters target is considered, as the presence of the necessary buffer gas decreases the signal to noise ratio. However, if He is used the perturbation occurs only in the low-mass range. When using a magnetron cluster source the buffer gas is usually argon, because of its high sputtering yield compared to lighter gases. As the flow of Ar has to be kept at high values of around 100 ml/min, the spectra are always dominated by signals from ion collisions with Ar (up to 95 %). Additionally, argon can be ionized multiply times, also outside of the extraction region, and due to electric fields the produced ions can be re-accelerated into the extraction region where they can hit metal surfaces, leading to an increased noise.

Stability of the cluster beam

To obtain a reasonable signal, one needs to use the cluster source with parameters that permit the production of a very intense cluster beam. This means that the parameters like temperature of the aggregation chamber has to be kept at around T_{source}=-170°C with a discharge power of around 20 W, a buffer gas flow of 100 ml/min and a variable exit aperture. Furthermore, the aggregation length is variable and can be kept at distances between 5 cm and 32.5 cm. As the clustering process is strongly dependent on the thermodynamic conditions inside the source even a slight shift of one of the above parameters may result in a drastic drop of the produced cluster intensity and in changes of the size distribution. Therefore, the cluster beam stability is frequently controlled by a measurement of the intensity and distribution of positively charged clusters which are also emitted from the cluster source.

Kinetic energy of neutral nanoparticles

For some metals like copper or silver, under such conditions already large clusters with size

distributions well above thousand atoms can be produced. The kinetic energy of these clusters rises with cluster size, assuming a more or less constant velocity of the large clusters (below the velocity of the Ar flow). As the time-of-flight is orthogonal to the cluster velocity vector, we face the problem of losses of very large clusters before they arrive in the field-free region or detection due to the limited electric fields. For example, it is not possible to observe all clusters which have kinetic energies above 6 eV (losses in horizontal directions). It is not possible to strongly increase the electric fields due to power/current supply limits. In order to partly overcome this problem, one could consider to use a material, where for similar optimal sputtering conditions the original size distribution is shifted to much smaller clusters.

Mass resolution

Large cluster sizes means as well long flight times in the range of several milliseconds (for masses above 10^6 amu). For the mass spectrum, the resolution of the mass spectrometer is estimated to be R=$m/\delta m \approx$ 500 which sets the limit of resolution in the case of a monoisotopic material like on the clusters to about n = 500. If the material is not monoisotopic (copper has two stable isotopes of masses 63 and 65 amu, silver has stable isotopes with masses 107 and 109 amu) singly ionized clusters exhibit very broad peaks, for the case of silver with n=500 atoms the peak spreads out over a range of δm= 1000 amu ($M_{Ag_{500}}\times$109 amu- $M_{Ag_{500}}\times$107 amu=2$\times$ 500 amu=1000 amu).Thus, in the present case the mass spectra for large clusters are not expected to be size-resovled.

Detection efficiency

Another difficulty one has to face was already discussed in the section related to the detection of clusters. It is known that the production of secondary electrons in a Daly type detector depends on the velocity of the hitting ion and is characterized by a minimum threshold value. Effective yield values for velocities below this threshold are not precisely known. Taking for example Ag_{1000} the final velocity is in the range of 5 km/s, which means that a yield/atom of 0.002 is required for the cluster to be detected. This might be obtainable, as also collective effects are discussed when a large number of atoms arrives at a surface spatially and temporally well focused.

Characterization of nanoparticles

A major problem to study neutral clusters with COLIMACON DUO set-up is the lack of possibility to characterize them in-vacuo, for example to provide their size/charge ratio distribution. There are numerous experiments of molecular beams of metallic clusters characterized by lasers in the regimes of single and multiphoton interactions. However, these methods are difficult to realize in the ARIBE facility which is part of the nuclear installation GANIL. Therefore, I have chosen another method based on the deposition of the cluster beam on a surface and their analysis by AFM or TEM microscopy techniques. These methods required the design and build-up of a separate deposition chamber. The limiting factors for observation are related on the one hand to the obtainable lateral or horizontal resolution (for AFM analysis it is the tip characteristics which counts, for TEM the resolution limit depending on the grid properties is about 1.5 nm) and on the other hand it is dependent on the roughness of the sample surface.

Some theoretical aspects of interactions between ions and metallic clusters

3

This chapter allows the reader to get familiar with some theoretical concepts and models concerning metallic nano-objects and their interaction with singly and multiply charged ions. In order to explain the experimental results it is important to understand in a quantitative manner the processes appearing during and after the collision on the side of the nanoparticle (de-excitation and relaxation, fragmentation and fission) as well as for the ion (de-excitation of excited states, electron emission). First, a theoretical approach will be given to describe metallic clusters/nanoparticles. Furthermore, I will divide the collisional processes into two classes depending on the impact parameter. For so-called „peripheral" collisions I will refer to the electron capture process which can be described by the so-called Classical Over The Barrier Model, whereas for penetrating collisions the concepts of stopping power and sputtering are introduced. The fate of a metallic object after the interaction is often treated in the framework of the liquid drop model, originally developed in nuclear physics for studies of the nucleus stability. The equations are presented in the atomic units.

3.1 Description of clusters

Clusters of particles like atoms and molecules can be held together by different forces, for example van der Waals forces like in the case of fullerenes with low binding energies of about 300 meV, or by ionic forces, like in the case of (NaCl) with binding energies between 2 and 4 eV. Furthermore, there exist clusters with covalent and metallic bonds. One should note that in particular in the latter case the type of bonding may change in the regime of very small clusters, where metallicity is found only when the number of atoms overcomes a certain value.

3.1.1 Metallic cluster

The current description of metallic clusters will be based on the model of a metallic conducting sphere. In such approximation one can easily follow the properties of the cluster as a function of the cluster size.

However, in this zero-order approximation specific properties like shell closing or geometrical tight packing are neglected, which is nevertheless a good approximation for large clusters containing more than a few hundreds of atoms.

Element	Wigner-Seitz radius (a_0)	Ionization potential (eV)
Li	3.25	2.38
Na	3.93	2.35
K	4.86	2.22
Ag	3.02	4.3
Au	3.01	4.3
Bi	2.25	4.4

Table 1 *The table presents the Wigner-Seitz radius and the first ionization potential values for selected metals [64].*

The size of the cluster, characterized by the radius of the metallic sphere $R_{cluster}$, can be obtained from formula 1:

$$R_{cluster} = r_{WS} n^{1/3}, \tag{1}$$

where n - is the number of atoms in the cluster, and r_{WS} is a Wigner-Seitz radius, which describes the average radius of the sphere the atom occupies in the solid. The values of the Wigner-Seitz radius for some metals are given in the table 1.

The cluster volume V is described by equation 2:

$$V = \frac{4}{3}\pi R^3_{cluster}. \tag{2}$$

The energy required to ionize a cluster, i.e. to remove the first electron to infinity, depends on the electronic structure. Therefore, it varies for different elements. Using the approximation of a metallic droplet and taking into account electrostatic interactions and image forces, the ionization potential of such a metallic cluster can be calculated. According to previous works [45], the 1st and higher ionization potential energies, according to the subsequent ionization processes:

$$M_n^{Z+} = M_n^{Z+1} + e^- \tag{3}$$

can be described by the following equation:

$$W_n^q = W_\infty + (Z + \frac{3}{8})\frac{e^2}{R_{cluster}} \tag{4}$$

,where $R_{cluster}$ is the radius of a cluster, Z is its charge and W_∞ is a value of the work function for bulk material.

The graph in fig. 3.1 shows the dependence of the 1st ionization potential on the cluster size for 4 different elements: sodium, silver, gold and bismuth, calculated with equation 4. Also shown are the 1st ionization potentials for single atoms (squares). The largest 1st ionization potential value is that for gold atoms, the lowest one for sodium. However in the cluster case it

is bismuth which has the highest potential values. The ionization potentials for silver and gold clusters are almost identical as the Wigner-Seitz radius and the bulk ionization energies are almost the same, although in case of the atoms they differ by more than 1.5 eV. Straight dash-dot lines indicate ionization potential values for the bulk. In the Jellium model for clusters, [65],

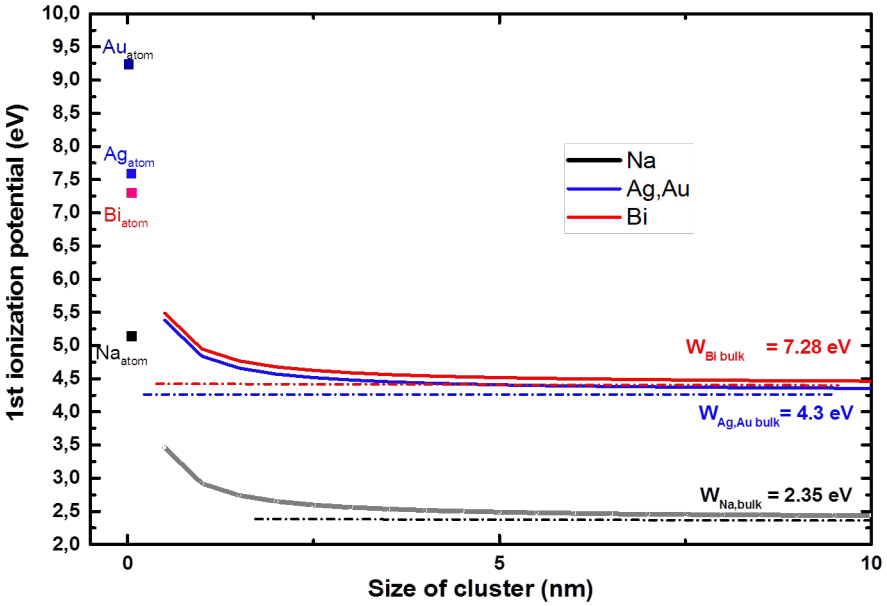

Figure 3.1 *The graph representing the 1st ionization potentials for different clusters : Sodium, Silver and Bismuth as a function of their size based on the metallic sphere approximation [45], with parameters taken from [64].*

the Fermi level ϵ_F is given as

$$\epsilon_F = -W_n^q. \tag{5}$$

Between the density of electrons ρ_{el} and the value of the bottom potential $V_{jellium}$ there exist the relation 6, [66]:

$$\rho_{el} = \frac{1}{3\pi^2}[2(\epsilon_F - V_{jellium})]^{\frac{3}{2}} \tag{6}$$

,where

$$\rho_{el} = \frac{3n_{el}}{4\pi n r_{W-S}^3} \tag{7}$$

and where n_{el} is the number of valence electrons present in the q-fold charged cluster containing n-atoms:

$$n_{el} = n - q. \tag{8}$$

The value of the potential $V_{jellium}$ is given by eq.9

$$V_{jellium} = \epsilon_F - \frac{1}{2}(9\pi n_{el}/4nr_{W-S}^3)^{\frac{2}{3}}. \tag{9}$$

It is important to know the potential experienced by the electron which is traversing along the radial distance r from the center of clusters towards its exterior. Naturally, for r≤$R_{cluster}$ an electron experiences the potential V_j. On the other hand, once it leaves "out of the cluster radius" it starts to experience the following forces: 1) The electrostatic force, arising from Coulomb interaction between charged sphere and the outgoing electron, which in atomic units is equal to:

$$F_{sphere} = \frac{q+1}{r^2}. \tag{10}$$

At the same time the electron induces the image charges (as the sphere is conducting and charged): first, localized at the centre ($q_{im,1} = -\frac{R}{r}$) and second, $q_{im,2} = \frac{R}{r}$ localized at position R^2/r, which gives the overall contribution to the forces acting on the hypothetical „leaving" electron to be

$$F_{im,1} = \frac{-R}{r^3} F_{im,2} = \frac{R}{r(r-\frac{R^2}{r})^2} \tag{11}$$

The energy necessary to move the electron from the cluster up to infinity is :

$$W = \int_r^\infty (F_{sphere} + F_{im,1} + F_{im,2}) dr, \tag{12}$$

The potential energy seen by the electron is equal to

$$V_r = V_{jellium} \; for \; (r \leq R) \, , \, V_r = -\frac{q+1}{r} + \frac{R}{2r^2} - \frac{R}{2(r^2-R^2)} for (r > R) \tag{13}$$

This potential as a function of distance r from the cluster center is well represented on fig.3.2 in case of silver clusters with n=200,1000 and 5000 atoms.

3.2 Collisions of projectiles with metallic nanoparticles

Collisions with atoms, molecules or ions (singly and multiply charged) are one of the typical methods of excitation of the systems present in the molecular beams, [67]. Fast highly charged ions and protons can be treated as structureless and with classicaly given trajectories $R_{ext}(t)$. If they are fast enough their trajectories are straight lines and the coupling with the cluster is due to the Coulombic field.

The ion trajectories are characterized by two main parameters: the ion velocity v_{ion} with respect to the target and by the so-called "impact parameter" b defined as the distance of closest approach between the cluster and a straight line ion trajectory. The ion velocity is a known parameter as it is given by the experimental conditions, however, the impact parameter can take a wide range of values. Therefore, observed results (like mass spectra) arise always from an accumulation and averaging of results corresponding to different b values. Furthermore, when clusters show geometrical structures, not included in the model of a conducting metallic sphere, different orientations of the cluster have to be considered. Also in the case of theoretical

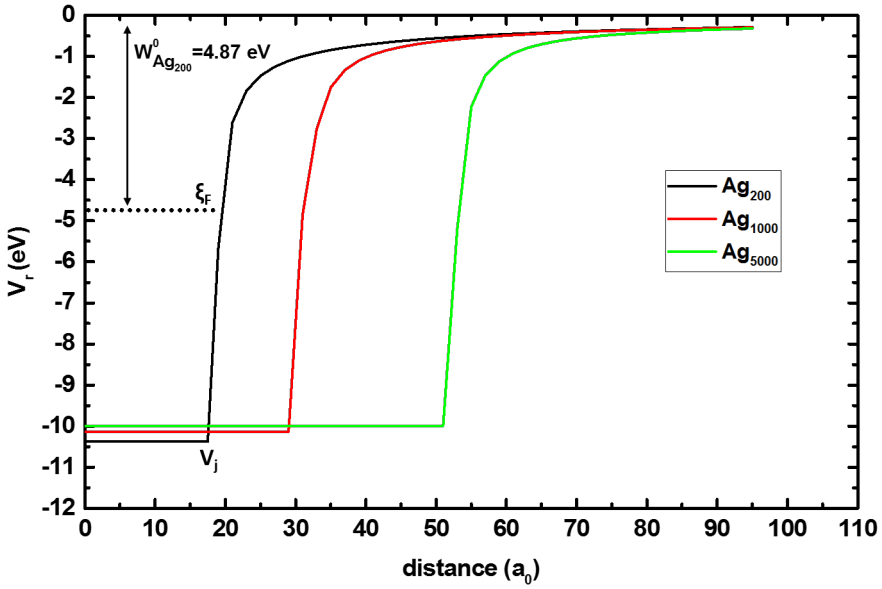

Figure 3.2 *Example of the potential seen by the electron inside and outside the metallic sphere for silver clusters of different sizes (n=200,1000,5000 atoms), based on values given in the table 1.*

descriptions, reaction cross-sections are computed by integration of the reaction probabilities over different impact parameters.

In this work, we will separate collisions of ions with nanoparticles or clusters according to their impact parameter b. For collision events, where $b > \mathrm{R}_{NP}$ we will talk about peripheral collisions, where the interaction is dominated by the Coulombic projectile field. For the case, when $b<\mathrm{R}_{NP}$, we deal with „penetrating" collisions, when the ion passes through the nanoparticle and can deposit the energy directly into the network of ions and electrons forming the nanoparticle. This classification is illustrated in fig.3.3.

In the case of peripheral collisions the dominant processes are single and multiple electron capture from the nanoparticle/cluster to empty states of projectile ion, polarization of the electron cloud of the metallic cluster on the femtosecond time-scale as well as Coulomb field induced coherent and localized electronic excitations (e.g. plasmon excitations or atomic giant resonances from electrons localized on d-shells of atoms) leading to the decay for example by emission of low-energy electrons [15].

In the case of penetrating collisions, especially when nanoparticles are composed of a few thousands of atoms, the collision is similar to that with a surface. Therefore, one can expect all the phenomena related to the approaching phase (electron capture, Coulomb field excitations, polarization of the cluster) occurring before the ion hits the target, as well as to the passage through a „solid" where the ion deposits a large amount of energy due to electronic and nuclear stopping processes. As the kinetic energy of the ions is in the range of 10s and 100s of keVs, the projectile will penetrate a nano-object with a diameter of several nanometers within a time

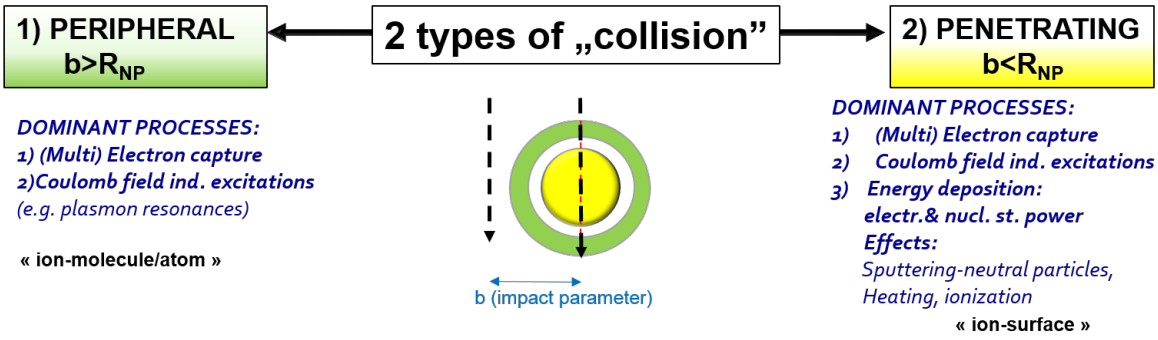

Figure 3.3 *Schematical separation of the collision between a charged projectile and a metallic nanosphere based on the impact parameter: peripheral collisions (with impact parameters larger than the radius of the cluster) and penetrating collisions (with impact parameter smaller than cluster radius) with associated phenomena.*

scale shorter than a few hundred fs. Thus, the deposition of the energy is an ultrafast process. Under such conditions one can expect rapid heating, ionization and collision cascades, leading to sputtering of the material atoms.

In the following section I will describe the main theoretical models necessary to understand the mentioned phenomena. At first I will start with peripheral collisions, where the most relevant model for ion-nanoparticle interaction will be the classical-over-the-barrier model treating the electron transport from the target (conducting sphere) to a highly charged projectile. Furthermore, the models of sputtering will be discussed in greater detail further below.

3.2.1 Peripheral collisions

The electrons localized in the potential formed by the ionic cores of the cluster, will experience the electric field of the incoming positive ion due to Coulomb interaction. We can describe the total system as consisting of a singly positively charged nanoparticle, an electron and a highly charged positive ion. At large nanoparticle/projectile distances the electron is bound to the cluster by a potential barrier between both particles. When the distance is reduced the barrier seen by the electron is strongly lowered and the electronic states are shifted towards lower energies due to the Stark effect. At a given so-called critical distance the barrier is so low, that the electron can overcome the barrier on a classical allowed trajectory: it becomes "molecular". When both particles separate again in the second phase of the collision, it is highly probable that the electron stays with the projectile due to its high electrostatic field, bound mostly in highly excited projectile states.

The electron transfer from a metallic sphere to excited states of a projectile can be described using the so-called classical-over-barrier-model, [68, 69]. The model describes the interaction of multiply charged ions, taking into account the transfer of many electrons, and it applies as well to the neutralization of ions approaching a surface [70]. Both processes are assisted by the

emission of multiple electrons mediated by Auger processes on the projectile side.

On the other hand, the dynamics of ionization, excitation and electron transfer for large impact parameter have been described by solving the Vlasov equation, performed for ion collisions with sodium clusters, [66]. It is shown, that in case of Na_{196} in collision with Xe^{25+} at impact parameter of $45a_0$ with kinetic energy of 500 keV the net charge of the cluster reaches its maximum q=12 and this occurs within 7 femtoseconds. The average net kinetic energy gain of the projectile estimates around 45 eV. The cloud of electrons is strongly displaced in the direction of the incoming ion during 1 fs, with dipole type oscillations of the remaining electrons with frequency of 3.3 eV, which is very close to the Mie dipole frequency of 3.4 eV. It is shown also, that depending on the charge state of the projectile (from q=8 to q=40 at velocity v=0.4 a.u) may lead to ionization of the cluster to the net charge from Q=3 up to Q=40 with the electronic excitation energy ranging from few eV even up to ∼200 eV.

3.2.2 Critical radius for capture in the over-the-barrier model

As already mentioned above, for all impact parameters $b>R_{cluster}$ the collision is called peripheral. The spherical potential of the cluster is more and more disturbed by the potential of the ion when the distance is getting smaller. This approach causes also a shift of the energy levels of the electrons in the cluster, called Stark shift :

$$\epsilon_F = -W_n^q - z/x \tag{14}$$

where +z is the charge of the ion and x is the distance of the ion from the centre of the cluster. The full potential experienced by an electron at distance of r>R has the form given by eq.13

$$V_r = -\frac{q+1}{r} + \frac{R}{2r^2} - \frac{R}{2(r^2-R^2)} - \frac{z}{x-r} - \frac{zR}{xr} + \frac{zR}{xr-R^2} \tag{15}$$

The first three terms are described already in the equation 9 and describe the interaction of an electron with the charge of the cluster and with image charges induced in the cluster by the electron itself. The other terms describe the interaction of the electron with the ion directly and with image charges induced by the projectile in the cluster, respectively. In figure 3.4 such a potential is schematically shown. As an example we choose the case of two silver clusters containing 1000 atoms and 5000 atoms, with a diameter of 2 and 5.5 nm. The charge of the projectile which is placed at a distance of 100 a.u. from the center of the cluster is set to q=3. Looking at the potential line for the cluster Ag_{5000}, we can describe most elements. The distance r_b is the position of the barrier, where the potential V_r has its maximum.

Judging by the equation 14 and 15, when an ion approaches the cluster, the height of the barrier is decreasing faster than the Fermi level. Below the specific distance $x_{t,1}$, the barrier falls below the Fermi level and the first electron can occupy molecular states, i.e. the electron can move - classically spoken - in the common potential of the projectile and the singly charged cluster, where:

$$V_r(r = r_b, x = x_{t,1}) = -W_n^0 - z/x_{t,1}. \tag{16}$$

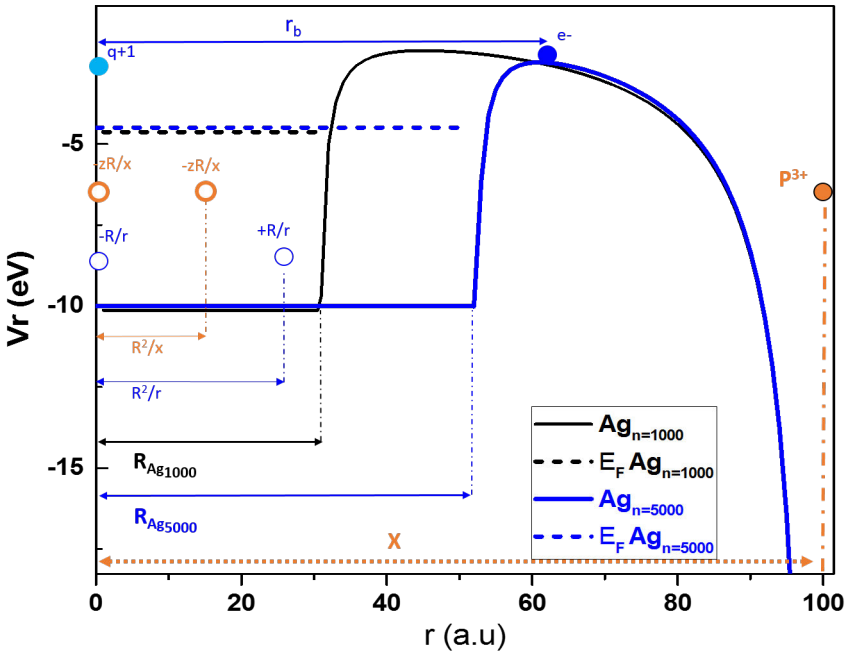

Figure 3.4 *The form of the potential seen by the electron during the peripheric collision of silver nanospheres with n=1000 and n=5000 atoms with projectile with q=3: Ag_n+P^{3+}. The centre of the cluster is in the origin of the x-scale and position of the ion is well above the radius of cluster. On the graph also the induced "image" charges coming both from the electron and the ion are marked, as well as the characteristic distances like position of barrier and ion. With dashed horizontal lines the Fermi level for both clusters is shown.*

This distance is called critical as this minimum approach is necessary to allow to transfer the electron on a classically trajectory. For the case of the cluster Ag_{5000} and projectile charge q=3+ one obtains $x_{t,1}$=68 a.u.

The fig.3.5 shows the difference of the potential seen by the electron with and without the projectile being present. The model takes into account that the transition of an electron has a resonant character, which means the electron is captured into a level which has the same energy which it has before in the cluster. The transfer of the electron has two main consequences. First, the charge of the cluster is increased by 1 unit, leading to a lowering of the Fermi level. Furthermore, the transferred electron reduces the charge of the ion when considering a total screening of the projectile by the captured electron. In order to transfer more than one electron, the impact parameter has to be smaller in order to further reduce the barrier for the second more tightly bound electron. The transfer of the electrons is continued as long as the projectile

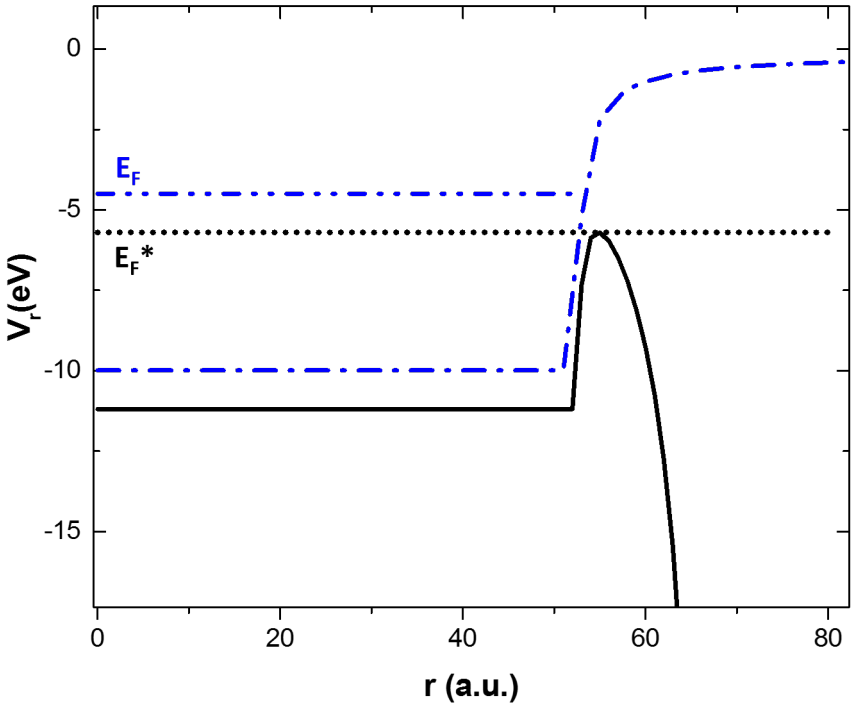

Figure 3.5 *The potential V_r seen by the electron without (blue dashed line)and with a projectile (black continous line) placed at a distance allowing for electron capture. The ion with q=3+ is localized at d=68 a.u from the center of the silver cluster Ag_{5000}. The black dotted line shows the Fermi level lowered towards the height of the barrier, which results in the transfer of the electrons into excited states of projectile.*

gets closer to the cluster and there are still free states for the electrons to be occupied in the projectile frame. Fig.3.6 shows a straight-line trajectory for the possible capture of 3 electrons.

In fig3.7 the dependency of the 1st electron capture distance is shown as a function of the silver cluster size for various charge states of the projectile. For a given charge state, the distance of the 1st electron capture increases with decreasing size of the cluster. Taking as an example a nanoparticle with a radius of 2 nm (38 a.u., corresponding to 2000 atoms) and a projectile with charge q=1, one observes that the 1st electron is transferred at a distance of b=10 a.u. above the cluster surface. which is already around 30 percent of the cluster radius. If we consider the charge of q=10 that distance increases up to 35 a.u, which is twice larger than the cluster radius. The higher charge of the projectile, the barrier gets lower strongly, which shifts the capture distances to higher values with higher charge state of projectile.

Using the classical-over-the-barrier model, one can calculate as well the distance for the capture of an electron from a metal surface to the projectile, [70]. This distance, depends only

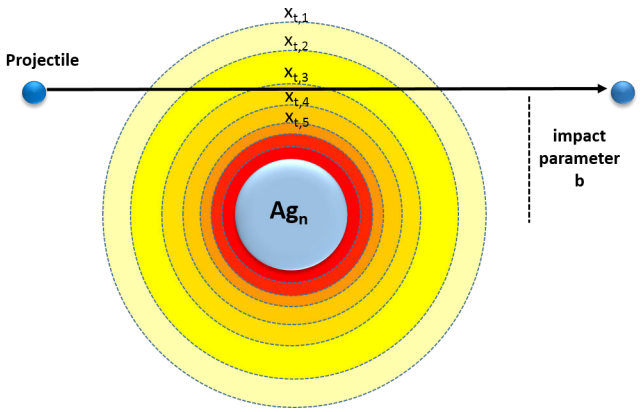

Figure 3.6 *Schematic picture of the situation of the peripheric collision between silver cluster Ag_n and the charged projectile. The concentric color-gradient rings represent the multi-electron capture cross-sections.*

on the charge state of projectile and material properties of the solid and is given by:

$$x_{t,1}^{solid} = \frac{1}{2W_{solid}}\sqrt{8z+2} \tag{17}$$

For large cluster radius values, the capture distance for clusters approaches the corresponding values for surfaces as to be expected (look fig.3.7 marked with dash-dotted lines).

3.2.3 Projectile after peripheric collision

As it was mentioned previously, the basic assumption of the over-the-barrier model is that the electrons undergo resonant transitions from the Fermi level (lowered by the Coulomb field of the projectile) to highly excited levels of the incoming ion. The ionization potential of silver clusters with 1000 to 5000 atoms is in the energy range from 4.5 to 5 eV. For multiply charged ions like Ar^{8+}, the recombination energy is 143 eV, which means that the electron will be captured into an excited level which lies at around 138 eV above its "ground" state energy. Therefore, the ion is formed in a so-called Rydberg state. In the case of multiple electron transfer to the projectile multiply excited states are formed, where a large number of electrons occupies levels which are above empty ones. Thus, deexcitation is likely to result in so-called Auger processes. The transition of one electron to a lower-energy state of the ion can induce the simultaneous emission of another (coupled) electron into the continuum. This process can occur sequentially, increasing the number of emitted electrons. Thus, not all electrons are stabilized on the projectile and in the experiment the measured charge state has to take into account this fact. In the same way, this process increases the number of electrons emitted into the continuum. A detailed study of these processes has been made in coincidence measurements of collisions of highly charged ions with fullerene molecules, detecting the number of emitted electrons, the charge state of the product ions and the charge state of the projectile after the

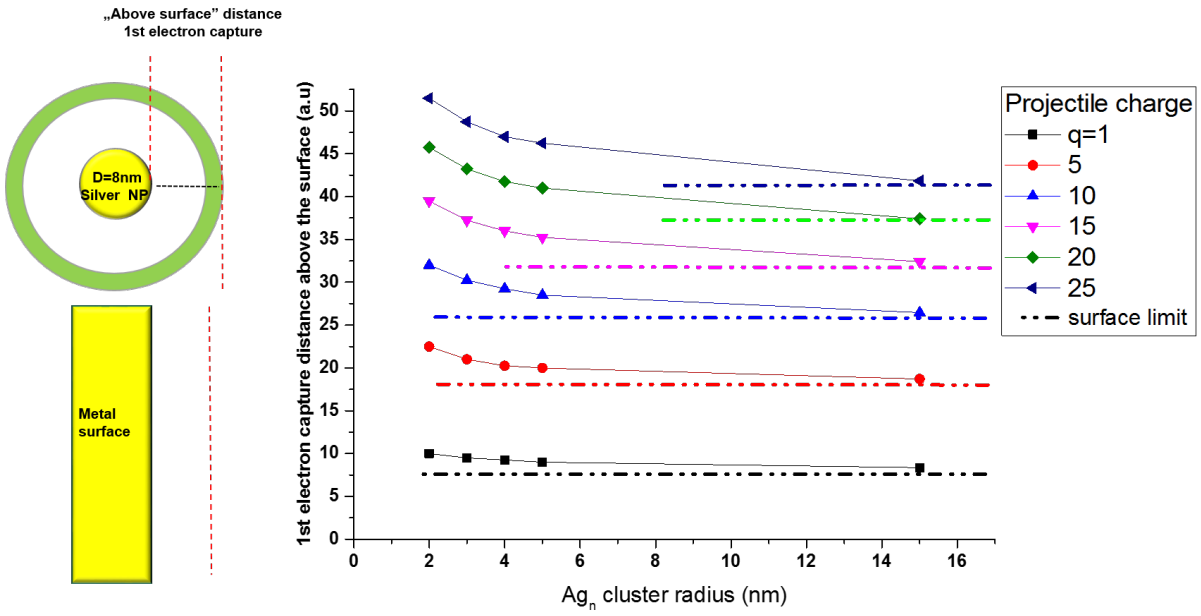

Figure 3.7 *Calculations of the 1st electron capture distance for the case of different charges of the projectile for q=1 up to q=25 (data points) compared with electron capture distance for the same charges in case of surface (dashed lines). The nanoparticle case taken for these calculations was silver with diameter of 8 nm.*

collision [71] or by estimating the total potential energy of highly charged fragmenting fullerene ions by analyzinsg the fragment kinetic energies, measured in correlation with the charge state of the outgoing projectile ion, [72].

3.3 Fragmentation of metal clusters and liquid drop model

In the previous part, the ionization of metal clusters was described as a consequence of electron transfer to multiply charged projectiles. However, it is important to analyze the behavior of the cluster after the interaction with an ion. Basically, for the charged sphere there are two forces which decide on the stability of the charged nanodroplet. One type are the cohesive forces, related to the formation of the surface which stabilize the cluster and tend to maintain their spherical form. On the other the charges are redistributed on the surface and repulse each other and destabilise the structure, leading to deformation. During this deformation process, the cohesive forces are increasing while the repulsion forces decrease, therefore there may exist an energetic barrier which maintains the system tied up together.

Cohesive forces by their nature are short-range forces, contrary to long-range Coulombic repulsion. The barrier is a result of competition between these two contradictory factors and

as long as cohesive forces are larger than repulsive ones, the system is stable and for any fragmentation the system has to be excited to be able to overcome the barrier. When the repulsive Coulombic forces are equal or larger than the cohesive forces, the barrier decreases and system gets unstable, even at temperature of 0 K. One can therefore define the parameter describing the stability of the system and its tendency for fragmentation. This parameter is known as fissility X and is defined by equilibrating the two forces:

$$X = F_{rep}/F_{coh}. \tag{18}$$

which in terms of the energy can be expressed as :

$$X = E_c/2E_s, \tag{19}$$

where E_c is the Coulombic energy (destabilising) and E_s is the surface energy (stabilising) of the system. The case where the repulsive electrostatic energy is equal to twice the cohesive surface energy, the fissility is X=1 and leads to a disappearance of the barrier. Thus, a deformation will lead automatically to charge separation, called also a fission process. This is true also for X>1. For values of the fissility X lower than 1, the fission may be initiated by thermal excitation of the cluster. It may enter in competition with another decay process, namely the emission of neutral atoms or molecules (evaporation). As will be discussed further below, the relative importance of fission and evaporation depends to a large extend on the height of the fission barrier and the activation energy for evaporation.

3.3.1 Liquid drop

The model of a liquid drop was developed in the field of nuclear physics in order to understand the stability of the atomic nuclei. It describes the behavior of the system in the case of an excess of charge and was first described by Lord Rayleigh [73] in order to theoretically explain the behavior of charged droplets.

In case of a nucleus ${}^{Z+N}A$, which is composed of Z protons and N neutrons, the positive charge is compressed inside the minimal volume. The Coulomb force, as a long-distance force is counterbalanced by short-distance strong forces between protons and neutrons. The fissility of fermions system can be expressed as

$$X = \frac{Z^2/N}{(Z^2/N)_{critical}} \tag{20}$$

and X=1 is given by $(Z^2/N)_{crit}$. The competition between forces implies the existence of the critical size for a given total charge value Z. Above this value the system is spontaneously fragmenting to remove the excess charge. In the analogic way we can describe the fissility of the cluster of metal (silver for example) as:

$$X = \frac{q^2/n}{(q^2/n)_{critical}} \tag{21}$$

and the critical value can be calculated by

$$(q^2/n)_{critical} = 16\pi r_{WS}^3 \sigma_s \tag{22}$$

where r_{WS} is a Wigner-Seitz radius and σ_s is the surface tension of the material, q is the cluster charge (parameters r_s and σ_s are temperature dependent). Comparing nuclear matter and metallic clusters, in the first case $(Z^2/N)_{critical}$ ∼50 and for sodium clusters (q^2/n)=0.4. In the case of metal clusters the strength of the cohesive forces is much lower than that of the nuclear force, which explains the difference in the critical values. In the nucleus case, the positive charge is redistributed homogenously over the volume as the charge is linked to the protons, while in the case of clusters the charge (which is due to a lack of electrons) is distributed over the metal surface. Thus the two systems differ as they represent a volume- and a surface-charged system, respectively. However, both resemble each other and one can use the same tools for the system description.

The fissility is the fundamental quantity concerning the fragmentation of charged droplets. Depending on the X value, different types of fragmentation can occur. In the nuclear case, one observes with high intensity the „quasi"-symmetric fission where the nucleus decays into charged fragments of similar size for fissilities of around 1. For fissilities inferior to 1, the asymmetric fission will be dominant, which has its realization in the emission of protons and alpha particles.

In the case of charged liquid droplets with a fissility larger or equal to 1, it was predicted by Rayleigh that multi-pole deformations are the ones which become first unstable. This leads to the formation of jets emitting a large amount of small charged particles. Indeed, these jet formations were observed in several experiments, in particular when observing the evaporation of highly charged trapped droplets of glycol approaching the fissility X=1 [74].

In the case of metal clusters the fissility can vary over a wide range of values in particular when the clusters are ionized in collisions with highly charged ions. As will be discussed further below, experimental studies of small systems showed the occurrence of asymmetric fission processes producing small-size fragments [19, 75] and also the signature of symmetric fission [76].

In the following, the emission of charged particles producing two charged particles will be called fission, the emission of neutral particles/atoms we will call evaporation and the largest fragment the residue of the process.

3.3.2 Energy of the cluster in the liquid drop model

In this part we are going to describe the total energy of the charged cluster based on the liquid drop model. Knowing the value of this energy we will be able to examine different fragmentation channels. In general, the cluster energy can be decomposed into several contributions, stemming from the volume, from the surface and from the excess charge. Following

the example of sodium or silver clusters Na_n with n-atoms, we consider the energy of a single atom as reference point with value 0. The different energy terms are as follows:

Volume term:

$$E_v = a_v n \tag{23}$$

where a_v is he energy of cohesion of the atom in the solid, $a_v = 1.11$ eV for Sodium [75] and $a_v = 2.66$ eV for Silver [77].

The surface energy can be calculated based on the surface size

$$S = 4\pi R^2 = 4\pi r_s^2 n^{\frac{2}{3}} \tag{24}$$

The surface atoms are less bound than volume atoms, and their energy is

Surface term:

$$E_{surface} = \sigma_s * 4\pi r_s^2 = a_s n^{\frac{2}{3}} \tag{25}$$

The values σ_s and a_s are related to each other.For sodium (surface tension) a_s is equal to 0.68 eV at 580 K [75] and for silver a_s=1.98 eV.

When charging the cluster q times it requires the energy of

$$E_q = \sum_q^1 W_q \tag{26}$$

where W_q is the q-th ionization energy of the cluster.

The electrostatic energy of a q-times charged metallic sphere with radius R is given by [75]:

$$E_c = 1/2q^2/R \tag{27}$$

The total energy of a metal cluster can be written as:

$$E_{total} = -E_{volume} + E_{surface} + E_q + E_c = -a_v n + a_s n^{\frac{2}{3}} + \sum_q^1 W_q + 1/2\frac{q^2}{R} \tag{28}$$

where R=$r_{WS} n^{\frac{1}{3}}$

3.3.3 Asymmetric fission

In this chapter I will describe the process of asymmetric fission according to the equation

$$Na_n^{q+} \rightarrow Na_{n-x}^{(q-1)+} + Na_x^+ \tag{29}$$

In this process a large parent cluster is emitting a small singly charged fragment. In this case we are interested in the variation of the size n-x of the small fragment with the fissility of the parent cluster. The schematic potential shown in fig. 3.8 defines the quantities that play

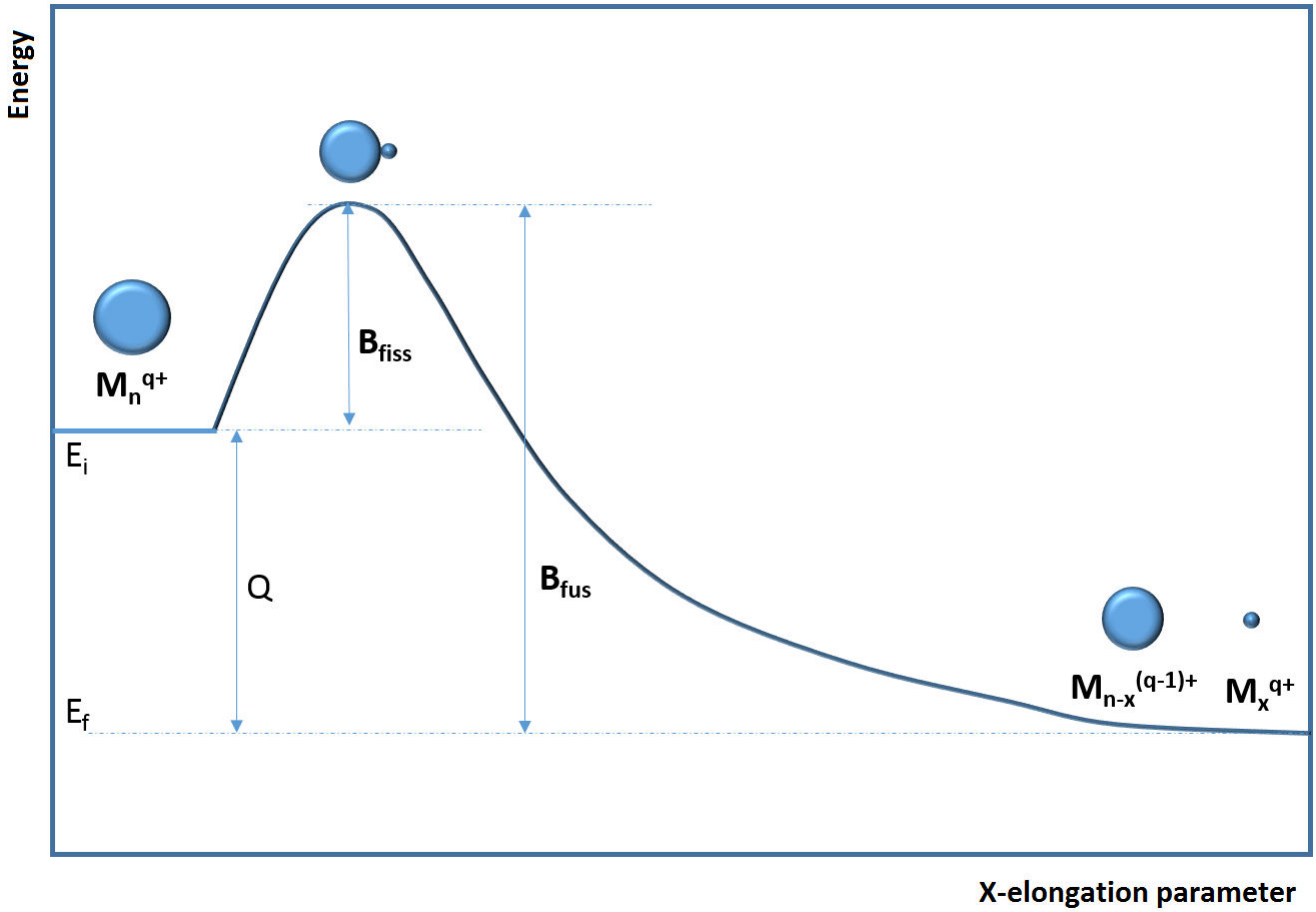

Figure 3.8 *Fragmentation scheme for a multiply charged silver cluster based on the liquid drop model. It illustrates the relation between different fundamental quantities. The Y axis represents the energy of the system and X is the elongation coordinate (for large values it is the distance between the small fragment and the residue). Shown are the initial and final total energies of the system E_i and E_f, the fission and fusion barriers B_{fiss} and B_{fus} as well as their difference Q.*

an important role in the asymmetric fission process. These entities are the total energy of the system before E_i and after fragmentation E_f, their difference, the Q value:

$$Q = E_f - E_i, \tag{30}$$

and energies of the barriers for the fission $B_{fission}$ and fusion B_{fusion} as well as the distance d_B of the separation between centres of the residue and the fragments. The position and height of the fission barrier depends on the fissility.

The more the value of the fissility X approaches 1, the smaller is the barrier of the fission. At X=1 the barrier disappears completely and a minimum deformation results in an irreversible change of the parent system, dividing into two or more subsystems. For a fissility X<1, the channel of fission is competing with other relaxation channels (for example emission of neutral

atoms). Their relative importance of different fission channels, leading to the emission of different-sized small fragments is a function of the respective barriers and the internal energy (temperature) of the initial system. This can be described as the ratio of intensities I_1 and I_2 as in the Arrhenius formula:

$$\frac{I_1}{I_2} = \alpha\, exp(-\frac{B_{fiss,1} - B_{fiss,2}}{kT}) \tag{31}$$

where I_x describes the number or fission events occurring via path x, $B_{fiss,x}$ is the corresponding barrier, T is the initial temperature of the system and the factor α takes into account other effects like the probability for the preformation of a given fragment.

The barriers of fission and fusion are related by the equation

$$B_{fission} = B_{fusion} + Q \tag{32}$$

where Q is negative value. To estimate the fusion barrier and hence the fission barrier one needs to take into account several factors : The Coulombic force between fragment and residue, their mutual polarisation and the distance d_b where the barrier is situated. However, the solution of the calculation is not trivial. Here, we will make a very crude assumption, namely that the shapes of the fusion barriers are the same if we consider only small singly charged fragments. In such an approximation the differences of the fission barriers will be determined by the differences of the Q energies:$B_{f,1} - B_{f,2} \simeq Q_1 - Q_2$. The intensity of different pathways will then be given by:

$$\frac{I_1}{I_2} = \alpha\, exp(-\frac{Q_1 - Q_2}{T}) \tag{33}$$

In order to identify the preferred fission channel (the size of the small singly charged fragment) one can compare in a first approximation the differences of the energies Q, taking into account only the energy criterion and assuming that the α factor is equal to 1. The energy of the initial cluster is calculated based on the liquid drop model (formula 28).as well as the energy of the larger fragment. For the small fragments we refer to values from the literature. These values are given in the table 2 for small clusters of sodium, silver and bismuth (data for sodium : [75], silver [78], bismuth [79]).

In figure 3.9 calculated Q values are shown for two cases: 1) Ag_{500}^{q+} and 2) Ag_{5000}^{q+} as a function of their fissilities varying between X=0.1 up to 1. The emission of small fragments of metal M_x^+ for x=1 to 5 (6 in case of bismuth) is taken into account.

As long as the hypothesis that δB$\approx\delta Q$ is taken as valid, for the case of silver we can say that the emission of monomers is the most favorable channel, followed by dimer and trimer for both small(n=500) and large(n=5000) clusters for fissility values of X between 0.1 up to 1.

It is interesting to compare the results for the case of clusters of sodium and bismuth, shown in fig.3.10. The left panel of fig.3.10 shows the result of Q values for fragmentation of Na_{200}^{q+} (q=9 to 4). It is worth noting that the most favorable pathway up to X=1 is the emission of the Na_3^+ trimer. The second most likely channel corresponds to the monomer Na_1^+, which converge into the same Q value for X=1. This is different for the case of silver clusters.

	Silver	Sodium	Bismuth
x	$E(Ag_x^+)$ [eV]	$E(Na_x^+)$ [eV]	$E(Bi_x^+)$ [eV]
1	7,58	5,14	7,28
2	6,04	4,16	5,13
3	3,86	2,95	2,18
4	2,49	2,44	-0,12
5	1,85	1,56	-2,72
6			-3,52

Table 2 *The table with the values of total energies of monocharged small fragments/clusters used for estimation of the Q barriers for case of silver,bismuth and sodium.*

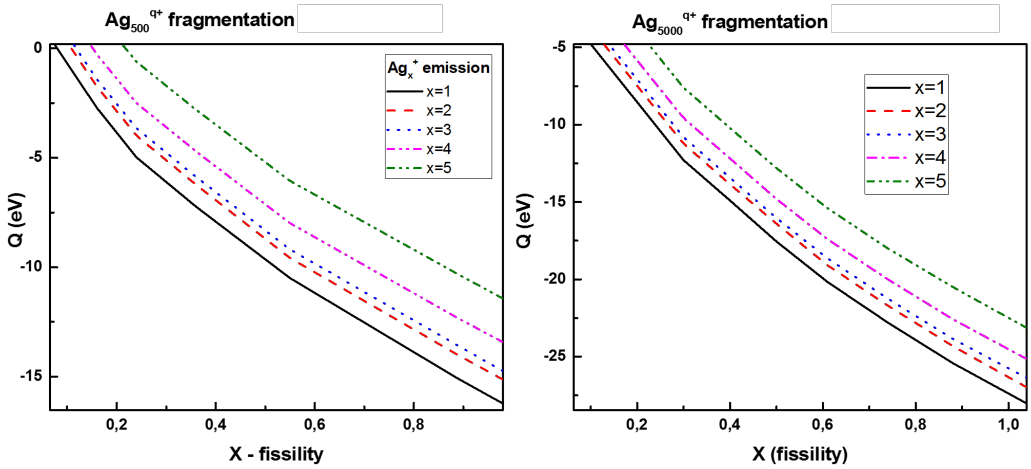

Figure 3.9 *The Q values for different Ag_x^+ fragmentation channels in assymetric fission in case of silver clusters with n=500 and n=5000 atoms as a function of their fissilites.*

In the case of bismuth, shown on the right part of fig.3.10, the main fragmentation channel corresponds to the emission of Bi_5^+, Bi_4^+,Bi_3^+ and Bi_6^+ for X=0.2-1 with decreasing probability, respectively. Monomer and dimer emission are not the dominant fragmentation pathways like in Na. It should be noted that these conclusions can only be drawn when the relation $\delta B = \delta Q$ is valid for the emission of small fragments (see discussion further above).

For low fissilities, fission of clusters enters into competition with evaporation processes. In the case of sodium, the fission is not anymore favored below X=0.3 which corresponds to an energy barrier which is comparable with the activation energy E_{coh}=1.11 eV for evaporation of neutral atoms [80]. Thus, competition between fission and evaporation occurs. For a given cluster size this leads to a maximum charge which can be observed in the experiment which is lower than the critical charge. On the other hand, for a given charge state q this leads to a so-called appearance size $n_{appearance}(q)$. For larger clusters (higher fission barrier) the

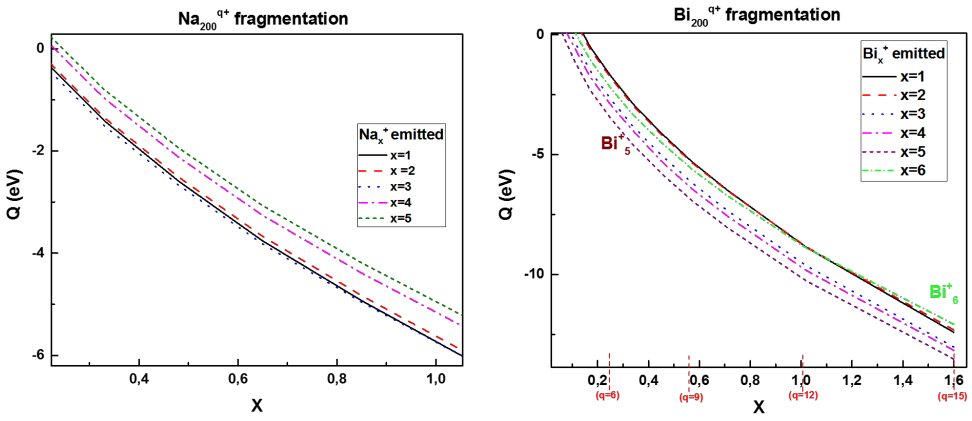

Figure 3.10 *The calculated Q values for different fragmentation channels in assymetric fission in case of sodium (n=200) and bismuth (n=200) clusters a function of their fissilities.*

system becomes metastable keeping its charge, but preferring a deexcitation by evaporation. For smaller sizes (lower fission barrier) it is fission with dominates. Thus, in the experimental spectrum these systems are not observed in charge state q. The appearance size depends in particular on temperature of the system [77]. For hot sodium clusters (ionized by laser) the appearance size $n_{app} \approx 8q^2$ [77], which corresponds to X≈0.3. For the critical size X=1, $n_{critical}$=2.5q^2.

Figure 3.11 shows the so-called stability diagram which defines the regions of stability and fragmentation as a function of the cluster charge q and of the cluster size n. The x and y axis are given in logarithmic scales. Clusters characterized by the same fissility parameter X, are lying along the given straight lines. The line corresponding to X = 1 separates this diagram into two regions. For X>1 all systems are unstable even at a cluster temperatures of 0 K. For the region with X<1 the systems are stable at a temperature of 0 K as they are stabilized by a fission barrier or the required activation energy for evaporation. The situation changes when the cluster temperature is increased provoking in hot clusters thermally activated processes.

In order to separate the regions for evaporation and fission, a third line is included in Fig. 3.11 corresponding to sodium clusters, with a fissility of X=0.3 (see discussion of appearance size above). For X<0.3 the hot system prefers to evaporate an atom or dimer for energetic reasons, whereas for X between 0.3 and 1 the fission process is dominant as the height of the fission barrier is lower than activation energy for evaporation.

It is worth noting that after the emission of a small fragment with charge 1 (most likely) the residue may still be unstable. Taking as an example Na_{200}^{8+} (X=0.8), if it decays with emission of a small singly charged fragment, the remaining residue can still have a fissility relatively large (X=0.6) that it can emit a second fragment. In case of symmetric fission, if the parent cluster has a fissility close to X=1, the multiply charged fragments will have X=0.5 and they won't be stable unless they are cold, which makes it difficult to observe them experimentally.

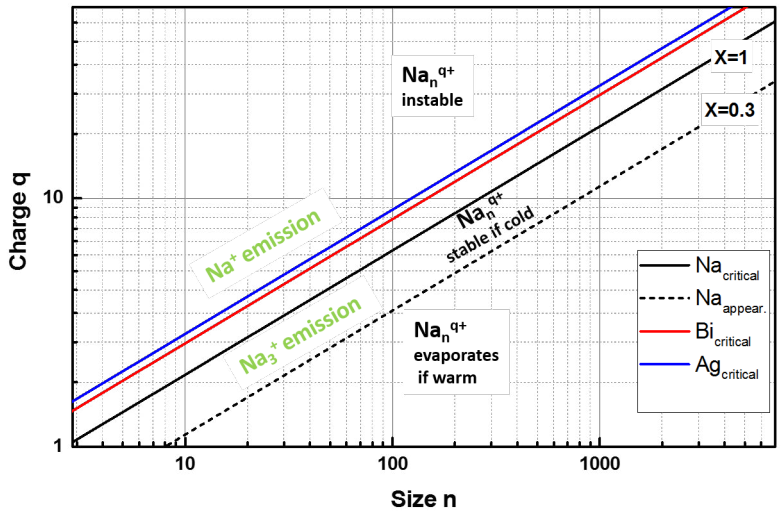

Figure 3.11 *Stability diagram comparing the critical charge/size values for the case of sodium, silver and bismuth clusters (continous lines). On the graph for the case of sodium the most probable decay mechanisms are marked (monomer/trimer emission, neutral evaporation) as well as the appearan6ce size (dotted line) for warm sodium clusters based on [77], related to the evaporation barrier (cohesion energy) for the atoms in sodium (X=0.3).*

In fig.3.11 the blue and red lines represent also critical size/charge lines for the cases of silver and bismuth, respectively. The clusters of silver are the most stable ones, requiring the smallest number of atoms to stabilize the charge against fission whereas sodium requires the most.

3.4 Short comparison with ion-solid collisions -Central cluster collisions and stopping power concept

When ions enter into a metallic solid, they penetrate a reservoir of heavy nuclei and light electrons, modifying their initial distributions. In case of positively charged ions, the electrons are attracted by the projectile and tend to screen its charge. During such interactions the ions are losing part of their kinetic energy and change their charge state, while the electrons and nuclei in the reservoir receive that lost energy.

3.4.1 Energy loss of the projectile

The interaction of charged projectiles with solids, the effects of the diffusion and the loss of the energy are generally treated within the concept of the stopping power, which represents

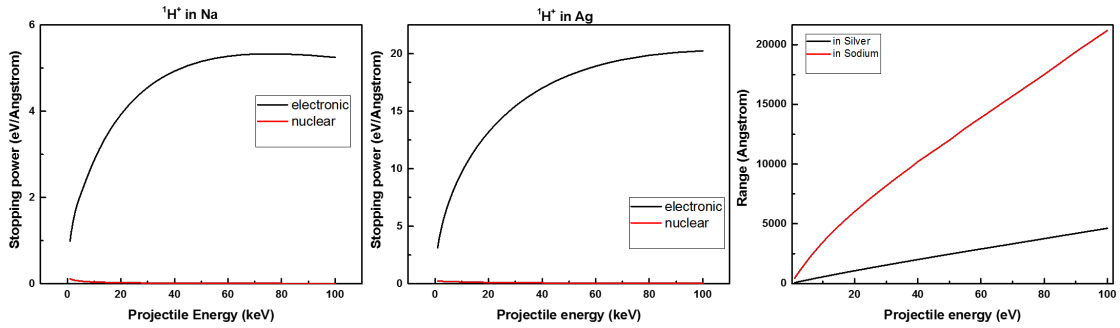

Figure 3.12 *Illustration of the electronic and nuclear stopping power dependencies of protons in sodium and silver as a function of the kinetic energy (left and middle). In figure on the right the penetration depth is shown as a function of the energy. Results are based on SRIM Program calculations with (E=1 to 100 keV).*

multiple types of interactions of a projectile with matter that is being penetrated. The solid matter is composed of a network of ions and an ensemble of electrons loosely or tightly bound. Due to the specific interaction the collision processes of the ions are separated into two parts. One is the interaction of the projectiles with the solid ionic network, which leads rather to a scattering of the projectile resulting from elastic collisions with network constituents (atoms, ionic cores) and the production of heavy atom cascades. The other part concerns the processes of the polarization and excitation of the electronic system of the solid by the projectile. In consequence, we talk about the nuclear stopping power and the electronic stopping power.The total penetration distance and the relative importance of both interactions depend very strongly on the nature of the projectile and target materials, as well as on the velocity of the incident projectile.

The electronic stopping power can be calculated from the formula given by Ziegler [81]. This approach is based on the theory of Lindhard, who described the interaction of an electron plasma with charged particles in an auto-coherent way. Numeric parameters and the notion of the effective charge were added to better reproduce the experimental values for slow ions. The prediction of the model states that the loss of the kinetic energy of the projectile per unit of the length $\frac{dE}{dl}$ is proportional to the velocity v of the ion and the square of the effective charge z_{eff} in the solid:

$$\frac{dE}{dl} \propto v z_{eff}^2 \tag{34}$$

The effective charge of the ion is the value which is reached in the equilibrium state produced by electron capture and loss processes. It depends on the nature of the ion in the solid as well as its velocity: the faster the ion the more the equilibrium charge approaches the initial charge. The only exception is the hydrogen ion $^1H^+$ where the equilibrium charge is considered always as $+1$. However for the case of helium $^4He^{q+}$ the equilibrium charge varies between 0.2q and q (q-initial charge).

In fig.3.12 the electronic and nuclear stopping power dependencies are shown as a function of the projectile energy. A comparison of sodium and silver target materials is given as well as the range of the ion within the material. First of all, in the case of proton as a projectile, the nuclear stopping power is almost negligible and the whole kinetic energy is transferred into the reservoir of the electrons in the material. The electronic stopping power is much lower in the sodium case over the whole range compared to silver by a factor of about 4. Of course, this is linked to a much larger penetration depth in sodium compared to silver. More information about stopping power and resulting phenomena will be presented later while interpreting the results of collisions of ions with large (up to 10 nm) metal nanoparticles.

3.4.2 Excitation and ionization of the cluster

What happens with the deposited energy? The ion traversing through the cluster makes the gas of electrons to get polarized and to screen the charge of the cluster. Such perturbation of the density of the electrons follows the trajectory of the projectile. If the velocity of the propagation of this perturbation is close to the velocity of the electrons there is the resonant transfer of the energy. The ion induces strong oscillations of the electron density in the frequency of plasmons, which can lead to statistical emission of electrons into the continuum [66]. The process of the collision and emission of the electrons takes place in the order of a few to a few tens of femtoseconds. On the scale of picoseconds the electronic excitation can be transferred into vibrational modes of the atomic network.

To estimate the final charge q_f of the cluster after the central collision (impact parameter b<$R_{cluster}$), we can compare the energy deposited with the energy necessary to eject a given number of electrons n_e=q_f. The energy deposition is calculated along the trajectory l corresponding to the impact parameter b:

$$\delta E = \frac{dE}{dl} l, \tag{35}$$

$$l = 2\sqrt{R^2 - b^2} \tag{36}$$

Statistically, the contribution of the trajectory l is obtained by multiplication with the probability dp per collision for the impact parameter b:

$$dp = \frac{2\pi b db}{\pi R^2} = \frac{2}{R^2} b db \tag{37}$$

The average distance traversed by the ion in the cluster is therefore equal to

$$\bar{l} = \int_0^R l dp / \int_0^R dp = \frac{2}{R^2} \int_0^R l b db = 4/3R \tag{38}$$

and the average energy deposition is

$$\delta \bar{E} = \frac{dE}{dl} \bar{l} \tag{39}$$

and $\bar{l}$ corresponds to the impact parameter

$$\bar{b} = \frac{3}{4}R \tag{40}$$

As an example we may consider silver nanoparticle of 6nm diameter in collision with O^{6+} with kinetic energy of 90 keV. For above mentioned kinetic energy of projectile, the electronic stopping power estimates $P_{electronic}$= 46 eV/ Ångstrom, whereas the nuclear stopping power estimates 16 eV Ångstrom. Thus, the energy deposited in the electronic degrees of freedom $dE_{elect.}$ of freedom is :

$$dE_{elect.} = \frac{3}{4} \cdot 46 \cdot 60 = 2070\, eV \tag{41}$$

and energy deposited in nuclear degrees of freedom $dE_{nuclear}$:

$$dE_{nuclear} = 3/4 * 16 * 60 = 720\, eV; \tag{42}$$

yielding finally total amount of the energy deposited in the whole cluster to be dE_{total}=2790 eV. Such big amount of the energy used only for multionization process of Ag nanoparticle would mean that a massive final charge state would yield ∼450, however according to some models for ion impact ionization of atoms, this value is reduced. A large part of the energy goes into collective excitations of the system, part of the energy is given to kinetic energy of formed scattered ions and electrons.

Performance and characteristics of the developed experimental devices

4

In this chapter I will describe some characteristic aspects of the performance of the experimental set-up COLIMACON DUO, developed and constructed during my thesis with the aim to investigate collisional processes between multiply charged ions and metallic nanoparticles.

The experimental challenges consist of producing an intense, well collimated beam of large metallic particles and to determine the size distribution of the neutral species. Furthermore, to let them interact with a focused beam of multiply charged ions and to mass/charge analyze the positively charged reaction products which are formed during the collision. Their sizes will reach from a single atomic ion up to heavy residues containing several thousands of atoms.

Firstly, I will characterize the magnetron-based metal cluster source and its capabilities to produce intense beams of neutral metal clusters. As the cluster source produces not only neutral nanoparticles but also charged ones, the source performance were optimized by measuring the count rate of positively charged species.

Secondly, in order to determine the size distribution of neutral species, we developed the deposition chamber and analyzed the neutral clusters by using microscopic methods based on AFM and TEM images.

A third aspect will concern the time-of-flight analysis of very large clusters with masses in the range of up to 200 000 amu. This required to perform simulations of the ion trajectory for cationic species produced during collisions in the present setup. In particular the influence of the directed initial velocity of the nanoparticles as well as their kinetic energy due to Coulomb explosion processes will be discussed (emphasis will be put on the extraction limitations for large and energetic objects).

Finally, we will discuss the overall detection efficiency of the experimental device which is important in particular for the coincident measurement of several cationic fragments stemming from one event.

4.1 Beam production of large neutral nanoparticles

Similar types of magnetron-based cluster sources were already used and developed over the last 25 years, mainly designated for the deposition of large clusters on substrates, for example

for the production of electrical contacts on isolating materials [45]. A short historical note was already given in chapter 2 in the description of cluster sources. Therefore, here we will only briefly discuss how different source parameters and conditions influence the production of specific size/charge distributions. I will concentrate on the production of Bi clusters and its dependence on the gas flow, the pressure in the cluster source chamber, the aggregation length, the discharge current, the cooling temperature and the presence of impurities and on the determination of the size distribution of silver neutral nanoparticles.

4.1.1 Spectra of positive bismuth clusters

For the production of bismuth clusters we used a sputter target in form of a disk of 5cm in diameter and 6 mm in thickness with purity of 99.99%, provided from the Kurt Lesker company. The production of metal clusters using a magnetron cluster source is not easily reproducible as the conditions vary often due to the large number of parameters which are partly correlated with each other. It was found that very often the cluster source works very stable once the target is exchanged by a new one and the cluster chamber is thoroughly cleaned.

During production of metal clusters a characteristic eroded ring due to sputtering is formed on the target, leading to a change of the effective distance between cathode and anode altering the discharge conditions with time. On the other hand, clusters that are formed inside the chamber, are deposited on the internal wall surfaces. Such contamination may affect the cluster formation and the plasma discharge. Relatively often an "unclogging" procedure of the exit nozzle is necessary, as the deposit of clusters on the surface reduces the size of the exit hole and leads to a reduction of the molecular beam intensity.

In order to establish optimal source conditions we relied on the observation of the signal of positively charged clusters, which can be extracted into the time-of-flight system. This allows obtaining a count rate as well as rough information on the cluster size distribution for positive clusters. Assuming in a first approximation that conditions for the production of intense beams of neutral and positively charged clusters are similar an optimization was possible. The variation of experimental parameters showed that there are several conditions which are crucial for the production of an intense beam of positive Bi clusters. First of all, we observed that the most important parameters are both low temperature of T_{source}<-150°C as well as a minimum flow of the argon gas. For a flow lower than 80 ml/min the cluster signal was totally lost, independent of the discharge power and the IRIS size (the pressure inside the cluster chamber can be regulated in two ways: changing the flow of the buffer gas while the IRIS diameter is kept constant or changing the IRIS size while the flow is kept constant).

4.1.1.1 Effect of buffer gas flow

Fig.4.1 presents spectra of positively, singly charged bismuth clusters, obtained for the following source conditions: the cluster source was cooled with LN_2 to the minimum temperature

of -170^{o}C, the aggregation length was L_{agg}=25 cm, the IRIS opening to a diameter of 5.5 +/- 0.5 mm, and the discharge was set initially to I_{disch}=20 mA at V_{disch}=230 V, yielding a discharge power of P_{disch}=4.6 W.

First we will analyze the influence of the pressure inside the cluster source which is proportional to the flow of the Ar sputter gas. As it was already mentioned before, below 80 ml/min no signal is recorded. The spectrum for a flow of 85 ml/min is shown in the fig.4.1 a). Very small positively charged clusters are produced and the distribution starts clearly at the Bi monomer, reaching a maximum for clusters Bi_4^+, Bi_5^+, Bi_6^+, followed by a strong decrease at about Bi_{10}^+. Weak cluster signals are detected up to n=60. Under these conditions, we observe an increased intensity for Bi_{10}^+ and Bi_{12}^+, which might indicate that these are magic numbers for the formation of bismuth clusters. A slight increase of the buffer gas flow results in a significant

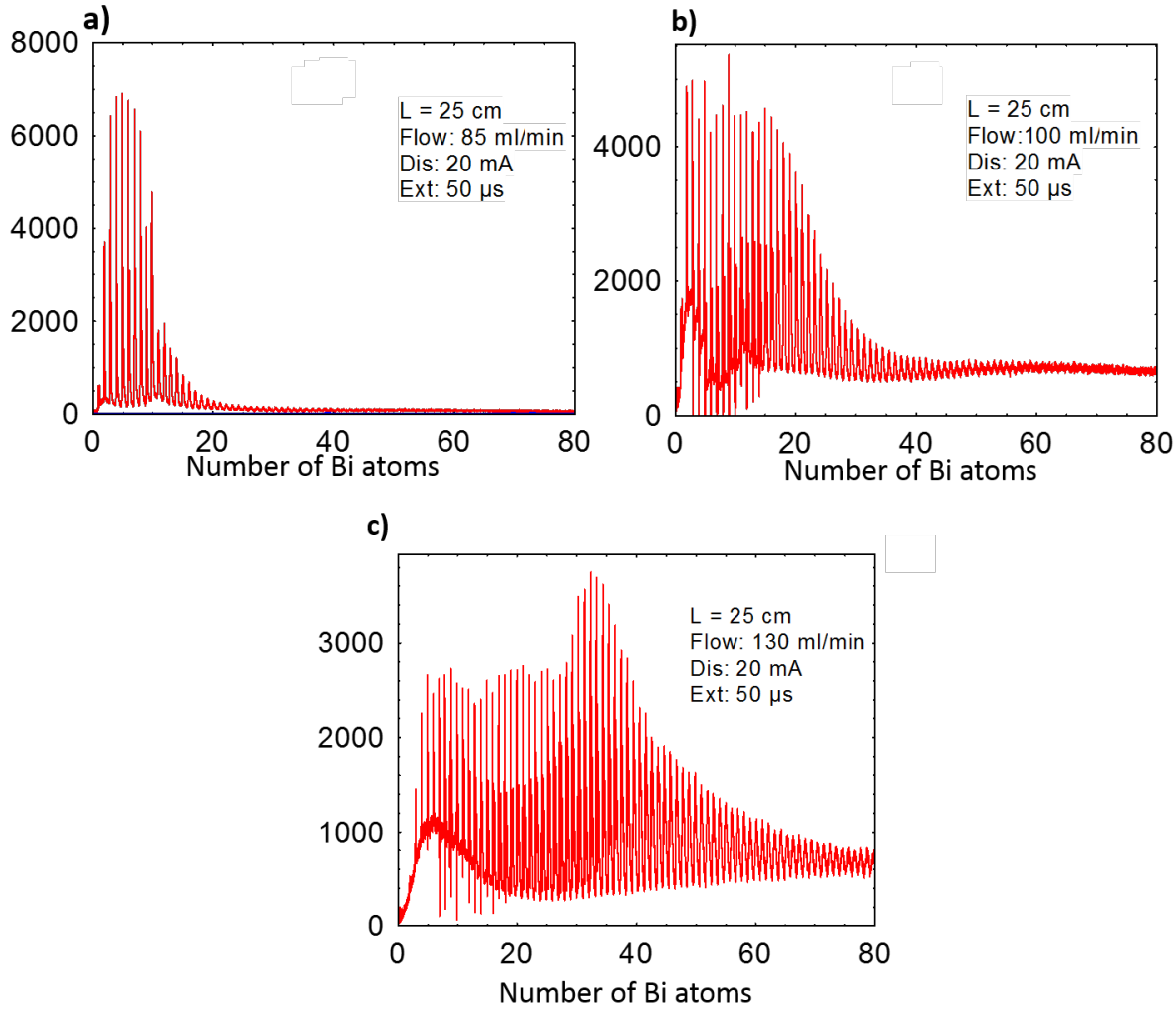

Figure 4.1 *Variation of the spectra of positively charged Bi clusters produced with a magnetron cluster source for different Ar buffer gas flow conditions: a) flow=85 ml/min, b) flow=100 ml/min, c) 130 ml/min.*

change of the size distribution of the formed clusters, showing a broad maximum up to n=20, with a parallel increase of the intensity of clusters with sizes of n=80 and more (see fig.4.1 b). Some of the cluster sizes are so intense that they are saturating the detection system. This is observed as a rapid drop of the intensity almost to 0 for the integer numbers of atoms values (from n=4 to n=15 in the picture). In the fig.4.1 c) we observe a further shift of the maxima to about Bi_{35}^{+} when the flow of the buffer gas is increased to 130 ml/min.

4.1.1.2 Effect of the IRIS diameter

When reducing the diameter of the IRIS, placed at the exit of the aggregation chamber, the pumping speed in the ion source chamber is reduced and hence the pressure inside the source increases, although the total gas flow is kept constant. Concerning the mass spectra one might expect a similar effect as discussed before for an increase of the Ar gas flow.

In fig.4.2 we see the evolution of the positive clusters spectra as a function of the diameter of the IRIS terminating the cluster source. The parameter settings for the cluster source are the following: discharge power P_{disch}=24 W, Ar flow = 100 ml/min, aggregation length 32.5 cm. It has to be noted that the change of the IRIS diameter influences as well the discharge conditions. According to the Paschen curve a lowering of the pressure increases the effective discharge voltage, thus, slightly changing the discharge power.

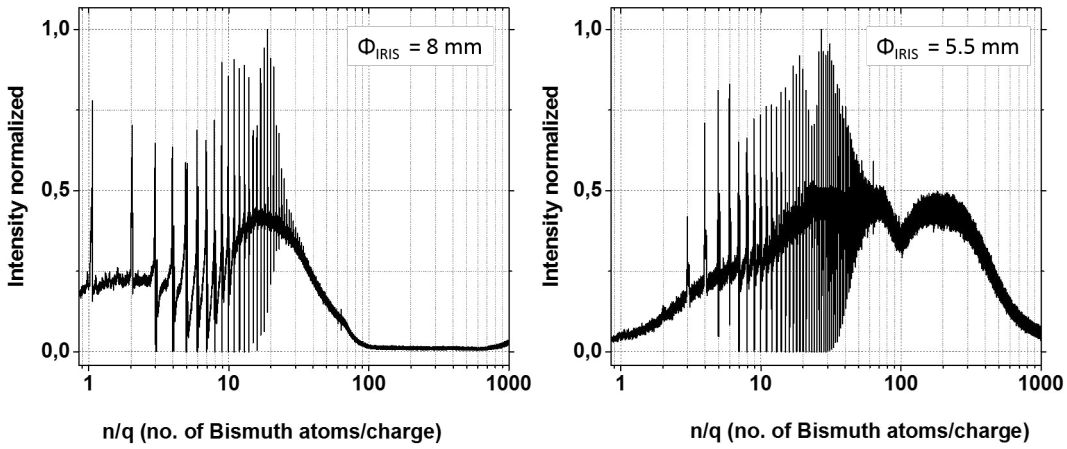

Figure 4.2 *The mass spectra of positively charged Bi clusters produced by magnetron cluster source for two different IRIS diameters: a) Φ_{IRIS}=8 mm and; b) Φ_{IRIS}=5.5 mm.*

The spectrum obtained with an IRIS diameter of about 8 mm shows very small clusters; starting from the monomer up to a maximum size of ∼100. The maximum in intensity occurs at about n=20 (see Fig.4-2a). When reducing the diameter to 5.5 mm, the cluster distribution starts essentially with the trimer and passes a maximum at n∼30. After having passed a second maximum at about n∼200 the spectrum extends to cluster sizes of n 1000 (see fig.4.2 b). If

the IRIS diameter is further reduced, large-size clusters are observed witha maximum centered at n∼700.

The pressure varies under these conditions from 0.01 mbar for total opening of the IRIS up to 2 mbar for a total closing of the IRIS at a given flow of 100 ml/min. Summarizing, a reduction of the IRIS size by 3 mm results in a shift of the maximum of the mass spectra from n=20 up to a wide range of n=300 to n=800 atoms. Thus, for producing large cluster sizes, the reduction of the IRIS diameter is more efficient than the increase of the Ar gas flow, which is limited by the pumping capacity of the experimental set-up.

4.1.1.3 Effect of the discharge power and impurities

The discharge power, in particular the discharge current, may have a strong influence on the sputtering and hence the cluster formation. Fig.4.3 shows superimposed two spectra obtained with a discharge power of 5 watts and 25 watts, respectively. Other parameters are equal for both cases. The spectra are normalized to 1 to allow for a better comparison. One can clearly observe that the maxima distribution shifts with increasing discharge power towards larger n values which is explained by an increased sputter yield. For the high-power spectrum saturation effects are observed due to high count rates (drop of the signal to zero).

In order to produce pure clusters it is important that the environment of the magnetron head, where the discharge takes place, is very clean. In principle, many impurities are trapped at the cold surfaces of the LN2 cooled chamber, however, close to the discharge the temperature is increased and particles emitted from the discharge region may desorb impurities also from the walls.

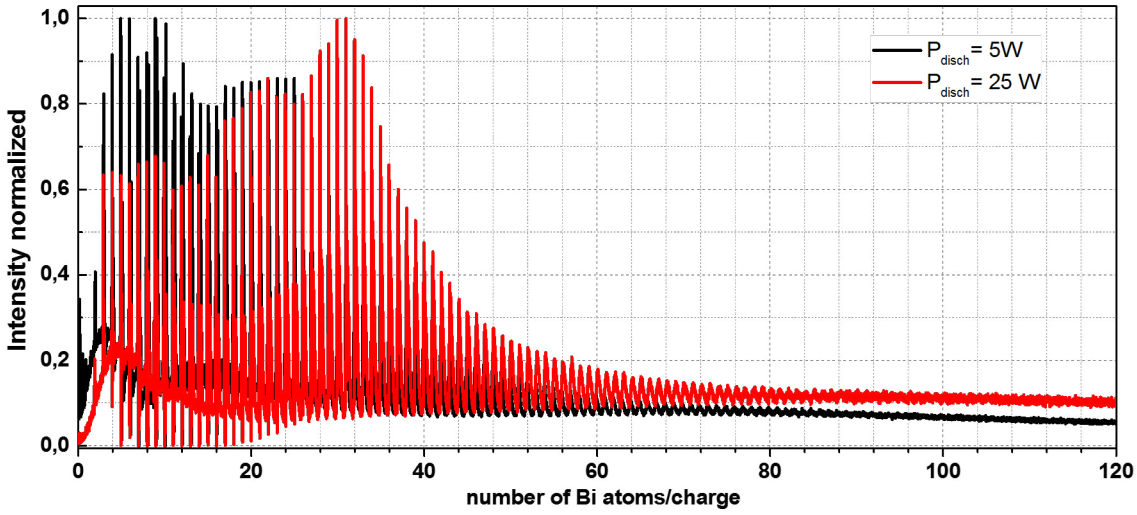

Figure 4.3 *Mass spectra of singly charged positive Bi clusters produced with different discharge powers. Black curve: 5 W; red :25 W.*

To demonstrate the ability of positive clusters ions to attach impurities we show in fig.4.4 some details of the spectrum which was measured after some water contamination. One observes a „fine-structure" for each Bi cluster with peaks which are separated by 17 amu, i.e. OH molecules. The number of attached molecules goes up to 6 or 7 and with increasing cluster size the fraction of the pure Bi clusters is reduced shifting the maximum to mixed systems which contain 2 OH groups. This effect is mainly observed for larger discharge powers, as then the impurity production is increased by plasma-wall interaction and heating effects.

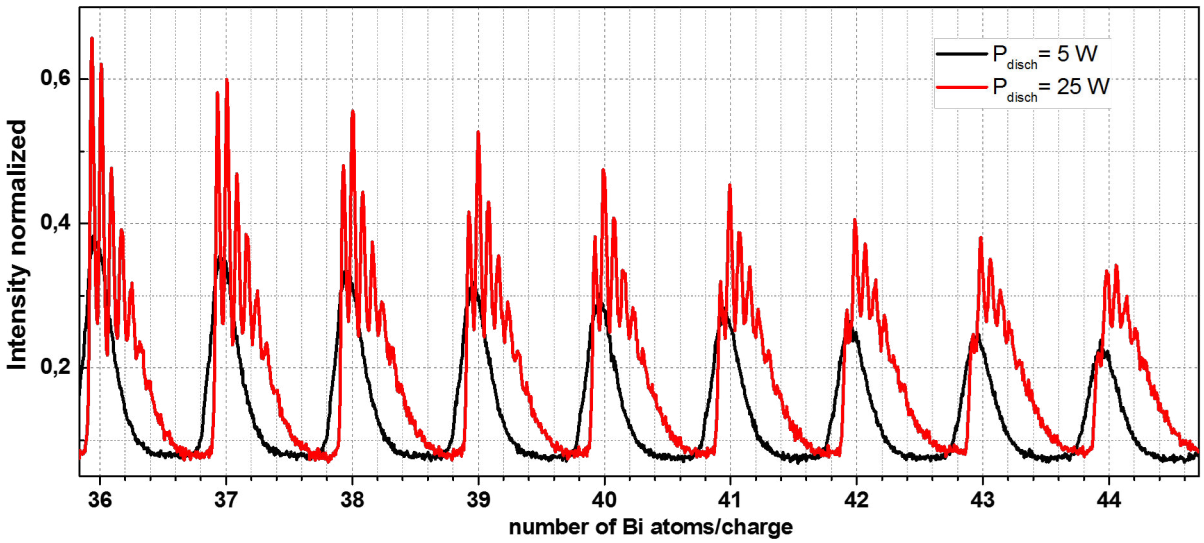

Figure 4.4 *Spectra of mixed clusters $Bi_n(OH)_m^+$ for two discharge powers.*

4.1.1.4 Effect of the temperature

As it was already mentioned before, the temperature of the cluster source and that of the buffer gas is very crucial for an effective clustering process. Over a large temperature range from T=20^{o}C down to T=-60^{o}C we observe the appearance of mostly monomers or very small clusters up to Bi_7^+. A further decrease by 30^{o}C results in the formation of clusters with less than 100 atoms. Only for temperatures below -110^{o}C, a strong and sudden shift towards the production of clusters containing a few hundreds of Bi atoms is observed. For the final temperature of T=-160^{o}C the maximum is concentrated on clusters sizes containing about 250 atoms. In parallel with the cluster size, the count rate which was for a temperature T=-60°C of the order of 3000 counts/s, increased for T=-160°C to roughly 300 000 counts/s.

The findings described so far for positively charged ions have been used to find the optimal conditions for the cluster source producing neutral species. It has to be reminded that the mass spectrometer has been developed for a point-like (5mm in diameter) object which is not the case for the pencil-like form (10 cm in length) of the primary positive ions. Therefore, details

of the measured mass spectra have to be treated with care for positive ions. Nevertheless, counting rates for neutral clusters, ionized by an ion beam, were found to be high when also the positive primary cluster yield had its maximum value, not specifying the cluster sizes. In the next section we describe how the size distributions for neutral clusters have been determined.

4.2 Size distribution of neutral nanoparticles

4.2.1 TEM studies of neutral bismuth clusters deposited on a carbon mesh

In order to measure the size distribution of neutral clusters, I have built a vacuum chamber which is separated from the main experimental device by a gate valve. This deposition chamber which contains a mountable sample holder, is localized after the interaction region (see fig.2.25 in the chapter 2). The sample holder is constructed in a way that it is possible to perform depositions both on a larger surface samples with sizes up to 10×10 mm appropriate for AFM studies as well as on small transparent meshes adapted for TEM microscopy.

We deposit Bi clusters on carbon grids and transfer such samples further to be characterized using the TEM microscope from the CIMAP laboratory (group of Isabelle Monnet). Fig.4.5 a) shows a typical image obtained for the following source conditions: aggregation length L=32.5 cm, the flow of the buffer gas (argon) was set to 100 ml/min with a discharge power of P=23 W (in contrast to the silver case, a rather high power of the discharge was necessary to obtain a reasonable signal during experiments with neutral clusters). Fig.4.5 b) is the resulting diameter histogram resulting from the analysis of the shown TEM image.

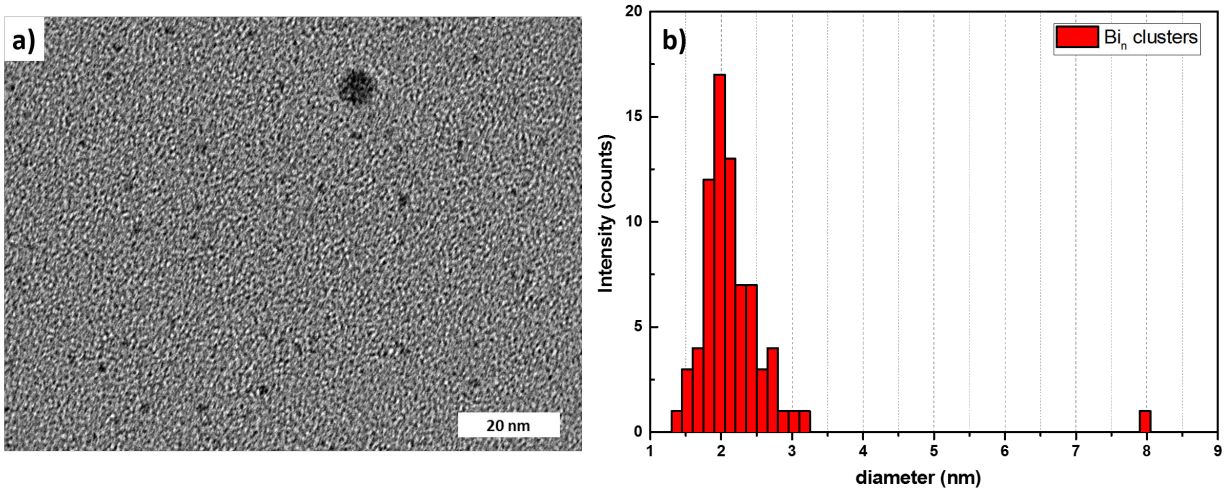

Figure 4.5 *a) TEM image of deposited Bi_n clusters; b) Histogram showing the size distribution of the deposited clusters with a intensity maximum at ∼2 nm.*

The majority (more than 97 %) of the observed clusters are in the diameter range of 1.5 to 3 nm, with a maximum of the distribution placed at 2 nm. In terms of number of atoms, this range corresponds to n=25 up to n=700 with n_{max}=100. In addition, sometimes a larger object is seen, as that one visible in the image having the diameter of 8nm (n$\sim$ 4500 atoms). However, the occurrence probability is only of the order of the 1 to 2%.

It is necessary to note that the resolution of TEM images depends on the kinetic energy of the electrons but also on the mesh characteristics. In our investigation, the mesh is made of carbon which means that the contrast is strongly damped when analyzing objects which are smaller than 1-1.5 nm. Therefore, the measured distribution shown in Fig. 4.5b, is only valid for diameters larger than 1.5 nm.

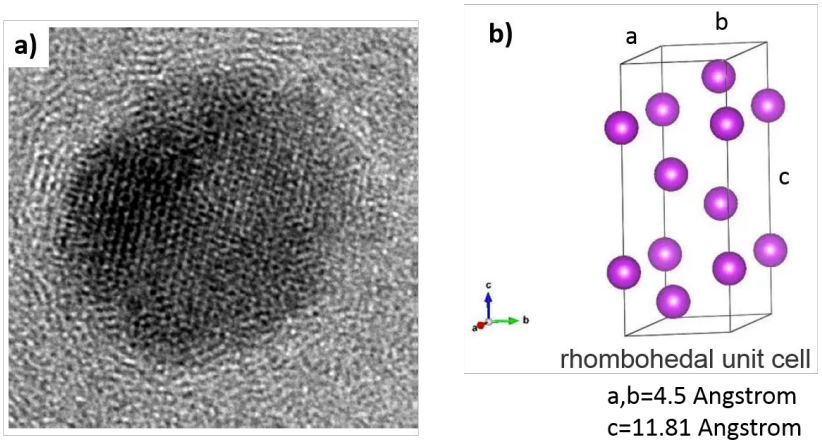

Figure 4.6 *a)Crystalline structure of a large Bi cluster with a diameter of 7.5 nm. b) primitive unit cell of a bulk Bismuth crystal*

Fig.4.6a) shows the image of a large deposited Bi clusters with a radius of 7.5 nm, while fig.4.6b) shows the primitive unit cell of a macroscopic Bi crystal: rhombohedral symmetry, with structure parameters a=b=(4.535 +/− 0.002)Å and c=(11.814 +/− 0.006) Å; angles $\alpha = \beta$ =90°,γ=120°. The distance between the observed lines given by the atomic arrangement is found to be around 0.36 nm +/− 0.05 nm. These values are close, but different to those for the bulk material. The small difference might be due to a specific layer orientation seen by the TEM microscope.

4.2.2 Silver nanoparticles

Similar microscopic investigations were performed as well for the silver clusters. In addition, we used an AFM microscope as the observed clusters turned out to be reasonably large.

In the fig.4.7 one can see some intermediary steps related to the procedure of deposition. Fig.4.7 a) shows the vacuum window of the deposition chamber, where the beam of nanoparticles is stopped. After a few hours of an experiment one starts observing a characteristic dark

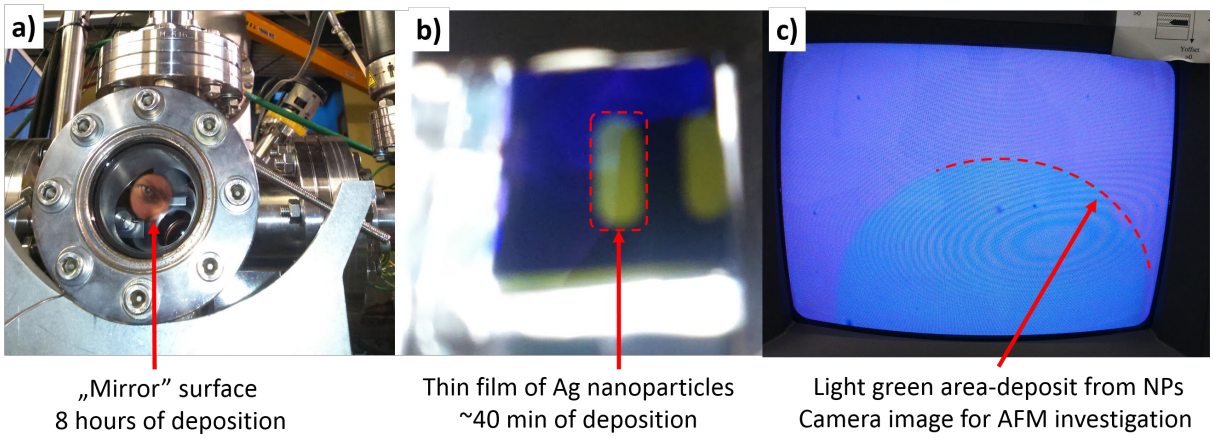

Figure 4.7 *Details of the deposition process: a) visible mirror-like surface of silver nanoparticles after long deposition time; b)thin films of metal nanoparticles as deposited on silicon wafer crystal; c) layer of AG NPs in camera image during AFM investigation.*

spot with dimensions of around 17 mm (vertical) and 15 mm (horizontal) resulting from the formation of multiple layers of nanoparticles on the glass. After around one day of an experiment one cannot see anymore through the glass window as the number of deposited layers is so large that the spot works as a perfectly reflecting mirror (on the picture the reflection of the author's eye was captured).

Fig.4.7 b) presents a sample of a Silicon wafer cut into dimensions 10x10 mm. Dark blue is the original color of the surface, while the yellow-greenish longitudinal shapes represent the result of 40 min deposition of silver clusters (the specific color is the result of the photo taken with a smartphone CCD camera equipped with very bright white LED diode light, illuminating the surface of a sample). To cover the surface of the sample with less than one layer, the most optimal time of the deposition is in the range of a few minutes; however, in this case it is impossible to really see such a spot later on with a naked eye, what poses difficulties to localize a good spot to position the AFM cantilever. This problem can be overcome by using a simple camera image with bright light illumination, as being visible on the screen in Fig.4.7 c). The brighter luminsecent region of the deposition area appears (the mask is a simple hole with a diameter of 600 micrometers).

Fig.4.8 shows the AFM microscopy results obtained in the tapping mode on the silicon wafer surface with deposition of silver clusters during 90 seconds under the following conditions: aggregation distance 20 cm, discharge power 18 W and flow of the buffer gas of 80 ml/min. The AFM technique is a powerful good technique for the investigation of nanometric sizes provided that the surface on which the object is lying is very flat. Silicon wafer samples that were used in our case showed an approximate rougness of the surface of 0.5 to 1 nm, which determines the accuracy of the final measurement. It is known that the AFM technique does not provide a perfect resolution in the lateral dimension due to the curvature of the tip, which in our case

was around 16 nm. On the other hand the technique is very sensitive in the vertical dimension (z-axis perpendicular to the surface of sample) yielding sub-nanometer resolutions under good conditions. Nanoparticles are deposited in the "soft-landing" conditions with very low vertical impact energy (less than 0.01 eV per atom), so definitely they do not undergo any deformations by the impact. Therefore, information of the height distribution obtained with AFM in tapping mode technique is a good indicator of the diameter of the nanoparticle. Fig.4.8a) shows the AFM-image of the deposited Ag_n nanoparticles, fig.4.8b) the resulting histogram of particle diameter distributions.

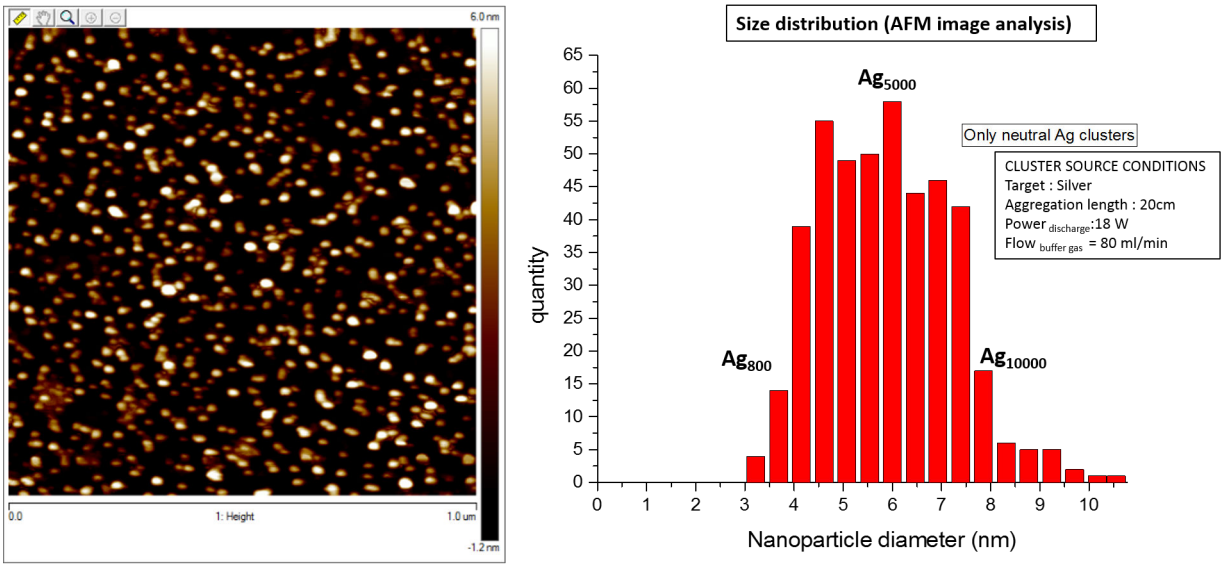

Figure 4.8 *a) AFM image of deposited silver clusters; b) histogram of the nanoparticle diameters ontained from the left image.*

The size distribution of silver clusters spans a diameter range from about 3nm up to objects with 10 nm. The majority of the clusters do have diameters between 4 and 7 nm and the maximum is centered at a diameter of about 6 nm, which corresponds to approximately 5000 silver atoms. Hence the silver clusters are much larger and contain more atoms than the Bi clusters described before.

We applied also TEM microscopy to analyze silver nanoparticles produced under similar conditions: 21 cm aggregation length, 80 ml/min buffer gas flow and 18 W of the discharge power. In contrast to Bi clusters, the visibility of the clusters is very high, as well as the number of deposited particles. Fig.4.9 a) shows the contrast image, while figure 4.9 b) represents the diameter histogram determined from the images. The smallest observed silver nanoparticles are 2.5 nm large while the largest objects are in the range of 8 nm. The majority of the nanoparticles is found in the range between 3.5 up to 6.5 nm with maximum centered at 5 nm. This result is in general agreement with the data obtained with AFM microscopy. The slight shift

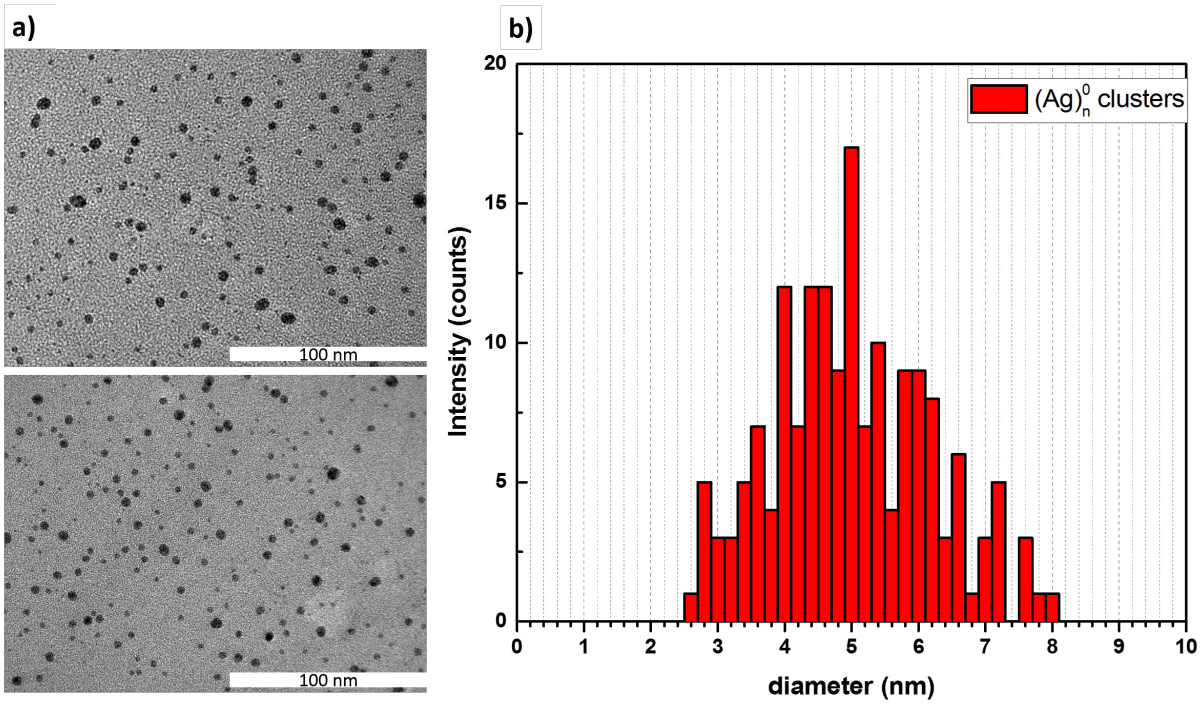

Figure 4.9 *Deposited clusters on a SiO_2 substrate; b) histogram showing the size distribution of deposited neutral Ag_n clusters*

by around 1 nm towards smaller sizes in case of the TEM image might be due to the lack of 100% reproducibility of the magnetron discharge. Another reason might be the fact that in TEM images we rely on the lateral dimensions of the observed object, whereas in the AFM we look at the height of the object. However, in general the resulting two size distributions are found to be very close to each other for similar source conditions. The structure of the Ag_n nanoparticles is shown in fig.4.10 in a zoom-in on particles having a diameter of 5nm and 6 nm. Clearly one can observe distinct atomic line arrangements in both cases. In the upper image we can see that there are more than one direction of such an arrangement. This may have its reason in the cluster formation process which includes for the formation of larger clusters also cluster-cluster collisions. The interatomic spacing is found to be approximately 0.25 nm in both cases. In the primitive unit cell of the bulk silver the symmetry is of fcc type with the structure parameter a=0.408 nm. Therefore, the intense atomic lines that are observed should have a spacing of around 0.204 nm which is a little bit smaller than that of the observed atomic lines.

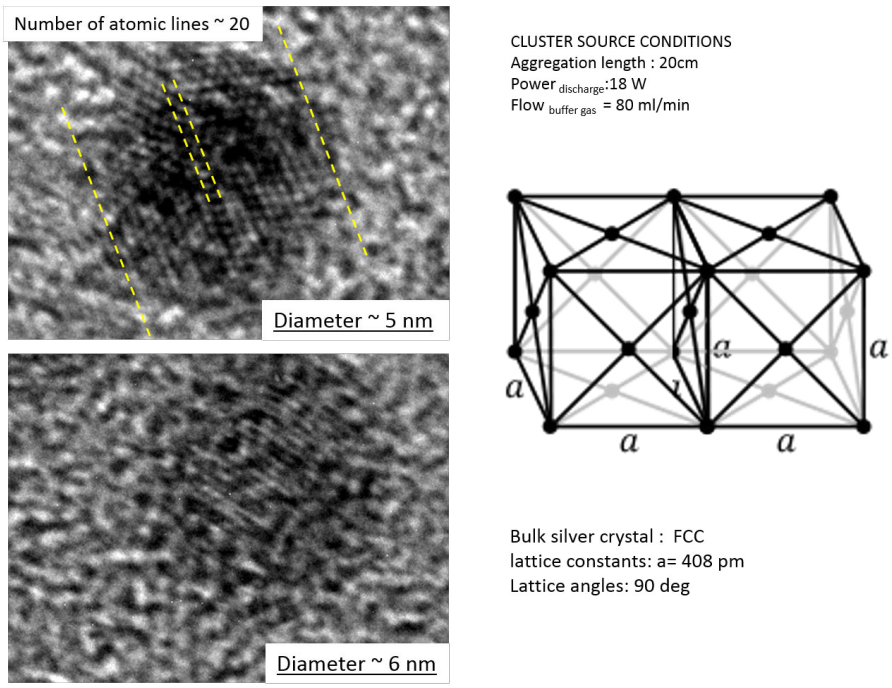

Figure 4.10 *a) TEM image of two selected silver nanoparticles; b)details of the structure of silver bulk crystals.*

4.3 Characterization of the molecular beam: kinetic energy and density

Up to this point we have concentrated on the performance of the cluster source and the influence of source conditions on the size distribution of produced species (analysis based on positive clusters spectra) and we have provided information about the size distribution of neutral clusters based on microscopic methods. Another aspect concerns the transport of the produced cluster beam. So here we will provide some insights about the transport of produced clusters/nanoparticles by determining their kinetic energy (thus the cluster velocity) and the density of the target beam.

4.3.1 Kinetic energy of positively charged species

Firstly, we focus on the determination of the kinetic energies (velocities) along the beam axes of the positively charged clusters present in the beam. The cluster velocity is due to the co-expansion of the clusters with the Ar gas flow. Initially their velocity is small as their mass is very large. However, due to many elastic collisions between the Ar atoms and the clusters, occurring in the high-density region of the cluster source, the clusters are accelerated and can finally reach the gas flow velocity, in particular when very small clusters are considered.

However, heavy clusters do not reach this velocity and are slower, a phenomenon which is described as velocity slip [82]. In previous experiments involving neutral sodium clusters which are produced in a gas aggregation source using Helium buffer gas, it was shown that buffer gas velocity of ∼600 m/s, the velocities of the sodium clusters varied from 350 m/s to 175 m/s when their size is increased from n=50 to n=750 [75]. The applied method was based on a chopped molecular beam and the measurement of the time-of-flight between the chopper wheel and the interaction zone.

The velocity of atoms in a gas depends on the temperature of the gas T and the atomic mass m and can be calculated in a good approximation from the Maxwell-Boltzman distribution function for an ideal gas :

$$f(v) = \sqrt{(\frac{m}{2\pi kT})^3} 4\pi v^2 e^{-\frac{mv^2}{2kT}} \tag{1}$$

with the most probable velocity given by :

$$v_p = \sqrt{\frac{2kT}{m}} = \sqrt{\frac{2RT}{M}} \tag{2}$$

Fig.4.11 shows such velocity distribution function calculated for 3 different buffer gases: helium, nitrogen and argon at the temperature of T=100K. In the case of helium the most probable velocity is 650 m/s, while for N_2 and Ar these velocities are slower and drop down to 240 m/s and 200 m/s, respectively. As the effect of an adiabatic expansion is believed to be small (pressure difference is of the order of 10^{-3} bar), these velocities are expected to be close to the beam velocities of the buffer gas. In the present experiment we analyse positively

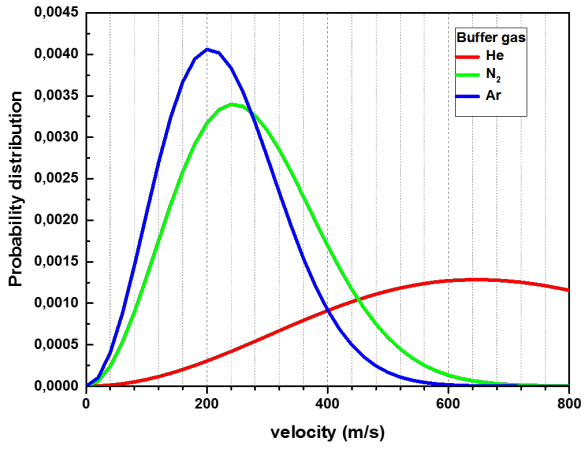

Figure 4.11 *Maxwell-Boltzmann velocity distribution for different gases at temperature T=100K.*

charged clusters as we can estimate their kinetic energy by applying an electric retarding field. As described in chapter 2, the clusters pass through a skimmer unit, which is localized right after the IRIS and hence separates the cluster source from the differential pumping chamber.

In the following a second element consists of two deflecting plates where normally positive and negative potentials are applied in order to deviate all charged particles and let pass only neutral clusters. In order to verify the kinetic energy distribution of positive clusters, a positive voltage in the range from 0 up to 20 V is applied to the skimmer, while both deflection plates were kept on a slightly negative potential in the range of a few volts in order to block the negative clusters. The same negative voltage is applied to both deflection plates which therefore do dot deviate positively charged species.

Fig.4.12 a) shows some mass/charge spectra obtained for different potential values applied to the skimmer. The spectrum obtained for a potential of -1 V shows a distribution of Ag clusters with a maximum intensity at around n∼2400. When the voltage on the skimmer is increased the intensity decreases not linearly. Iin fig.4.12 b) the relative intensities taken for the nanoparticle Ag^{+}_{2400} are shown for increasing skimmer potentials (up to 15 Volts). Taking the derivative of the resulting „retarding curve" yields a kinetic energy distribution, where the majority of clusters have energies from 2 up to 6 eV with a maximum at ∼4 eV. In terms of velocities, these values correspond to values between 30 and 60 m/s with the most probable velocity of v_p ∼50 m/s.

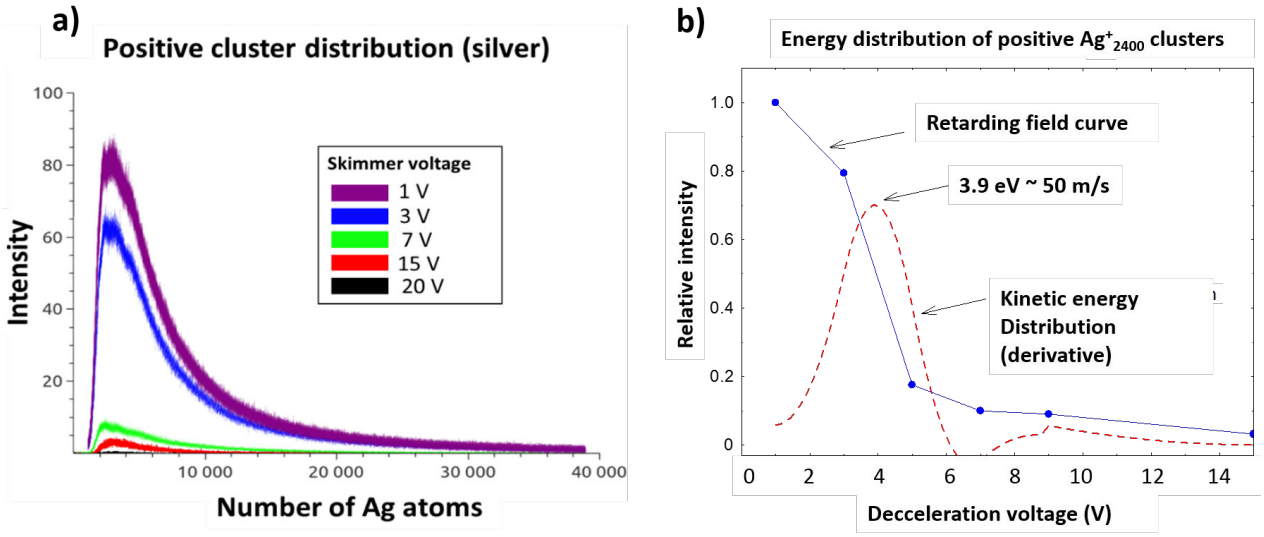

Figure 4.12 *a) Mass spectra of positively charged Ag clusters measured for different retarding voltages; b) Intensity decrease of the cluster Ag^{+}_{2400} with increasing deceleration voltage and derivative corresponding to the kinetic energy distribution.*

4.3.1.1 Particle density of the molecular beam

From the microscopy images it is possible to estimate the average coverage of a given area with a number of silver nanoparticles. From the deposition time one can estimate the particle flux in numbers/s. On the other hand, we know what is the velocity of the clusters in the

beam, so we can estimate the amount of nanoparticles within 1 cm^3, i.e. the average cluster density in the ion beam. Taking as an example the TEM images shown in fig.4.9 where the deposition lasted for 60 seconds, we find for the particle flux Φ:

$$\Phi = \frac{n_{particles}}{S \times \tau_{dep}} = \frac{280}{(170 \times 225 \times 60)}[\frac{1}{nm^2\, sec}] \approx 1.19 \times 10^{10}\ [\frac{1}{cm^2 \times sec}] \quad (3)$$

Taking an average velocity of 50 m/s, during one second the particle makes a distance of 5000 cm. Therefore final density in the volume of 1 cm^3 is

$$\rho = \frac{n_{particles}}{V} = 1.19 \times 10^{10} \times \frac{1}{5000}[1/(sec \times cm^2) \times sec/cm] \approx 2.4 \times 10^6\, \frac{particles}{cm^3} \quad (4)$$

This density determination assumes that the sticking coefficient of clusters on the TEM grid is 100%. This might be somewhat lower, nevertheless the order of magnitude of the density of Ag clusters in the beam is estimated to be between 10^6-10^7 nanoparticles/cm^3.

4.3.1.2 Target sputtering efficiency

The target is a silver disk, where after approximately 25 days of operation (8 hours per day) the eroded volume of the silver surface counts for about

$$V_{sputtered} = 1373.5 mm^3 \quad (5)$$

The sputtered mass can be calculated according to mass = density x volume = 10500 kg/$m^3\times$ 1.37 cm^3 and amounts to 14.6 g.

The total sputter yield is the sputtered mass per second, i.e.=14.6/720000 g/s = 2.03 x 10^{-5} g/s.

From this we obtain for the number of sputtered silver atoms per second: the atomic yield can be calculated as atomic mass yield Y_{atoms}:

$$Y_{Ag\,atoms} = 2.03 \times 10^{-5}[g/sec] \sim 10^{17}[Ag\,atoms/sec]. \quad (6)$$

We know that the number of NPs leaving the cluster source is 10^{10} nanoparticles per second (per cm^2), that 1 nanoparticle has on the average around 5000 atoms, which means 5×10^{13} atoms leave the source. We also know that about up to 10^{17} atoms are sputtered per second. This means that the fraction equal to $(5{\cdot}10^{13}/10^{17}) = 5{\cdot}10^{-4}$ is leaving the source in the form of the molecular beam. We may conclude that the main part of the formed atoms and clusters is deposited on the internal walls of the ion source and elements of the beam line and that only a fraction of 10^{-3} to 10^{-4} of the sputtered material is delivered as a neutral beam to the interaction region.

4.4 Detection capabilities of large clusters: SIMION simulations

In the following I will discuss several aspects of the detection capacity of the TOF system by performing simulations with the SIMION software. These aspects are the following :

1) Trajectories of large clusters/ nanoparticles containing several thousands of atoms (for example of silver clusters Ag^{+}_{5000}) for both lower (122 V/cm) and higher (244 V/cm) extraction fields

2) The effect of the kinetic energy released during the collision given to the fragments and its impact on the observed mass spectra.

3) The length of the extraction pulse and its impact on the detection possibility and the measured distribution.

4.4.1 Ion trajectories - effect of the velocity in the molecular beam

The orthogonal configuration of the molecular beam (target), the ion beam (projectile) and the axis of extraction has the consequence, that there exists an upper limit for the kinetic energy/velocity in the lateral direction (along the molecular beam) above which target ions can no more be detected. Fig.4.13 shows results of the trajectory calculations performed using the SIMION software for the Wiley-McLaren mass-spectrometer used in the COLIMACON DUO set-up. Fig.4.13 a) shows a cut through the instrument (extraction, acceleration, free-flight zone and detection plate are clearly visible) with trajectories for the nanoparticle Ag^{+}_{5000} having different kinetic energies, ranging from 0 (black color) up to 9 eV(light green). These calculations are made for a static electric extraction field of 244 V/cm.

One clearly sees that with increasing kinetic energies, the trajectories are bent towards the edge of the upper electron-emitting conversion plate. For energies up to 5-6 eV all particles still hit the top plate. Above this value the ions do not hit the plate anymore, which means that they are not detected. The resulting transmission curve which depends on the "lateral" kinetic energy of the ion are shown in fig.4.13 b) for the higher extraction field (244 V/cm) and in Fig.4.13 c) for lower extraction field (122 V/cm). From these curves one finds that the upper limit of the kinetic energy for a 100 % transmission of ions is 6 eV when we extract with high electric field, or 4 eV if the extraction field is two times smaller. It should be noted that the lower field increases the time-of-flight and may lead, therefore, to an improved mass resolution. Furthermore, the experiments can be performed with a higher repetition rate, making the experiment more efficient.

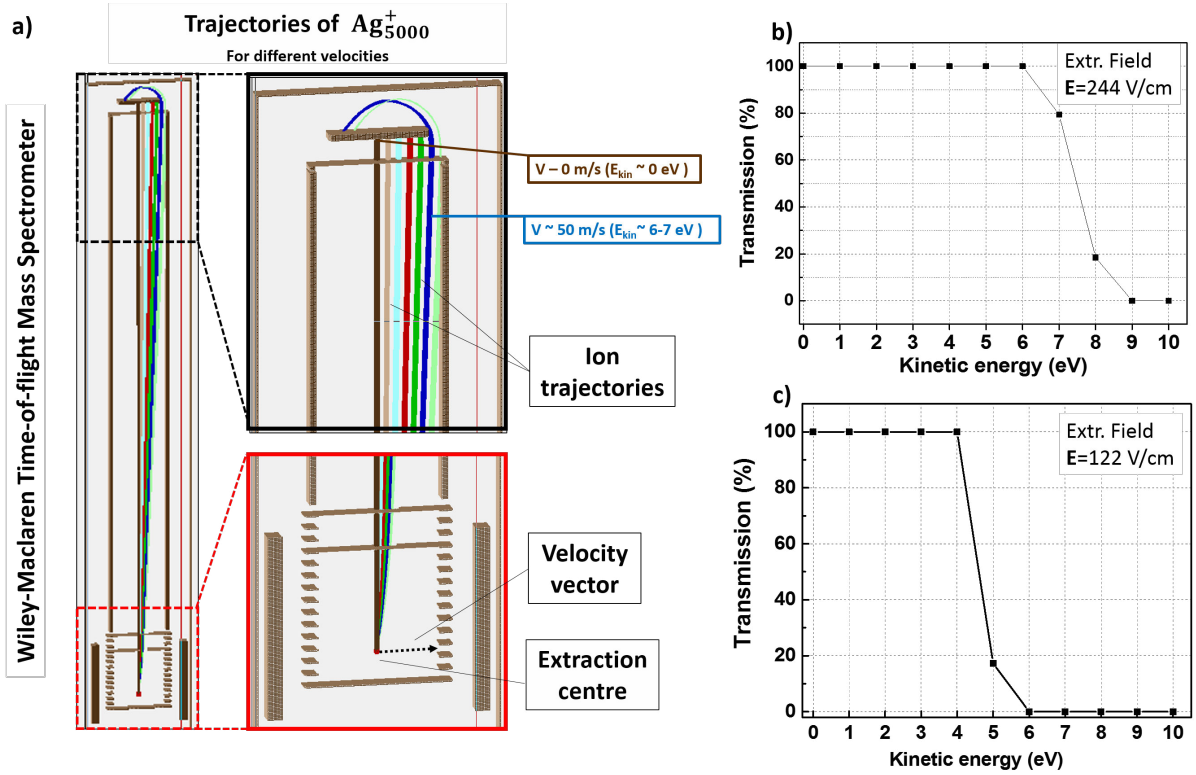

Figure 4.13 *a) Scheme of the TOF-system with ion trajectories for lateral ion energies between 0(brown color) and 8 eV (green color). b) Transmission curve for an extraction field of 244 V/cm. c) Transmission curve for an extraction field of 122 V/cm*

4.4.2 KER and its influence on the observed spectra

Due to the kinetic energy release (KER) occurring in fragmentation processes an important amount of kinetic energy can be transferred to the fragments; in particular small fragments will receive the major part of the KER.

The question is how this kinetic energy translates into the observed peak form in the mass spectrum. The small fragments are assumed to be emitted in an isotropic manner in all directions. As discussed just before, the transmission of the set-up is limited if fragments posses high kinetic energies in the lateral direction. Therefore one can expect that fragments emitted along the z-axis (extraction axis) will be detected and those emitted perpendicular to it may be lost.

Figs.4.14 a) to i) show the peak forms in the time-of-flight spectra of bismuth ions, extracted by a field of 122 V/cm for different kinetic energies (for the calculations we have used 1000 trajectories). Fig. 4.14 a) shows a perfectly thin single peak when the ion has no kinetic energy at all. When increasing the energy by 1-2 eV (fig,4.14 b) the form of the peak becomes clearly broadened and is spread out over 300-500 ns centered at its original position. For higher kinetic energies (3 to 4 eV; fig.4.14 c)) we observe a further broadening of the peak showing

now a form close to a slightly asymmetric square. For energies above 4 eV (fig.4.14 d to i) the dominant contributions occur at the "border" times-of-flight values, while the intensity in the middle part of the peak strongly decreases. This corresponds to the so-called "backward" and "forward" peaks, which are created by the ions having velocity vectors oriented along the z-axis (extraction direction). Loss of the middle part of the peak corresponds to atoms with velocity vectors aligned perpendicularly to the extraction direction. With the increase of the energy the peak-form is spreading out more and more in the time-domain and the total intensity is decreasing.

From simulations one can also observe, that the "backward" peak (longer flight times) is a bit narrower and more intense than the "forward" peak. This is probably due to different focusing effects of stray fields.

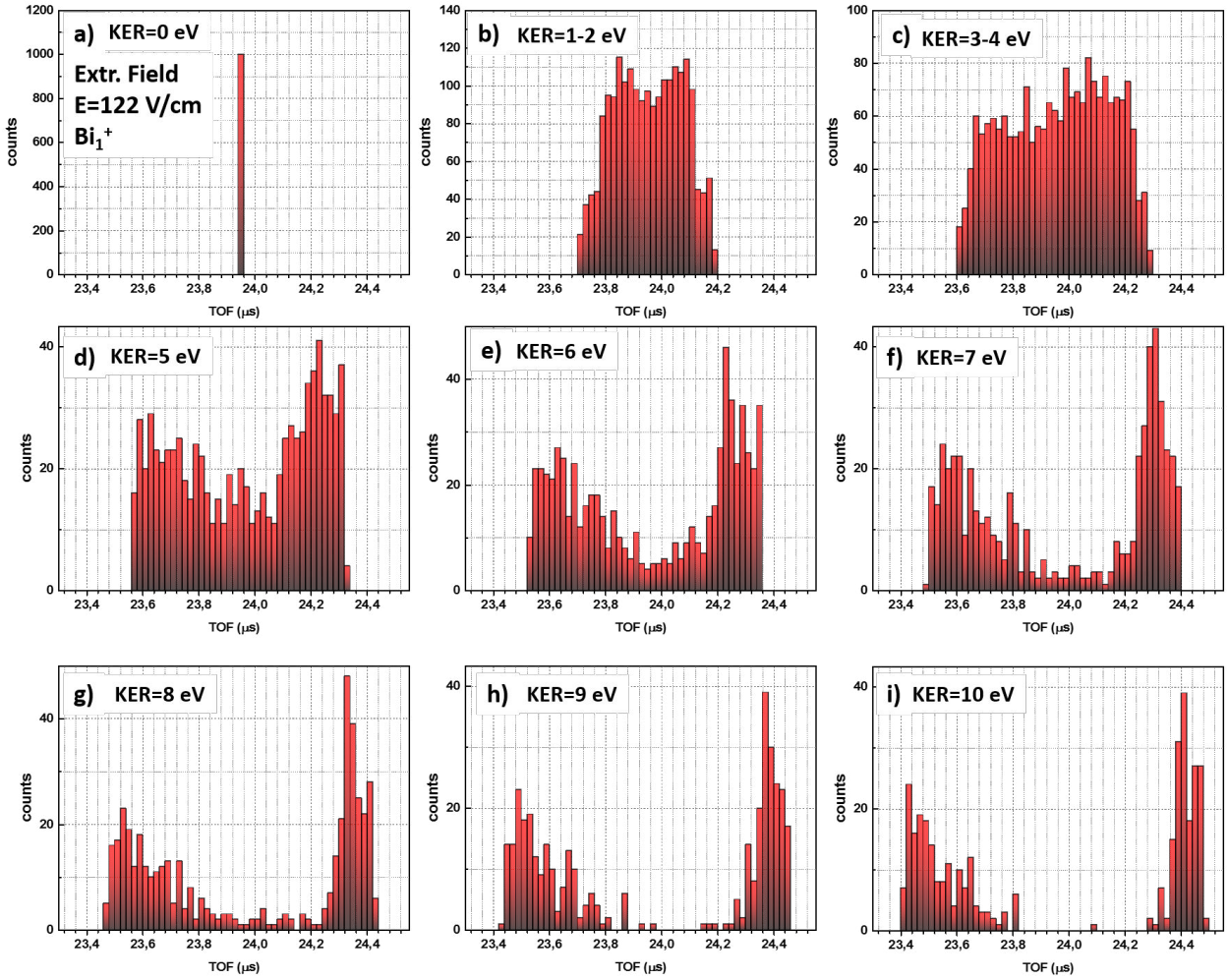

Figure 4.14 *Peak profile for Bi^+ ions calculated for an extraction field of 122 eV/cm and for different kinetic energies of an isotropic fragmentation.*

4.4.3 Effect of the limited extraction time

All previous calculations were performed for the case of a static extraction, meaning that the considered ions are experiencing the acceleration due to electric field over the whole time they spent in the extraction and acceleration zone. However, in some experimental cases, this may not be true, in particular for heavy ions, as we have to limit the time, during which the potential is applied to extraction region plates. This is due to the technological limitation of the electrical current from the power supply and the current intensity which the resistors between the extraction plates can handle. Thus, a balance has to be made between the count rate (so total time of the experiment) and the limit of the particle masses which we aim to extract properly. Increasing the extraction time increases the mass limit, but it increases also the required electrical current, on the other hand reduction of repetition rate decreases that current, however limits the count rate of the experiment, which is crucial also due to the limited availability time of the projectile ion beam.

Therefore, it is important to know for given conditions (electric field and time of extraction) the theoretical m/q limits in order to further interpret the spectra properly. Fig.4.15 a) provides the estimation of the m/q limit for properly extracted masses as a function of the extraction time by fitting a second order polynomial to data points. For a given extraction time width, all particles with masses lying below the red curve are correctly detected in so-called "Wiley-McLaren" time-of-flight conditions. On the other hand, all particles with m/q ratios larger than indicated by the red curve arrive with some delayed time-of-flight values - TOF_{real}. For each value of m/q above the $(m/q)_{limit}$ we can calculate TOF_{real} and TOF_{ideal} and find a „TOF correction factor", which is a function of a mass and extraction time. It is necessary to multiply TOF_{real} with this factor in order to obtain the correct value of TOF_{ideal}. This correction of the time-of-flight spectra has to be performed before the transformation into a mass/charge scale is done. Fig.4.15 b) provides two correction curves, obtained for the extraction widths of T_{ext}=50μs and an extraction field of 244 V/cm. For T_{ext}=50μs the TOF of all particles with m/q up to 34485 amu (for Bi clusters it's n$\leq$165) are correct whereas all particles with m/q above 34485 amu (n$>$165) have to be multiplied by a factor read-out from the blue curve.

A reduced width of the extraction pulse will not change only the TOF values, but it will influence also the ion trajectories. An example is shown in Fig.4.16 for large particles containing 5000 silver atoms. Their kinetic energy in lateral direction is set to 3 eV, the electric field of 122 V/cm and different extraction times are chosen. It is observed that for short extraction times, which are preferable for experiments where we concentrate on the detection of the small fragments, large clusters do not even leave the extraction zone and hit the plates of the set-up and internal walls, which may induce ejection of secondary particles and a strong noise background. Only when extraction times reach values above 150-200 μs extracted large nanoparticles manage to hit the upper plate properly. This example shows that one of the potential sources of noise signals are larger energetic clusters which are not properly extracted.

Figure 4.17 shows, how the described results depend on the lateral kinetic energy of the

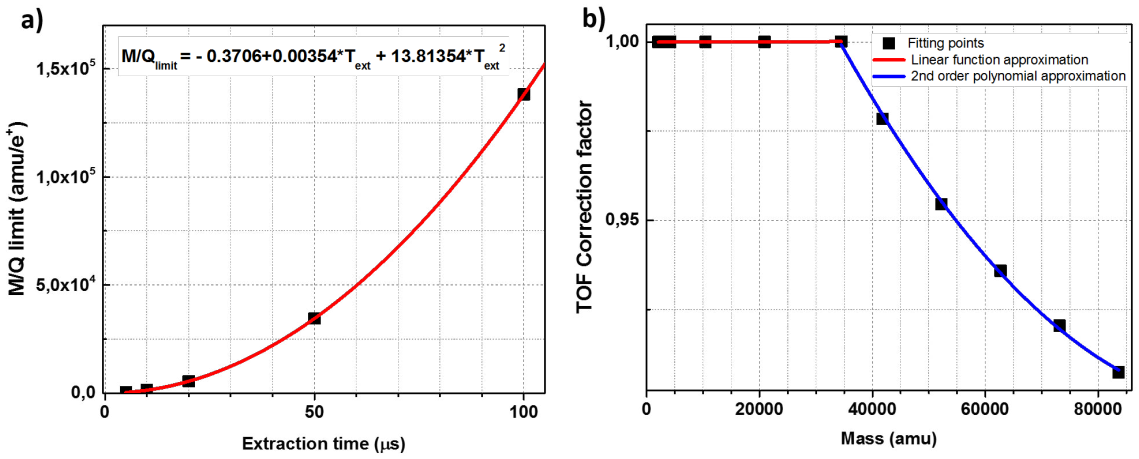

Figure 4.15 *a) The estimation of the $(m/q)_{limit}$ for the proper extraction of ions in mass spectrometer as a function of the extraction pulse width; b) two correction curves for TOF of properly extracted (red curve, factor value of 1) and not-properly extracted particles (blue curve, approximation with 2nd order polynomial) in case of the extraction pulse width of 50μs.*

ion (Ag^{+}_{5000}). In the case of fig.4.17a), when a 10 μs field pulse is used, only clusters with 0 eV have a chance to arrive properly at the detector and all higher energies (represented by colors, from 1 to 5 eV) terminate on the extraction plates or internal walls. The situation changes when the extraction time is increased to 50 μs (fig.4.17b). Clusters possessing energies up to 2 eV are well detected, not so for larger kinetic energies.

These calculations have shown that depending on the aim of the measurement the extraction conditions have to be chosen in an appropriate way, in particular for higher masses and higher lateral kinetic energies long extraction times have to be used in the experiment, taking into account lower repetition rates and hence count rates.

4.5 Detection efficiency

The overall detection efficiency for large cluster ions depends on different parameters which are on the one hand, linked to the experimental device and on the other hand, to more fundamental properties of the detector system.

The spectrometer contains three grids which are required for the creation of homogeneous electric fields, separating the regions of the extraction, the acceleration, the free field and the post-acceleration. As the grids have a transmission of 85% and 95%, the transmission for the passing particles is limited to about 69%.

Cluster ions are detected after a strong post-acceleration via a metallic conversion plate, where most likely several secondary electrons are emitted. However, for very large clusters, the

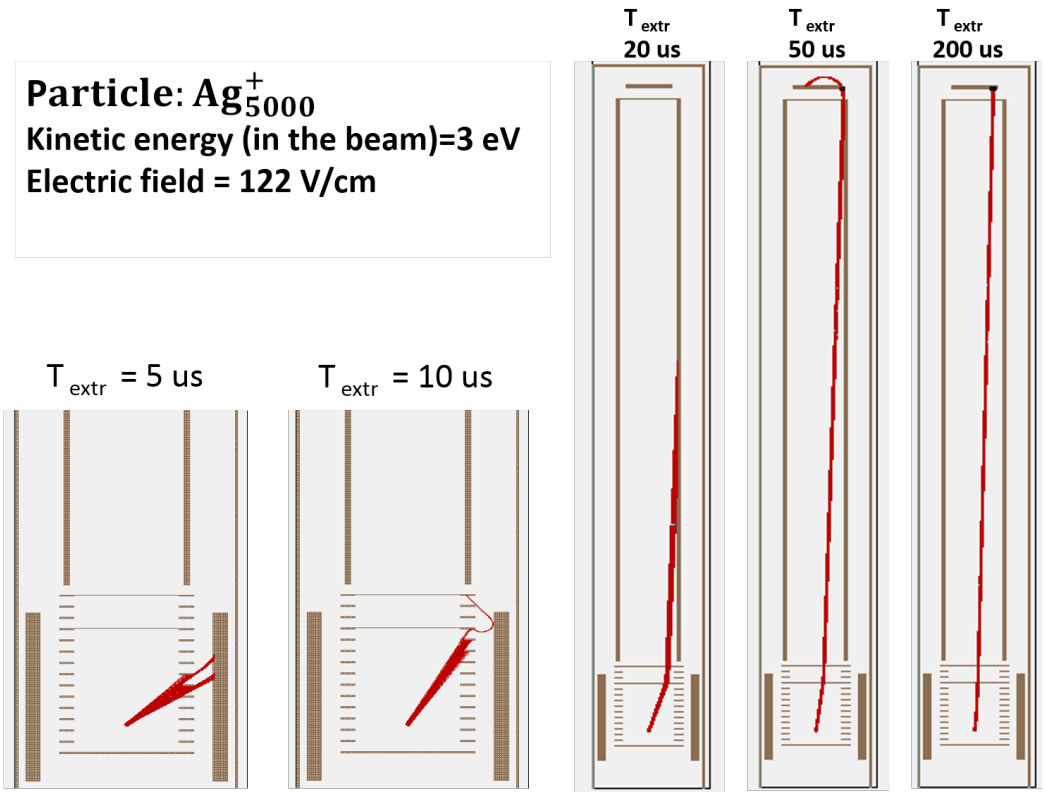

Figure 4.16 *Ion trajectories for Ag^{+}_{5000} ions extracted with an electric field of 122 V/cm with a lateral kinetic energy of 3 eV. The different graphs show the trajectories for different lengths of the extraction pulse.*

number of electrons is expected to decrease due to the lower velocity. The electrons are guided to a MCP device on which they impact with 1.5 keV. According to the data sheet the efficiency is of the order of 65%. When several electrons arrive in different MCP channels, the efficiency might be higher. For average cluster sizes we assume an efficiency of ∼65%. This yields a total efficiency of 45%.

In specific situations other limitations exist lowering the efficiency which are due to the kinetic energy of the initial cluster beam and due to the kinetic energy of fragments produced by Coulomb explosion processes. In the first case, the example a silver cluster ion Ag^{+}_{1000} can only be detected for lateral energies below 6-8 eV(for higher extraction field). In particular, the detection efficiency for small size fragments is strongly reduced for fragmentation energies above 4 eV (lower extraction field), leading to the formation of a forward and a backward peak. This has to be taken into account during the analysis procedure. A consequence of the low detection efficiency is a change of the event statistics. Thus, an event which produces n charged fragments is no longer attributed uniquely to the n-stop spectrum as some charged fragments may be not detected.

If the total detection efficiency is called ϵ and if we regard an event with n charged particles,

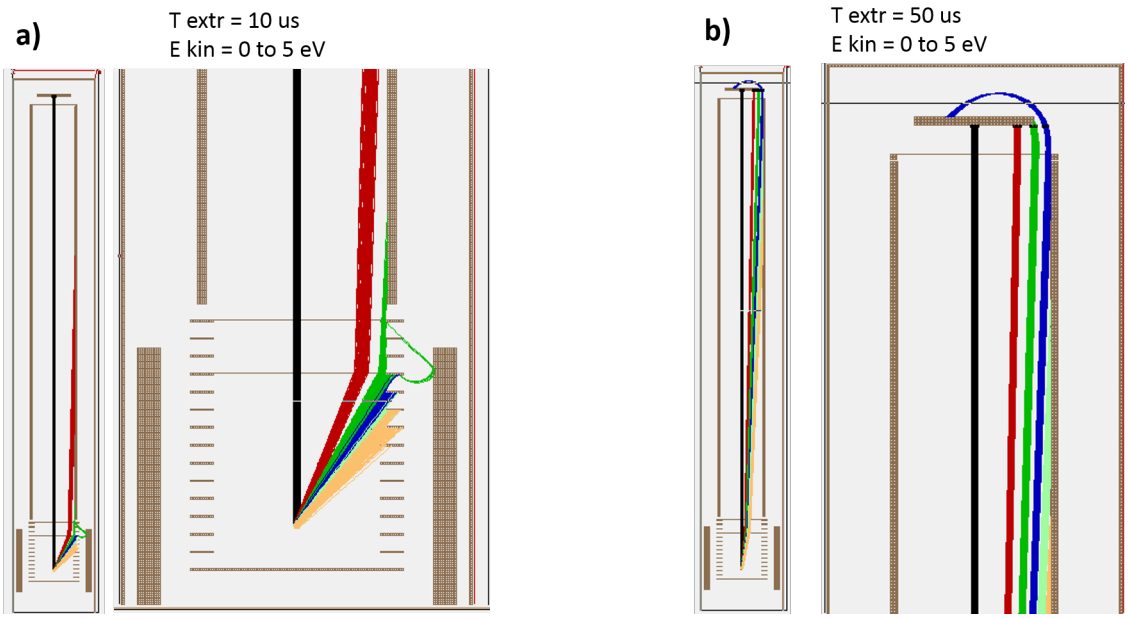

Figure 4.17 *Ion trajectories as in Fig.4.16b) shown for different lateral kinetic between 0 and 5 eV. a) extraction time:10μs; magnified part shows the extraction region; b) extraction time 50μs; magnified part shows the region of the detector plate. Color code: E_{kin}=0 eV (black) to E_{kin}=5 eV (yellow).*

the probabilities p_n to find this event in different n'-stop spectra is given by the binomial formula. Thus, an event leading to 1 charged particle can be found in the constructed 1-stop and 0 stop

Number of charged particles in one event	Fraction in the registered 1-stop spectrum (%)	Fraction in the registered 2-stop spectrum (%)
1	45.0	0
2	24.8	21.5
3	14.0	23.6
4	7.5	19.8
5	4.2	14.4
6	2.1	9.9
7	1.3	6.4
8	0.6	3.9

Table 1 *Relation between the number of produced charged particles in a single event and their final contribution to the constructed 1-Stop and 2-Stop spectra.*

spectra with the probabilities of ϵ and $(1-\epsilon)$, respectively. For events with two charged particles the relative probabilities are ϵ^2, $2\epsilon(1-\epsilon)$ and $(1-\epsilon)^2$ to be attributed into the 2, 1, and 0-stop spectra. For events with a larger number of charged particles the probabilities are calculated on the basis of the binomial formula. From these calculations one can determine the fractions of events characterized by the formation of n charged particles within a constructed n' stop

spectrum. A corresponding analysis is made for 1-stop and 2-stop spectrum with a detection efficiency of ϵ= 0.45 and assuming that the intensities of events producing n charged particles are proportional to the corresponding multi-electron capture cross sections. The result is shown in the following table 1. It turns out that in the registered 1-stop spectra about the half is due to single particle events. However, only ∼22 % of events characterized by two charged particles contribute to the 2-stop spectra; about two thirds are due to events where 2, 3 and 4 charged particles have been formed. This has to be kept in mind when „2 particle correlations" are discussed with the aid of the 2 stop correlation map. In particular this means that the total kinetic fragment energies of a given event as well as the initial charge states of the fragmenting systems might be larger.

Results: Ion-Metal cluster collisions | 5

In this chapter results concerning collisions between multiply charged ions and clusters of metals will be presented.

The model metal systems that were used in the experiments were silver and bismuth.

Bismuth is a material with very particular properties as it has a rather large resistivity (80 times larger than that of silver and copper) and is the most diamagnetic one among all metals. It has drawn recently an increased attention as potential radiosensitizing agent with X -Ray irradiation connected with its low toxicity.

The second system -silver- is a noble metal, known especially as antibacterial agent having therapeutic properties in the nanoscale due to its oxidative properties with electronic configuration Ag:[Kr]$4d^{10}5s^1$, having only 1 s-type valence electron as sodium.

A more detailed discussion concerning the choice cof these two targets was given in the Introduction chapter.

5.1 Ion collisions with free,small ($\sim$2nm) bismuth clusters

The experimental studies of collisions of ions with Bi clusters will be presented in this section. The bismuth target was represented by a wide distribution of neutral clusters. Their exact distribution is difficult to determine. When analyzing singly positively charged clusters, the time-of-flight measurements yielded clusters which contained between $\sim$5 and a few hundreds of atoms with an intensity maximum at about 30 atoms. The distribution of neutral clusters might be different, therefore, TEM investigations of clusters were performed to analyze the size of neutral clusters, deposited on carbon grids. These clearly showed that many clusters do have diameters between 1nm to 2.5 nm. Because of the low contrast of small clusters on the carbon grids we cannot clearly identify objects with a diameter smaller than 1 nm. A diameter of 2nm corresponds to clusters which contains around 180 atoms.

5.1.1 Mass spectra, stability diagram and kinetic energies

5.1.1.1 TOF mass spectra

Fig.5.1 a) shows a time-of-flight spectrum resulting from collisions of Ar^{8+} ions at E_{kin}=120 keV with neutral Bismuth clusters. The range of the spectrum extends from TOF=20μs up to 480μs, which corresponds to clusters with sizes from Bi_1^+ up to Bi_{340}^+. The black curve

represents the total yield based on the interaction of the ion beam with the cluster target and with the molecular beam of the argon buffer gas, coming from the magnetron based cluster source. The red curve corresponds to the same projectile interacting with the Ar flow alone, namely when the discharge is turned off and the Ar flux is maintained. The 'noise', related to background residual ions formed by the ion beam, spans a range from the beginning of the spectra up to about 100 μs. In Fig.5.1 b) the background signal due to the buffer gas has been

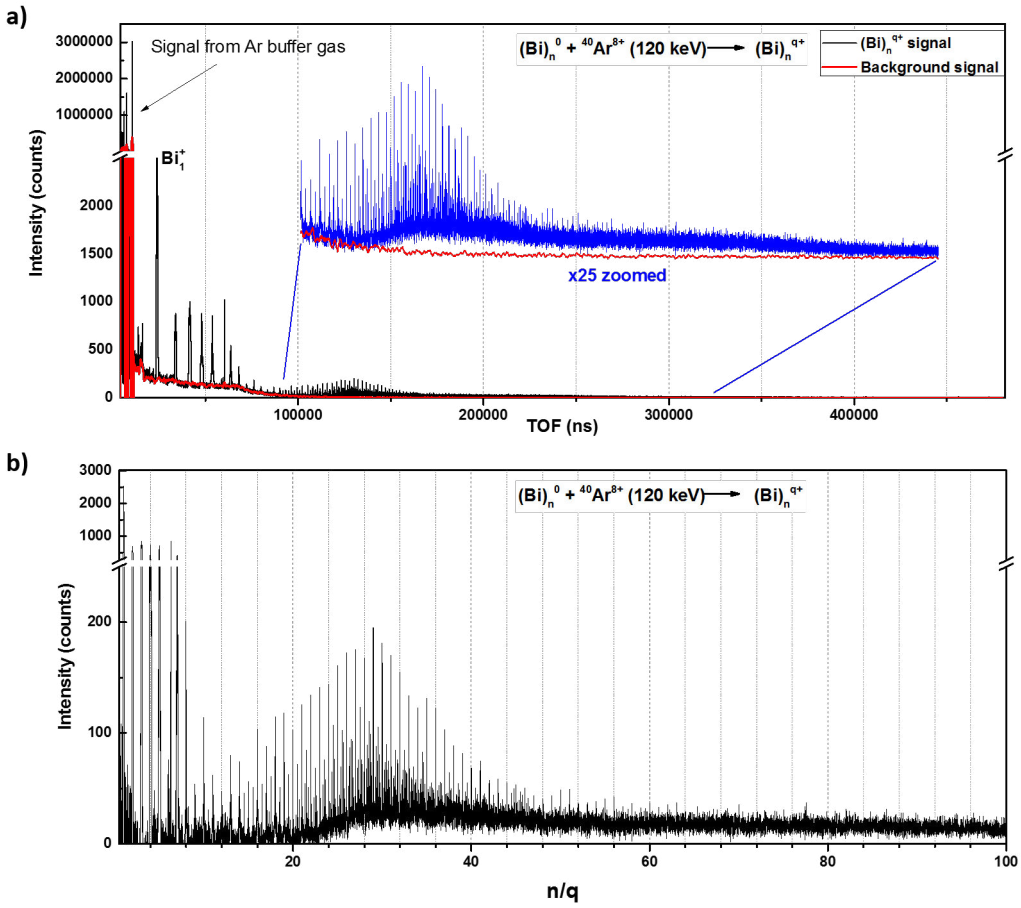

Figure 5.1 *a)Mass spectrum resulting from the collision of Ar^{8+} ions with neutral Bismuth clusters at a collision energy of E_{kin}=120 keV. The black curve corresponds to the signal when clusters and the carrier gas Ar are present in the interaction zone, whereas the red curve corresponds to collisions of the projectile only with the buffer gas Ar at a flow of 100 ml/min; b) Spectrum obtained after the subtraction of the "noise" signal from the Ar buffer gas.*

subtracted and transformed into the scale n/q showing the range from n/q=0 to 100 (n is the number of atoms in the cluster and q its charge). Before transformation the time-of-flight had been corrected according to the finite extraction pulse width (T_{extr}= 60 μs which assures the proper extraction of masses up to 50000 amu, which corresponds to total time-of-flight of 250

μs. In comparison with the spectrum in Fig.5.1 a), the contributions due to the multi-ionization of Ar atoms, which have been dominant in the first place, disappear nearly totally.

The mass spectrum consists of two main distributions: first, a very strong signal related to the presence of small clusters in the range from Bi_1^+ up to Bi_{12}^+ is observed; second, a broad distribution for sizes above ∼15 with an intensity maximum at around n/q = 30, is composed of mulitple equidistant peak series, where for the most intense series, the peaks are separated by each other by 209 amu, which is the mass of the Bi atom. Furthermore peak series characterized by non-integer number are present and demonstrate the presence of multiply charged Bi clusters.

For n/q<10 the mass spectrum is clearly dominated by small singly charged clusters, with Bi_1^+ being the most intense peak and Bi_3^+ the second most intense one. In general, the intensity of these small-size fragments decreases with increasing size, before it increases again towards the second distribution of the observed clusters. Although well resolved, the peaks for clusters with n/q > 25 are placed on a continuous contribution. This has two reasons: On the one hand, the mass resolution m/δm decreases with increasing mass so that the base part of the peak structures can no longer be resolved. On the other hand, as we will see in the following, many peak series overlap corresponding to higher charge states of the produced clusters. This will lead to a „continuous spectrum" below the resolved structures. For n/q > ∼100, the peaks are no longer resolved.

Fig.5.2 shows some selected regions of the mass spectrum in greater detail allowing to investigate the ionization degree of Bi_n clusters, ionized by Ar^{8+} ions. For the lowest cluster sizes we observe only wide peaks positioned at integer numbers of n/q. Although integer numbers may contain contributions from all charge states, this part shows only singly charged species, as for example doubly charged clusters, which should show up at n/q=7.5 are not present. Furthermore, the width of the peaks indicates high kinetic energies being due to fragmentation events.

When increasing the cluster size to n/q=14-15, we observe in fig.5.2 b) the occurrence of singly and doubly charged clusters. A peak at n/q=14.5 is is attributed to Bi_{29}^{2+}. Peaks n/q=14 and 15 are characterized with relatively wide base and very narrow upper part, which are superpositions of singly and doubly charged clusters, in this case Bi_{14}^+ with Bi_{28}^{2+} and Bi_{15}^+ with Bi_{30}^{2+}. Surprisingly the peak widths depend strongly on the charge state. Whereas singly charged clusters at n=14 and 15 are still very broad, doubly charged species with sizes between 28 and 30, are very narrow. Their low kinetic energy can be explained by the direct ionization of clusters already being present in the cluster beam. Thus the lower limit of the initial cluster size distribution is somewhere in the range of n∼15-20.

For larger cluster sizes (see figs.5.2 c) to f)) one observes the appearance of signals which we attribute to charge states between 1 to 6, or even higher. The peaks are rather narrow and the signals at integer numbers of n/q are always dominant as they contain contributions from all charge states.

In the case of triply charged Bismuth clusters one finds additionally peaks at $n + 0.33$ and

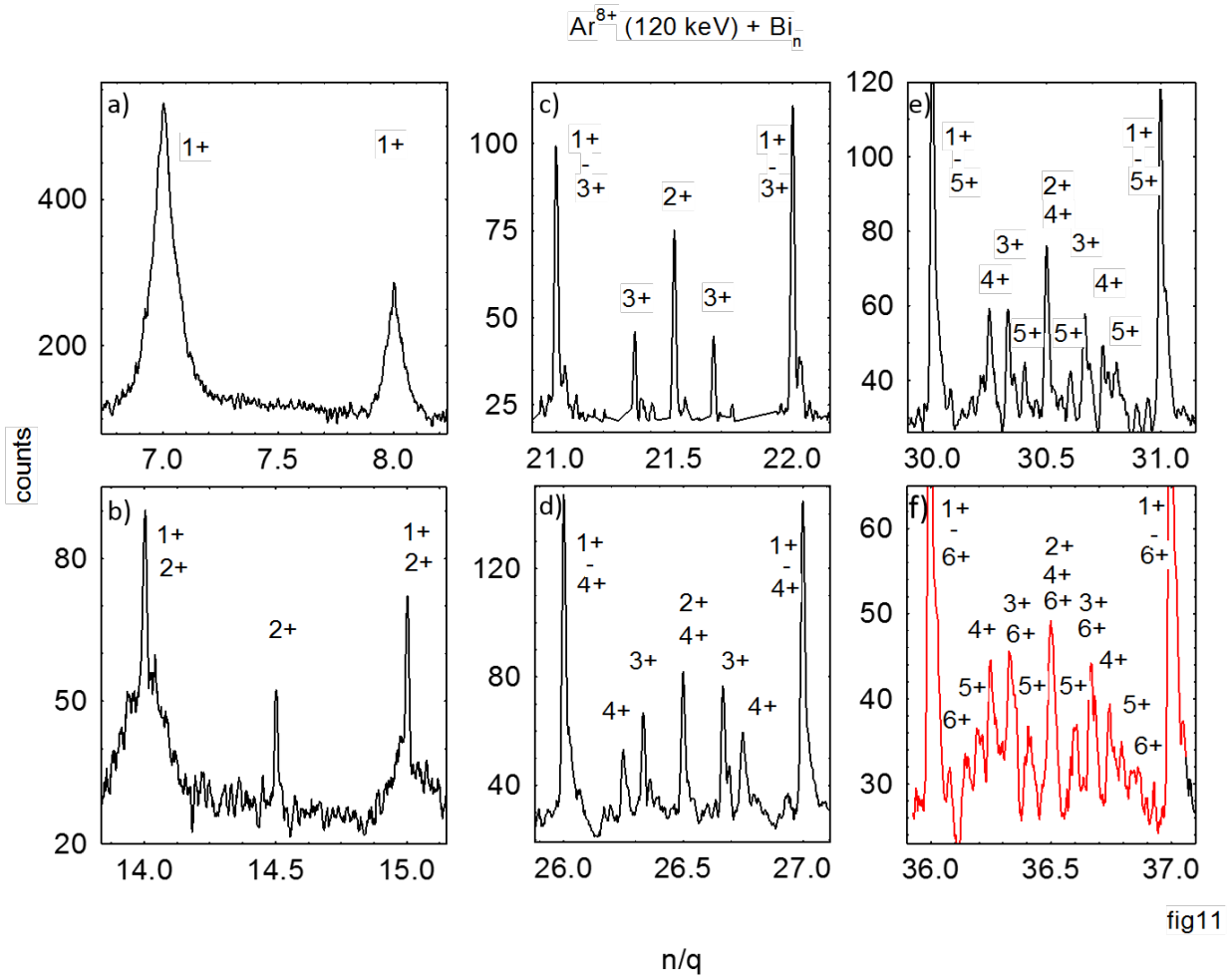

Figure 5.2 *Selected regions in the mass spectrum, resulting from ionization of Bi_n clusters by Ar^{8+} ions at 120 keV. Peaks present at the non-integer positions n/q represent contributions from multiply charged clusters.*

$n+0.66$, whereas 4 times charged clusters contribute to the signal at $n+0.25$,$n+0.5$,$n+0.75$. From spectra e) and f) of the fig. 5.2 one finds, that clusters with charge q=5 and q=6 are present and clearly visible. Values of peaks from singly and multiply charged bismuth clusters which are shown in fig.5.2 are summarized in the tab.1.

5.1.1.2 Separation of different charge state contributions

As the time of flight of a charged particle is determined by the ratio of its mass/charge, clusters with number of atoms n and charge q will exhibit the same TOF values as clusters with number of atoms 2n,3n,4n and charge 2q,3q,4q and so on. Their peaks in the time-of-flight (mass/q) spectrum are found at the same position and, therefore, it is not possible to verify their original n and q without any additional information.

q=1	q=2	q=3	q=4	q=5	q=6
7.0 8.0					
14.0 15.0	14.5 (1/2)				
21.0 22.0	21.5	21.33 (1/3) 21.66 (2/3)			
25.0 26.0	25.5	25.33 25.66	25.25 (1/4) 25.5 (2/4) 25.75 (3/4)		
30.0 31.0	30.5	30.33 30.66	30.25 30.5 30.75	30.2 (1/5) 30.4 (2/5) 30.6 (3/5) 30.8 (4/5)	
36.0 37.0	36.5	36.33 36.66	36.25 36.5 36.75	36.2 36.4 36.6 36.8	36.167 (1/6) 36.334 (2/6) 36.5 (3/6) 36.667 (4/6) 36.834 (5/6)

Table 1 *n/q positions of peaks of the mass spectrum shown in the zooms fig.5.2 correlated with the charge state of the Bismuth cluster.*

In figure 5.3 an idealized mass spectrum of such a situation is shown. The charge states which are considered are q=1 to q=4, and the X axis is calibrated with respect to the number of Bi atoms/charge. Naturally, singly charged clusters are found at integer numbers of n/q=30.00 and 31.00. Doubly charged clusters are found in a spacing of half n/q units (30.0, 30.5, and 31.0) and triply and quadruply charged clusters will be separated by the third and the fourth of a unit,i.e at n/q of 30.0, 30.33, 30.66, 34.0 and 30.0, 30.25, 30.5, 30.75, 32.0, respectively.

The integrals of the peaks represent the total number of counts measured at a given n/q value. In order to determine individual contributions of different charge states and cluster sizes, a subtraction procedure is applied starting from peaks which are uniquely identified without contributions from overlapping peaks. In the spectrum, shown in fig.5.3, this is the case for the triply and four times charged systems, namely Bi_{91}^{3+} and Bi_{92}^{3+} as well as Bi_{121}^{4+} and Bi_{123}^{4+}. In the next step, the peak at n/q = 31.5 is analysed which has contributions from doubly and four times charged clusters. As the approximation we assume that the intensities of neighboring cluster sizes of a given charge are similar, i.e. we neglect possible even-odd effects or sharp variations of the cluster size distribution. Thus we assume that

$$I(Bi_{122}^{4+}) = \frac{I(Bi_{121}^{4+}) + I(Bi_{123}^{4+})}{2} \tag{1}$$

and correspondingly

$$I(Bi_{61}^{2+}) = I(n/q = 30.5) - I(Bi_{122}^{4+}). \tag{2}$$

With the same extrapolation or interpolation we obtain the intensities of all charge states contributing in particular to the integer values of n/q=30 and 31, knowing from the spectrum analysis that in this n/q range contributions from charge states q>4 are not present.

In general, for deconvoluting the mass spectrum it is necessary to apply this procedure for all peaks, starting with the highest visible charge state of the clusters. For larger n/q values

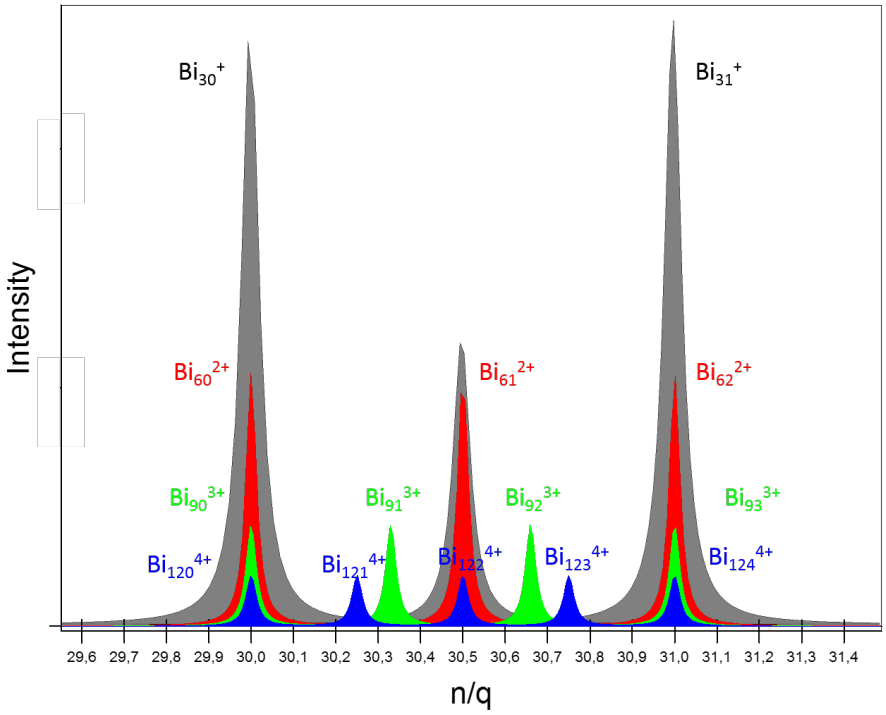

Figure 5.3 *Idealistic mass spectrum showing the distribution of Bi_n^{q+} clusters for charge states $q = 1$ to $q = 4$. The height of the peaks can vary in any arbitrary way. Colors represent different contributions of mulitply charged clusters peaks.*

the peaks tend to overlap and it is necessary to apply the procedure of deconvolution using a combination of peak functions of gaussian or lorentz type. This is done by using a data processing software like OriginLab. The type of the function used is important, especially if one has to deal with some asymmetrical shapes which can be related for example to evaporation processes. The form of the peaks is varying considerably and evolves with the n/q ratio, which is related to the transmission of the spectrometer.

5.1.1.3 The abundance spectra for different charge states

For the majority of the peaks the procedure of deconvolution was not necessary, only in case of larger n/q values and large bin-width some peaks of multiply charged clusters started to overlap with each other. Fig.5.4 shows the cluster size distributions for different charge state, extracted from total mass spectrum obtained by direct integration. Blue bars correspond to the integrated intensities of the peaks, the red vertical line corresponds to the smallest cluster size for a given charge state. As discussed above, these values correspond to the appearance sizes of the Bismuth clusters for given charge states. For example, for the case of doubly charged

clusters, the distribution starts from n/q=10.5, i.e. n_{app}(q=2)=21.

Figure 5.4 *Abundance spectrum of Bi_n^+ clusters ionized in collision with Ar^{8+} ions at a kinetic energy of 120 keV, shown for charge states q=2 up to q=6. The height of the blue bars corresponds to the integrated peak intensities.*

One can observe that the intensity distributions do not show, in particular close to the appearance size for q=2 and 4, a smooth behavior. Thus, some species are missing before reaching the limit. This might be due to slightly different fission barriers and thus stability for individual systems.

The appearance sizes are summarized in tab.2 for charge states between 2 and 6. They increase, as to be expected, with increasing charge, as more atoms are required to stabilize the increasing charge. Furthermore, table from tab.2 specifies also the maximum size observed in the spectrum for a given charge state. These values have been obtained by a deconvolution procedure. The result is astonishing, as one would expect to find the same value for all charge states, as it is determined by the size distribution of the initial clusters. The result indicates that the overall detection efficiency (trajectories in the analyzing system, secondary electron emission yield) is better for highly charged systems. Whereas singly charged clusters bombard the conversion plate with an energy of ∼20 keV, 6 times charged clusters hit the plate with an energy of 120 keV.

In case of triply charged clusters the observed appearance size corresponds to n∼43 (Bi_{43}^{3+}). Just below n=90 we observe a rapid increase of the intensity (vertical black dashed line)

q=2	n_{app}=21 ±2	n_{last}=150
q=3	n_{app}=43 ±3	n_{last}=168
q=4	n_{app}=87 ±4	n_{last}=200
q=5	n_{app}=121 ±4	n_{last}=225
q=6	n_{app}=181 ±4	n_{last}=250

Table 2 *Data summarizing the appearance sizes and lthe maximum sizes being observed in the distributions of multiply charged Bi clusters, resulting from collisions with Ar^{8+} at 120 keV.*

towards smaller cluster sizes. This coincides with the appearance size for the series of 4-times charged clusters, which spans from n=87 up to n=200. This phenomenon occurs also in the distributions of other charge states, however, it is less prominent (q=2 at n∼43, q=3 at n∼87, q=4 at n∼121). This finding indicates that when a cluster in a given charge state q is formed at a size below its appearance size, it decays by a fission process leading to an increase in the intensity of the distribution q-1. We will describe this in more detail further below.

5.1.1.4 Stability diagram

The results obtained in the previous section concerning the distribution of multilpy charged clusters (fig.5.4 and table 2) can be summarized in the form of a graph illustrating the charge stabilized on the cluster as a function of its size. The Y axis represents the charge q of the system and the X axis the cluster size n (both axes are given in a log-scale). This presentation is called the stability diagram, which gives insight into the stability of the systems and follows a concept used in nuclear physics describing the stability of nuclei, (described in the part sacrificed to theoretical models - chapter 3). The blue straight line corresponds to the so-called critical size of the cluster, where the fissility parameter is equal to X=1 and is related to the maximum critical charge which a system of a given size n can still sustain if it is perfectly cold. This is the region where the barrier for fission processes is dropping to zero and the system decays by emission of charged particles, reducing its overall charge. For lower charges a fission barrier exists and the system becomes metastable. The lifetime will depend on the internal energy (decreasing with increasing size) and hence on the ionization method, as well as on the strength of the bonding forces (increasing). When further reducing the charge, the height of the fission barrier increases and reaches the value of the activation energy for evaporation of neutral particles. In this case the charge of the cluster does not change during fragmentation. Hence, charged fragments can only be observed for cluster sizes above this value, the appearance size. As an example, for q=5 the critical size is about n_{cr}= 40, whereas n_{aap} is much larger - namely 121. The red points in Fig.5.5 are the experimental data for the appearance sizes as determined in this work, resulting after collision of Bi_n with Ar^{8+} ions. By fitting the points, one obtains a linear dependence in the double-log plot with a slope which corresponds to a fissility of X∼0.27. This is in agreement with the results of the liquid drop model as shown for the case of metallic

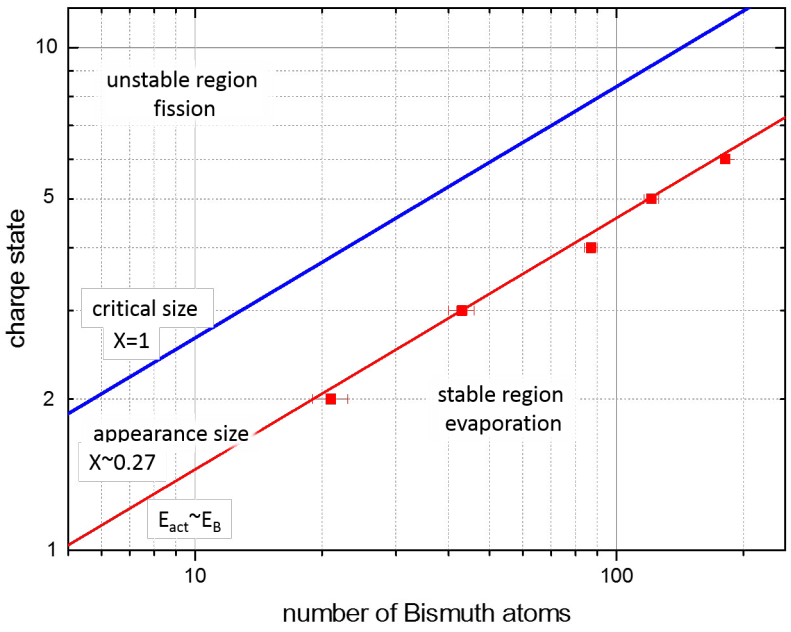

Figure 5.5 *Stability diagram for multiply charged Bi clusters resulting from collisions with Ar^{8+} ions at E_{kin}=120 keV.*

sodium clusters. Also there, the fissility value X∼0.27 was found to characterize the appearance size in previous studies [75]. Although when producing multiply charged cluster ions with lower internal energy (use of very highly charged projectiles, like Xe^{28+}), the appearance size has been shown to approach the critical size for large cluster sizes, [19].

In the present case, doubly charged Bismuth clusters are observed for a size of n∼21, a value which might depend on the experimental conditions like the initial cluster size distribution. This has been proposed in earlier experiments, where small Bi clusters were ionized by electron impact, [83]. The authors report, that for small cluster sizes (the spectrum has its maximum at the monomer) doubly charged clusters are observed for sizes as small as n_{app}=5, whereas for somewhat larger cluster sizes (the maximum occurs at n∼9) the appearance size shifts to n_{app}∼9 (see fig.5.6).

The difference with respect to the present measurement cannot be explained by different internal energies. Before the interaction with an ion, bismuth clusters have a low intrinsic energy (temperature of about 70 K) redistributed in ro-vibrational states. After ion interaction the observed signals are stemming from somewhat heated clusters, however, the energy transfer for double-ionization by a 8 times charged projectile is much less than that occurring during electron impact ionization. Thus in the present case, the cluster temperature is expected to be lower.

The different behavior must be due to different binding conditions or different geometrical polymer structures. In the case of lead clusters, produced from a gas-aggregation source and

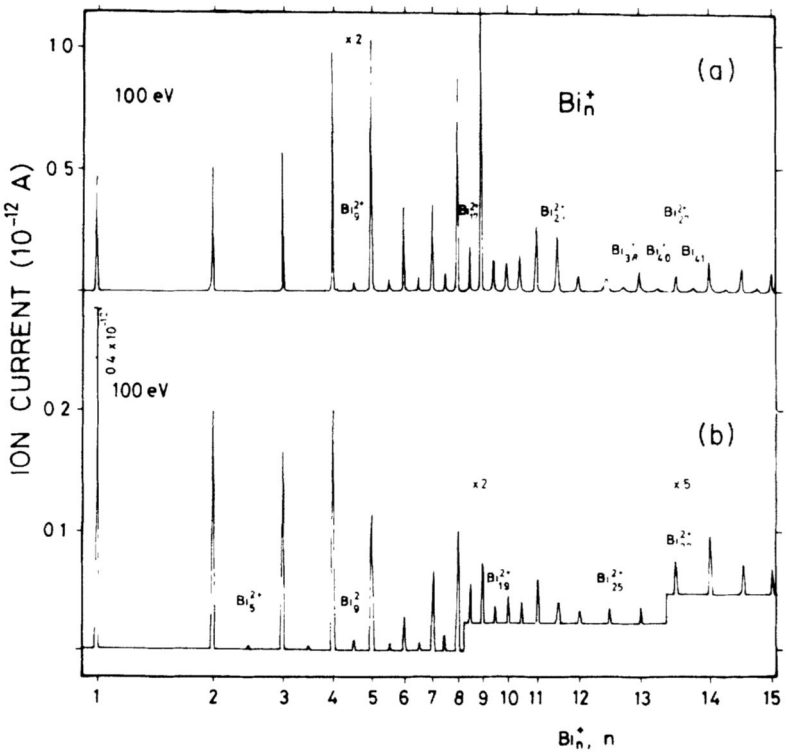

Figure 5.6 *Mass / charge spectrum of Bi clusters ionized by electron impact at 100 eV for two different initial cluster distributions. a) larger cluster sizes; b) smaller sizes. Taken from ref. [83]*

ionized by electron impact, initially a size limit of $n_{app} = 31$ [84] was reported, which in another experiment was reduced down to $n_{app} = 7$, [85]. This was explained to be related to the occurrence of structural isomers in the cluster beam. For linear structures the appearance size is larger than for more compact clusters.

The structure of the spectra differs strongly between Bi clusters and those obtained from experiments with lead and gold by Goldenfeld [83]. These differences (especially relative intensities of singly charged clusters) can possibly be explained by a larger amount of polymeric molecules that are present under equilibrium conditions, thus leading to different nucleation behavior/initial conditions for the production of small cluster sizes.

In fact, the present Bi measurements have been performed with a cluster distribution which shows its maximum intensity at about n$\sim$30; clusters with sizes below $\sim$15 are not present in the initial cluster beam. Therefore, these larger systems might be more metallic than the smaller ones used in earlier experiments and might behave like small pieces of metal.

As we already mentioned, in the isolated spectra of multiply charged clusters q=2,3,4 (see Fig.5.3) there are certain regions where the intensity is increased, localized between the red solid and black dashed lines. This effect is especially strong for q=3, where the step in

intensity occurs at the appearance size of the cluster in the next higher charge state (q=4). The explication is given in Fig.5.7. When a neutral cluster is multiply ionized into the charge state q at a size below the corresponding appearance size (see red crosses in Fig.5.7) the system will decay by the emission of a small singly charged fragment forming a residue in the charge state q-1 according to:

$$Bi_n^{q+} \rightarrow Bi_{n-x}^{(q-1)+} + Bi_x^+ \tag{3}$$

with x being small, preferentially 1 or 3. After the emission the cluster becomes stable (black dots); only in the case of high internal energies further evaporation processes may occur. In the case that the size of the q-times charged cluster is even below the appearance size of the charge state q-1, at least two fragments have to be emitted in order to reach a stable system.

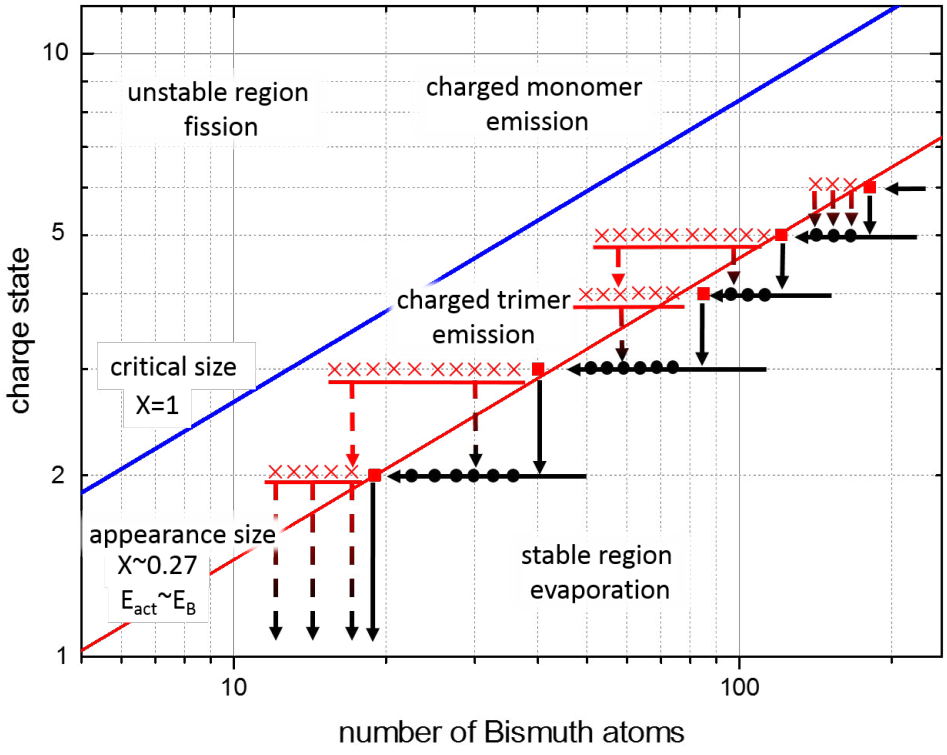

Figure 5.7 *Stability diagram for Bi clusters as shown in Fig.5.5, but including transitions due to evaporation and fission processes.*

5.1.1.5 Analysis of small fragments/cluster of Bi - collisions with different projectiles - effect of charge state of projectile

Under experimental conditions optimized for the detection of small fragments, different projectiles: Xe^{17+}, Ar^{11+}, Ar^{8+}, O^{6+} and O^{3+}, were used in order to examine the effect of the

charge state of the projectile on the intensity distribution of smaller fragments. Fig.5.8 shows the variation of the spectra as a function of the above mentioned projectiles. We see that emission of Bi_1^+ is a dominant peak for projectiles from Xe^{17+} to O^{6+}, however the contribution of other larger fragments ($Bi_2^+$to Bi_5^+) becomes more and more visible if the charge of projectile decreases. For O^{3+} the intensity of Bi_3^+ is the most intense one. In this case the average charge state of the produced intermediate Bi cluster is expected to be lower. Therefore, these observations are in agreement with the previously discussed liquid drop model for the fission processes in case of large (higly ionized) and low fissilites of the parent Bi cluster.

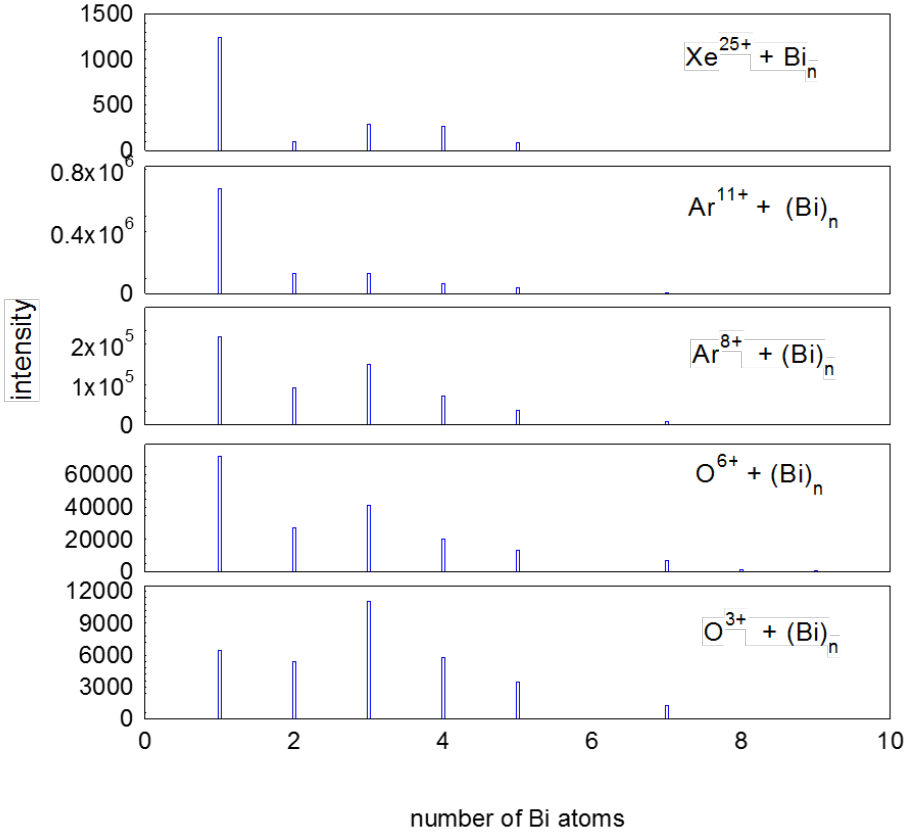

Figure 5.8 *Intensity distribution of small fragments resulting from collisions of Bi clusters with different projectiles- Xe^{25+},Ar^{11+},Ar^{8+}, O^{6+}, O^{3+}. Characteristic change of the maximal peak towards trimer from monomer is observed while the charge state of the projectile decreases.*

As it was shown previously, the magnetron source produces Bi clusters with a number of atoms which less than a few hundreds. It is an interesting question what kind of geometrical structures for a specific cationic isomers one can expect, especially as a semi-metallic character of bismuth may not necessarily lead to formation of very compact structures typical for other metals. Fig.5.9 shows indeed the geometries calculated by Kelting et al. [79], where Roman numbers indicate different isomers and Arabic number is the number of atoms in the cationic

cluster. In all cations where n≤5 characteristic pentagons are present in the structure. Among the most stable ones, with n up to 8, we see that structures are rather compact, where each atom has at least 3 other neighbors (coordination number is given by the color - red:4, yellow:3 and blue:2). However for n > 8 the isomers are becoming more prolate with low coordination numbers, which is observed usually in semiconducting materials rather than in metals.

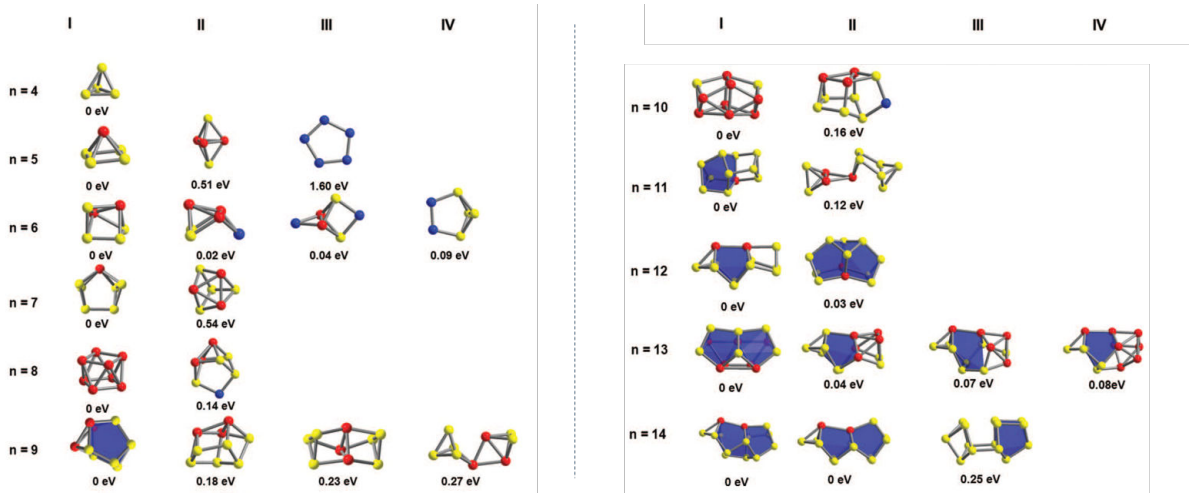

Figure 5.9 *Calculated local minimum structures for Bi_4^+ to Bi_{14}^+ with optimized geometries at DFT level, based on the work of the group of Kappes, [79]. Roman numbers correspond to respective global minima (different isomers) while arabic number describe the number of Bi atoms in the cluster. Color of an atom refers to coordination number : 2-blue, 3-yellow, >4-red. Taken from [79].*

5.1.1.6 Kinetic energy of fragments and clusters

The observed multiply charged clusters have two types of origin: either they are ionized with projectiles within their stability limits and, therefore, are detected as stable systems, or they are initially ionized into charge states that induce instabilities of the system and due to fragmentation processes only remaining stable residues and small clusters are recorded. To a large extent charged-particle assisted fragmentation occurs in the pico-to nanosecond time domain, whereas in mass spectrometry the products are analyzed on the microsecond time scale (sometimes milliseconds, depending on the size of the system). Therefore, it is possible to study the mechanism that is associated with an energy release, as for example fragmentation, by studying the shape of the peak form. This broadening effect is strongly visible for small clusters/fragments because they are well resolved and carry most of the fragmentation energy. For the fragmentation of mass M into m_1 and m_2 we find

$$E_{kin1} = \frac{m_2}{m_1 + m_2} \times KER \tag{4}$$

$$E_{kin2} = \frac{m_1}{m_1 + m_2} \times KER \tag{5}$$

where KER is the total energy released during the process, $m_{1,2}$ are the masses of the two fragments and $E_{kin,1,2}$ their kinetic energies. From these equations it follows that the energy release is shared among both fragments, favoring the lighter one. For the fragmentation of Bi_{200}^{2+} into the small fragment Bi_3^+ and the residue Bi_{197}^+ more than 98 % of the energy release will be transferred to Bi_3^+.

In a hypothetical situation the emission of fragments is assumed to be isotropic in space (see fig.5.10a). For simplicity we may assume the fragments to be of the same mass and to have the same kinetic energy, therefore the same velocity. Naturally, these particles which have the z-component of the velocity directed towards the detection axis will arrive much faster at the detector than those having the opposite vectors (opposite to detection direction). Generally, this results in the signal being spread over all times between so-called forward and backward peaks. The examples of the peak form for two discrete kinetic energies for a fragment of the same mass is given in the upper graph in fig.5.10 b). Differentiation of such a spectrum in the time domain reveals the two contributions (4 peaks in time domain) that after conversion will give the information about energy distribution contributing to the overall form of the peak.

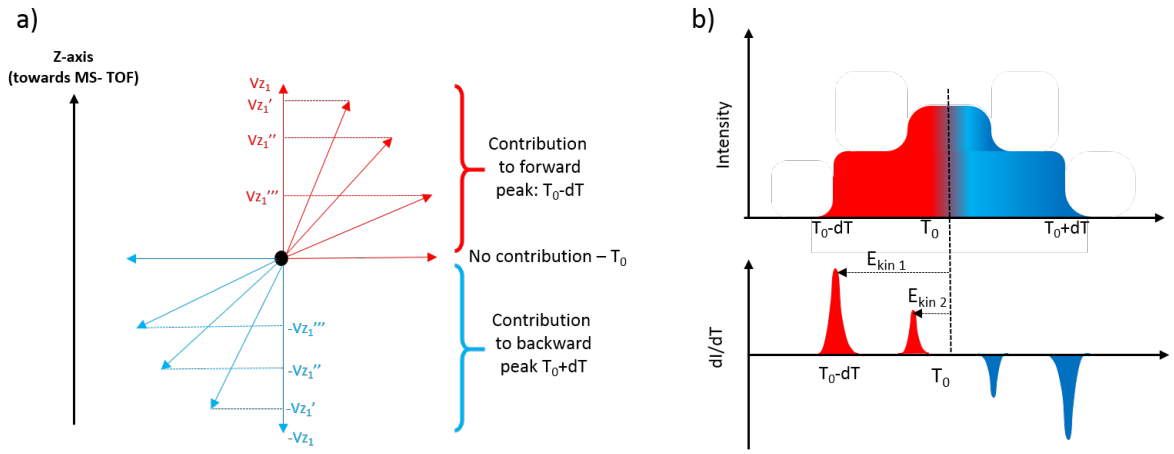

Figure 5.10 *a) Schematical representation of the fragmentation of a charged particle into all possible directions with the given kinetic energy, with marked z-component of the velocity affecting time-of-flight. b) Upper graph shows hypothetical time-of-flight spectrum for a fragment with given mass m with two specific kinetic energies (all fragments emitted isotropically are detected), while the lower graph is the result after differentation with characterisitc peaks revealing kinetic energy components to the TOF spectra.*

Fig.5.11 a) shows the distribution of small Bi fragments resulting from the collisions with Ar^{8+} projectiles, spanning the range from Bi_1^+ up to Bi_{17}^+. Particular peak shapes are due to different energy contributions for a specific fragment. Fig.5.11 b) to d) show those forms for

Bi_3^+ to Bi_5^+ with two characteristic features present in all 3 cases, however with different relative proportions. The broader one is spanning more than 1000 ns in the time-of-flight domain and the second one, which is narrower, having less than 400 ns. A more exact analysis will be performed further below, where we will apply the method described in fig.5.10 b).

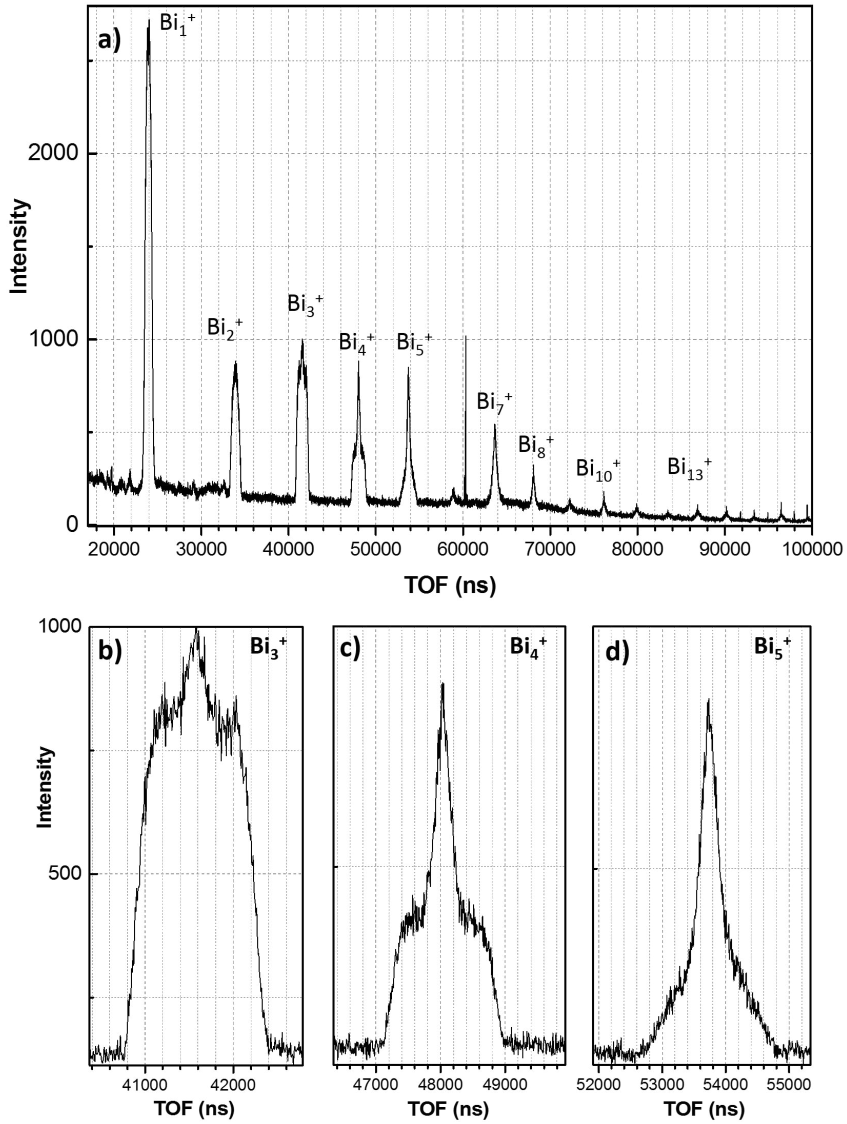

Figure 5.11 *Peak forms from the monomer up to Bi_{15}^+ produced in collisions of Ar^{8+} ions with Bi clusters. The sharp peak at 60 μs corresponds to noise signal produced at the end of extraction pulse.*

In fig.5.12 the peak forms of Bi_1^+ and Bi_2^+ resulting from collisions of neutral Bi_n clusters with Ar_8^+ are shown (pink and red line, respectively). As discussed above, the differentiation of the peaks with respect to time allows to obtain the distribution of the energy causing this width broadening. The results are shown as blue lines in the graph 5.12 (the red line for the case

of monomer is obtained after smoothing). From the analysis of the maxima of the resulting curves the main energy is determined. For the monomer the peak width obtained is δT = 824 ns with a variation between 1000 ns and 400 ns, and for dimer it is δT=1070 ns with a variation between 1300 ns and 600 ns. The recalculation into the energy scale gives energy values of δE_{kin}=5.85 eV in the interval [8.6 eV : 3.4 eV] for the monomer and δE_{kin}=4.7 eV in the interval [7.2 eV; 1.5eV] for the dimer. (The interval is estimated by the half width of the peaks in the derivative).

For the case of the peak form of the Bi_3^+ fragment, presented in fig.5.13, it is different than for cases of the monomer and dimer. It consist of two main contributions - one related to very broad δT_1=1382 ns and second much narrower of δT_2=198 ns. In terms of the energy it is 5.4 and 0.11 eV, respectively. This is important observation as it points out on the origin of these two distributions for case of Bi_3^+.

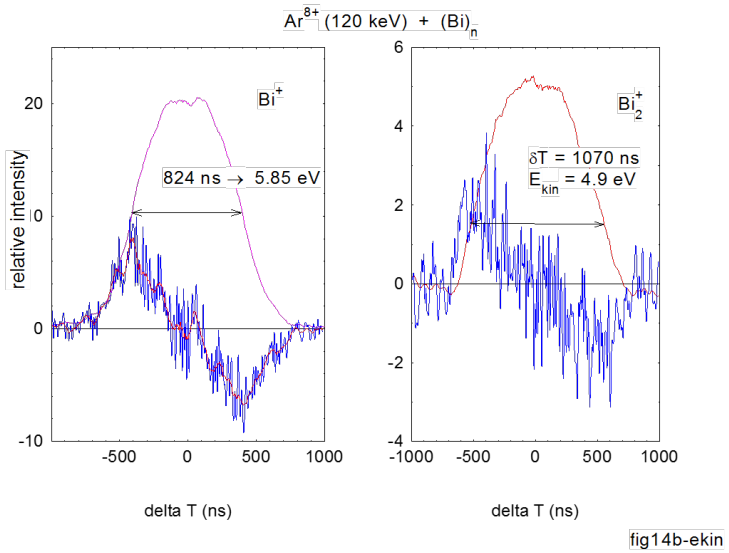

Figure 5.12 *Peak forms of the monomer and dimer produced in collisions of Ar^{8+} ions with Bi clusters. The red and pink curves represent the redlative peak intensity measured as a function of time.*

The analysis performed so far assumes that all fragments are measured in the TOF- and detection system. However, as described in chapter 4, there is a limit with respect to high kinetic fragment energies which is, depending on the applied voltages, of the order of 4 eV. I.e. the transmission of the high-energy small fragments is lower than 100 %.

In order to further analyse this effect and to determine more precisely the contribution of lower energy distributions for those peaks, the procedure involving SIMION simulations is performed and the results are shown in fig. 5.14. Fig.5.14 a) shows the peak form for the case of Bi_4^+ with a smoothed shape (red line). From the time difference of the large energy distribution shoulders the maximum kinetic energy is deduced, being 5.5 eV and taken for

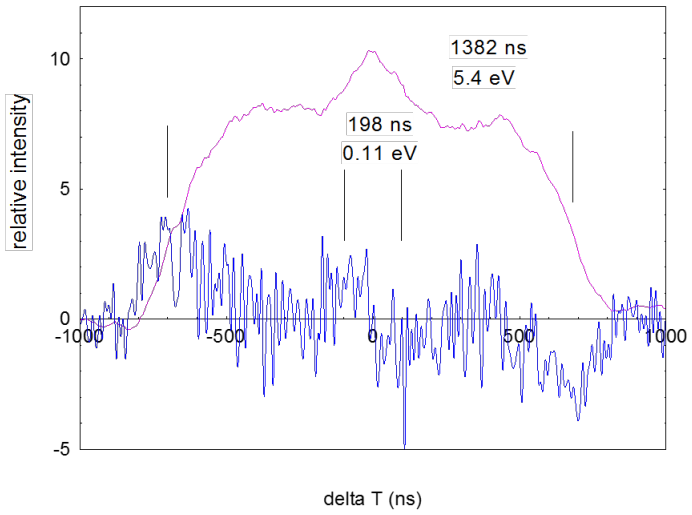

Figure 5.13 *Peak form of the trimer produced in collisions of Ar8+ ions with Bi clusters. The red curves represent the relative peak intensity measured as a function of time. The blue curve is its derivative*

further spectra simulations. Fig.5.14 b) is a peak form of Bi tetramer resulting from SIMION simulations of gaussian distribution of kinetic energies in SIMION simulations with FWHM of 3 eV and maximum centered at 5.5 eV (look inset in the graph).

The theoretical curve shows a narrow dip at the center of the curve and slight forward and backward structures. The assymetry is not well reproduced in the experiment. Nevertheless, we used the average of both peaks and subtracted it after normalization from the experimental peak form shown in fig.5.14 a).

This procedure is shown on fig.5.15 a). The blue curve is the final form of the peak after exclusion of more energetic contribution. In fig.5.15 b) an overview on the halfwidths and kinetic energies of tyhe low- and high-energy parts is given for Bi_1^+ to Bi_5^+ fragments. In general, the energies decrease with increasing fragment size.

When we regard the peak structures for clusters in the range up to n=7, we continue to observe a wide and a narrow distribution. The relative intensity of both contributions varies with size as shown in Fig.5.16. The total peak intensity is represented by blue bars, that of the wider distribution in red, and that of the more narrow distribution in black. Whereas for n<4 the wide distribution strongly dominates, in the range from n=4 to n=7 the situation changes and both contributions become equally important.

The dependence of the kinetic energy associated with the width of the peak is shown in fig.5.17 as a function of the observed fragment/cluster size. On this graph one can see 3 main contributions. At first singly charged ions are observed as energetic fragments starting from the monomer and propagating up to the heptamer. With increasing size their average kinetic energy decreases and approaches for n=8 energy values which are typical for a second series

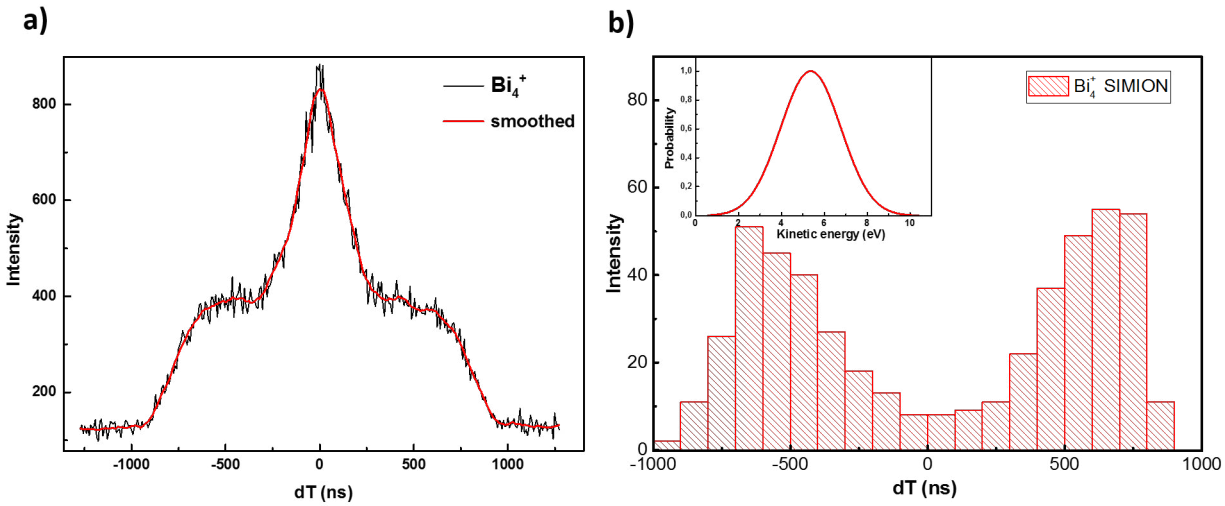

Figure 5.14 *a) Peak form of the Bi tetramer seen as in the experiment;b) peak form of Bi tetramer with Gaussian kinetic energy distribution (centred at 5.5 eV with FWHM of 3 eV) resulting from SIMION simulations.*

of singly charged cluster ions. Their average energy is of the order of 100 to 200 meV up to n∼18 (only for Bi_3^+ it increases to 900 meV). Furthermore, a series of doubly charged clusters is observed for $n/q > 10$, which are characterized by ultrathin peaks corresponding to kinetic energies of about 10 meV. These doubly charged clusters with sizes above the appearance size $n_{app}(q=2)$ are formed by direct double ionisation, thus, only a small amount of energy is transferred in long-distance collisions with highly charged projectiles.

When clusters are singly ionized, the energy transfer is expected to be comparable or even smaller than for double ionization, and, therefore, very narrow peaks are also expected for singly charges species. However, for $n<10$ this is not the case. This means that in this size region no clusters are present in the primary neutral cluster beam.

As we will discuss in the next section when analyzing coincidences, the two series of singly charged clusters observed at very small cluster sizes are both due to fragmentation processes. Whereas the low energy part represents fragments or residues from preferentially doubly ionized systems with $n<n_{app}(q=2)$ or from evaporation processes, the high-energy part represents fragments from clusters formed in higher charge states. A more detailed discussion will follow further below.

5.1.2 Coincidence measurement

All spectra presented up to this point were inclusiv spectra, which means that all clusters and all fragments that were detected, were included independent of the multiplicity of the event. The recorded spectra contain clusters which are formed in a stable state and those

a)

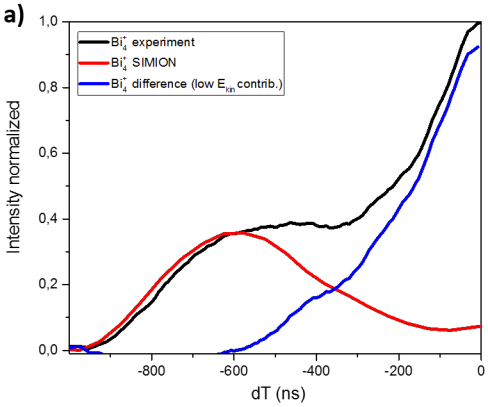

b)

	High energy part		Low energy part	
Fragment	dT (ns)	Energy (eV)	dT (ns)	Energy (eV)
Bi_1^+	800	5,4	-	-
Bi_2^+	980	4,1	-	-
Bi_3^+	1296	4,76	580	0,95
Bi_4^+	1616	5,5	364	0,281
Bi_5^+	1440	3,52	300	0,15

Figure 5.15 *a) Superimposed experimental (black), simulated(red) and final (blue) peak forms after performing the procedure of the subtraction of high-energetic kinetic energy contribution of the fragment, shown on the example of Bi tetramer. b) Summary of the average/most probable energies in the low kinetic energy contributions determined with the help of SIMION simulations for the trimer,tetramer and pentamer.*

which have undergone fragmentation. The actual multiplicity of events is the number of recorded fragments during one single event. In the case that some particles are not registered due to the limited detection probability, the real multiplicity is higher than the measured one. Nevertheless, by choosing the events according to their measured multiplicity it is possible to examine the correlations between particles that are produced in one event, which we call „in coincidence". By such procedure one can examine the possibility of the emission of small or larger fragments in correlation with heavy residues, yielding an approximation in terms of its original size and charge and giving insight into the possible dynamics of such process.

5.1.2.1 Correlations

During the measurement, all of the events are recorded and stored as data in form of a list file. As it is shown in an earlier chapter, the most abundant signal the is due to the buffer gas, which in our case is Argon as well as - to a minor extent - to the residual gas present in the interaction chamber (mostly consisting of water and nitrogen, however, due to the cooling of the walls around the interaction region to the temperature of liquid nitrogen, the water signal is strongly reduced as these molecules stick to the cold surfaces).

In order to measure true coincidences the number of events per ion pulse, i.e. occurring in one extraction pulse, must be small compared to one. This guarantees that the probability for two or more events to occur in one analyzing period is very small as well (in the % range).

In the present case of collisions of Ar^{8+} ions with Bi_n the intensity of the ion beam was chosen in a way that around 1 event occurs in 20 pulses of extraction linked to a signal in the

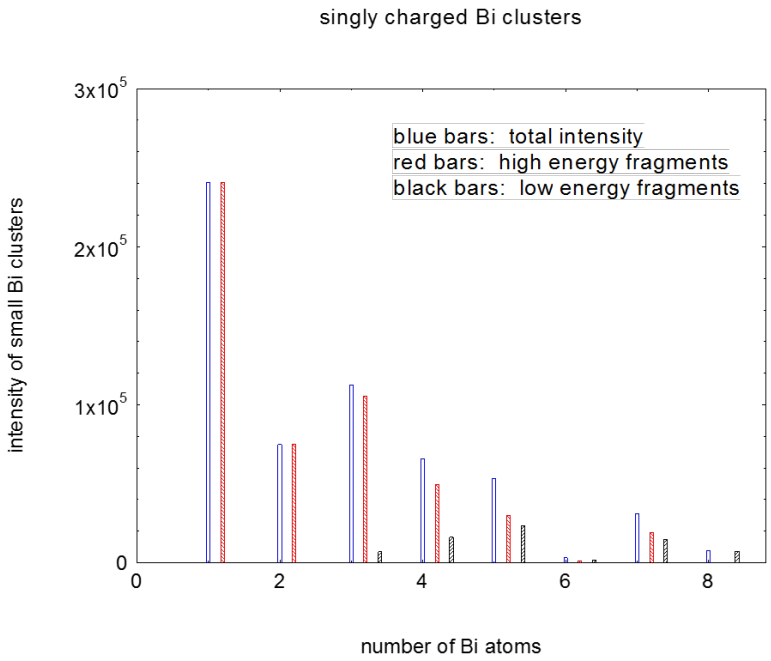

Figure 5.16 *Intensity distribution of small fragments produced in the collision system* $Ar_8^+ + Bi_n$.

mass range above 40 amu (the largest impurity ion which is well below the smallest fragment of Bi_n with a mass of 209 amu). Under these conditions, the total count rate is still very high due to the Ar contributions. As a consequence the measured multiplicities are not correct and an „event cleaning" has to be performed during the analysis with the ROOT software. For example, the time-of-flight of the first ion observed in an event with multiplicity m is analyzed. If $TOF_{1st\,ion}$ is below or equal to TOF_{Ar^+} we exclude the first ion as „false" and place the m-multiplicity event into the category of multiplicity m-1. The same procedure is repeated for the time-of-flight of the second and third ion, and so forth until the event shows only ions with masses above 40 amu.

Before the procedure of removal of false coincidences, the total number of events was around 20 milions, while after the removal of false coincidences the number of relevant events dropped down to 2 milions, which is around 10 % of the total number of events. Within these 2 million events around 90% are events with multiplicity 1 (1STOP - one charged fragment/cluster was detected), 8.6 % with multiplicity 2 , 1 % with multiplicity 3. For the 1STOP spectrum the signal arrives mostly from singly and multiply charged clusters or fragments which are stable having already lost neutral moieties. Of course also contributions from 2 stop events might be present when the second charged fragment is not detected.

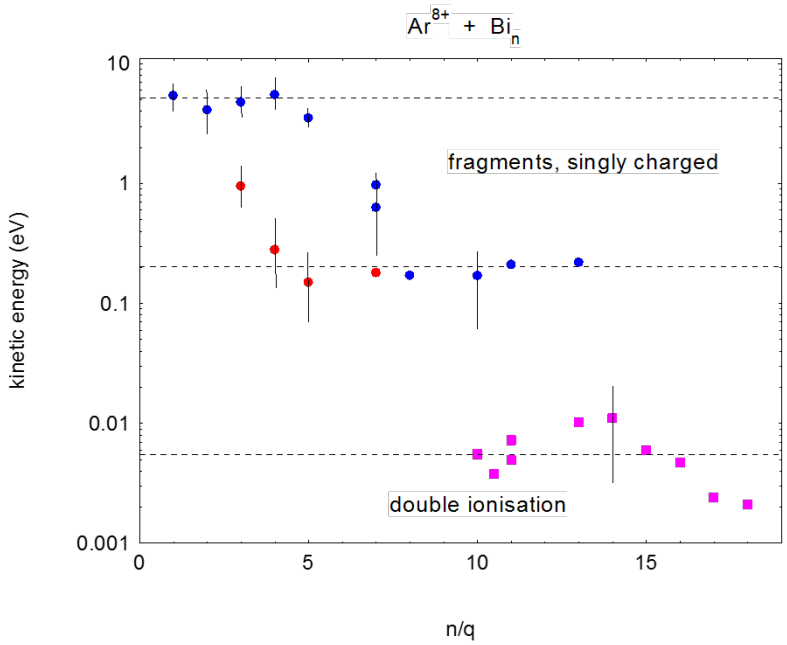

Figure 5.17 *The most likely kinetic energies of the fragments in the size range from n/q=1 to n/q=18. Ar^{8+} + Bi_n.*

5.1.2.2 Full coincidence Map

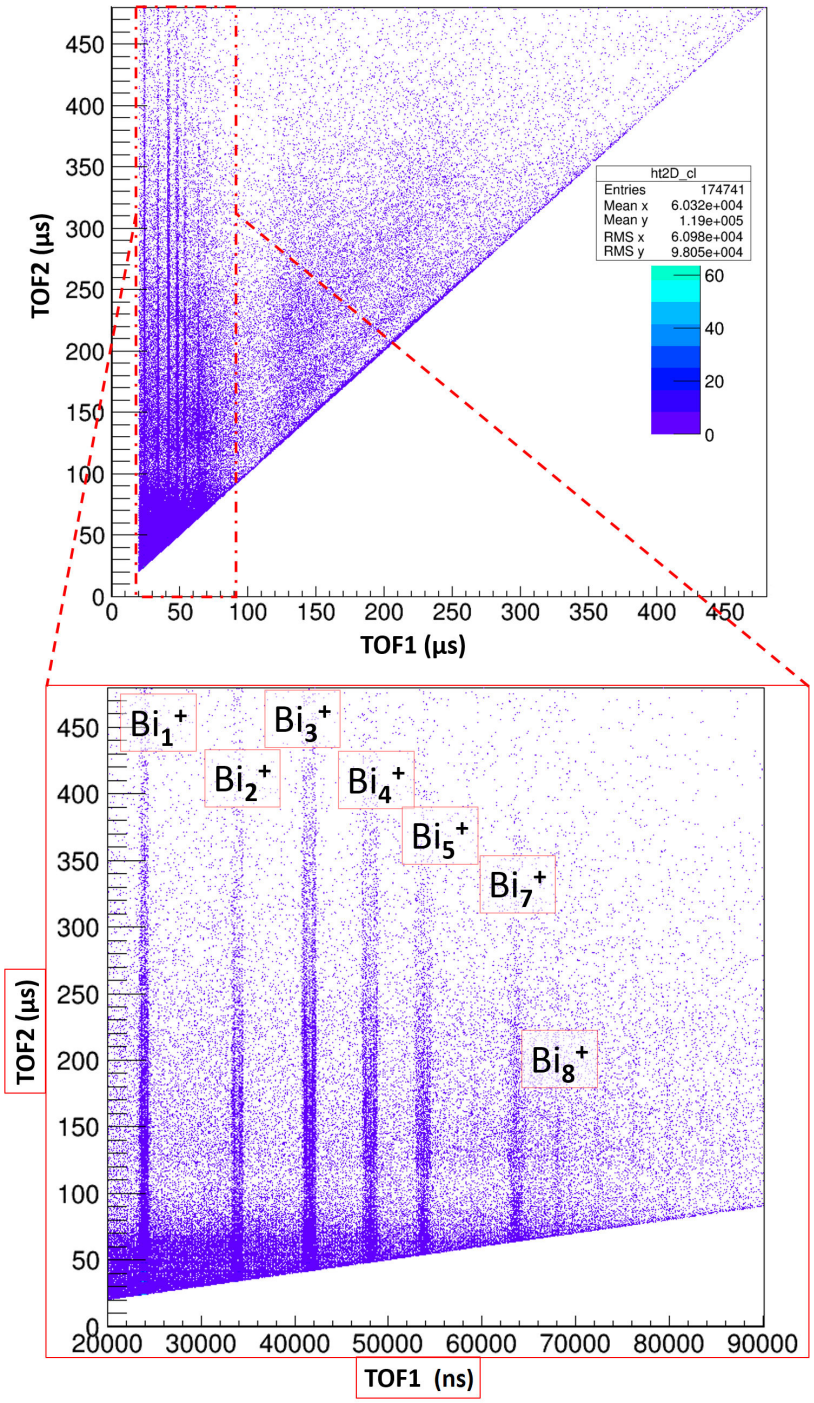

Figure 5.18 *Two-dimensional representation of 2-Stop events of the corrected cleaned data set resulting from collisions of Bi_n with Ar^{8+} at 120 keV.*

Figure 5.18 shows the 2-dimensional representation - a so called 2D map- which is created as two dimensional histogram of the events with multiplicity m=2 resulting from collisions of Bi clusters with Ar^{8+} at the energy of 120 keV.The X-axis represents the time-of-flight of the first recorded cation and the Y-axis represents the time-of-flight of the second cation. The color represents the intensity of the specific event. The full scale of the TOF from 0 to 480 μs corresponds to n/q=0 to n/q=340 ($Bi_{n=0}^{q+}$ to $Bi_{n=340}^{q+}$).

The fact that the first event is always correlated with a shorter time-of flight TOF1 and the second event having always a longer time of flight TOF2 implies that the 2D map has only events above the diagonal line with slope of 1. For the interpretation, one can select on the TOF1 scale a given time-interval representing a specific Bismuth cluster fragment with n'/q' and follow on the corresponding vertical line all larger $n''/q''>n'/q'$ coincident fragments. On the other hand, to determine correlations with fragments n'/q' smaller than the initially chosen n'/q' one has to follow the horizontal line given by this n/q value on the TOF2 axis.

Furthermore, one can zoom into the 2D map to investigate mass coincident spectra in more detail. In the lower part of the fig.5.18 a zoom into TOF1 :20 to 90 μs and TOF2 :0 to 480 μs is made showing very clear vertical blue lines - corresponding to coincident events of Bi_1^+ up to even Bi_8^+ with larger cluster ions. One observes that the intensity and the widths of the spectra is different for different fragments. For Bi_1^+ and of Bi_3^+ the signal spans over almost the whole range of time-of-flight (n/q from 0 to 300), while for the other fragments like Bi_2^+ and Bi_4^+ to Bi_8^+ are of significant intensity only for smaller sizes of the coincident larger residue.

5.1.2.3 Correlation with small fragments

To study the fragmentation dynamics in more detail from the 2STOP coincidence spectrum, I concentrated mostly on the correlations with Bi_1^+ and Bi_3^+ fragments because of their high intensity. However correlations with other "energetic" fragments were partially investigated as well. Fig.5.19 represents the abundance spectrum of Bi_n^{q+} clusters detected in coincidence with Bi_1^+ (red line) and Bi_3^+ (blue line), in the time-of-flight domain up to 450 μs reduced to binning of 100 ns. Fig.5.19 consists of two separate graphs: the left one showing smaller clusters,up to Bi_{17}^+ and right one, spanning from n/q = 20 up to n/q =100. Note the significant difference in the intensity of small and large Bi clusters. Small fragments dominate larger clusters in intensity by a factor more than 100 (comparing the intensity of Bi_1^+) and $Bi_n^{q+}(n/q = 30)$ for example). This indicates that the signal of the monomer and trimer fragments is related to a broad distribution of multiply ionized clusters.

By comparing the relative peak intensities in the spectra of monomer and trimer in coincidence with other small residues up to Bi_{17}^+ (left part of Fig.5.19), one can clearly see that the most abundant peaks are correlated with Bi_1^+ to Bi_7^+ . For the case of fragments correlated with the monomer, the relative intensities of peaks decrease with increasing cluster size by a factor of 10 from Bi_1^+ to Bi_7^+. Also, the distribution of the second fragment has its maximum at Bi_1^+. For the correlations with trimer, the distribution of the second fragment is rather

flat with the exception of the monomer, that also dominates the spectrum. For correlations with larger clusters, the spectrum (right part of Fig.5.19) differs significantly. Although the intensity maxima of both distributions occur in a similar range, the monomer spectra is shifted more towards smaller n/q values concentrated mainly within n/q=20 and n/q=50, whereas the trimer spectrum extends easily with significant count number above n/q=50 and drops at around n/q=95.

This shows that signal of monomer and trimer comes from the broad distribution of multiply ionized clusters and not particular given size and/or charge. Also, the difference of the intenisty of small fragments correlated with monomer and trimer would suggest different fissilities of parent cluster.

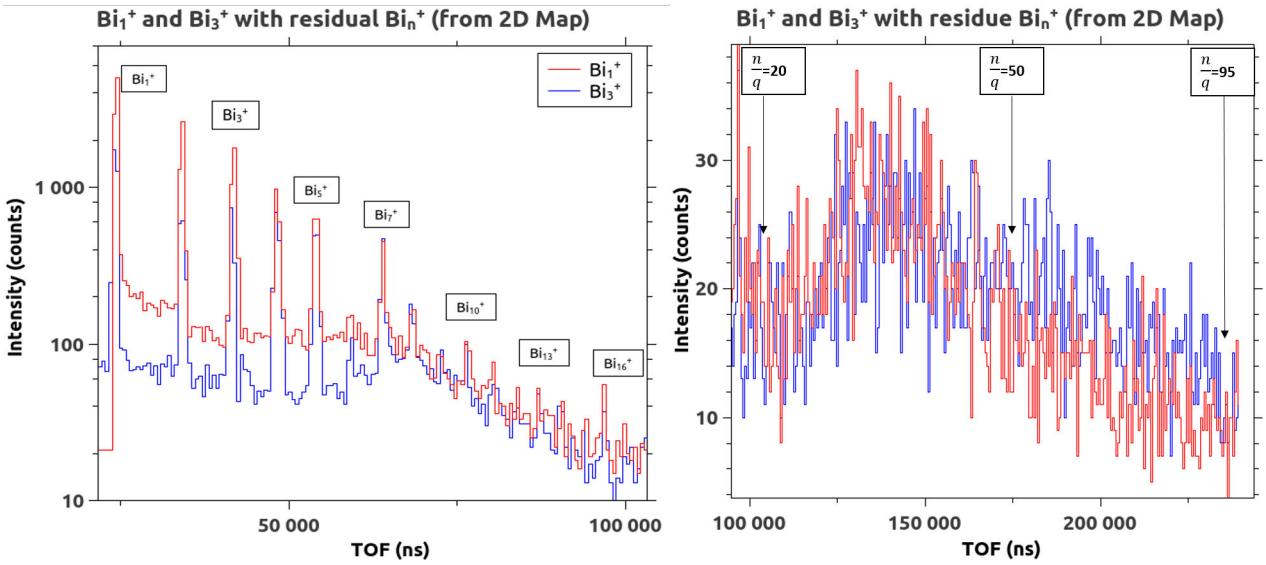

Figure 5.19 *Correlations with the monomer Bi_1^+ (red curves) and Bi_3^+ (blue curves (residual shiuld be changed into residue; TOF (ns) should be changed into n/q))*

In a similar manner one can set-up coincidence spectra for other fragments. Correlations of each fragment from Bi_1^+ to Bi_7^+ (exception Bi_6^+ the intensity of which is very low) with larger residues are presented in fig.5.20 for 3 different TOF (n/q) regions.

For n/q $<$ 15 the distribution correlated with the monomer ion is strongly peaked at the monomer although dead time effects reduce the intensity. However due to the large peak width 2 monomer ions can be easily detected. With increasing fragment size the distribution of the second ion shifts to larger sizes, thus, for the heptamer one can clearly observe distinct peaks of nearly equal intensities from n/q=8 up to n/q=16. There is a tendency, that when two small fragments are observed their sizes become similar. Concerning the correlations with large residues, the position of the intensity maxima shift to smaller residue sizes when the fragment size is larger, for example for the heptamer the narrow n/q distribution is centered at low n/q values (maxima for n/q=25 and n/q=30). The wide extension, in particular for the monomer

and trimer ion towards large residues, is explained by the higher charge states of the initially formed clusters with high fisilities leading to the emission of very small fragments in asymmetric fission processes (see discussion further below).

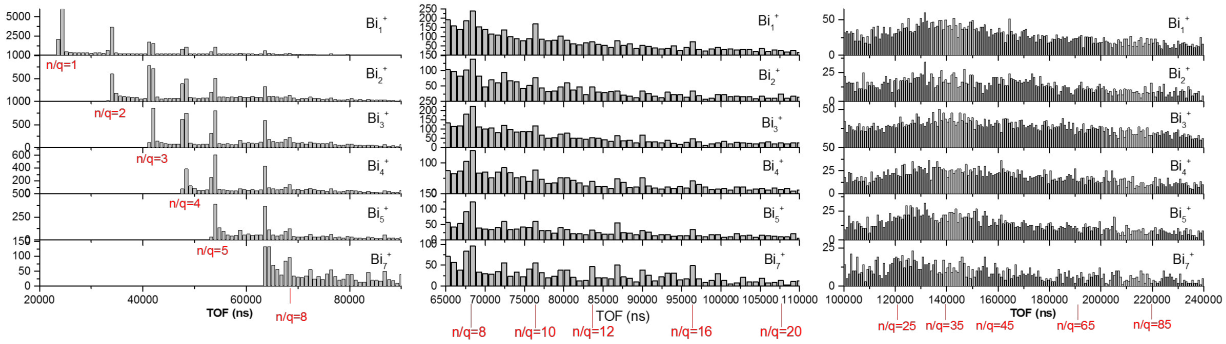

Figure 5.20 *Correlations of small Bi_n^+ fragments with larger residues.*

5.1.3 Kinetic Energy of $Bi_{1,3}^+$ in coincidence with Bi_n^{q+}

As it was mentioned previously, Bi_1^+ and Bi_3^+ were chosen for the closer analysis as they represent the most intense species resulting from fragmentation processes. Furthermore, their emission plays an important role in the stabilization of unstable multiply charged clusters.

In order to investigate the dynamics of Bi cluster fragmentation in greater detail we come back to the 2STOP coincidence map and study the peak form of Bi_1^+ and Bi_3^+ signals correlated with larger n/q residues. Fig.5.21 shows the full coincidence map with horizontal cuts at given n/q values (TOF ranges). The red dashed vertical rectangle is amplified in figure to the the right. It presents correlations between Bi_3^+ and larger residues showing a characteristic V-shape in TOF domain. The horizontal distance of the two branches increases with the n/q value of the residue (TOF2). Depending on the count number in terms of statistics, the first 8 horizontal cuts have been made with a constant width of 10 μs in the TOF2 domain, the next 4 cuts with a width of 50 μs. The counts present in the different cuts were integrated in the TOF2 domain (residues) and are represented as number of counts in the TOF1 domain. In this way we can study the shape/form of a given fragment Bi_1^+ and Bi_3^+ in correlation with a given n/q residue size. The left part of figure 5.22 shows the peak form for the case of the monomer, the right part for the trimer in correlation with Bi_n^{q+} residue clusters characterized by n/q = 89-97 (TOF=230-240 μs).

The peak forms are not a simple gaussian/lorentzian curve that one usually observes in mass-spectra, but they are structured. For coincidences with the trimer (right part) two distinct maxima are observed, that are well separated from each other, resembling in their form two separate peaks. The peak form differs strongly from that one reported in fig.5.11 for the case of the inclusive spectrum.

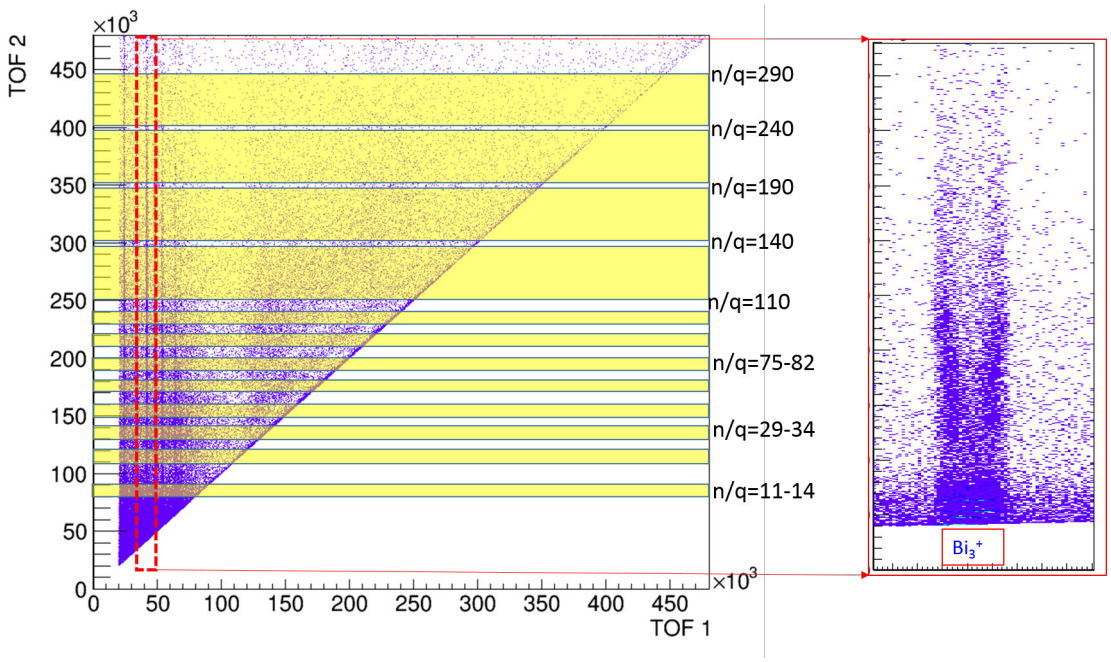

Figure 5.21 *2D coincidence map with the selected n/q regions (marked in yellow) taken for further analysis of coincidences. In the right side the zoom into the map showing the correlation of Bi_3^+ with all other fragments n/q >3.*

As discussed before, the Bi_3^+ peak contains mainly a forward and a backward peak, corresponding to a kinetic energy distribution of 5.5 eV with a halfwidth +/- 1 eV. This can be verified by SIMION calculations. The characteristic feature of the spectrum in fig.5.22 b) shows, that the trimer fragments measured in correlation with residues of n/q=90 to 98 are always emitted with high kinetic energies; no significant low-energy component is observed.

This is different in the case of the Bi monomer (figure 5.22a) and figure 5.23a)). Also for the monomer we observe as indicated by with blue dashed line a wide distribution with δToF$\sim$900 ns that corresponds to a kinetic energy of 6eV. However, we observe a further structure in the middle between the two most energetic peaks, which corresponds to low-energy fragments with mean kinetic energies of 0.4 eV +/- 0.2 eV. These three peaks are also well reproduced by the SIMION simulations as shown in 5.23a).

A tentative explication of the results is as follows. Whereas the high-energy fragments are attributed to fission processes of multiply and highly charged cluster ions, formed by multi-electron capture, yielding a larger variety of small fragments (monomers up to heptamers), the low energetic monomer ions have to be attributed to another process. One possible explanation might be based on the sputtering process, where predominantly monomer ions are emitted from the cluster surface in close collision, characterized by kinetic energy below 2 eV.

The described method allows to study the peak form of a given fragment (like Bi_1^+) in coincidence with another larger residue (identified by its n/q ratio) and to determine its kinetic

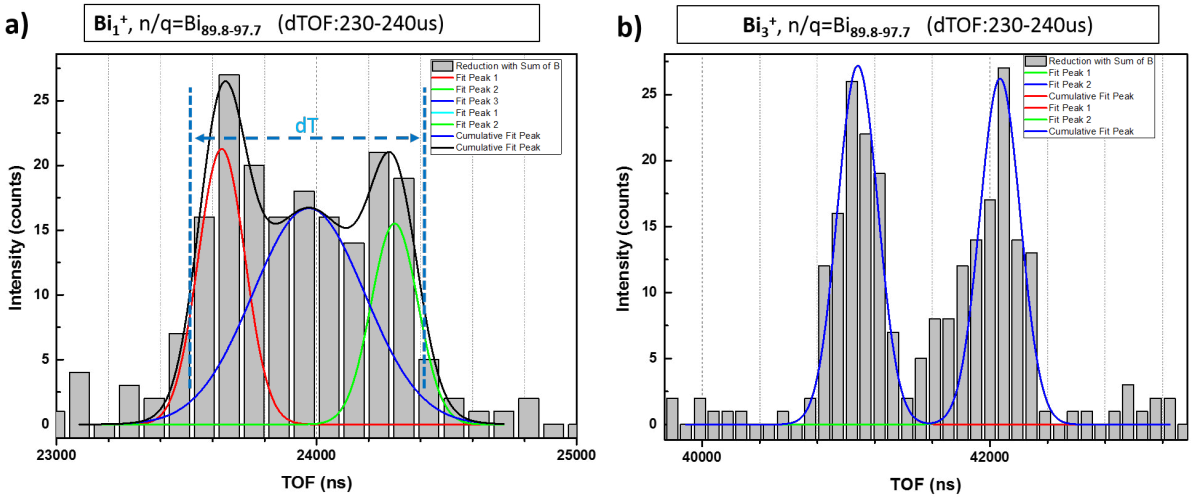

Figure 5.22 *Peak forms of the Bi_1^+ (a) and the Bi_3^+ trimer (b), measured in correlation with Bi_n^{q+} residues in the n/q range between 89 and 97.*

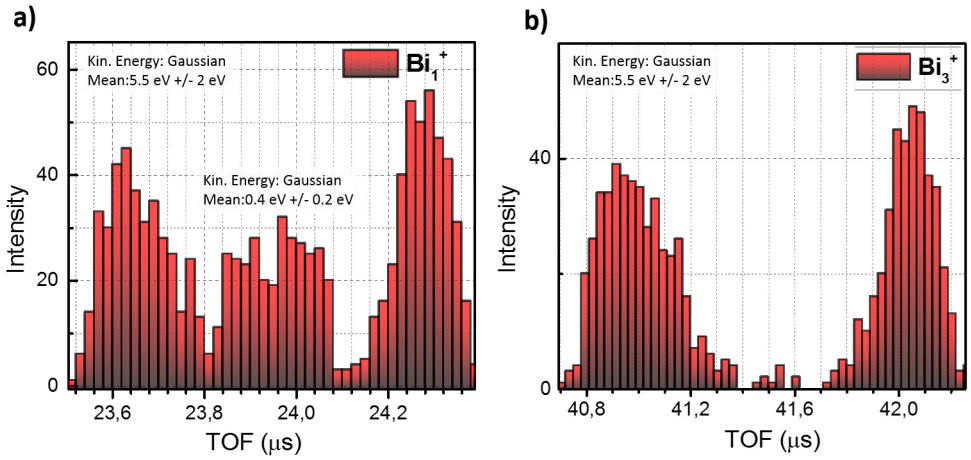

Figure 5.23 *Peak forms simulated with the SIMION program for the Bi monomer with two kinetic energy gaussian distributions and b) for the trimer with one kinetic energy gaussian distribution.*

energy and the energy release of the process as a function of the residue size n/q.

In Figure 5.24 we show the variation of the peak form of the Bi_3^+ fragment measured in correlation with a residue cluster in the n/q range from 11 to 355. We observe that at small n/q values the hole in the distribution is filled up. This may have to reasons: 1) the kinetic energy of the trimer becomes slightly smaller and, thus, the transmission increases; 2) as already discussed above, at very small n/q values fragmentation processes occur with low energy release which are probably due to the fission of doubly charged clusters. Probably both phenomena contribute. For the largest values of n/q of the residues, again low energy contributions are

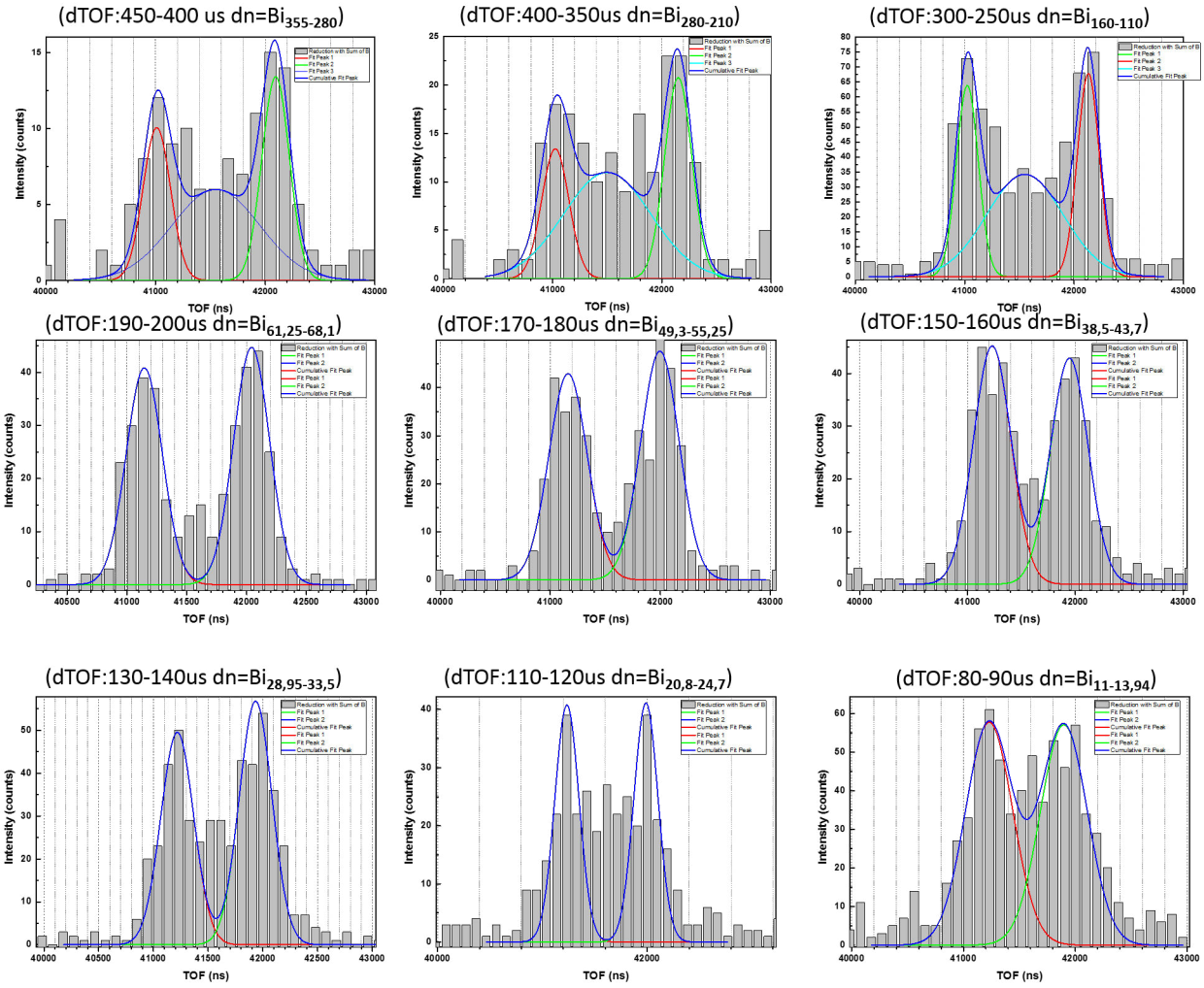

Figure 5.24 *Variation of the Bi_3^+ trimer peak form as a function of the size/charge of the heavy residue. n/q varies from 11 to 355.*

observed, which might be linked to sputtering phenomena, which become more important due to the increasing cluster size.

In Fig.5.25 the results for the monomer Bi_1^+ are shown for the same n/q values of the residues. In this case always high and low energy monomers are observed.

Using the above described procedure of fitting and decomposition into forward and backward peaks, the kinetic energy of Bi monomer and trimer was determined for coincidences with the residues with n/q>11. The results are shown in fig.5.26. The Y axis represents the kinetic energy of the small fragment (black squares for Bi_1^+ , red points for Bi_3^+) and the X axis represents the ranges of the correlated residues. The given kinetic energy values correspond to the most likely values of the „high-energy" distribution.

For the monomer, coincident with clusters of n/q 11.0 to 44, the kinetic energy is found to be E_{kin}=5.5 +/- 0.2 eV. The observed kinetic energy rises with increasing n/q values to

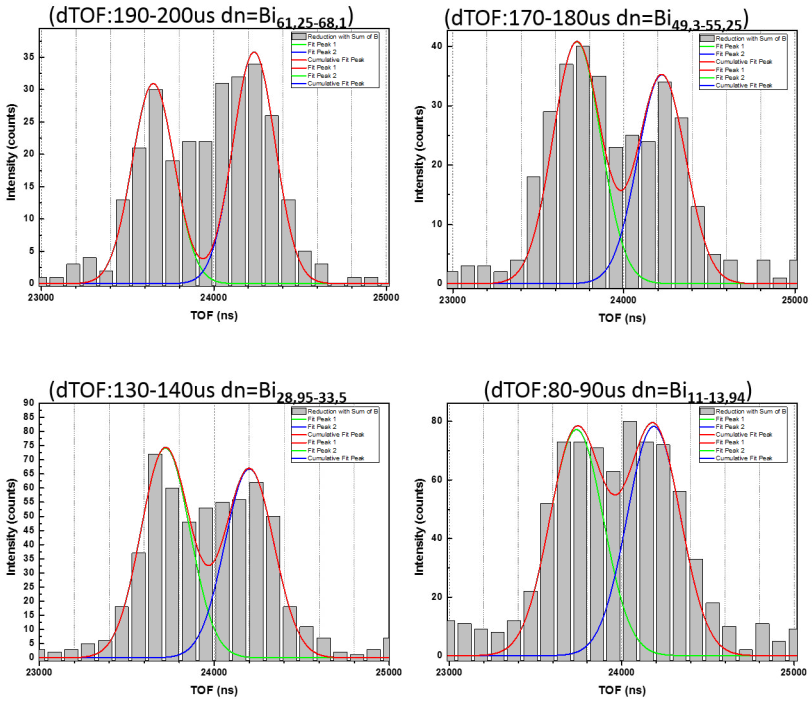

Figure 5.25 *Variation of the Bi_1^+ monomer peak form as a function of the size/charge of the heavy residue. n/q varies from 11 to 62.*

values of about 7 eV. (It should be noted, that a „low" energy distribution is always present as discussed before).

For the case of the Bi trimer, the kinetic energy constantly rises. For n/q∼11 up to n/q∼33 the kinetic energy is of the order of E_{kin} ∼3-3.5 eV, for the highest n/q values a value of ∼5.5 eV is obtained.

The given values are the kinetic energies of the small fragments, however, another part of the energy release KER is given to the residue ion. In the present case, the monomer receives 91 % of the KER for the correlation with residue of n/q = 11, which increases to 99% for n/q= 100. Thus, a slight increase of the kinetic energy of the monomer is caused by the increasing residue mass. In the case of the trimer, the percentage increases from 73% to 97%. This cannot explain the increase of the kinetic energy with n/q, and we conclude that also the energy release KER increases with the size (n/q) if the residue increases.

5.1.4 Kinetic energies and fission channels

5.1.4.1 Binary fission of Bismuth clusters

Small fragment ions are very intense and the fact that they are measured in coincidence with small, as well as with large residues, shows, that fission of Bismuth clusters is a strongly

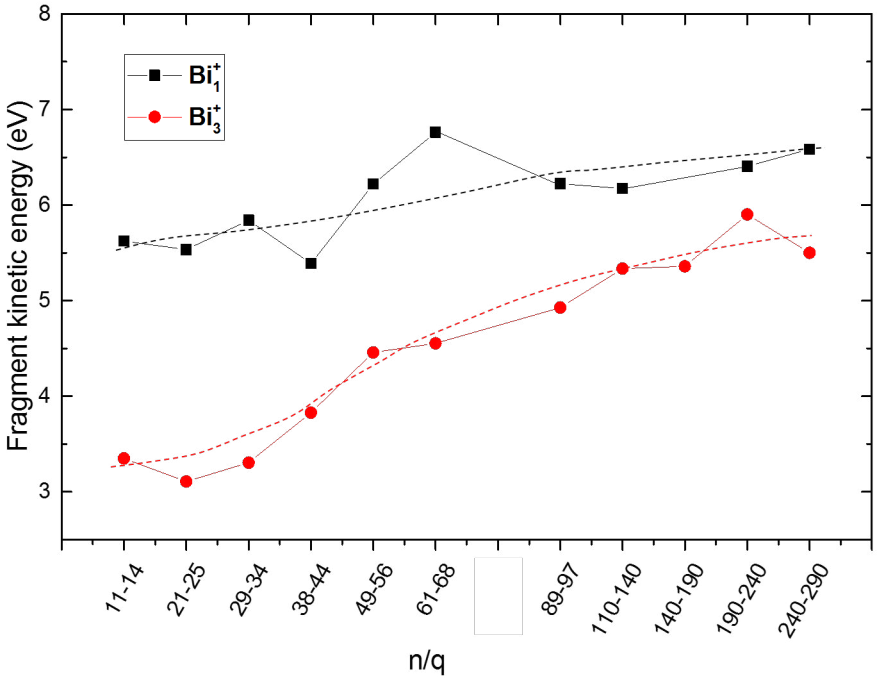

Figure 5.26 *Most likely kinetic energy (high-energy component) of the monomer and trimer fragments as a function of n/q value of the residue ion (dashed lines for better eye-guiding).*

asymmetric process, as observed for other metal clusters like K or Na [76].

In order to analyze and explain the mass spectra as well as the observed fragmentation energetics for collisions of Bismuth clusters with Ar_8^+ at 120 keV, we will come back to the stability diagram for multiply charged Bi clusters shown in fig.5.7. Fragmentation of multiply charged clusters occurs for fissilities above X=0.3 according to the following scenario:

1) Bi clusters are ionized by projectiles into charge states where the ratio of n/q is such that the fissility of the cluster X exceeds X∼0.27 (X=0.27 is the fissility determined from our experiment corresponding to the appearance sizes). Furthermore, we assume that X is still below 1 (critical size), so that the system shows a finite fission barrier. Different cases can be considered. If the internal energy of the cluster E_i is lower than the barrier energy for the emission of a charged particle (fission barrier) E_b, but still higher than the final energy of the system after fragmentation E_f

$$E_f < E_i < E_b \tag{6}$$

the system which has finite temperature is meta-stable. In practice the meta-stability of Bismuth clusters can be further specified concerning a decay by evaporation of neutral atoms or by the emission of charged particles (fission). Both mechanisms compete with each other. Summarizing, there are 3 conditions for cluster stability:

a)spontaneous fission occurs: $E_B<E_i$
b)metastable with respect to fission: $E_i<E_B<E_v$
c)metastable with respect to evaporation: $E_i<E_v<E_B$

When fission occurs and when the residue ion with the reduced charge is stable we call the process a binary fission process, as one complex particle decays into 2 charged sub-particles. In addition to the n/q values of the products, it is the kinetic energy release (KER) which characterizes the process. The ionized cluster has to be excited to overcome the energetic barrier and to perform the required deformation or elongation. Thus, one may assume that also after separation of both charged particles, which is dominated by Coulomb forces, the fragment and in particular the residue are vibrationally excited. Therefore, in a coarse approximation we can equate the KER value with the Q-value of the reaction and compare it with experimentally determined corrected kinetic energies of the fragments.

As described before, the kinetic energies of the monomer observed in correlation with residues with $10 < n/q < 40$ vary between $E_{kin} = 5$ eV and $E_{kin} = 6$ eV. In addition, as it was seen on fig.5.22, monomer fragments with lower kinetic energies contribute as well to the overall peak form. In the case of Bi_3^+ the kinetic energy in correlation with the same residue size/charge range yields values of E_{kin}=3 eV to E_{kin}=4 eV.

Fig. 5.27 shows the calculated Q values (difference of the energy between the initial and final state of the system, using the liquid drop model). The Q values were calculated for the emission of the monomer and trimer as a function of the size of the initial intact system (n=number of atoms, n=10 to 250) for various charge states ranging from q=2 up to q=15 (fig.5.27 a and b).

In the present part we discuss fissilities of X<1. In fig.5.27 a) and b) large blue balls connect the n/q points which correspond to X=1, while black ones correspond to the appearance size. Therefore, we will consider only systems which are below this curve. As an example I regard the case of the emission of the Bi_3^+, where the characteristic energy observed in the experiment was E_{kin}=3.5 eV. If we assume this value to be equal to Q ($Q = E_{kin}$), we can identify the following possible initial Bi cluster systems: Bi_{35}^{4+} (X=0.57), Bi_{80}^{5+} (X=0.45), Bi_{140}^{6+} (X=0.37), Bi_{200}^{7+} (X=0.31). All of the mentioned systems are metastable and can decay by the emission of a trimer with the energy of $E_{kin} = 3.5$ eV. However, if the deposition of the energy during collision is not negligible, the system may shrink by evaporation of neutral atoms until the point, where the fission barrier will be low enough to emit another charged trimer. As an example in the tab.3 illustrates fragmentation of clusters with X=0.35-0.3 for sizes n=200-230 atoms in the cluster with q=7. The fissility is very low and close to the value for the appearance size, therefore, the decay with the emission of only one charge is expected. Assuming the emission of a Bi_3^+ fragment, the energy attributed is in agreement with the value observed in the experiment. After reducing the charge to value of q=6, the cluster remains stable, unless the temperature of the system is large enough to provoke evaporation.

On the other hand, the kinetic energy of the monomer emitted in correlation with the same

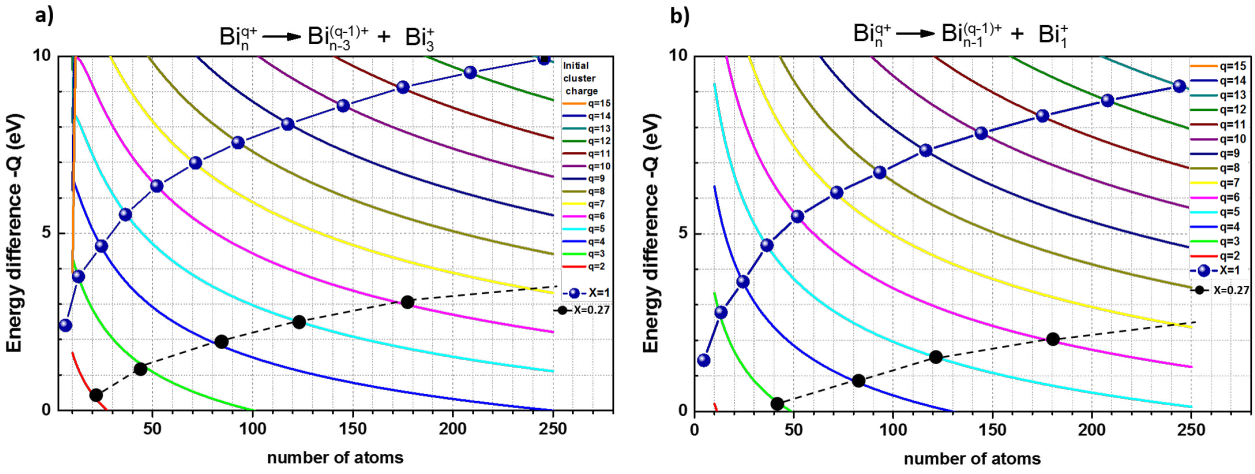

Figure 5.27 *Q-values as a function of the cluster size for given charge states in case of the trimer emission a) and b) monomer emission.*

residues is higher than that observed for the trimer with a value of around $E_{kin} \sim 5-6$ eV. The same procedure as before yields for the initial ionized clusters: Bi_{60}^{6+} (X=0.86), Bi_{100}^{7+} (X=0.71), Bi_{150}^{8+} (X=0.62) and Bi_{220}^{9+} (X=0.53). If we compare both cases (monomer and trimer), the fissilities for the emission of a monomer with such kinetic energy are higher than the fissility values for the emission of a trimer. After emission of a monomer, the residue still has the fissility value of X>0.27, which will lead to further decay processes into charged fragments. We can try to calculate Q values for such a sequential emission processes. In the tab.4 we consider the case of Bi_{100}^{7+} with X=0.71. For the first fragmentation process, emitting a charged monomer, the energy difference of Q=4.98 eV is released and transformed into kinetic energy of fragments, where 99% is taken by the monomer. In the second step, where the fissility X=0.52, we can consider the emission of a monomer or trimer. If a monomer is emitted again, its kinetic energy would be in the range of E_{kin}=3.5 eV, which is compatible with the low energy distribution of monomers. Considering trimer emission, the expected energy of Q=4.5 eV is rather high for trimers measured in correlation with residues of ratios n/q<40. After the emission of 2 monomers, the fissility of the system is still X=0.37 and might result in the emission of a trimer with Q=3.0 eV and a residue characterized by n/q 23, which is in agreement with observed data.

We have to note, that the scenario described in Table 4 has some drawbacks. On the one hand, for a high detection efficiency the just described event should be observed only in a 4STOP spectrum (3 fragments and 1 residue). However, we know that the efficiency is rather low under the present conditions and that therefore also events with 4 charged particles can contribute to the „2STOP" spectrum. Furthermore, Q-value calculation are based on 2 particle decays. Therefore, the discussion above is only „valid", when the emission of fragments occurs well separated in time, i.e. in a sequential manner. On the other hand, the measured kinetic

Fragm. step	Initial size of $(Bi)_n^{q+}$	Inital charge $(Bi)_n^{q+}$	Fissility X	Fragm. channel	Stability	Final size	Final charge	Ratio	Q (eV) – energy between final and initial states (~Kinetic energy of fragments)
Step 1:	n=200-230	q=7	X=0,35-0,31	**Bi_3^+**	Metastable ($n<n_{app}$ for q=7)	n'=197-227	q'=6	n'/q'~33-38	**Q=3,8-3,5 eV**
Step 2:	n=197-227	q=6	X=0,24-0,26		Stable ($n>n_{app}$ for q=6)			n'/q'~33-38 (observed on MS)	

Table 3 *Fragmentation scenario for $Bi^{7+}_{200-230}$clusters.*

Fragm. step	Initial size of $(Bi)_n^{q+}$ cluster	Inital charge $(Bi)_n^{q+}$	Fissility X	Fragmentation Channel	Stability	Final size	Final charge	Ratio	Q (eV) – energy between final and initial states (~Kinetic energy of fragments)
Step 1:	n=100	q=7	X=0,71	**Bi_1^+**	Metastable ($n<n_{app}$ for q=7)	n'=99	q'=6	n'/q'~18	**Q=4,98 eV**
$Step2_a$: $Step2_b$:	n=99 n=99	q=6 q=6	X=0,52 X=0,52	**Bi_1^+** **Bi_3^+**	Metastable ($n<n_{app}$ for q=6)	n'=98 N'=96	q'=5 q'=5	n'/q'~20 n'/q'~19	**Q_a=3,50 eV (ok)** **Q_b=4,50 eV (not-observed in experiment)**
Step 3:	n=98	q=5	X=0,37	**Bi_3^+**	Metastable ($n<n_{app}$ for q=6)	n'=95	q'=4	n'/q'~23	**Q=3,01 eV**
Step 4:	n=95	q=4	X=0,23	-	Stable ($n>n_{app}$ for q=4)	-	-	n'/q'~23 (observed on MS)	

Table 4 *Fragmentation scenario for Bi^{7+}_{100}clusters.*

energies are only the centroids of a distribution, making the choice of the decaying state less definitive.

5.1.4.2 Simultaneous emission of small fragments, X>1

The processes of binary fission as described before cannot explain the kinetic energies observed for correlations with much larger n/q residues (n/q>50). High kinetic fragment energies require a high charge state of the intermediate cluster ion and the high n/q value of the produced residue ion require also a large size n of the initial cluster. Thus, n as well as q must have large values before fragmentation. By Q value calculations and by assuming that only one charged trimer with Q=E_{kin}=5 eV is emitted, one would have to conclude that the initial clusters have to contain around 3000 atoms and must be ionized at least 30 times in order to reach the range of n/q=100. Both is extremely unlikely because the charge of the projectile is only 8+ and the initial size is only n∼300. Therefore, a different mechanism has to be involved which might be linked to ionized cluster systems with X>1, where no fission barrier is present anymore. In such a situation the cluster is highly unstable and provokes a rapid explosion, so-called Coulomb explosion or scission, characterized by a significant reduction of its charge state and fragmenting into many small particles. It is possible to ionize clusters into charge states q>8 with Ar^{8+} projectiles and to form systems with X>1, due to contributions from Auger processes occurring in the projectile frame during the collision.

Figure 5.28 presents the results of Q calculations in a 3D graph for the case of Bismuth clusters with n=200 atoms ionized q=12 times. The X-value of the system is 1.03. The z-axis shows the Q energy, the X-axis describes the size of the smaller fragments while the Y-axis describes the number p - being the number of emitted fragments. In these calculations one might assume, that the fragmentation pathway follows the sleepest slope on the calculated energy surface as no barrier is present.

First of all, the energy surface obtained from calculations can be decomposed into separate lines for given Bi_x^q fragment. If we consider that Bi_{200}^{12+} decays with the emission of Bi_1^+ fragments the minimum Q=-40 eV occurs for p=8∼9 fragments and the charge state of the final residue is 3 to 4. Therefore, the average energy of monomer fragments is around 5 eV and the final cluster ratio n/q∼ 48-60, which could explain the observed experimental data. On the other hand, considering the emission of only trimers, the Q values drops even further down to Q -48 to -50 eV but the number p of fragments shifts to p=9,10. In this case the average kinetic energy for the emitted fragment is E_{kin} ∼5 eV that would correlate with residues of n/q∼85,as $n' = 200 - 30 = 170$, $q' = 12 - 10 = 2$, $n'/q' = 85$. Multifragmentation normally can yield fragments with different sizes, however the fragment size does not exceed a few atoms.

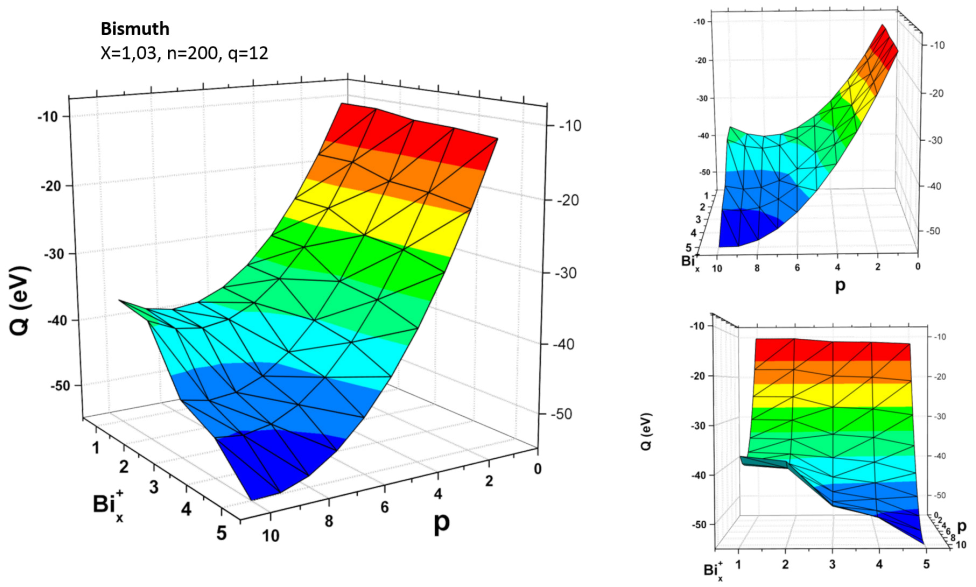

Figure 5.28 *3-dimensional representation of the energy surface of the system Bi_{200}^{12+}. p = number of emitted small singly charged fragments; other axes: fragment size between 1 and 5; vertical axes: energy values Q.*

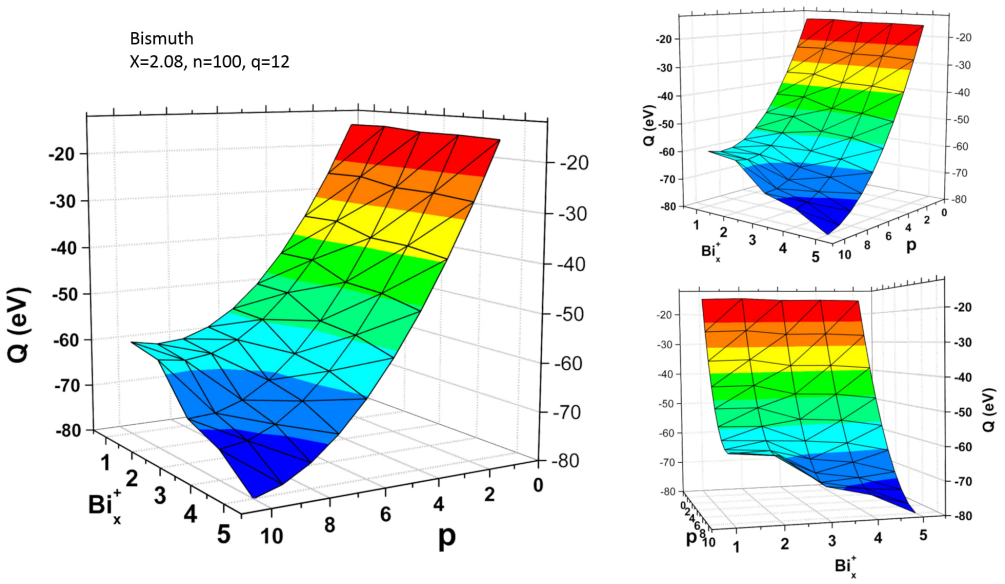

Figure 5.29 *3-dimensional representation of the energy surface of the system Bi_{100}^{12+}. p = number of emitted small singly charged fragments; other axes: fragment size between 1 and 5; vertical axes: energy values Q.*

The graphs in fig.5.29 clearly show that the emission of 4-mers and 5-mers is associated with even lower values of Q, and can explain why such fragments are observed in the spectra as well. We have to mention that the fragmentation path is not only governed by energetic aspects, but it is to be expected that also entropic aspects play an important role in the preformation of larger fragments, which might explain the dominance of monomers and trimers in the experimental sepctra.

In Fig.5.29 a second example is showing a system with much higher fissility (Bi_{100}^{12+} , X=2.08). In this case, the Q values are much larger, the minimum for the emission of monomers occurs at p=8 with value Q_{min}=-62 eV (7 to 8 eV per monomer). For the trimer the average kinetic energy is of 6.5 eV with the emission of 10 fragments.

5.1.4.3 Coincidence islands in the region of small fragments

The investigation of the mutual correlations between small fragments yields valuable information about the dynamics of fragmentation processes. Therefore we decided to analyze the magnified region from the 2D map (see the red frame inset in the bottom right corner of the figure 5.30) displaying TOF1 and TOF2 in the range of 20 to 50 μs corresponding to all ion pairs (A,B) with n= 1 to 5. Each visible island represents events, where fragment A arrives in coincidence with fragment B. As to be seen in Fig.5.30 the shape of each island is different due to different dynamics and mechanisms governing the fragmentation processes. The islands can be decomposed into several main components - for example smaller "sub-islands". Looking from the perspective of TOF1 domain we see two clearly separated regions with clear maxima, whereas in TOF2 domain we would observe mostly only one single maximum.

Before analysing the island forms in more detail, we have to mention that the sum of both fragment masses shown in fig.5.30 is below the mass of the decamer Bi_{10}^{+}. As these clusters are not present in the primary cluster beam, the fragmentation process must include the emission of at least one third fragment, either neutral or charged. Thus in general, the momenta of those fragments, which are not detected, have to be considered as well, limiting the information from 2-particle coincidences.

Fig.5.30 shows the correlation between Bi_1^+ to Bi_4^+ with Bi_2^+ to Bi_5^+. First of all, all the islands differ from each other in terms of their geometry/topology, often they maintain "butterfly"-like shapes.

Looking at correlations of the Bi_5^+ fragment with all other smaller fragments (horizontal line) one can see, that the vertical width of the islands and hence the kinetic energy of the Bi_5^+ fragment increases with increasing size of the second correlated fragment. The separation of the two sub-islands belonging to forward-backward peaks is increasing in the TOF2 scale, while it keeps approximately the same distance in the TOF1 scale.

Fig.5.31 shows the change of the most probable kinetic energy which is deduced from the island widths (obtained in the same way as kinetic energies in subsection 5.1.1.6) of the tetramer and the pentamer as a function of the second coincident detected smaller fragment. Fig. 5.31

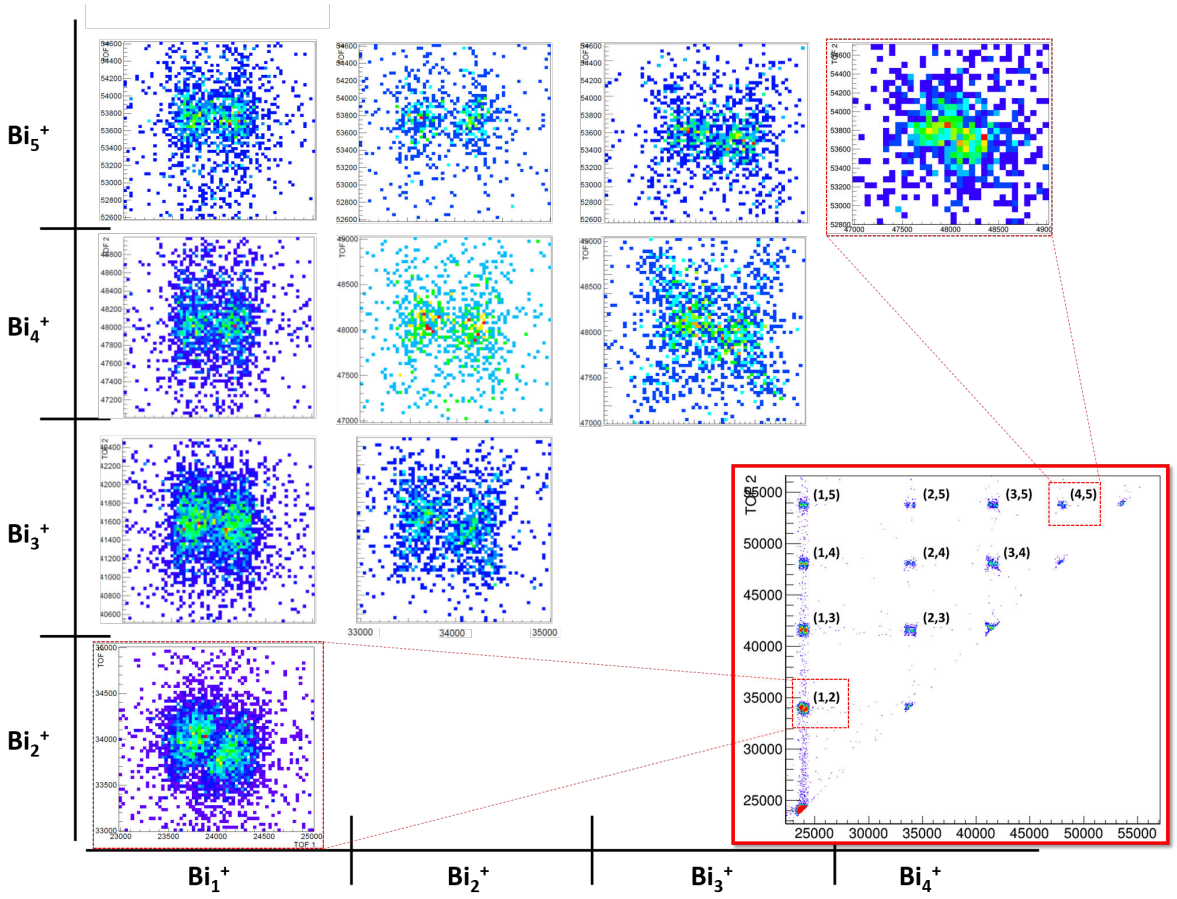

Figure 5.30 *Correlation islands for small Bi fragments. The red frame inset in the bottom right is a maginified region of 2D map, from which the correlation islands were extracted in higher detail.*

a) shows that for Bi_5^+, the kinetic energy is E_{kin}=0.34 eV when measured in correlation with the monomer, and systematically increases up to 0.7 eV when measured in correlation with Bi_4^+. As Bi_5^+ is the larger fragment in the correlation pairs, it receives a smaller fraction of the total KER, in particular if the second fragment is much lighter, i.e. for the correlations of the pentamer with the monomer. At the same time, the energy of the smaller fragment from correlation pair decreases from E_{kin}=5.5 eV for Bi monomer down to E_{kin}=1.5 eV for the bismuth tetramer.

On the one hand, we observe that the sum of the energies for a pair of fragments in general decreases with increasing total mass of both fragments. Albeit the absence of a third undetected fragment, this might indicate, that the pairs originate from parent clusters with increasing size or decreasing initial charge.

On the other hand, the different dependencies of the kinetic energies of the Bi_5^+ fragment, which increases, and of the smaller fragments, which decrease with increasing total mass of both fragments, are partially linked to the mass ratio of both fragments.

This similarity might indicate that in the present case where more than two fragments are involved, for example a third fragment might have a much larger mass and therefore might take only a small part of the KER, leading to a "quasi"-2 fragment system. This is likely, as the detection efficiency for heavier residues is expected to be smaller due to their heavy mass.

As shown in fig.5.31 b) a similar increase and decrease of the corresponding kinetic energies is observed for the case of correlations with Bi_4^+ fragments.

In the following we will analyze the shape of the correlation islands with the aid of schematical island shown in fig. 5.32. The TOF mass spectrometer yields sensitive information on the velocity and the time-of-flight along the spectrometer axis (z-axis). Therefore, we can distinguish in the island contributions from particles possessing momentum vectors mutually aligned. In the upper right corner of figure 5.32, two particles arrive both delayed - contributing to the so-called backward peak - which means that during the fragmentation both momenta were pointing in the same, "out-of-detector" direction. Going along the diagonal line through the center of the graph towards the lower left corner, the situation is the same but now the momentum vectors were directed towards the detector- both ions contribute to the forward peak. In the upper left corner (lower right corner) the momentum vectors of both fragements are pointing in opposite directions, which means that the fragmentation is indeed a process where the heavier particle is emitted downwards and the lighter one upwards. Following the diagonal line towards the center, directions of the momenta remain the same but their magnitudes decrease, until the central point is reached where the velocity vector has no longer a component along the z-direction.

In the following section we will examine in larger detail three examples of the islands with the aim to separate and identify dominant fragmentation mechanisms. We have chosen the pairs of (Bi_1^+ ,Bi_2^+),(Bi_1^+ ,Bi_5^+) and finally (Bi_3^+ ,Bi_4^+).

Correlation pair (Bi_1^+,Bi_2^+)

Fig.5.33 shows the correlation of Bi monomer and dimer fragments. In fig.5.33a) the 3-dimensional graph of the intensity is presented, where X, Y axes (in plane) correspond to TOF1, and TOF2 of the monomer and dimer fragments and the Z-axis to the number of counts. One can clearly observe the characteristic separation into two sub-islands corresponding to a forward peak for Bi_1^+ and a backward peak for Bi_2^+ (left part of the island) and inverse for the right part of the island. In between both sub-islands, i.e. at the center of the graph the intensity is very low. This means that in this fragmentation process no Bi_1^+ and Bi_2^+ fragments with very low kinetic energies are formed.

Fig.5.33 b) is a flat projection onto the plane TOF1 and TOF2 of the 3D graph 5.33 a). In addition 1-dimensional projections along the TOF1 and TOF2 axes show cuts through the intensity profile. As to be seen, the average slope of the line passing through the center of both sub-islands is found to be -0.71. According to the scheme shown in fig.5.32 in the main process the two fragments are emitted into opposite directions. However, the average slope does not coincide with a value of -1, which one has to expect for a pure binary fission process. In that case fragmentation occurs into opposite directions with equal momentum and

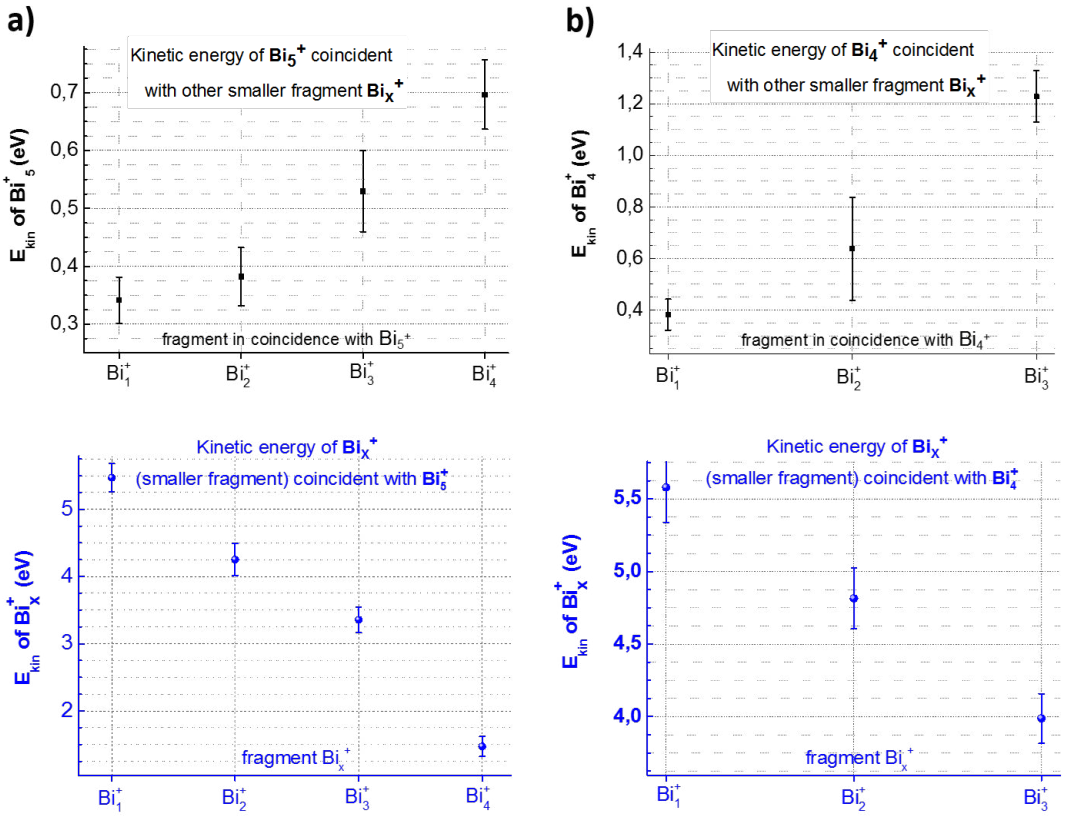

Figure 5.31 *The measured kinetic energies of Bi pentamer (a-upper graph) and smaller fragment Bi_x^+ (a-lower graph) for correlation islands series ($Bi_{x=1-4}^+$,Bi_5^+). b)- the Analogical graphs for series of ($Bi_{x=1-3}^+$,Bi_4^+).*

the corresponding slope is given by

$$slope = -\frac{\delta TOFy}{\delta TOFx} = -\frac{m_2 v_2 q_1}{m_1 v_1 q_2} = -\frac{p_2}{p_1} \times \frac{q_1}{q_2} \tag{7}$$

For equal momenta and charges, this yields the quoted value of -1.

The observation of slope values which are different from -1 indicates that the fragmentation event must involve another, third particle (that may be charged or neutral) which will need to carry the missing momentum. Especially, the 3D or 2D images show, that in addition to the two intensity maxima there are two symmetrically localized broader regions spanned over the angle of ∼150° with relatively large count rates. This indicates that the undetected particles do have a broad energy and momentum distribution, which we attribute to a wide mass distribution of the residual particle.

Correlation pair (Bi_1^+,Bi_5^+)

The second example concerns the correlation between a "lighter" and a "heavier" small fragment, namely the correlation pair (Bi_1^+,Bi_5^+), shown in fig.5.35. Here, the situation is

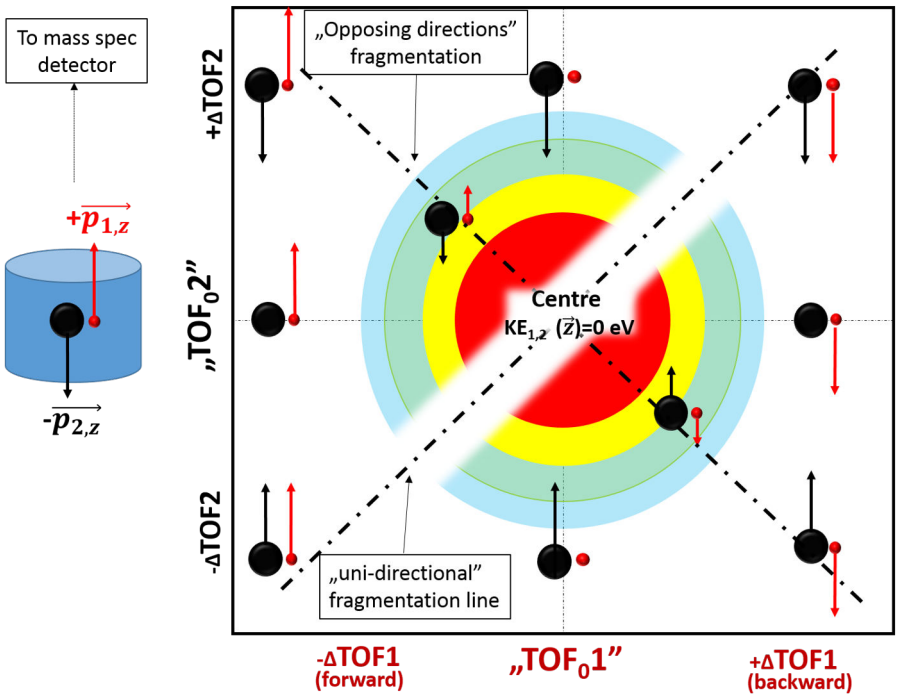

Figure 5.32 *a) Schematic representation of a coincidence island with possible two-body fragmentation scenarios.*

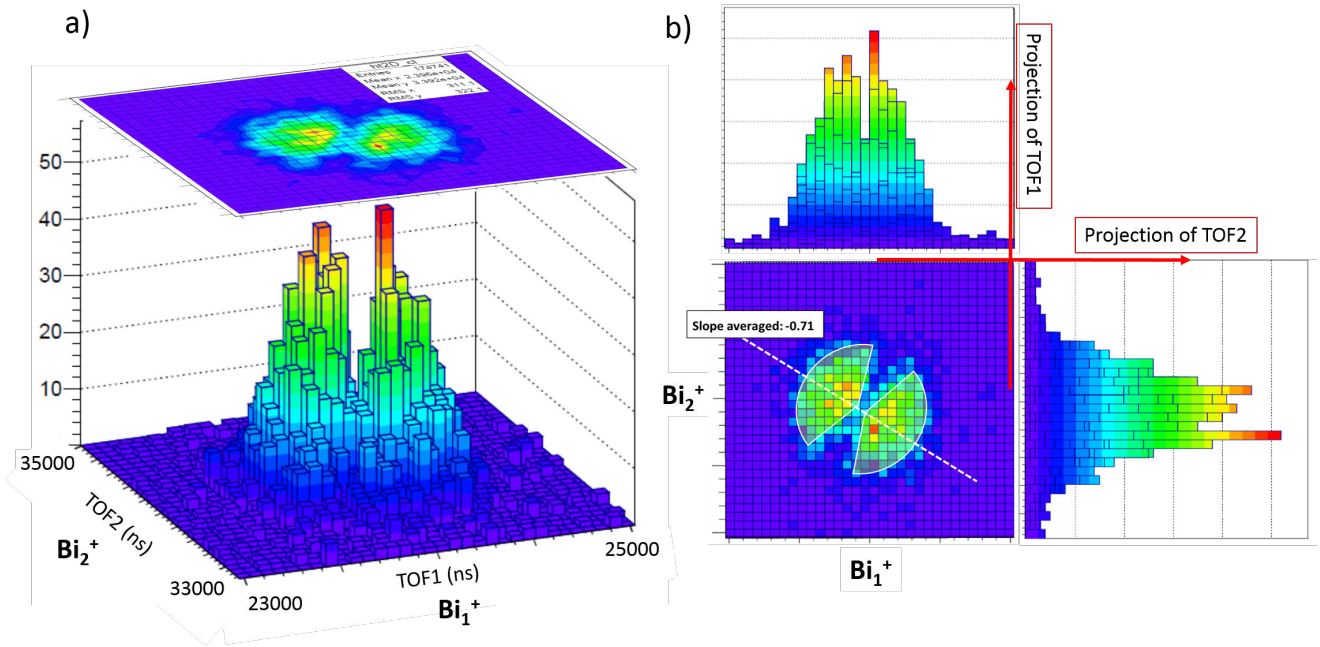

Figure 5.33 *a) 3-dimensional intensity histogram of the island of the correlated pair (Bi_1^+,Bi_2^+), b)2d TOF representation of the same island with horizontal and vertical profile cuts.*

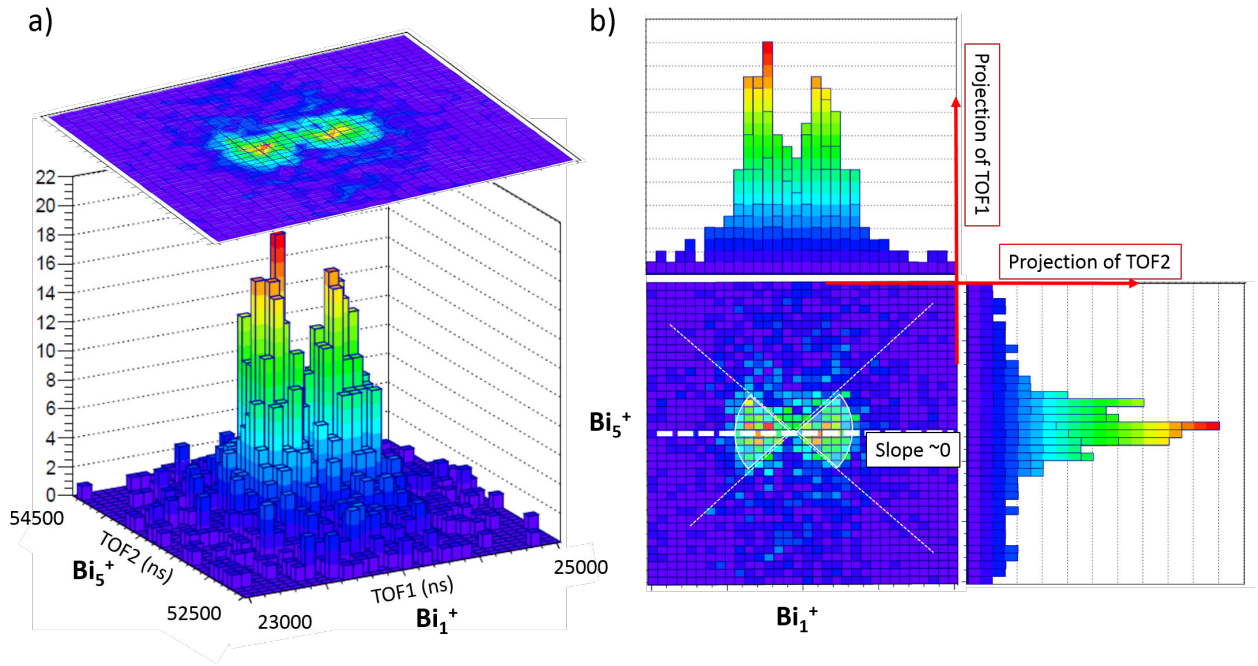

Figure 5.34 *a) 3-dimensional intensity histogram of the island of the correlated pair (Bi_1^+,Bi_5^+), b)2d TOF representation of the same island with horizontal and vertical profile cuts.*

different than in the previous case. Firstly, there are also two separate islands, however, the two clear maxima of forward and backward peaks occur only in the TOF1 domain (Bi monomer). The projection on to the TOF2 axis reveals a very narrow energy distribution (rather a single peak) of the Bi pentamer. This means, as already discussed before, that the monomer is produced with high kinetic energies, whereas the pentamer is rather slow. In consequence the determination of the slope yields a value of ∼0. However, similarly to the previous case, also broader spherical regions around the maxima exist, which is again a sign for contributions from emitted "third" particles. In terms of the energy distribution, we see that at the central spot ($TOF1_0$, $TOF2_0$) a reasonable count number is measured indicating that also slow monomer ions are involved in the formation of this correlation pair.

Correlation pair (Bi_3^+,Bi_4^+)

The last example is devoted to the case of the topology of the island of (Bi_3^+,Bi_4^+) pair. This island has a characteristic star- or butterfly-like form with edges along the diagonal lines. It consists of three different main contributions, indicated by three different "slopes" (1,2,3) shown in fig.5.35:

1). One slope is close to +1 and thus corresponds to the emission of both particles in the same direction, as discussed before. It is clear, that in this case a third particle has to be involved in the process to account for momentum conservation. One of the possible explanations of the uni-directional fragmentation can be related to the semi-metallic/semi-conducting behavior of small Bi clusters. During the electron capture process, positively charged local sides can be

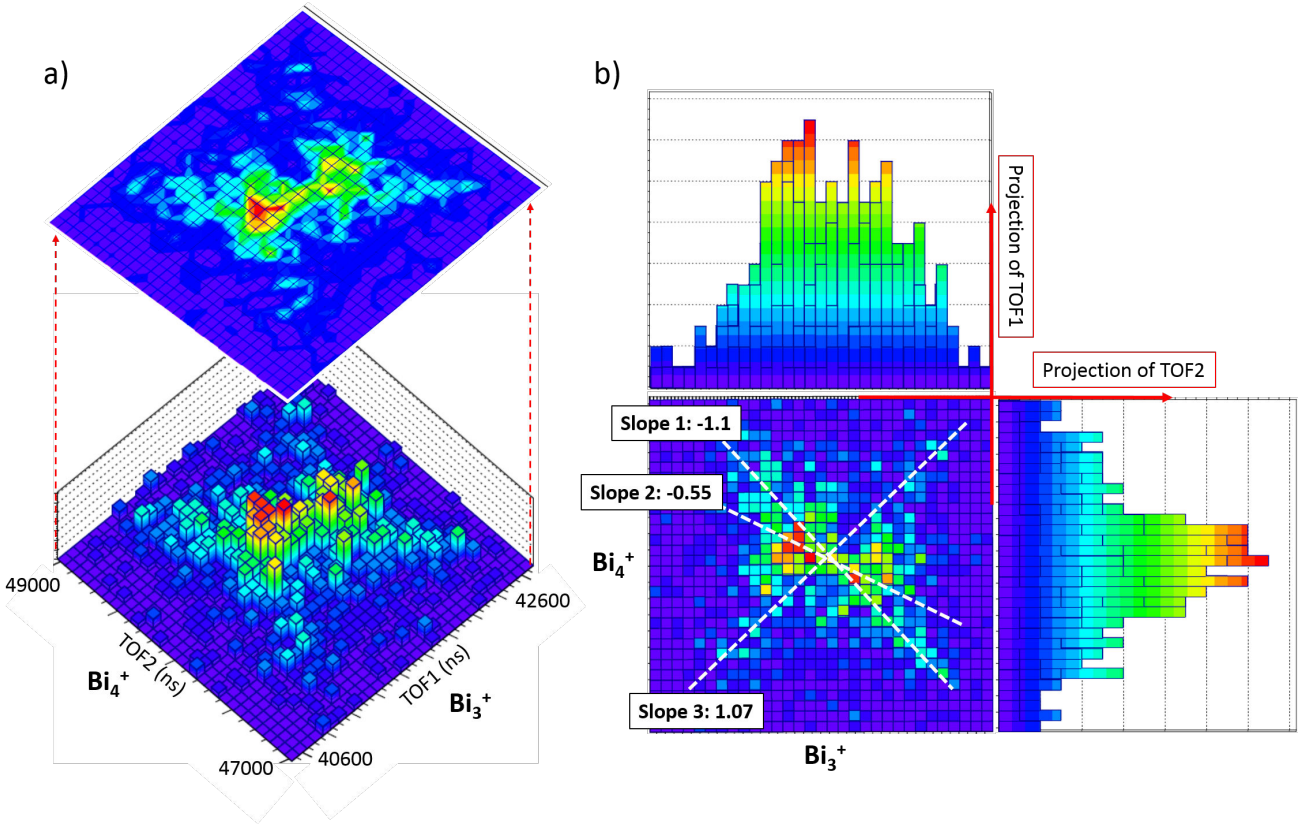

Figure 5.35 *a) 3-dimensional intensity histogram of the island of the correlated pair (Bi_3^+,Bi_4^+), b)2d TOF representation of the same island with horizontal and vertical profile cuts.*

produced on the cluster. If the electrons cannot equilibrate this localized charge fast enough, probably the local emission of small charged fragments may take a place from one cluster side.

2). A second process is characterized by a slope of -1.1, which is close to the value for binary fission (slope =-1). The small deviation from the value -1 can be explained by the additional emission of a (neutral) fragment with low momentum. As to be seen in fig.5.35 a), this process does not show a clear forward and backward peak structure, it rather represents a straight line with appreciable energy. This is similar for both fragments.

3). The 3rd and most intense contribution corresponds to a slope of about -0.5. The analysis of the involved kinetic energies shows that the momentum of the tetramer fragment is approximately twice as large as that of the trimer. This means that also here a third fragment must carry the missing momentum which equates that one of the detected Bi_4^+ ion.

As all processes are overlapping, the projection cuts shown in fig.5.35 b) do not manifest any specific structure. The table 5 gives an overview on the observed island slopes. The determined values show that for coincidences between small fragments in the size range from Bi_1^+ to Bi_5^+ at least 3 fragments are produced from which in the present case only two are detected.

	Bi_2^+	Bi_3^+	Bi_4^+	Bi_5^+
Bi_1^+	Slope 1 ~ - 0,71	Slope ~ - 0.16	Slope ~ 0	Slope ~ 0
Bi_2^+		Slope ~ - 0.34	Slope ~ - 0.3	Slope ~ - 0.13
Bi_3^+			Slope 1 ~ - 1.10 Slope 2 ~ - 0.55 Slope 3 ~ 1.07	Slope ~ - 0.14
Bi_4^+				Slope ~ - 0.32

Table 5 *The summary of the observed correlation island slopes determined for small Bi_x^+ fragments (x=1 to 5).*

5.1.5 Summary of the results for Bi_n clusters

KeV collisions between multiply charged ions and Bi clusters are found to produce mass spectra with dominant contributions from small singly charged Bi_n^+ clusters with n $<$ 15, as well as weaker contributions from larger multiply charged cluster ions. From the spectra, reconstructed for individual charge states for q=2 to 6, appearance sizes have been determined which are found to be in agreement with the liquid drop model corresponding to a fissility of ∼0.28. The intensity distribution of small Bi fragments showed a strong dependence on the projectile charge state. The observed distributions show that highly charged parent system (formed by electron capture from highly charged projectiles) stabilize by the emission of the smallest charged fragment (Bi_1^+), whereas parent ions produced with projectiles in lower charge states (lower fissilities of the parent cluster ions) tend to produce larger fragments, in particular the charged trimer system becomes dominant for O^{3+} projectiles.

The analysis of the peak shape of small fragments allowed to determine the kinetic energies of individual fragments and to separate contributions from different processes as a function of the fragment size. It is found that small singly charged clusters (n=1-4) are formed with two energy distribution: one high-energy component is characterized by ∼5 eV attributed to the asymmetric fragmentation of highly charged parent clusters and a second low-energy part with energies below 1 eV which results from the fragmentation of clusters in low charge states (q=2,3) or from a sequence of evaporation processes. Contributions from sputtering processes cannot be excluded.

Coincidences between the fragments Bi_1^+ or Bi_3^+ and other small cluster ions show a different behavior. Whereas the monomer is measured principally in coincidence with a second monomer, while the intensity of the second fragment strongly decreases with increasing size, the trimer shows a broad mass distribution of the second fragment (up to n=7). This result is interpreted as being due to different charges of the parent intermediate Bi clusters. This is also confirmed

by the analysis of coincidences with heavy residues. For monomers and trimers it is found that for residues with small n/q values (10 to 35) the measured kinetic energies (Bi_3^+: 3-4 eV) can be explained with binary asymmetric fission or sequential processes, whereas for large n/q values (n/q = 40 to 150) the increased energies (4-5 eV) require the simultaneous emission of several small fragments (high initial charge of the intermediate state and low charge of the final state of the residue). The increased energies of Bi_1^+ fragments (5-7 eV) shows the corresponding fragmentation involves Bi clusters in higher charge states. Interestingly, coincidence islands for small fragments also demonstrate the emission of both particles in the same direction which might be a signature of the semiconductor behavior of the semi-metal Bi ("localized" charge sites). The dominant part of the observed reaction products is found to be due to multi-electron capture processes occurring in peripheral collisions with multiply charged ions.

5.2 Ion collisions with free, large silver nanoparticles

Up to this point we were dealing with nanoparticles of bismuth, which do not contain more than a few hundred of atoms and, therefore, are characterized by diameters smaller or equal to 2.5 nm. However, magnetron based cluster sources are rather universal in terms of availability of elements used for cluster production. This allowed us to study metal clusters of silver nanoparticles. These were shown to posses radiotherapeutic properties specific for high Z-elements, similar to those of gold nanoparticles. For some specific cell lines they even surpass the effect of gold nanoparticles [86, 87].

In the following, I will present results concerning the interaction of multiply charged ions with nm-sized silver nanoparticles and I will discuss especially the first experimental data relevant for the concept of sputtering of free nanoparticles (not supported nanoparticles) by ion impact.

5.2.1 Cross-sections for peripheral and penetrating collisions - comparison of small Bismuth clusters and large silver nanoparticles

Before starting the discussion of experimental results it is worth to characterize the collisions between NP and highly charged ions as a function of the impact parameter b.

In fig.5.36 such schematic separation is shown; for collisions where the impact parameter is larger than the nanoparticle radius $b > R_{NP}$ we deal with peripheral collisions, whereas for those where the impact parameter is smaller than the radius of the nanoparticle $b < R_{NP}$ we deal with penetrating collisions (the ion will pass through the nanobject). For the case of peripheral collisions the dominant effects (at this range of kinetic energy of an ion) are those of (multi-) electron capture and collective excitations induced by the time-dependent Coulomb field (like volume/surface plasmon excitations). On the other hand, for the case of penetrating collisions in addition to previously mentioned mechanisms, the kinetic energy of an

ion is deposited within electronic and nuclear degrees of freedom due to nuclear and electronic stopping processes involved when the ion penetrates matter.

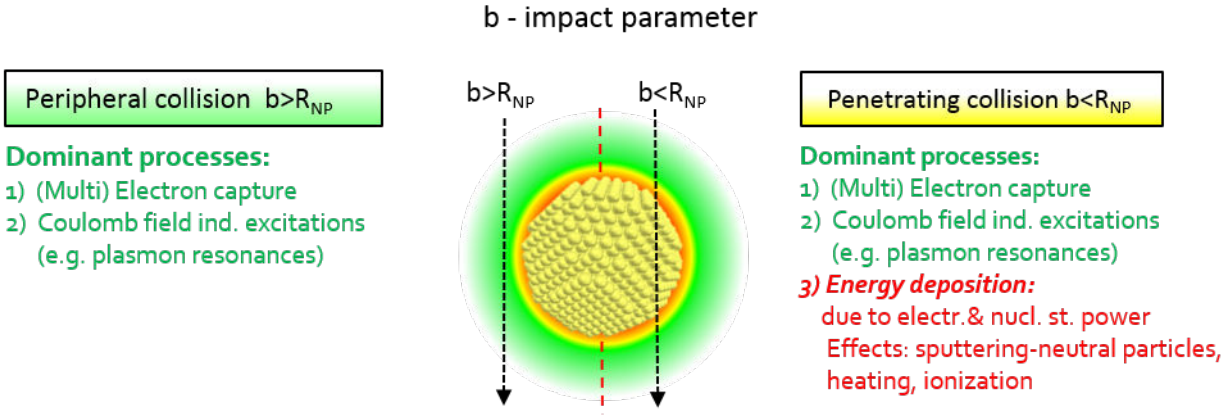

Figure 5.36 *Schematic view of the type of collision and of the expected processes*

Previously studied systems of bismuth clusters were relatively small with an average diameter of 2 nm compared to silver nanoparticles which are characterized by an average value of 6 nm. Therefore, the cross-section for penetrating collisions (determined only by the radius of the object) is about one order of magnitude smaller for bismuth than for silver in the present experiments. More important is the ratio between penetrating and peripheral collisions (determined by the 1st electron capture distance from the surface of the nanoparticle). For bismuth clusters the majority of effects will be associated mainly to peripheral processes like multiple electron capture. When the size of an object increases, its geometrical cross-section increases with second power of its radius (area of an object); other effects related to penetrating collisions become more and more important. Figs.5.37 a), b) present cross-sections (related to penetrating and peripheral collisions) for Bi clusters with a diameter of 2nm and larger silver nanoparticles with 6nm diameter. The cross sections are shown as a function of the initial charge of the projectile. Cross-sections were calculated in the following manner: the geometrical cross section is the simple geometrical area of the nanoparticle $\sigma_{geom} = \Pi R_{NP}^2$ and the peripheral cross-section is taken as difference of the total electron capture cross-section and the geometrical one: $\sigma_{periph} = \Pi(R_{capt}^2 - R_{NP}^2)$.

Firstly, considering small Bi clusters (fig.5.37 a)) the cross-section for penetrating collisions is only 40 % of that for peripheral collisions if the projectile charge is equal to q=2. As the experiments with bismuth clusters were done preferentially using projectile charge q=8 (Ar^{8+} at kinetic energy of 120 keV), this ratio drops down further to only 15% and for a projectile charge q=15 it is estimated to be only around 10 %. Therefore, this explains why in the case of collisions of slow, highly charged ions with bismuth clusters the dominantly observed physical processes were associated to ionization due to multiple electron capture processes.

Considering now larger systems of silver nanoparticles of an approximate diameter of

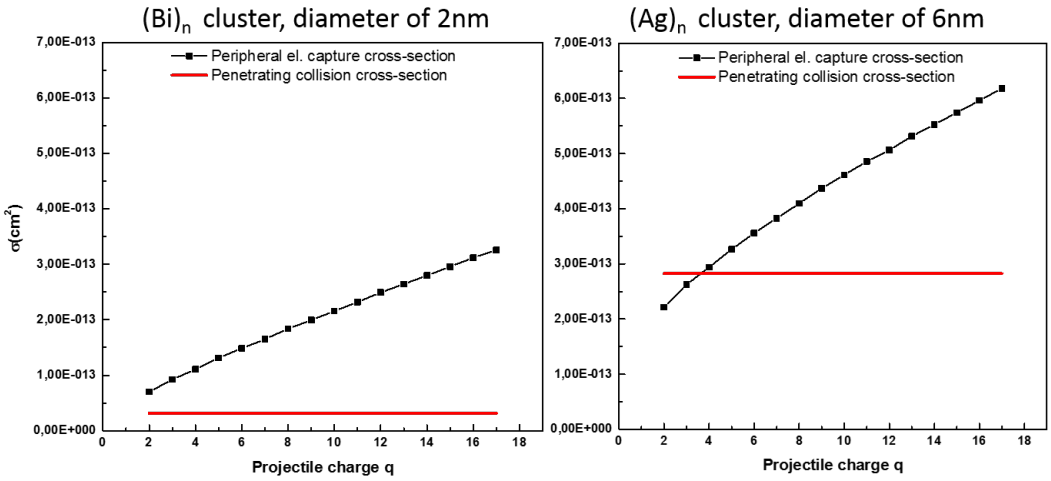

Figure 5.37 *Comparison of the 1st electron capture (black dots/line) and the geometrical (red line) cross-section for two cases: a)„smaller" Bi cluster with radius 1 nm and b) „larger" nanoparticle with radius of 3 nm.*

d=6nm, the geometrical cross-section increases by a factor of 9 compared to the bismuth case (see Fig.5.37 b)). For the case of low projectile charges (q up to 4) the cross section ratio is found to be $\sigma_{geom}/\sigma_{capt} \geq 1$. As in the bismuth case, calculations for electron capture are based on the classical over the barrier model. For higher charge states of the projectile, the capture cross-section rises and for the charge q=15 its value reaches $\sigma_{capt} \approx 6.0 \times 10^{-13}$ cm^2, so almost twice the geometrical one. Therefore, in contrast to the bismuth system, both types of collisions are expected to contribute to the reactions. For low charge states of the projectile more than 50 % of collisions will relate to the fact that ions are passing through the nanoparticle, for higher charge states this value is still very high, estimated around 30 %.

Which product ions might we expect for ion collisions with Ag nanoparticles of the present size? For bismuth we have observed either stable multiply charged clusters above their appearance size or, in particular, small fragments which are emitted from unstable multiply charged clusters formed by fission processes. The situation is expected to be different in the silver clusters due to the large number of atoms they contain. In figure 5.38 we show the stability diagram for Ag clusters which one may compare with that for Bi clusters (see fig.5.5). Shown is the Rayleigh limit as a solid line, which defines the maximum charge that a system can withstand (calculated according to [77]). The dashed-dotted line represents the appearance size which corresponds to about X=0.2, as shown by an experimental point obtained from electron impact ionization experiments [88]. The dashed curve represents a modified appearance size

curve which takes into account that for very large clusters and high projectile charge states the cluster temperature increases only by a small amount due to the collisional energy transfer. This is due to the increased number of degrees of freedom of large clusters. Therefore, the appearance size approaches the critical size. This was demonstrated for collisions of highly charged ions (Xe^{28+}) with sodium clusters [19].

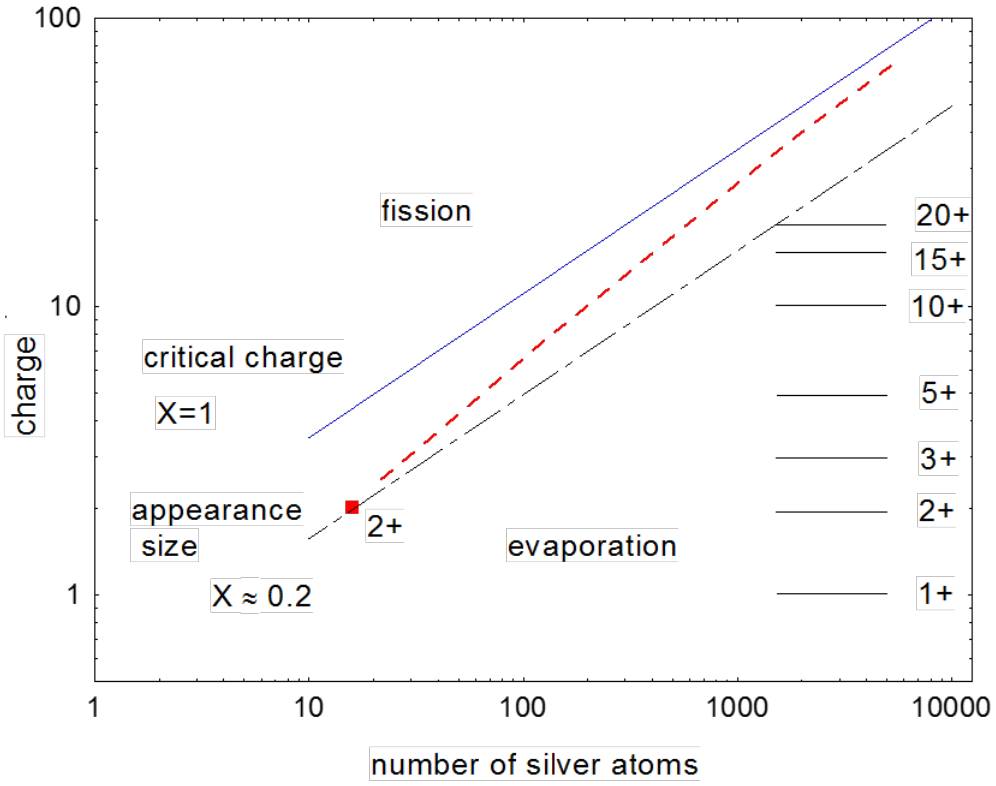

Figure 5.38 *Stability diagram for highly charged silver clusters.*

The horizontal lines in fig.5.38 characterize the initial cluster distribution around n∼5000 atoms. Even for very high charge states (q=20), eventually produced by electron capture and follow-up processes, the produced system is still in the stable region, where internal energy can only be reduced by evaporation processes. For low charge states, the system has to evaporate a huge number of atoms in order to arrive at the limit of stability. Therefore, we do not expect a high formation yield of small fragments due to fission processes. Rather highly charged stable Ag nanoparticles might be formed. The critical charges, calculated using the model of a liquid drop based on Lord Rayleigh, are summarized in table 6 for given sizes: So far I discussed the influence of peripheral collisions due to electron capture processes. What about penetrating collisions when the ion passes through the nanoparticle? Electronic and nuclear stopping processes will lead to a high energy deposition, to excitation, ionization and evaporation of neutral clusters as well as to sputtering phenomena. Here one might expect in particular the emission of small fragments from the nanoparticle surface, although the fraction

Diameter	Number of atoms	Critical charge q
4 nm	2000	38
4.6 nm	3000	46
5 nm	4000	54
5.4 nm	5000	60
6 nm	6000	65
6.1 nm	7000	71
6.4 nm	8000	75

Table 6 *Critical charges for given Ag nanoparticle diameters.*

of charged ones compared to neutral ones is not so clear. So one might ask the question, whether a few nm large particles behaves in collisions with ions more like an atomic system or does it show mainly the characteristics of an isolated nano-surface. In this chapter this question will be addressed.

5.2.2 Mass spectra produced in collisions of multiply charged ions with Ag_n nanoparticles

Before proceeding to the description of mass spectra resulting from collisions of multiply charged ions with silver nanoparticles, information about the size distribution of neutral silver nanoparticles has to be provided (see fig.5.39). The size distribution of neutral nanoparticles is obtained by microscopic investigation of silver clusters deposited on a silicon surface and examined using AFM technique (Atomic Force Microscopy) in Tapping Mode. Fig.5.39a) shows the histogramm of the cluster diameters, fig.5.39b) the intensity as function of the cluster size n, fitted by a log-normal distribution.

Fig.5.40 shows the inclusive mass spectrum (events with all nSTOPS are included) created in collisions of Xe^{17+} at $E_{kin} = 255$keV with free, neutral silver nanoparticles characterized by the size distribution shown in fig.5.39 b).

First of all, we have to remind that the intensity maximum of the initial neutral cluster distribution occurs at n equal to 4000-7000 atoms ($\sim$ 5-7 nm). In the case of the mass spectrum, the largest observed signal corresponds to n/q$\sim$500. Thus, singly charged clusters, which are produced with high probability in collisions with highly charged projectiles are not observed. This strongly imposes the question about the detection efficiency of large, weakly charged metal clusters and this subject was discussed already in the chapter 4. Looking at the mass spectrum itself, we observe two main features that are 1) a very wide distribution expanding from n/q $\sim$75 up to 500, with a maximum positioned at n/q=125 and 2) a very strong (compared to the rest of the spectrum) signal on the side of small clusters with n/q $<$ 20. In the following we will discuss both contributions separately.

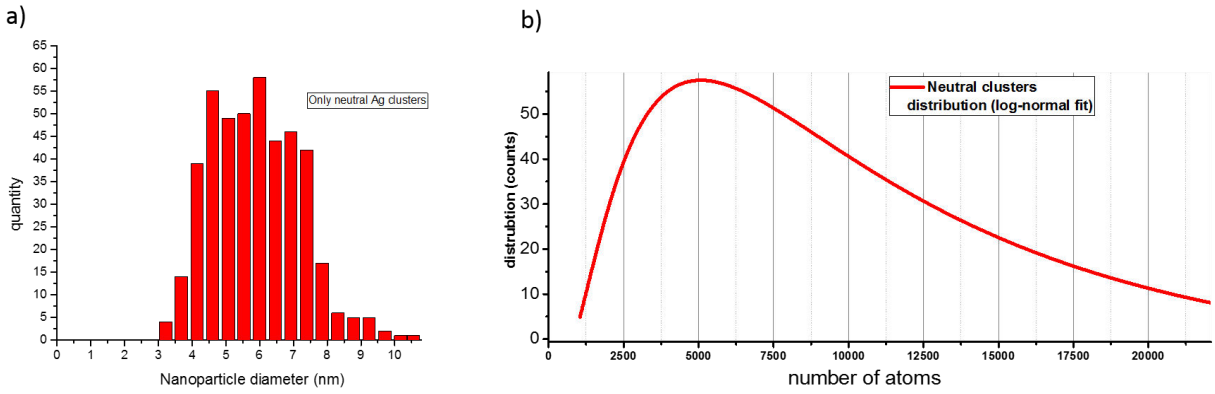

Figure 5.39 *a) Size distribution of silver nanoparticles as a function of their diameter; b) Size distribution of silver nanoparticles as a function of the number of atoms (log-normal fit).*

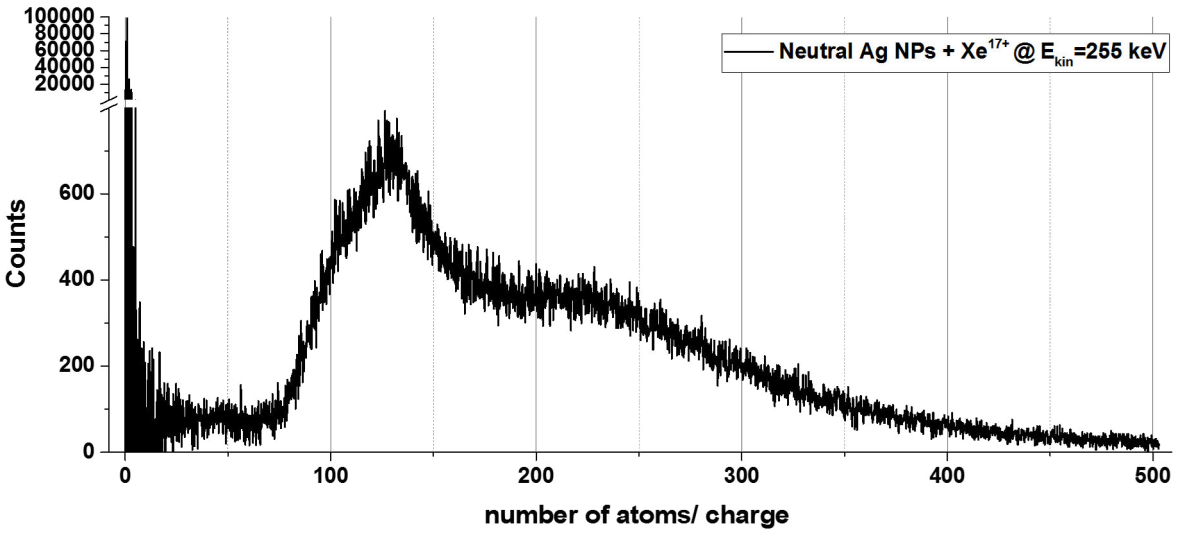

Figure 5.40 *Mass spectrum resulting from the collisions of Xe^{17+} ions with the beam of neutral Ag_n nanoparticles characterized by size distribution shown in fig.5.39.*

5.2.2.1 Production of small clusters - comparison of sputtering from macroscopic and nanoscopic surfaces.

Fig.5.41 a) shows a zoom into the spectrum of small-size clusters produced in collisions of Xe^{17+} projectiles with 6nm large (in average) Ag nanopartciles. The most intense peak is the monomer, followed by signals from the dimer and trimer. These three peaks - Ag^{+}_{1-3} - are the most dominant ones and constitute in total around 75 % of the whole small clusters signal (up to Ag^{+}_{21}). A characteristic feature of the spectrum is the occurrence of so-called

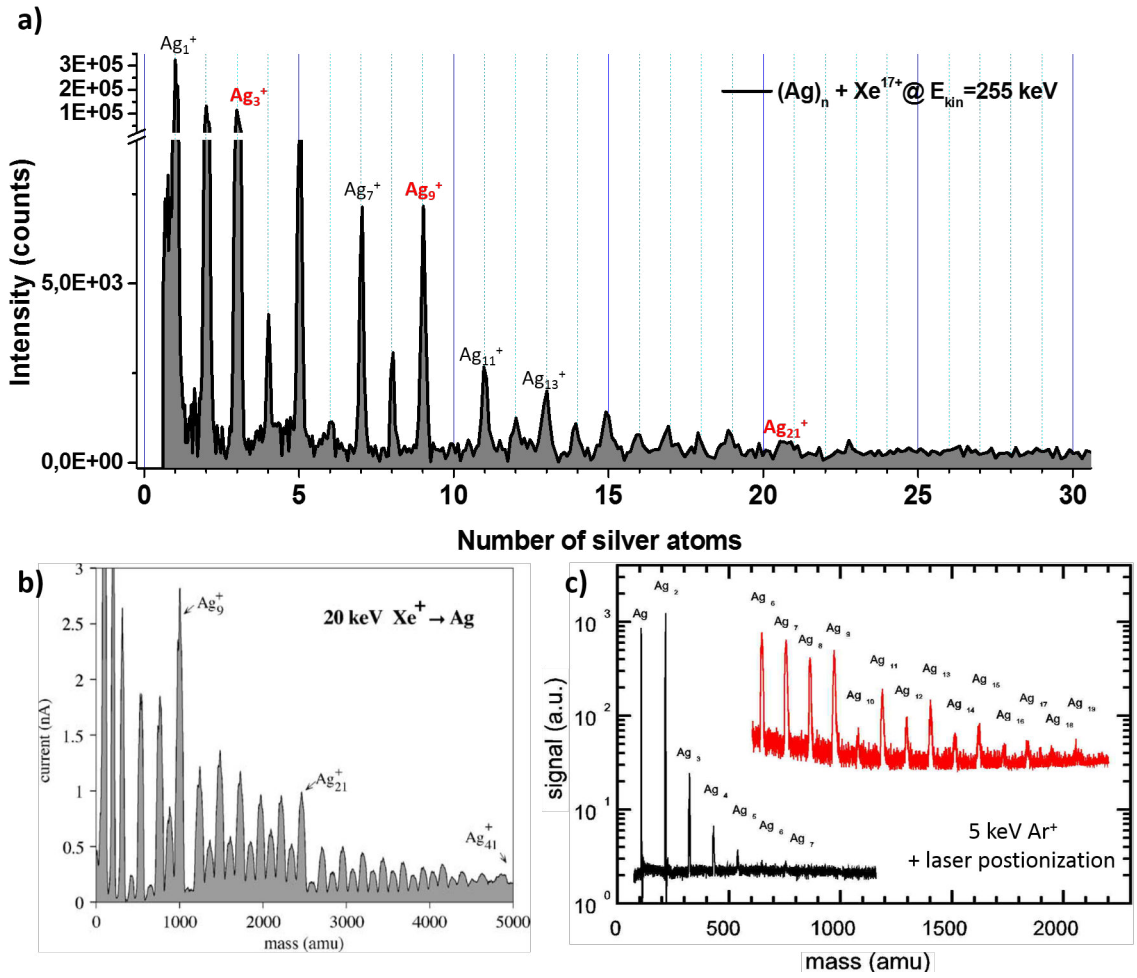

Figure 5.41 *a) Magnified n/q spectrum of small cationic fragments resulting from collisions of Xe^{17+} ions with neutral silver nanoparticles; b) mass spectrum of small fragments from sputtering of polycristalline silver surface with 20 keV Xe^{+} ions, [89]; c) The mass spectrum of singly charged Ag_n clusters, sputtered from a polycrystalline silver surface as neutral clusters, post-ionized during the expansion phase by a laser pulse [90].*

even-odd oscillations as a function of the cluster size. These have been shown to occur also in the ionization energies and electron affinities for neutral Ag_n clusters. The ionization energies which are in the range of about 6 eV are higher for even-numbered clusters with an even-number of valence electrons, [91].In the present case of singly charged clusters, the intensities of odd-numbered clusters are consequently higher than those of even ones.

Furthermore, we observe a strong drop in intensity after the cluster sizes of n=3 and 9 and to some extent for n=21. These structures are attributed to shell effects, due to the closing/filling of electronic shells that are characterized by 8, 20 or 40 electrons in the valence band of metallic clusters. In the case of singly charged silver clusters, where the electronic structure of the atom

is [Kr]4d^{10}5s^{1} and where each atom donates one electron to the delocalized electrons, electronic shell closing will be pronounced for singly charged clusters containing 9, 21, and 41 atoms.

Similar spectra were observed in experiments of Harbich et al. [89] where the sputtering of energetic ions from surfaces was studied. The resulting mass spectrum is shown in fig.5.41 b). In this experiment, silver cluster ions are produced by sputtering, namely by irradiating a polycrystalline silver surface with Xe^+ ions at a kinetic energy of $E_{kin} = 10$ keV. Similar to the mass spectrum obtained in our experiments, even-odd oscillations and shell closing effects are observed.

A second example for sputtering is shown in fig.5.41 c).This is a mass spectrum of singly charged Ag_n clusters, sputtered by 5keV Ar^+ ions from a polycrystalline silver surface as neutral clusters, ionized in the following during the expansion phase by a laser pulse, [90]. The displayed spectrum represents an average over 1000 data acquisition cycles (primary ion and laser shots) and shows clusters containing up to 19 atoms. It was obtained using a laser power density of 3 $\times 10^6$ W/cm^2 for post-ionization. As the photon energy is slightly above the ionization potential ($\hbar\nu$=6.4 eV) and single photon absorption was guaranteed, the observed distribution should correspond to the distribution of sputtered neutral Ag_n clusters. In contrast to the data shown previously for the direct sputtering of ions, the intensity of small clusters exhibits a monotonic decay with increasing cluster size and only for larger cluster sizes a slight even-odd alternation is observed.

In order to compare the experimental results obtained in our experiment with those obtained by sputtering of surfaces, we will compare the relative yield of sputtered clusters, obtained by intensity integration of each cluster peak and normalization to the intensity of the monomer. Fig.5.42 shows the relative yields for a): our experiment with free silver nanoparticles irradiated with highly charged Xe^{17+} ions (corresponding to mass spectrum from 5.41a); b): relative yields for positive and negative clusters from silver surfaces from the group of Matsuda, [92].

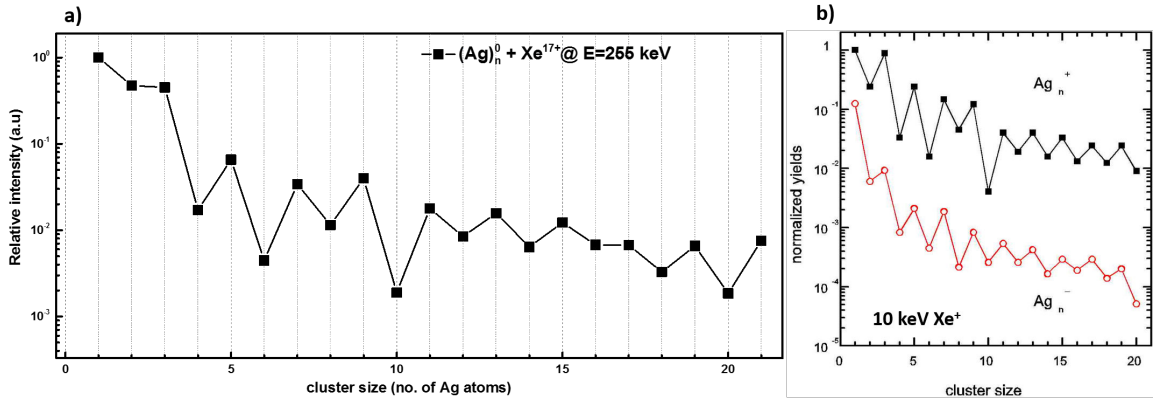

Figure 5.42 *a) The relative intensity of small Ag_n^+ fragments resulting from the collision of neutral silver nanoparticles with Xe^{17+} as a projectile; b)relative yields for positive and negative clusters from silver surfaces by sputtering, studied by Matsuda et al., [92].*

Comparing the distributions for singly charged clusters for the case of a surface (fig.5.42b) and for a free nanoparticle (fig.5.42a), one sees a strong similarity between both data sets. So the most intense peak is the monomer and the characteristic even-odd alternation is visible in both cases for exactly the same number of atoms in the cluster. The cluster with the lowest intensity is in both cases Ag_{10}^+. These similarities propose, that the formation of small charged clusters produced in collisions of ions with large silver nanoparticles can be described within the sputtering mechanism. However, there are some differences concerning the relative intensities of individual peaks (particularly, monomer and trimer): in the case of sputtering from nanoparticles, the signal from Ag_3^+ is much weaker than that for the monomer, whereas for the surface (fig.5.42) both show nearly the same intensity. A second difference concerns the decrease of the intensity with the clusters size in the given range up to n=20. The average drop for the case of surfaces corresponds to a factor of about 50 (fig.5.42b), whereas for the case of nanoparticles this drop is stronger by a factor of 2 to 3.

In the discussion of surface sputtering it is worth to mention that one can produce also clusters of very large sizes, [92]. Fig.5.43 shows the relative intensity for sizes up to n=100 in a logarithmic scale for polycrystalline silver sputtered by 10 keV Xe ions. Two characteristic features are observed superimposed on the "exponential" decrease of the ion intensity. First, one observes even-odd alternations and second, steep decreases in the ion intensity occur at the magic numbers 3, 9, 21, 35, 41, 59 and 93. These numbers are compared with potential well energy levels for electrons bound in a spherically symmetric square well potential with infinite walls (shown on the right side of the graph) and can be explained by shell closures.

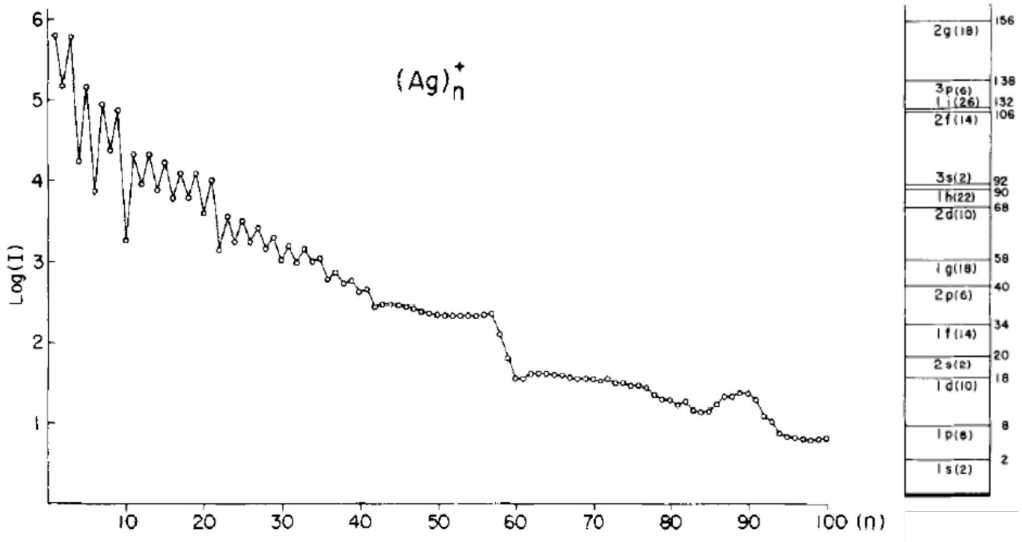

Figure 5.43 *Mass distribution of silver clusters Ag_n^+ up to size n=100 sputtered by 10 keV Xe ions (plot in log-scale), [92].*

A parameter which might influence the intensity distribution of small clusters as well is the

charge state of the projectile. Fig.5.44 shows the yields for clusters up to size n=5 normalized to the primary ion beam as well as to the acquisition time. The charge state of the projectile varies from z=2 to z=9. When analyzing the intensities of the monomer to the trimer we find a similar decrease of the yield with size, independent of the charge state. For a given size, the yields decrease in the following sequence: Ar^{6+}, Ar^{9+}, O^{2+} and O^{3+}. This series corresponds as shown further below (figure 5.48) to the decrease of the nuclear stopping power. This supports the interpretation given before that the production of small-size fragments is very likely to be due to sputtering events. Furthermore, for charge state ions, like O^{2+}, the presence of these small fragments cannot be explained by fission or fragmentation of multiply charged nanoparticles, as in this case only low charge states of the ionized nanoparticles are to be expected forming stable states in view of the size of the nanoparticles.

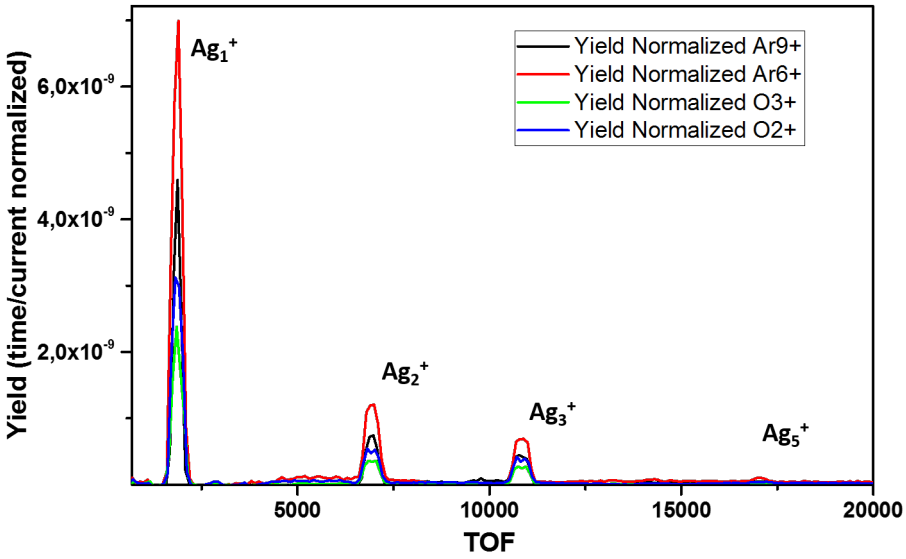

Figure 5.44 *Yield (time and ion beam current normalized, binwidth 100ns) of small Ag_n^+ fragments for different projectiles and projectile charge states.*

5.2.3 Sputtering of metal nanoparticles - molecular dynamics simulations and experiment comparison

To our knowledge there are no experiments that investigate the concept of ion sputtering of free metal nanoparticles, however, some theoretical approaches using molecular dynamics calculations indeed exist and treat problems of the sputtering of metal nanoparticles by ion/atom irradiation, although the specific systems which we have studied are not treated theoretically. In this section we will discuss some of the works considering potential sputtering mechanisms that lead to the creation of small clusters.

5.2.3.1 Enhanced sputtering from nanoparticles - size effects

The group of K.Nordlund et al. from the University of Helsinki performed molecular dynamics simulations of gold nanoparticles and thin films in collisions with Gallium atoms at a kinetic energy of 25 keV, [93]. In their work they showed, that for thin films and nanoparticles in the range of up to 10 nm, the sputtering process is strongly enhanced compared to the case of the bulk. Fig.5.45 a) presents the dependence of the total sputtering yield as a function of nanoparticle size from 1 up to 15 nm in diameter which corresponds to 55 up to 130000 atoms (nanoparticles were represented as cuboctahedra and relaxed at 300K).

For the smallest clusters the total yield is lower than that of the bulk. This is due to the fact that ions are passing through the nanoparticle and do not deposit all of their energy within the cluster. With increasing size, more target atoms will be accelerated by nuclear collisions with the projectile and by cascade effects. Due to their high energy the majority can leave the finite-size cluster in contrast to a surface or solid where only a 2Π emission angle is possible. Therefore, the sputtering yield rises above the bulk value, reaching a maximum for sizes of around 6-8 nm with a value which is about 3 times higher than the standard bulk value. If the nanoparticle diameter is further increased, the yield drops again and slowly approaches the bulk value, as not all energetic particles can leave the cluster.

Of course the quantitative results depend on the projectile, its kinetic energy and the material composition of the target.

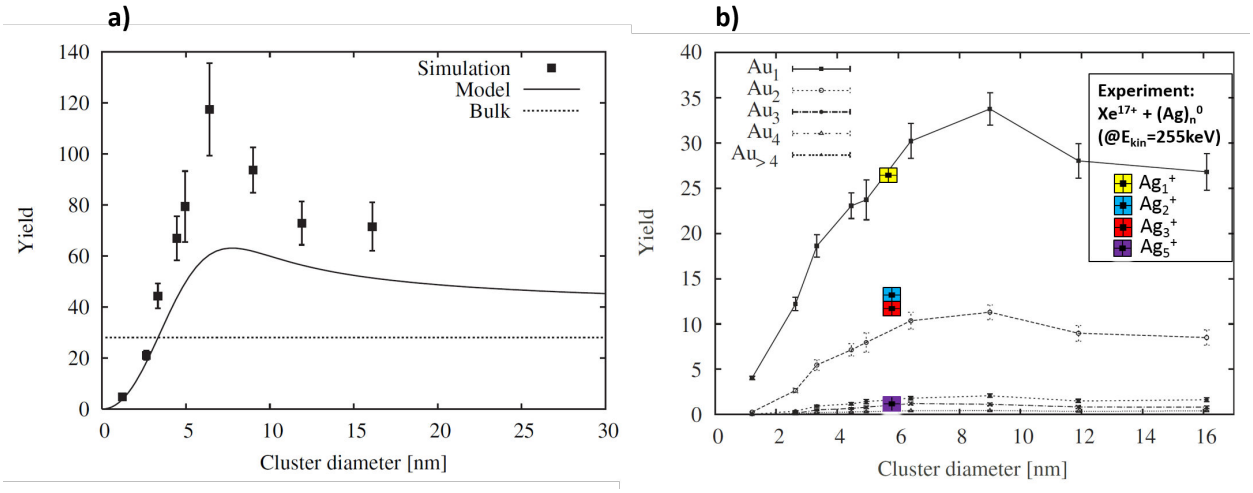

Figure 5.45 *a) Theoretical sputtering yields for the 25 keV collisions of Ga atoms with gold clusters obtained as a function of the cluster size; b) comparison of the absolute production yields of small clusters Ag_1 to Ag_5 by sputtering in the same collision simulation [93].*

In fig.5.45 b) absolute sputter yields for neutral monomers to tetramers are shown as a function of the nanoparticle size. The calculations show, that the most intense species is the monomer with a maximum yield of about 30 particles per impinging projectile. The intensity

of the dimer is lower by about a factor of 3, that of the trimer and larger emitted clusters by a factor of $\sim$15.

For silver clusters no such calculations exist. However, silver and gold atoms have similar electronic structure ($5d^{10}6s^1$ vs $4d^{10}5s^1$) and almost identical Wigner-Seitz radius for the bulk. Therefore, we decided to include in Fig. 5.45b the relative yields for Ag_n clusters obtained with Xe^{17+} @ 255 keV, which are marked with colored rectangles. As in the gold case, the relative yield of the monomer is the highest followed by the dimer. However, the decrease in intensity with increasing size of the emitted particle is much lower (see trimer). As discussed above, this is also found in experiments where neutral and charged emitted cluster distributions are compared (Matsuda et al. [92]).

Another molecular dynamics study concerns penetrating collisions of 20nm gold nanoparticles with 200 keV Xenon atoms, performed by Sandoval and Urbassek [94] and allows to better understand the dynamical mechanisms leading to particle sputtering and the formation of spikes.

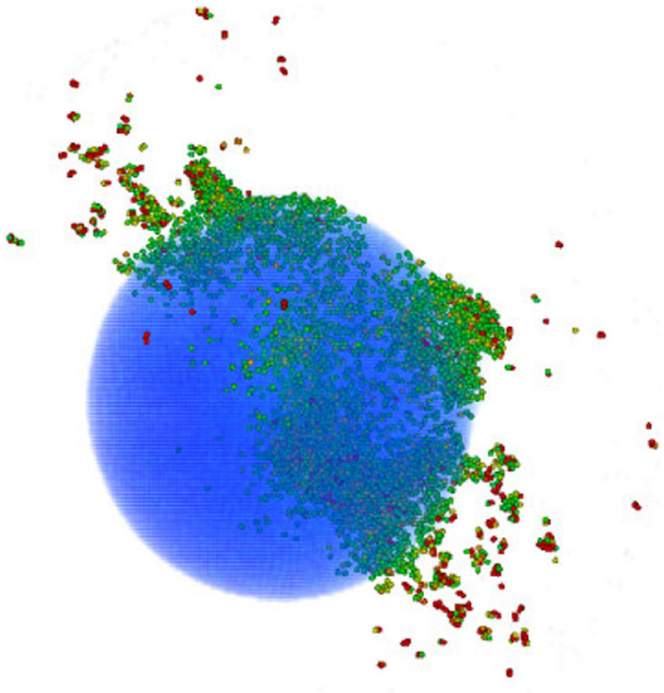

Figure 5.46 *Snapshot showing energetic particles 11 ns after the collision of 200 keV Xe atoms with gold nanopartciles (diameter 20nm) (taken from Urbassek et al., [94].)*

Figure 5.46 represents a snapshot of the molecular dynamics simulation which shows the distribution of energetic particles (E $>$ 0.4 eV) 11 ns after a particular impact event. The Xe atom impacts perpendicular from the top passing through the center of the nanoparticle. At this time sideways and forward sputtering have already set in. Thanks to image rendering one can see how internal cascades evolve to reach the surface spots and initiate new particle emission

localizations. Color of each atom corresponds to its kinetic energy: green to light red color correponds to particles having energies between 0.4 to 1 eV, while dark red are species/clusters with kinetic energy exceeding 1 eV. Figure 5.47 shows the time evolution of the same event.

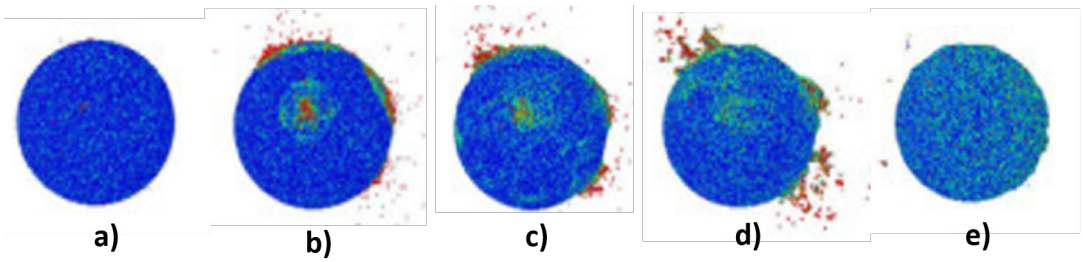

Figure 5.47 *Snapshots of a selected impact event at 0.1 (a), 1.0 (b), 3.5 (c), 10 (d), and 100 ps (e),figures from [94].)*

The emission of the first products occurs very fast within the first picosecond (fig.5.47 a and b) and starts from the surface (fig.5.47 b) and neighboring spots. After 3.5 ps (fig. 5.47 c) essential particle emission occurs at the exit of the projectile trajectory, and up to times of 10 ps (fig. 5.47 d) strong spikes are produced at different parts of the surface. Finally after 100 ps (fig. 5.47 e) the particle emission comes to an end, and the recoil ions within the cluster are slightly heated ($\sim$0.4 eV). In the present event, a kinetic energy of 42 keV is deposited in the heavy particle motion, whereas the traversing projectile keeps the rest of 158 keV. Furthermore, the total sputter yield of this event amounts to 1164 particles. It has to be noted, that snapshots may change drastically for different events due to the statistical nature of the collision cascades, thus, yielding also different sputtering yields and only values averaged over a large number of events should be used.

Coming back to our experimental results, fig.5.48 shows the relative yields measured for silver clusters for different projectiles and a comparison with existing empirical data about sputtering yields for a silver surface for different atoms and energies. Such data are available online [95]. The relative yields have been normalized to the sputtering yield of Xenon at a kinetic energy of 375 keV which corresponds to the kinetic energy of Xe^{25+} in the present experiment. The total experimental sputter yields for Ag nanoparticles (this work) were taken as the sum of the intensities of the monomer, dimer and trimer observed in the cationic mass spectrum, as these constitute around 90 % of the signal concerning small clusters.

When we compare the relative yields for nanoparticles determined in the present experiment with empirical values for Ag surface [95] data as a function of $\frac{\sqrt{m}}{v}$, which is proportional to the nuclear stopping power in the present energy region, we find a very good agreement between both data sets. In particular we find, that the same projectiles in higher charge states have a lower sputter yield due to their higher velocity. The observed agreement also proposes that the production of small-size fragments is due to the sputtering of free, non-supported metal clusters rather than due to the fission of multiply charged clusters formed by electron capture

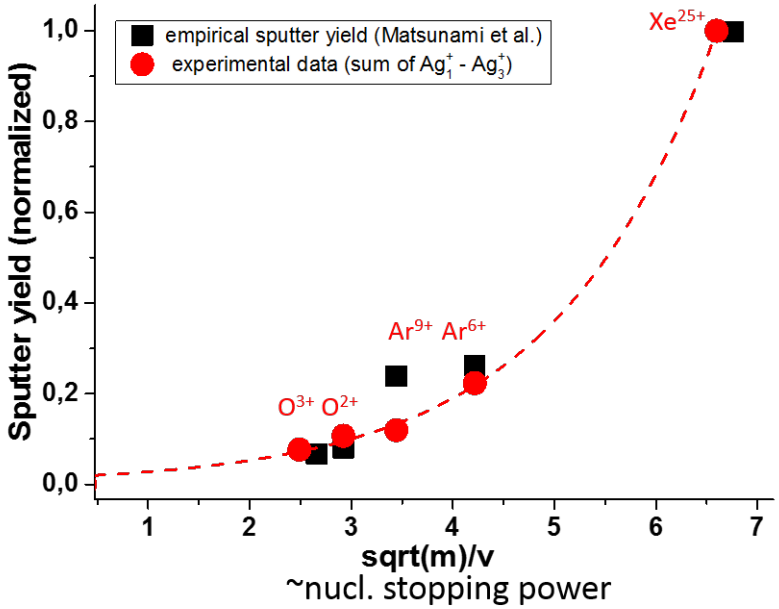

Figure 5.48 *Comparison of the relative sputtering yields of the experimental data (red dots, red dashed line is the exponential fit for eye-guiding) obtained for collision of Ag_n NPs with different projectiles and empirical data for surface sputtering yields for the same projectiles and kinetic energies as a function of nuclear stopping power [95]. Normalization was made with respect to Xe with 325 keV.*

as observed in the case of Bi clusters.

5.2.4 Kinetic energy of emitted clusters

Motivated by theoretical simulations based on molecular dynamics, in this section I will discuss the kinetic energy distributions of monomers produced in collisions of different projectiles in different charge states with silver nanoparticles. The information about kinetic energies of a particle is based as discussed in the previous sections on Bi clusters, on the analysis of the peak form in the mass spectrum. A typical example of such a monomer peak is shown in fig.5.49. In contrast to results measured for Bi clusters, the peak contains at least 3 structures.

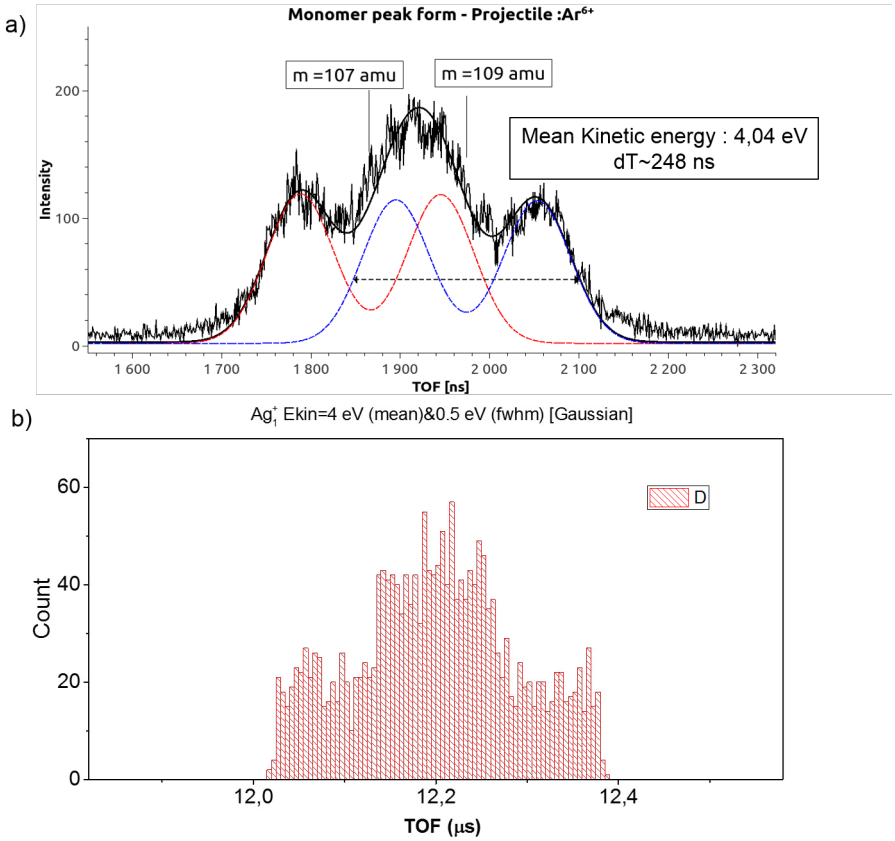

Figure 5.49 *a) Peak form of the monomer produced in collisions of Ar^{6+} ions at 90 keV; b) SIMION simulated peak form of monomer with mean kinetic energy 4 eV and width at full maximum of 0.5 eV (Gaussian distribution).*

This is easy to explain as silver has two stable isotopes with masses 107 and 109 amu with an intensity ratio of 51% and 49%. The expected positions of these two isotopes are marked on the graph by black vertical lines. When both fragments do have some kinetic energy, as we have seen previously in chapter 4 the peaks blur out and, in consequence, the two energetic isotopes will superimpose each other in the middle of the peak. In fig.5.49 one fitted contribution from isotope of 107 amu is drawn with a red line, the other one of the second isotope is shown with a blue line. Taking the time difference in the half width of the maxima for one of these isotopes, we obtain information about kinetic energy for a fragment. The time separation of δT=248 ns is equivalent to a fragment kinetic energy of 4.05 eV. For comparison the simulated peak form (SIMION) of the monomer with a gaussian kinetic energy distribution centred at 4 eV and a width at half maximum of 0.5 eV is presented in fig.5.49b).

Fig.5.50 a) is listing the kinetic energies of the monomer for different projectiles used in the experiments in tabular form, while fig.5.50 b) shows the result of a molecular dynamics simulation for the kinetic energy distribution of the monomers for the case that 8nm large gold nanoparticles have been irradiated by 200 keV gold atoms [94].

a)

Projectile	Impact energy (keV)	Kinetic energy of Ag_1^+ (eV)
O^{2+}	30	3,7
O^{3+}	45	3,95
Ar^{6+}	90	4,04
Ar^{9+}	135	2,25

b)

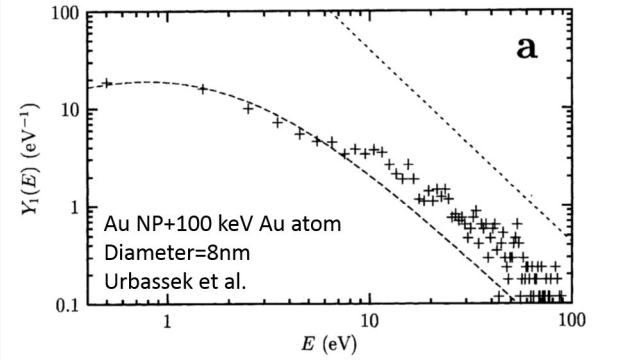

Figure 5.50 *a) Summary of the most probable kinetic energies of Ag monomers resulting from collisions with different projectile ions;b)Kinetic energy distribution of gold monomers sputtered from gold nanoparticle obtained in molecular dynamics simulations, by Sandoval and Urbassek [94].*

The experimentally determined kinetic energies of emitted monomers from our experiments are in the range between 2eV and 4 eV. The energy values do not clearly depend on the charge of the projectile, neither on the total kinetic energy of the impact. Compared with the results for collisions of Au atoms with AuNP (shown in fig.5.50 b), the majority of monomers is emitted with kinetic energies from 0 up to 3 eV, with a maximum centered at around 1 eV.

Unfortunately, there are no theoretical values for similar collisions for a case of silver clusters, especially as the cohesive energy of silver (2.95 eV) is lower by 0.9 eV than the cohesive energy of gold (3.81 eV). Furthermore, all calculations are performed for the emission of neutral clusters and no effect of the charge of the projectile and on the emitted and emitting clusters is taken into account. The kinetic energies of positive clusters might differ from those of neutral ones as the metallic nanoparticle can be multiply ionized after the collision, as the impinging ion deposits also energy into electronic degrees of freedom (depending on the projectile,in the range of $\sim$100s eV). We have investigated the kinetic energy of emitted monomers as a function of the multiplicity of the events. The result is shown in fig.5.51.

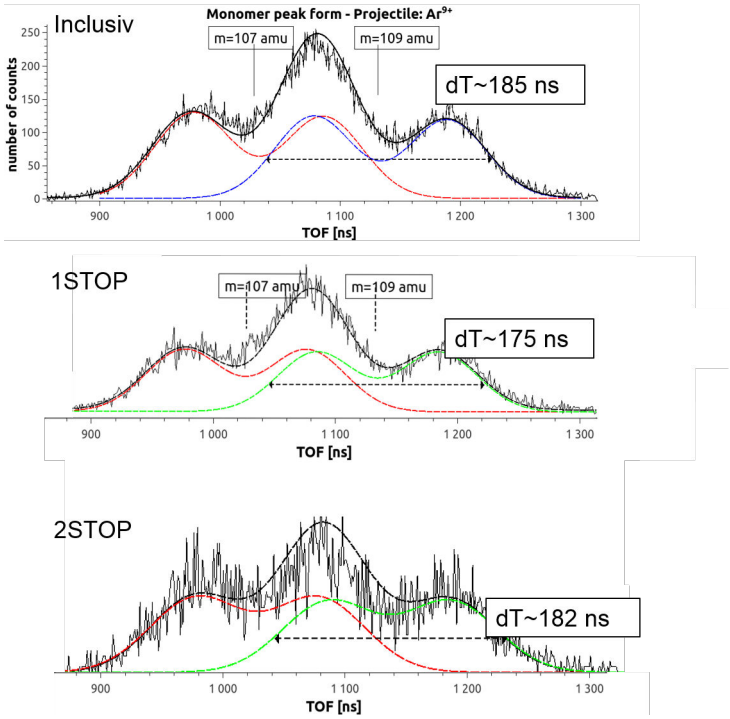

Figure 5.51 *The comparison of the peak-forms (with hypothetical fits) of Ag monomer in case of inclusiv and 1,2 STOP spectra for the collision of silver neutral nanoparticles with Ar^{9+} at kinetic energy of 135 keV.*

In case of bismuth clusters, we observed when going to events with higher multiplicities that the shape of the peak changed, meaning that more energetic fragments characterize the multi-stop spectra. In case of silver clusters, no such effect is observed indicating that in both cases different mechanisms are at play.

5.2.5 Heavy ionized clusters with n/q in the range 70 to 500

As shown already in figure 5.39, the total mass spectrum produced in collisions of Ar^{9+} ions with Ag nanoparticles consists of two parts: 1) the dominant fraction of small singly charged fragments discussed just before, 2) a wide distribution characterized by n/q values between 70 and ∼600.The structures (2) are not mass resolved due to the presence of two isotopes of the silver atoms and the presence of possible contributions from multiply charged species. Therefore, we cannot identify the mass and charge of the large fragments separately as it was possible for the Bi clusters.

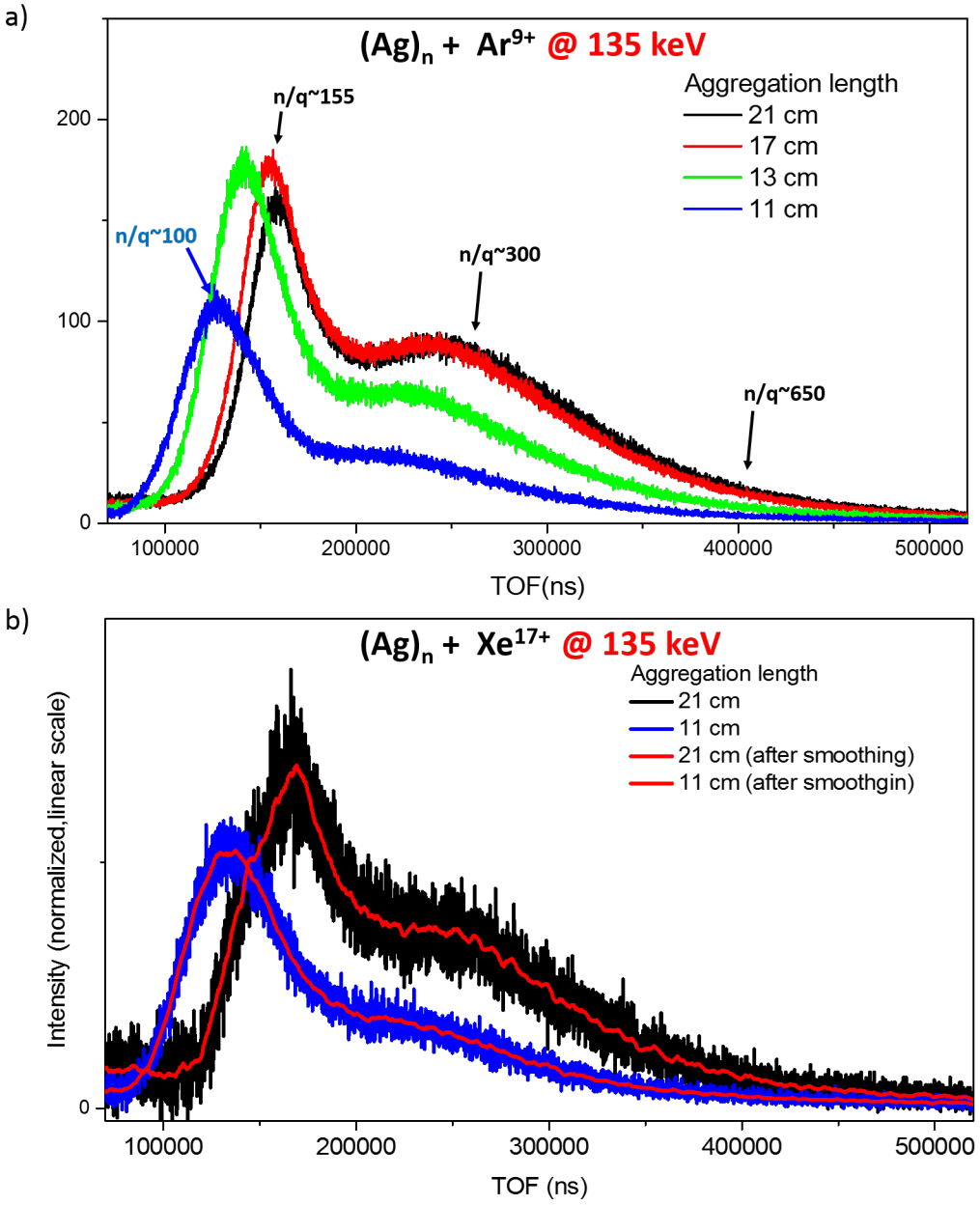

Figure 5.52 *Mass spectra in the n/q range >50 and <700 for two different projectiles: a)Ar^{9+} and b) Xe^{17+}. The spectra correspond to different aggregation lengths in the magnetron cluster source.*

The four curves shown in Fig.5.52 a) correspond to different lengths of the aggregation path in the cluster source, i.e. to aggregation distances between 11 cm to 21 cm. This leads to a strong variation of the average cluster size, being smallest for 11 cm and largest for 21 cm. We observe that the maxima of the distributions clearly shift to smaller values when the initial

nanoparticle size decreases. Similar results are obtained when the projectile Ar^{9+} is replaced by Xe^{17+} projectiles, as shown in fig. 5.52 b).

In fig.5.53 we show the spectra normalized to the ion current and acquisition time, for different projectiles, ranging from O^{2+} to Xe^{25+} for a aggregation length of 11 cm (NP distribution shifted towards smaller sizes). We observe for a fixed initial cluster size, that the maximum of the intensity does not change strongly from O^{2+} up to Ar^{9+} , as well as the position of the intensity maxima varies only slightly (n/q∼100). However, for Xe^{25+} the maximum position shifts towards lower values n/q∼70, as well as the maximum intensity increases by factor 3∼4.

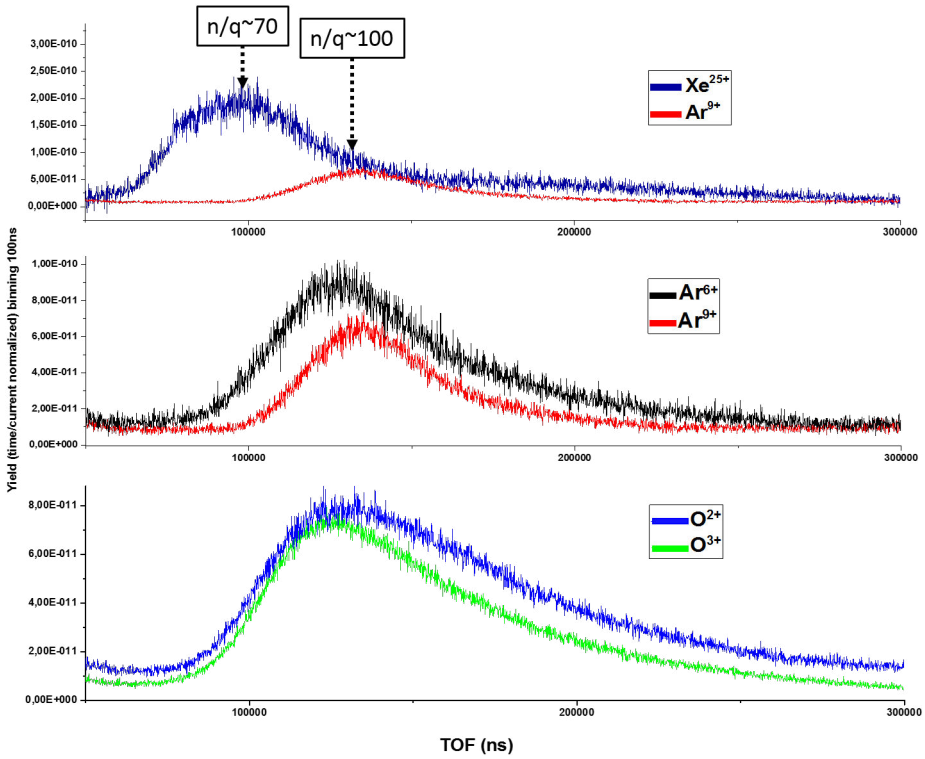

Figure 5.53 *Mass spectra up to n/q∼400 for 4 different projectiles:Xe^{25+} (graph on top),Ar^{9+} (top and middle graph),Ar^{6+} (middle graph),O^{2+} and O^{3+} (bottom graph).*

The mass spectra of silver clusters discussed so far have been measured under conditions which are optimal for the detection of small clusters. This means that we applied relatively short extraction times (20 μs), low extraction fields (1340 V) and short ion beam pulses (1 to 5 μs). This allowed to increase the repetition rate of the experiment and to achieve a sufficient statistics in the spectra. In order to better understand the measured mass spectra, we intended to have access to large cluster masses. Thus, we increased the extraction voltage (2680 V) and the extraction length (300 μs) and, in order to obtain a sufficiently high count rate, also the length of the ion beam pulse (up to 250 μs). As under these conditions the noise during the extraction phase increased, only the spectrum for ToF values larger than the extraction time

can be analyzed with confidence.

A corresponding mass spectrum is shown in fig.5.54 for collisions of Xe^{25+} projectiles with silver clusters. The spectrum shows now masses with n/q values reaching out to ∼3000, with a small maximum at about n/q=1250. As shown by the microscopic investigation of the deposited clusters, the most probable cluster sizes contain for the present reduced aggregation length of 15 cm less or about 3000 atoms. Therefore, we try to attribute the observed structure at n/q∼1250 to the presence of singly or doubly charged species $Ag_n^{1,2+}$.

The intensity of the spectrum increases towards clusters with smaller n/q values. This may have two reasons. On the one hand, the detection efficiency increases towards smaller masses; on the other hand, if we assume multi-electron capture to be an important process (according to the fig.5.37) the presence of multiply charged species and the overlapping of their contributions may explain the intensity increase. The intensity reaches two local maxima at about n/q∼142 and n/q∼230. Starting from an initial average cluster size of Ag_{2500}, without taking into account evaporation processes, these values would correspond to charge states of ∼18 and 11, respectively. The strong decrease towards n/q∼85 would require a charge state of about 30, a value which seems to be reachable with projectiles in charge state q=25+.

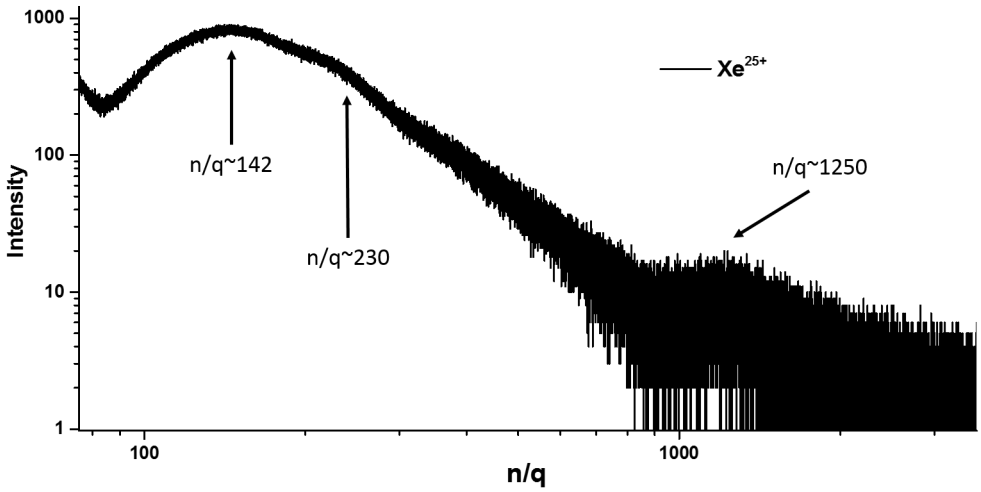

Figure 5.54 *Large n/q mass spectrum after collision with Xe^{25+} for aggregation length of 15 cm.*

As to be seen in fig.5.38, large clusters in these high charge states are still stable as it is likely that they are produced in the stable region of the stability diagram, thus, not provoking the emission of charged small size fragments. Based on the liquid drop model we can estimate that Ag_{2500}^{q+} can withstand a critical charge of about 50, whereas the appearance charge is of the order of ∼30. Thus, the spectrum of clusters with large n/q values, obtained with Xe^{25+} projectiles, can be understood on the basis of multi-electron capture processes, provided that

no long evaporation chains occur.

This interpretation is confirmed in experiments where Cu_n clusters are collided with Xe^{25+} projectiles, which will be discussed further below.

However, when returning to the mass spectra shown in fig.5.53, which are due to collisions with projectiles in low charge states, serious problems arise with the interpretation of the relevance of multi-electron capture processes. For example, the explication of a maximum at n/q$\sim$100 a charge state of 25+ has to be obtained, which is very unlikely by electron capture and contributions from molecular Auger processes in the case of an O^{2+} projectile. Therefore, we attribute these phenomena for ions in low charge states to penetrating collisions. Several arguments support this hypothesis. As already shown in figure 5.37 the geometrical cross section for doubly charge projectiles is larger than that for electron capture. Furthermore, a much larger amount of energy is transferred into the cluster system in electronic and nuclear degrees of freedom (several keV) as it is the case in peripheral capture collisions. Also in penetrating collisions multiple ionization will occur.

Thus, penetrating collisions will also lead to the formation of multiply charged clusters in elevated charge states q, but in particular to a strong reduction of the cluster size n due to long evaporation chains. This might explain the cluster intensities at relatively low values of n/q ($\sim$100) when starting from large n values of about 3000.

Other phenomena which might contribute are: a) the emission of hot electrons, b) the production of convoy electrons following the penetrating projectile, or electron emission by the decay of excited plasmons.

Based on these findings we propose that the experiment supports the formation of clusters with n/q values above n>50 depends strongly on the projectile charge. Ionization and evaporation are favored for projectiles in low charge states penetrating the nanoparticle, whereas multi-electron capture seems to be responsible for the production of clusters in very high charge states when highly charged projectile pass a nanoparticle in peripheral collisions. For intermediate charge states, both contributions might be expected to be important.

5.2.5.1 Copper clusters

During the test phase of the experimental set-up some experiments have been performed with Cu clusters. Unfortunately, the Cu atom has also two isotopic species with the following masses and fractions: 63 amu (69%) and 65 amu (31%), limiting also in this system the obtainable mass resolution. However, it was possible to produce Cu clusters in a medium size range (3.8 nm) and to obtain much higher intensities of the Cu nanoparticle beam. Therefore, higher count rates and a better signal to noise ratio were obtained. The spectra have been measured under similar conditions as used for the Ag_n spectrum shown in fig.5.54. Fig.5.55 shows the mass/charge spectrum measured in collisions of Xe^{25+} projectiles at 375 keV with Cu_n nanoparticles containing about 2500 Cu atoms. Dominant are again contributions from small size fragments, in particular from the monomer to the trimer, with an extension up to

n=40 or 50. A strong contribution of a distribution of clusters in the size range of n/q = 100 to 500 is observed (the signal was about 10 times higher than in the Ag case). This distribution extends to n/q = 2500 where a small peak can be identified as a signal from singly charged clusters (at a mass of ∼150 000 amu).

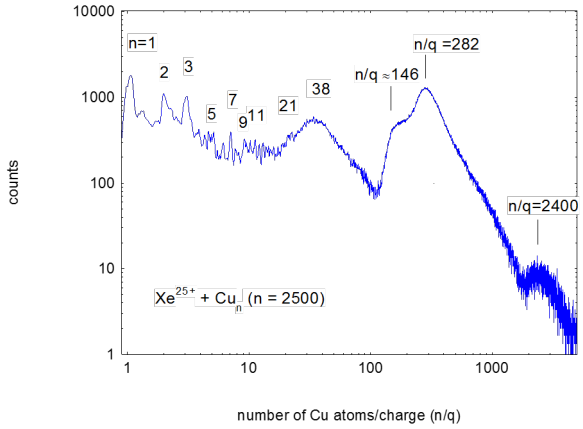

Figure 5.55 *n/q spectrum measured for 375 keV collisions of Xe^{25+} projectiles with Cu clusters containing on the average 2500 atomes. The given numbers represent n or n/q values.*

As in the silver case, which we discussed just before, this distribution can be attributed to multiply charged clusters. The strong maximum can be explained by a superposition of clusters in different charge states. Starting from the signal of singly charged clusters (at n = 2400), small shoulders at n/q =1200 and 800 would correspond to charge states 2 and 3. The maximum occurring at n/q = 282 corresponds to a charge state of 9, the drop in intensity at n/q=146 to the charge state 16, and the minimum at n/q∼100 to a charge of 24. These values are reasonable for a highly charged projectile like Xe^{25+}. Furthermore, the copper cluster Cu_{2500}^{25+} is still stable, as the critical charge for this system is q∼42. On the other hand, this means that the occurence of small fission products is rather unlikely as the fissility is below the appearance size limit.

In fig.5.56 the spectrum obtained after collisions of Cu clusters with O^{6+} projectiles at a kinetic energy of 90 keV is shown in comparison with the Xe^{25+} spectrum. In this case, the drop of the intensity towards smaller n/q sizes occurs much earlier, i.e. at a position which corresponds to a charge state of about 10-11. This indicates that the maximum charge states produced in collisions with O^{6+} are lower than that with Xe^{25+} projectiles. Therefore, these measurements support also the hypothesis that multi-electron capture is the underlying process for the observed distribution at n/q > 50.

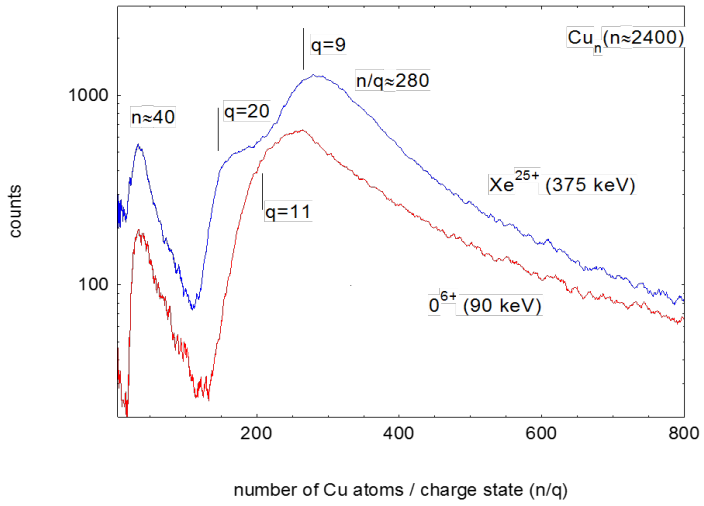

Figure 5.56 *Comparison of two mass/charge spectra obtained with 0^{6+} (90 keV) and Xe^{25+} (375 keV) projectiles. The numbers along the curves give the hypothetical charge states.*

5.2.6 Summary of the results for Ag_n results

Silver nanoparticles with a diameter of ∼6nm containing about 3000 to 5000 atoms have been irradiated with multiply charged positive ions. The resulting mass spectrum of positively charged product ions consists of two distributions representing singly charged small size fragments as well as heavy clusters in the n/q range up to 2000.

The monomer is found to be the dominant fragment independent of the projectile charge state as observed in sputtering events from surfaces. Furthermore, strong shell effects at n=3,9 and 21 and even-odd oscillations are observed in agreement with spectra obtained for the the sputtering of polycrystalline Ag surfaces by 20 keV Xe^+ ions. The relative decrease of the intensity of small fragments with increasing size agrees also well with theoretical predictions concerning the sputtering of Au surfaces by Xe^{17+} ions. Finally, the normalized yield of the three smallest fragments (mainly of the monomer) agrees very well with an empirical formula describing the monomer emission by sputtering through different projectile ions at different kinetic energies. Furthermore, the kinetic energies of emitted monomers yield low values between 2 and 4 eV. These values do not depend on the charge state of the projectile, neither on the multiplicity of the event. This finding disagrees with expectations for the emission of monomer ions by fission of multiply charged clusters, but it is in agreement with energies calculated for the sputtering of Au atoms from Au surfaces.

The position of the observed spectrum of heavy Ag clusters depends on the cluster size. For larger clusters the spectrum is shifted towards larger n/q values. For a given cluster size and low and intermediate charge states (q=2-9) of the projectile, the maximum of the distribution does not shift (n/q∼100), only for very high charge states (Xe^{25+}) the maximum occurs at smaller n/q values (n/q∼70). Measurements, performed with long ion and extraction pulses

showed that the spectrum extents to large n/q values representing large singly or doubly charged clusters (for example Ag_{2500}^{2+}). The intensity increase towards smaller n/q values, is explained by the increasing detection efficiency and by the overlapping of contributions from clusters in different (higher) charge states. Foe Xe^{25+} projectiles, the interpretation of the spectrum requires the presence of clusters in the charge states up to $\sim$16 (or with decreasing intensity up to 28). This is possible as large silver nanoparticles are stable or metastable up to these charges. Test experiments with O^{6+} ions colliding with Cu clusters, support this hypothesis and predict clusters formed in lower charge states. However, the production of clusters with n/q$\sim$100 with doubly charged oxygen projectiles can hardly be explained by this multi-electron capture process. In this case the cross section for penetrating collisions is larger than that for multi-electron capture in peripheral collisions. Thus, we propose that a large amount of energy is deposited in the nanoparticle favoring processes like sputtering, evaporation and ionization.

Summarizing, in ion collisions with large Ag nanoparticles penetrating and peripheral collisions are important. Whereas small fragments are proposed to be formed mainly by ion sputtering from the nano-surface, heavier stable residues or clusters are formed by multi-electron capture as well as by penetrating collisions, their relative importance being dependent on the projectile charge state.

Conclusions and perspectives | 6

In order to study irradiation effects in nanoparticles of Bismuth and Silver, I built up a new experimental set-up based on crossed beams of multiply charged ions and free neutral nanoparticles. Concerning the ion beam I installed an Ar ion beam line which could be used for test experiments replacing the beam of multiply charged ions from the accelerator the use of which was limited in time. Concerning the nanoparticle beam I modified a magnetron discharge to produce intense beams of neutral nanoparticles. This development required the construction of a charge cleaning device (the discharge delivers neutral, positively and negatively charged clusters) and in particular a unit where the size of the neutral nanoparticles could be determined. For this purpose a separate chamber was developed where nanoparticles could be deposited on SiO2 substrates or TEM meshes. By applying AFM and TEM microscopy the size distributions and their dependencies on experimental parameters could be determined.

In addition, a new detection PIPS-based (PIPS detector-Passivated Implanted Planar Silicon detector) device has been constructed, although not yet used in the framework of this thesis, which will allow to measure the number of electrons in coincidence with the mass/charged analyzed, positively charged collision products. As the planned experiments will be performed with a continuous ion beam and constant extraction, the extraction plates geometry had to be modified, for which I have performed specific SIMION simulations. In addition, a PIPS detector and preamplifier had to be integrated at a high potential of -25 kV and the signal to be transferred on ground potential by fiber optics. The electronic device is actually finalized and will be used in near future (see Annex).

6.1 Results on Bismuth Nanoparticles Bi_n

We have studied for the first time the interaction of several multiply charged ions, ranging from O^{3+} up to Xe^{25+} at an acceleration voltage of 15 kV, with Bi clusters containing from about 15 atoms up to several hundreds of atoms. The observed mass spectra yield dominant contributions from small Bi_n^+ ions with $n < 15$, as well as smaller contributions from larger multiply charged clusters. The spectra could be resolved up to charge states of q=6 allowing to construct mass spectra for individual charge states. It was possible to determine from the "cut-off" of the spectra towards small cluster sizes the charge dependent appearance sizes for charge states from 2 to 6. These are the smallest cluster sizes required to stabilize a given charge. These were compared with critical sizes obtained within the liquid drop model and good agreement is found with earlier measurements with sodium clusters concerning the

corresponding fissility values of X$\sim$0.27. In particular we observed an appearance size for doubly charged Bi clusters of $n_{app} = 21$, which is found to be in contrast with earlier electron impact ionization experiments with Bi clusters, yielding a value of 5. This finding is discussed in terms of the semi-metallic or semi-conductor character of the Bi clusters.

A study of the intensity distribution of the small Bi fragments showed a strong dependence on the projectile charge. Whereas for Xe^{25+} projectiles a clear dominance is observed for Bi_1^+ monomer ion, for lower projectile charges the mass distribution becomes more wide, finally showing for O^{3+} projectiles the dominant production of the Bi trimer. These findings can be summarized by stating that highly charged parent system (most likely produced with highly charge projectiles) with high fissilities stabilize by the emission of the smallest charged fragment (Bi_1^+) whereas parent ions in lower charge states (lower fissility) tend to produce larger fragments, in particular charged trimer systems. Furthermore, it is observed that the intensity of the hexamer is strongly reduced indicating the low stability of the hexamer ion.

An analysis of the peak shape of small fragments was performed for the inclusive spectra. This allowed to determine the kinetic energies of individual fragments and to separate contributions from different processes as a function of the fragment size. It is found that small singly charged clusters (n=1-4) are formed with two energy distribution: one high-energy component is characterized by $\sim$5 eV attributed to the asymmetric fragmentation of highly charged parent clusters and a second low-energy part with energies below 1 eV which results from the fragmentation of clusters in low charge states (q=2) or from a sequence of evaporation processes. When increasing the cluster size (n=5-8) the intensity of the high-energy part as well as the correlated energy decreases finally reaching for n=8-18 the energy level of about 200 meV corresponding to evaporation processes. The stable doubly charged fragments with an intrinsic energy of tens of meV are due to pure double ionization processes.

An important part of the analysis was devoted to coincidence spectra, in particular studies were performed for the case of two detected particles (2STOP spectrum, due to the limited detection probability also 3 and 4STOP events contribute to these 2STOP spectra). In particular, coincidences between the prominent small fragments Bi_1^+ and Bi_3^+ and other clusters have been analyzed. The results are the following:

1. The monomer ion is measured with decreasing intensity (by a factor of 10) with small clusters up to n=7, whereas the trimer is measured with similar intensity for n=2 to 7 (exception for n=1). This is in agreement with the conclusion given above, that monomers are emitted from highly charged parent clusters and that larger fragments are correlated with parent clusters in lower charge states where an increased fragment size is favorable.

2. Further insight into the fragmentation processes is given by the analysis of the kinetic energy of small fragments (Bi_1^+ and Bi_3^+) measured in correlation with heavy residues. For the trimer it is found that for the correlation with small residues (n/q=11-40) low- and high-energy contributions are present. The low energy part disappears for n/q= 40 to 60

and comes back for n/q=160 to 360. These results propose that for small n/q values low energies are produced by the fragmentation of systems in low and intermediate charge states. With increasing n/q values, fragmentation of systems in higher charge states produce mainly high-energy fragments, whereas for even higher n/q values, due to the limitation of the cluster sizes in the initial beam, lower charge states of the parent systems become dominant forming again low-energy fragments. In the case of the monomer low and high-energy parts are always present with a particular dominance for high n/q values. This might be interpreted as contributions from sputtering events which favor the emission of monomers.

3. By a comparison of the kinetic fragment energies with calculated Q-values of the fragmentation processes different mechanisms are discussed depending on the n/q values and the fissilities of the decaying system. This concerns for the small systems binary asymmetric fission events or the sequential emission of several small fragments and for systems with fissilities X>1 the simultaneous emission of a large number of singly charged small-size fragments, yielding final residue ions in low charge states and hence with high n/q values.
4. Finally, the analysis of small particle islands in the 2D coincidence map allowed to separate different fragmentation mechanisms. On the one hand the emission of two fragments in the same direction which might be a sign for charge localization; on the other hand the emission in opposite directions close to a binary fragmentation where a third fragments carries only a small momentum; and finally, the emission of two fragments in opposite directions where a large amount of the missing momentum is carried by another particle.

6.2 Results on Silver Nanoparticles Ag_n

We have studied collisions of multiply charged ions (Xe^{25+}, Xe^{17+}, Ar^{9+}, Ar^{6+}, O^{6+}, O^{3+}, and O^{2+}) with large metallic silver nanoparticles. In addition, some collisions with Cu_n nanoparticles have been performed. The size of the neutral nanoparticles has been determined after deposition on a substrate with the aid of AFM and TEM microscopy. The average size of the Ag nanoparticles was found to be 6nm in diameter corresponding to 5000 atoms. For smaller aggregation lengths this value decreased to about 2500 atoms. The average copper clusters were found to have a diameter of 3.8 nm containing 2400 Cu atoms. Concerning the Ag particles, the measured mass spectrum consists of two distinct distributions: 1) a high-intensity part which includes small singly charged fragments with the dominance of the monomer, and 2) a wide distribution of multiply charged clusters at n/q values above 50, reaching out to $\sim$ 2000.

The distribution of the small-size fragments shows some typical characteristics:

1. The dominant fragment is always the monomer ion, independent of the projectile charge and hence the average charge state of the parent ion.

2. A strong intensity decrease towards larger fragments occurs for n=3, n=9 and n=21, which is interpreted as a consequence of electronic shell closures
3. A strong even-odd oscillation is observed favoring the intensity of "odd" systems. This observation (1. and 2.) is in excellent agreement with the sputtering of polycrystalline Ag surfaces by 20 keV Xe^+ ions.
4. The normalized yield of the three smallest fragments (mainly of the monomer) agrees very well with an empirical formula describing the monomer emission by sputtering through different projectile ions at different kinetic energies
5. The analysis of the kinetic energy of emitted monomers yields a value of 2 to 4 eV. No systematic dependence on the charge state of the projectile, neither on the multiplicity of the event is observed. This disagrees with expectations for the emission of monomer ions by fission of multiply charged clusters, but it is in agreement with energies calculated for the sputtering of Au atoms from Au surfaces by Au projectiles.

From all these observations and arguments we conclude that the production of small size fragments in ion collisions with large Ag nanoparticles is mainly due to sputtering phenomena. The distribution of heavy fragments (n/q $>$ 50) is proposed to have different mechanisms.

1. The position of the observed spectrum depends on the aggregation length in the cluster source and hence on the cluster size. For larger clusters the spectrum is shifted towards larger n/q values.
2. For projectiles in low and intermediate charge states (q=2 to 9) the spectrum position is nearly constant (n/q$\sim$100), but it shifts towards smaller values (n/q$\sim$70) for projectiles like Xe^{25+}.
3. The spectrum, measured with Xe^{25+}, shows, when measured under optimized conditions for the detection of large particles, a structure due to the formation of doubly charged Ag^{2+}_{2500} ions. The intensity which is increasing towards smaller n/q values, is explained by the increasing detection efficiency and by the overlapping of contributions from clusters in different (higher) charge states.
4. This interpretation is reasonable as such large nanoparticles can resist excess charges up to about 30. Further support for this hypothesis is given by experiments with Cu_n particles, which demonstrates that the charge states required to explain the measured spectrum are lower in the case of O^{6+} projectiles than for Xe^{25+} ones.
5. For projectiles in very low charge states like O^{2+} the described scenario seems not to be realistic. Here the cross section for penetrating collisions is larger than that for multi-electron capture in peripheral collisions. Thus in most collisions, a large amount of energy is deposited in the nanoparticle favoring processes like sputtering, evaporation and ionization.

Summarizing, in ion collisions with large Ag nanoparticles penetrating and peripheral collisions are important. Whereas small fragments are proposed to be formed mainly by ion

sputtering from the nano-surface, heavier residues or clusters might be due to both types of collisions depending on the projectile charge state. Low charge state favor a high energy deposition inducing ionization and evaporation processes, whereas high projectile charge state will lead to the production of multiply charged nanoparticles which turn out to be mostly stable due to their large size. This interpretation has to be confirmed by further experimental and theoretical studies where the dependencies on the initial cluster size and the projectile charge have to be analyzed in more detail.

6.3 Comparison of the ion interaction with Bi and Ag clusters

Both targets have been studied in a different size range. Whereas the average Bi diameter was of the order of 2 nm, containing about 300 Bi atoms, the silver nanoparticles measured on the average 6 nm, containing up to 5000 atoms. This difference, in addition to others, changes the ratio of penetrating and peripheral collisions very strongly. In the case of Bismuth, most product ions are formed in peripheral collisions by electron capture to multiply charged ions. Thus, stable multiply charged clusters are produced which are stable when the cluster size is above the appearance size. For smaller sizes, the intermediate clusters decay by various fission processes, forming singly charged, high energetic small fragments. Therefore, the findings can be explained by the characteristics of an "ion-atom" or "ion-small molecule" collision.

In the case of large Ag nanoparticles, one has to separate between projectiles in high and in low charge states. In the first case, a large amount of the particles is multi-ionized in peripheral collisions up to very high charge states. Due to the large number of atoms, contained in the cluster, the systems are stable even in very high charge states (for example for q=25) and do not emit small size fragments, which are nevertheless being measured. As the geometrical cross section becomes larger, for projectiles in low charge states even above the electron capture cross section (in peripheral collisions), penetrating processes become important leading to preferential sputtering of monomers and high energy transfers to the nanoparticles. Thus, in this case both mechanisms do occur. On the one hand multi-electron capture in peripheral collisions, representing the "ion-atom" character of the collision, on the other hand sputtering and evaporation due to the high energy transfer, underlining the "ion-nano-surface character" of the collision system.

6.4 Consequence in the context of future nanoparticle-based hadrontherapies

The main damaging mechanisms of radiosensitizers is believed to be due to an increased production of radical ions and secondary electrons, although also the presence of metallic species

might induce toxic effects in the cells which can reduce their lifetimes.

In this thesis I have shown, that the interaction of low energy ions in the range of 10s to 100s of keV with "free" metallic nano-objects in the nm-size range is destructive and produces many charged metallic particles, from atomic ions up to large metallic clusters and fragments. This was explained to be due to two different mechanisms- multi-ionization of nanoparticles up to very high charge states by electron capture followed by the emission of small fission products (depending on the cluster size), as well as the production of small clusters due to ion sputtering at the nanoparticle surface. In both cases the spectra are dominated by small energetic fragments, thus increasing the concentration of small metallic particles. The toxicity effects associated with the presence of heavy metal particles in cells are known and can be associated to numerous mechanisms. They can act as a pseudo-element in the body and thus may interfere with metabolic cellular processes. Especially, metal-induced increased production of free radicals leads to oxidative stress and excessive damage. The antibiotic properties of silver are known since many years. Silver nano-surfaces get easily ionized by O_2^+ ions as well as other molecules in the bio-environment. This leads to the release of the toxic ion Ag_1^+ that can penetrate easily through cellular membranes. By doing so, it can damage the cell by the activation of antioxidant enzymes, the depletion of the antioxidant molecules like glutathione, by the binding and consequent disabling of proteins and by the induction of cell membrane damages. Thus, the increased concentration of small metal particles, induced by ion impact with larger ones, may also increase the toxic effects within the cells, finally leading to cell death.

In Hadron Therapy treatments normally coated or liganded nanoparticles are supposed to be used. When the ion passes in the proximity of a metallic core (for example through the coating that can span few nm out of the radius of metallic core) the interaction and energy deposition may lead to its local destruction, leaving the surface of the nano-metal unprotected to the cellular environment. In such a way, for example molecular oxygen can reach and react with the silver surface atoms to form silver oxides, which later in other reactions may release toxic silver ions.

In our experiments we were using low energy beam of ions, which in case of a hadrontherapy treatment would correspond to the final stage of the traversing ion and last few mm of the trajectory (end of the Bragg peak). However, because of the "depth-profiling" character of the irradiation (SOBP), such phenomena would occur in the whole volume of interest.

Multi-electron capture processes, in particular by highly charged ions, occur into highly excited projectile states. Thus, the probability for Auger processes becomes important and may increase strongly the secondary electron yield. However, a quantification of this phenomenon requires a direct measurement of the electron yield (see Perspectives).

6.5 Perspectives

Based on the obtained results and the constructed experimental device the following studies are foreseen in the near future.

Determination of the number of electrons emitted during ion collisions with metallic nanoparticles

As discussed further above and in the Annex, a device has been prepared and constructed which will allow measuring the number of electrons liberated in a single collision event. This information is important in the framework of the nanoparticle-enhanced hadron therapy, as secondary electrons are supposed to be the most efficient ingredients in damaging biological tissues in addition to radical formation. The principle of the measurement will be based on a coincidence between extracted negative electrons and the positive metal cluster ions or fragments. The experimental device has been completed; only the electronic chain, including the transfer of the signal from a high potential (25 kV) to ground potential, has to be finished. First test measurements are foreseen with a target of the radio-sensitizer halo-uracil, which can be easily realized as no buffer gas is required, which contributes to the secondary electron production. In a second step, Ag, Au and Bi nanoparticles will be used.

Experiments with decorated metal systems

Administered metallic nanoparticles will be in a cellular environment when irradiation occurs in ion beam cancer therapy. Therefore, irradiation studies in the gas phase are mainly relevant when the metallic nanoparticles are decorated with organic molecules and ligands which are also required for a selective uptake in the tumorous cells. In these studies a beam of initially pure metal NP will be produced and guided through a pick-up cell before being irradiated with multiply charged ions. This device has already been developed and can be installed easily. This will allow to fix water molecules or amino acids or peptides on the metallic NPs.

Experiments with mixed carbon systems of atmospheric relevance

The present device is capable to irradiate also mixed carbon systems or soot particles which are relevant for the chemistry of the Earth's atmosphere. It has been shown that low-energy ions may not only provoke fragmentation of molecular clusters of polycyclic aromatic hydrocarbon molecules (PAHs), but can also induce growth processes based on the formation of covalent bonds. These mechanisms can be studied in mixed clusters as well. Preliminary experiments have shown that the diameter of soot particles increases strongly when they are passing through a gas target containing PAH molecules. It is interesting to study these growth and adsorption processes in more detail using the magnetron aggregation source as a soot-particle generator, the pick-up cell and the present setup.

Bibliography

[1] Henri Becquerel. Sur les radiations émises par phosphorescence. *Comptes Rendus*, 122:420–421, 1896.

[2] W. C. Röntgen. On a new kind of rays. *Science*, 3(59):227–231, 1896.

[3] Katsura Kosaki, Swantje Ecker, Daniel Habermehl, Stefan Rieken, Oliver Jäkel, Klaus Herfarth, Jürgen Debus, and Stephanie E. Combs. Comparison of intensity modulated radiotherapy (imrt) with intensity modulated particle therapy (impt) using fixed beams or an ion gantry for the treatment of patients with skull base meningiomas. *Radiation Oncology*, 7:44, 2012.

[4] Claude Le Sech, Katsumi Kobayashi, Noriko Usami, Yoshiya Furusawa, Erika Porcel, and Sandrine Lacombe. Comment on "therapeutic application of metallic nanoparticles combined with particle-induced x-ray emission effect". *Nanotechnology*, 23:078001, 2012.

[5] Suneil Jain, Jonathan A. Coulter, Alan R. Hounsell, Karl T. Butterworth, Stephen J. McMahon, Wendy B. Hyland, Mark F. Muir, Glenn R. Dickson, Kevin M. Prise, Fred J. Currell, Joe M. O'Sullivan, and David G. Hirst. Cell-specific radiosensitization by gold nanoparticles at megavoltage radiation energies. *International Journal of Radiation Oncology Biology Physics*, 79:531–539, 2011.

[6] E. Surdutovich, A. V. Yakubovich, and A. V. Solov'yov. Multiscale approach to radiation damage induced by ion beams: complex dna damage and effects of thermal spikes. *The European Physical Journal D / Atomic, Molecular, Optical and Plasma Physics*, 60:101–108, 2010.

[7] Eugene Surdutovich, Alexander V. Yakubovich, and Andrey V. Solov'yov. Biodamage via shock waves initiated by irradiation with ions. *Scientific Reports*, 3:1289, 2013.

[8] James F Hainfeld, Daniel N Slatkin, and Henry M Smilowitz. The use of gold nanoparticles to enhance radiotherapy in mice. *Physics in Medicine Biology*, 49(18):N309, 2004.

[9] Lawrence F.; Driessen Wouter H. P.; Arap Wadih; Pasqualini Renata; Gillin Michael Polf, Jerimy C.; Bronk. Enhanced relative biological effectiveness of proton radiotherapy in tumor cells with internalized gold nanoparticles. *Applied Physics Letters*, 98, 2011.

[10] Xiang-Yu Su, Pei-Dang Liu, Hao Wu, and Ning Gu. Enhancement of radiosensitization by metal-based nanoparticles in cancer radiation therapy. *Cancer Biol. Med.*, 11:86–91, 2014.

[11] Deep Kwatra, Anand Venugopal, and Shrikant Anant. Nanoparticles in radiation therapy: a summary of various approaches to enhance radiosensitization in cancer. *Translational Cancer Research*, 2(4), 2013.

[12] Lenka Štefančíková, Sandrine Lacombe, Daniela Salado, Erika Porcel, Eva Pagáčová, Olivier Tillement, François Lux, Daniel Depeš, Stanislav Kozubek, and Martin Falk. Effect of gadolinium-based nanoparticles on nuclear dna damage and repair in glioblastoma tumor cells". *Journal of Nanobiotechnology*, 14(1):63, Jul 2016.

[13] Sean X. Zhang, Junfang Gao, Thomas A. Buchholz, Zhonglu Wang, Mohammad R. Salehpour, Rebekah A. Drezek, and Tse-Kuan Yu. Quantifying tumor-selective radiation dose enhancements using gold nanoparticles: a monte carlo simulation study. *Biomedical Microdevices*, 11:925, 2009.

[14] Erika Porcel, Samuel Liehn, Hynd Remita, Noriko Usami, Katsumi Kobayashi, Yoshiya Furusawa, Claude Le Sech, and Sandrine Lacombe. Platinum nanoparticles: a promising material for future cancer therapy? *Nanotechnology*, 21:85103, 2010.

[15] Alexey V. Verkhovtsev, Andrei V. Korol, and Andrey V. Solov'yov. Electron production by sensitizing gold nanoparticles irradiated by fast ions. *The Journal of Physical Chemistry C*, 119:11000–11013, 2015.

[16] J. Conde, G. Doria, and P. Baptista. Noble metal nanoparticles applications in cancer. *Journal of Drug Delivery*, 2012:751075, 2012.

[17] C. A. Hoffman, J. R. Meyer, F. J. Bartoli, A. Di Venere, X. J. Yi, C. L. Hou, H. C. Wang, J. B. Ketterson, and G. K. Wong. Semimetal-to-semiconductor transition in bismuth thin films. *Phys. Rev. B*, 48:11431–11434, 1993.

[18] Mainul Hossain and Ming Su. Nanoparticle location and material-dependent dose enhancement in x-ray radiation therapy. *The Journal of Physical Chemistry C*, 116(43):23047–23052, 2012. PMID: 23393610.

[19] F. Chandezon, C. Guet, B. A. Huber, D. Jalabert, M. Maurel, E. Monnand, C. Ristori, and J. C. Rocco. Critical sizes against coulomb dissociation of highly charged sodium clusters obtained by ion impact. *Physical Review Letters*, 74:3784, 1995.

[20] P. Blaise, S. A. Blundell, C. Guet, and Rajendra R. Zope. Charge-induced fragmentation of sodium clusters. *Phys. Rev. Lett.*, 87:063401, Jul 2001.

[21] T. Schlathölter, F. Alvarado, S. Bari, A. Lecointre, R. Hoekstra, V. Bernigaud, B. Manil, J. Rangama, and B. A. Huber. Ion-Induced Biomolecular Radiation Damage: From Isolated Nucleobases to Nucleobase Clusters. *ChemPhysChem*, 7:2339–2345, 2006.

[22] B. Manil, L. Maunoury, B. A. Huber, J. Jensen, H. T. Schmidt, H. Zettergren, H. Cederquist, S. Tomita, and P. Hvelplund. Highly charged clusters of fullerenes: Charge mobility and appearance sizes. *Physical Review Letters*, 91:215504, 2003.

[23] T. Jahnke, H. Sann, T. Havermeier, K. Kreidi, C. Stuck, M. Meckel, M. Schöffler, N. Neumann, R. Wallauer, S. Voss, A. Czasch, O. Jagutzki, A. Malakzadeh, F. Afaneh, Th. Weber, H. Schmidt-Böcking, and R. Dörner. Ultrafast energy transfer between water molecules. *Nature Physics*, 6:139–142, 2010.

[24] Melanie Mucke, Markus Braune, Silko Barth, Marko Förstel, Toralf Lischke, Volker Ulrich, Tiberiu Arion, Uwe Becker, Alex Bradshaw, and Uwe Hergenhahn. A hitherto unrecognized source of low-energy electrons in water. *Nature Physics*, 6:143–146, 2010.

[25] R Maisonny, M Capron, S Maclot, J C Poully, A Domaracka, A Méry, L Adoui, P Rousseau, and B A Huber. Ion interactions with pure and mixed water clusters. *Journal of Physics: Conference Series*, 438(1):012007, 2013.

[26] B. Liu, S. Brøndsted Nielsen, P. Hvelplund, H. Zettergren, H. Cederquist, B. Manil, and B. A. Huber. Collision-induced dissociation of hydrated adenosine monophosphate nucleotide ions: Protection of the ion in water nanoclusters. *Phys. Rev. Lett.*, 97:133401, 2006.

[27] Pal Markush, Paola Bolognesi, Antonella Cartoni, Patrick Rousseau, Sylvain Maclot, Rudy Delaunay, Alicja Domaracka, Jaroslav Kocisek, Mattea C. Castrovilli, Bernd A. Huber, and Lorenzo Avaldi. The role of the environment in the ion induced fragmentation of uracil. *Physical Chemistry Chemical Physics*, 18:16721–16729, 2016.

[28] Nam Joon Kim, Yung Sam Kim, Gawoon Jeong, Tae Kyu Ahn, and Seong Keun Kim. Hydration of dna base cations in the gas phase. *International Journal of Mass Spectrometry*, 219:11–21, 2002.

[29] A. Domaracka, M. Capron, S. Maclot, J.-Y. Chesnel, A. Méry, J.-C. Poully, J. Rangama, L. Adoui, P. Rousseau, and B. A. Huber. Ion interaction with biomolecular systems and the effect of the environment. *J. Phys.: Conf. Series*, 373:012005, 2012.

[30] G. Rizza, P. E. Coulon, V. Khomenkov, C. Dufour, I. Monnet, M. Toulemonde, S. Perruchas, T. Gacoin, D. Mailly, X. Lafosse, C. Ulysse, and E. A. Dawi. Rational description of the ion-beam shaping mechanism. *Phys. Rev. B*, 86:035450, 2012.

[31] G. Rizza, H. Cheverry, T. Gacoin, A. Lamasson, and S. Henry. Ion beam irradiation of embedded nanoparticles: Toward an in situ control of size and spatial distribution. *Journal of Applied Physics*, 101:014321, 2007.

[32] V. Bechtold, N. Chan-Tung, S. Dousson, R. Geller, B. Jaquot, and Y. Jongen. *Nucl. Instrum. Methods*, 178:305, 1980.

[33] Y. Higurashi, T. Nakagawa, M. Kidera, T. Kageyama, T. Aihara, M. Kase, and Y. Yano. *Nucl. Instrum. Methods A*, 510:206, 2003.

[34] K. Bernhardi and K. Wieseman. *Plasma Physics*, 14:1073, 1972.

[35] S. Bliman, R. Geller, W. Hess, and B. Jaquot. *IEEE Trans. Nucl. Sci*, NS-19:200, 1974.

[36] R. Geller. *Electron Cyclotron Resonance Ion Source and ECR Plasmas*. Institute of Physics. Publishing, Bristol, 1996.

[37] D. Hitz, G. Melin, and A. Girard. *Rev. Sci. Instrum*, 71:839, 2000.

[38] I. Yamada, H. Usui, and T. Takagi. The formation and kinetics of ionized cluster beams. *Z Phys D - Atoms, Molecules and Clusters*, 3:137, 1986.

[39] W. Lotz. *Z. Phys.*, 216:241, 1968.

[40] A. Mueller, E. Salzborn, R. Frodi, R. Becker, H. Klein, and H. Winter. *J. Phys. B*, 13:1877, 1980.

[41] Makoto Asakawa Hitoshi Tanaka Takashi Maekawa Masaki Uchida, Shiho Fukumoto and Yasushi Terumichi. Electron cyclotron resonance plasma produced with a closed spheroidal electron cyclotron resonance surface in a simple cusp field. *Japanese Journal of Applied Physics*, 38(8A):L885, 1999.

[42] E. W. Becker, K. Bier, and W. Henkes. *Z. Phys.*, 146:333, 1956.

[43] W. Z. Henkes. *Naturforschung*, 16a:842, 1961.

[44] H. W. Kroto, J. R. Heath, S. C. O'Brien, R. F. Curl, and R. E Smalley. C_{60}: Buckminsterfullerene. *Nature*, 318(6042):162–163, 1985.

[45] H. Haberland. *Clusters of Atoms and Molecules Theory, Experiment, and Clusters of Atoms*. Springer, Springer Series in Chemical Physics, 1994.

[46] V. Bernigaud. *Etude de la fragmentation de molécules d'intérêt biologique isolées et nanosolvatées induite par collision avec des ions multichargés et des particules neutres*. PhD thesis, université de Caen Basse-Normandie, 2009.

[47] F. Chandezon, B. Huber, and C. Ristori. A new-regime Wiley-McLaren time-of-flight mass spectrometer. *Rev. Sci. Instrum.*, 65:3344–3353, 1994.

[48] C. Bréchignac and Ph. Cahuzac. Threshold behavior of laser ionization spectra for small potassium clusters. *Chemical Physics Letters*, 117(4):365 – 370, 1985.

[49] C. Bréchignac, Ph. Cahuzac, F. Carlier, M. de Frutos, A. Masson, and J. Roux. Generation of rare earth metal clusters by means of the gas-aggregation technique. *Zeitschrift für Physik D Atoms, Molecules and Clusters*, 19:195–197, 1991.

[50] C. B. Alcock, V. P. Itkin, and M. K. Horrigan. Vapor pressure of metallic elements: 298-2500 k. *Canadian Metallurgical Quarterly*, 23:309–313, 1984.

[51] *Handbook of Chemistry and Physics*. CRC press, 78th edition, 1997.

[52] Platinum. *Metals Rev.*, 51, 2007.

[53] Ch. Siekmann, H. R.and Lüder, J. Faehrmann, H. O. Lutz, and K.H. Meiwes-Broer. The pulsed arc cluster ion source (pacis). *Zeitschrift fur Physik D Atoms, Molecules and Clusters*, 20(1):417–420, 1991.

[54] H. Haberland. Filling of micron-sized contact holes with copper by energetic cluster impact. *Journal of Vacuum Science & Technology A Vacuum Surfaces and Films*, 12:2925, 1994.

[55] Omar Kamalou, Jimmy Rangama, Jean-Marc Ramillon, Patrick Guinement, and Bernd A. Huber. Production of pulsed, mass-selected beams of metal and semiconductor clusters. *Review of Scientific Instruments*, 79:063301, 2008.

[56] Peter Sigmund. Theory of sputtering. i. sputtering yield of amorphous and polycrystalline targets. *Physical Review*, 184:383–416, 1969.

[57] O. Almen and G. Bruce. Sputtering experiments in the high energy region. *Nuclear Instruments and Methods*, 11:279 – 289, 1961.

[58] L. I. Maissel. The deposition of thin films by cathode sputtering. *Physics of thin films*, 3:61, 1971.

[59] N. Laegreid and G. K. Wehner. Sputtering yields of metals for ar^+ and ne^+ ions with energies from 50 to 600 ev. *J. Appl. Phys.*, 32:365–369, 1969.

[60] Omar Kamalou. *Faisceau d'agrégats sélectionés en taille: Réalisation et premiers experiences*. PhD thesis, université de Caen Basse-Normandie, 2007.

[61] N. R. Daly. Scintillation type mass spectrometer ion detector. *Review of Scientific Instruments*, 31:264–267, 1960.

[62] H.P. Winter, M. Vana, G. Betz, F. Aumayr, H. Drexel, P. Scheier, and T.D. Maerk. Suppresion of potential electron emission for impact of slow multicharged fullerenes on clean gold. *Phys. Rev. A*, 56:3007–3010, 1997.

[63] F. Thum and Hofer W.O. No enhanced electron emission from high-density atomic collision cascades in metals. *Surf. Sci.*, 90:331–338, 1979.

[64] Paul-Gerhard Reinhard and Eric Suraud. *Introduction to Cluster Dynamics*. Wiley, 2003.

[65] Matthias Brack. The physics of simple metal clusters: self-consistent jellium model and semiclassical approaches. *Review of Modern Physics*, 65:677, 7 1993.

[66] L. Plagne and C. Guet. Highly ionized but weakly excited metal clusters in collisions with multicharged ions. *Physical Review A*, 59:4461–4469, 1999.

[67] B.H. Brandsen and M.R.C. McDowell. *Charge exchange and Theory of Ion-Atom Collisions*. Clarendon, Oxford, 1992.

[68] Hiroshi Ryufuku, Ken Sasaki, and Tsutomu Watanabe. Oscillatory behavior of charge transfer cross sections as a function of the charge of projectiles in low-energy collisions. *Physical Review A*, 21:745, 1980.

[69] A Niehaus. A classical model for multiple-electron capture in slow collisions of highly charged ions with atoms. *Journal of Physics B Atomic and Molecular Physics*, 19:2925, 1986.

[70] Joachim Burgdörfer, Peter Lerner, and Fred W. Meyer. Above-surface neutralization of highly charged ions: The classical over-the-barrier model. *Physical Review A*, 44:5674, 1991.

[71] Serge Martin, Li Chen, Alain Denis, and Jean Désesquelles. Very high multiplicity distributions of electrons emitted in multicapture collision between xe^{25+} and c_{60}. *Phys. Rev. A*, 59:R1734–R1737, 1999.

[72] S. Tomita, H. Lebius, A. Brenac, F. Chandezon, and B. A. Huber. Energetics in charge-separation processes of highly charged fullerene ions. *Phys. Rev. A*, 67:063204, 2003.

[73] F.R.S. Rayleigh. Xx. on the equilibrium of liquid conducting masses charged with electricity. *Philosophical Magazine*, 14(87):184–186, 1882.

[74] Denis Duft, Tobias Achtzehn, Rene Müller, Bernd A. Huber, and Thomas Leisner. Coulomb fission: Rayleigh jets from levitated microdroplets. *Nature*, 421:128, 2003.

[75] T. Bergen, X. Biquard, A. Brenac, F. Chandezon, B. A. Huber, D. Jalabert, H. Lebius, M. Maurel, E. Monnand, J. Opitz, A. Pesnelle, B. Pras, C. Ristori, and J. C. Rocco. Multiply charged cluster ion crossed-beam apparatus: Multi-ionization of clusters by ion impact. *Review of Scientific Instruments*, 70(8):3244–3253, 1999.

[76] C. Bréchignac, Ph. Cahuzac, F. Carlier, J. Leygnier, and A. Sarfati. Unimolecular coulombic fission in doubly charged alkali-metal clusters. *Phys. Rev. B*, 44:11386–11393, 1991.

[77] U. Näher, S. Bj{ornholm, S. Frauendorf, F. Garcias, and C. Guet. Fission of metal clusters. *Physics Reports*, 285:245–320, 1997.

[78] Mingyang Chen, Jason E. Dyer, Keijing Li, and David A. Dixon. Prediction of structures and atomization energies of small silver clusters, (ag)n, n $<$ 100. *The Journal of Physical Chemistry A*, 117:8298–8313, 2013.

[79] Rebecca Kelting, Alexander Baldes, Ulrike Schwarz, Thomas Rapps, Detlef Schooss, Patrick Weis, Christian Neiss, Florian Weigend, and Manfred M. Kappes. Structures of small bismuth cluster cations. *The Journal of Chemical Physics*, 136:154309, 2012.

[80] C. Bréchignac, Ph. Cahuzac, F. Carlier, and M. de Frutos. Asymmetric fission of na_n^{++} around the critical size of stability. *Phys. Rev. Lett.*, 64:2893–2896, 1990.

[81] J.F. Ziegler, J.P. Biersack, and U. Littmark. *The stopping and range of ions in solids*. Pergamon Press, 1985.

[82] Giovanni Sanna and Giuseppe Tomassetti. *Introduction To Molecular Beams Gas Dynamics*. Imperial College Press; Distributed by World Scientific Pub, 2005.

[83] W. Schulze, Winter B., and Goldenfeld I. *Physical Review B*, 38:18, 1988.

[84] P. Pfau. PhD thesis, University of Konstanz, 1985.

[85] A. Hoareau, P. Melinon, B. Cabaud, D. Rayane, B. Tribollet, , and M. Broyer. *Chem. Phys. Lett.*, 143:602, 1988.

[86] Jun Ma, Jun Ma, Ruizhi Xu, Ruizhi Xu, Jianfei Sun, Jianfei Sun, Di Zhao, Di Zhao, Jinlong Tong, Jinlong Tong, Xinchen Sun, and Xinchen Sun. Nanoparticle surface and nanocore properties determine the effect on radiosensitivity of cancer cells upon ionizing radiation treatment. *Journal of Nanoscience and Nanotechnology*, 13(602):1472–5, 2013.

[87] Liu P., Jin H., Guo Z., Ma J., Zhao J., Li D., Wu H., and Gu N. Silver nanoparticles outperform gold nanoparticles in radiosensitizing u251 cells in vitro and in an intracranial mouse model of glioma. *Int J Nanomedicine*, 11:5003–5014, 2016.

[88] S. Krückeberg, G. Dietrich, K. Lützenkirchen, L. Schweikhard, C. Walther, and J. Ziegler. Collision induced dissociation of doubly charged silver clusters ag_n^{2+}, n=21,22,23. *Hyperfine Interactions*, 108(1):107–114, Jun 1997.

[89] Wolfgang Harbich; Christian Félix. Mass selected cluster deposition in strongly or weakly interacting media. *Comptes Rendus Physique*, 3, 2002.

[90] A. Wucher and M. Wahl. Cluster emission in sputtering. *Conference Invited Lecture Proceedings of 10th International Conference on Secondary Ion Mass Spectrometry,Ed.A. Benninghoven, B. Hagenhoff and H.W. Werner Wiley*, pages 65–72, 1997.

[91] Julius Jellinek, editor. *Theory of Atomic and Molecular Clusters: With a Glimpse at Experiments*. Springer, 1999.

[92] I. Katakuse, T. Ichihara, Y. Fujita, T. Matsuo, T. Sakurai, and H. Matsuda. Mass distributions of copper, silver and gold clusters and electronic shell structure. *International Journal of Mass Spectrometry and Ion Processes,*, 67:229–236, 1985.

[93] T. T. Järvi, J. A. Pakarinen, A. Kuronen, and K. Nordlund. Enhanced sputtering from nanoparticles and thin films: Size effects. *EPL (Europhysics Letters)*, 82:26002, 2008.

[94] L. Sandoval and H. M. Urbassek. Collision-spike Sputtering of Au Nanoparticles. *Nanoscale Research Letters*, 10:314, 2015.

[95] N. Matsunami, Y. Yamamura, Y. Itikawa, N. Itoh, Y. Kazumata, S. Miyagawa, K. Morita, R. Shimizu, and H. Tawara. Energy dependence of the yields of ion-induced sputtering of monatomic solids.

Annexes

Device to measure the number of emitted electrons

A

In order to study the radio-sensitizing effect of large metallic nanoparticles in the treatment of cancer by ion irradiation, I have developed an experimental device which will allow to measure the number of electrons which are emitted during the collision event. These secondary electrons are suspected to be one reason for killing cancer cells more efficiently as their number is expected to be increased when ions collide with large metallic nanoparticles. In long term, the

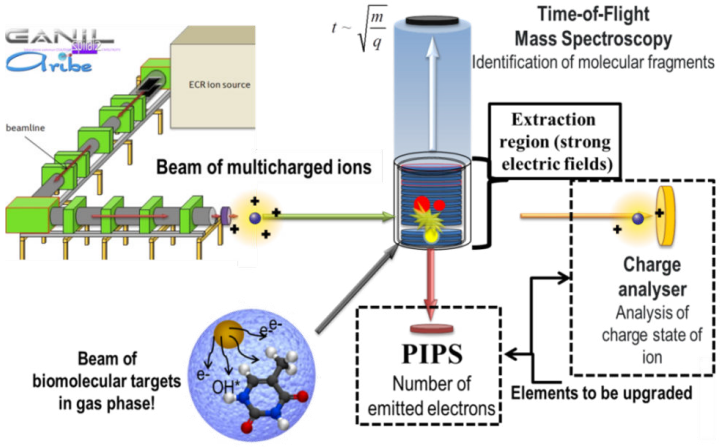

Figure A.1 *The overall schematics of the experimental set-up COLIMACON DUO adapted for multicoincidence experiments.*

measurement will be based on a triple coincidence between the charge state of the projectile after the collision, the spectrum of the produced fragmentation products and the number of the emitted electrons. This required several modifications of the existing experimental set-up, as the experiments have to be performed with a continuous ion beam and an electron statistics detector had to be developed. (in addition to the new cluster source, the cluster preparation chamber and the deposition chamber to determine the size distribution of neutral clusters. All this has been described in the main body of the thesis.). Concerning the modification of the extraction region and integration of the electron statistics detector, I have performed electric field and trajectory calculations with the SIMION program (with the aid of Violaine Vizcaino). As the experiment will be performed with a continuous beam and ion and electron extraction, the ion beam has to be redressed before and after the interaction zone. After optimization the final extraction geometry was defined and has been constructed. At present the electronic

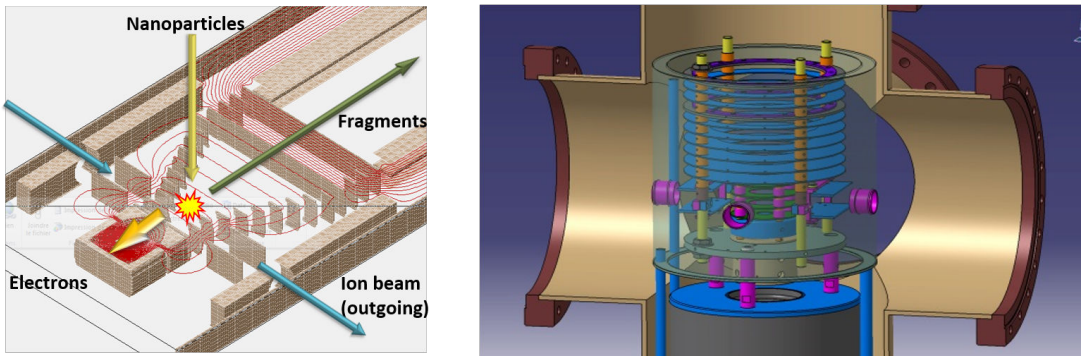

Figure A.2 *a)SIMION simulation geometry for the modified extraction system with embedded PIPS detector and deflection plates for ion beam; b)3D design of the interaction region adapted for coincident electron detection (Catia Software).*

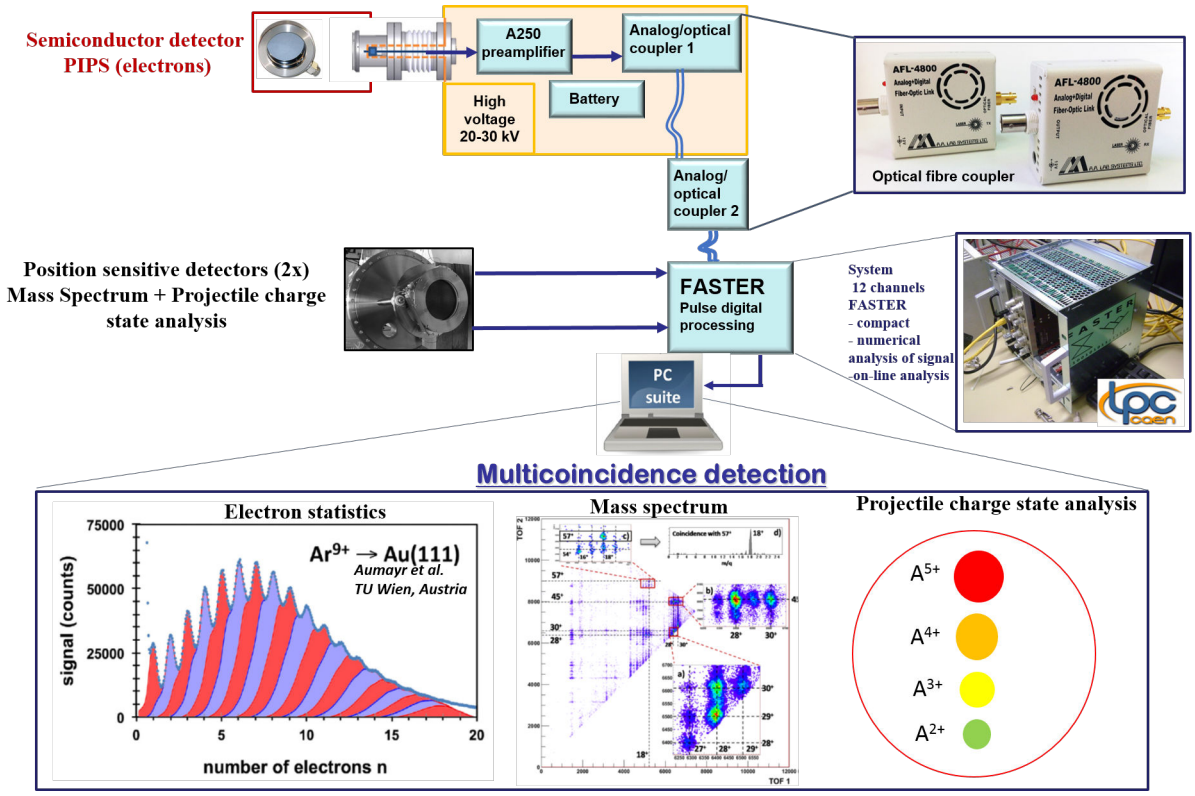

Figure A.3 *Systematics of the detection and counting system illustrating all crucial components for the multicoincidence study of the interaction of multiply charged ions and nanoparticle/molecular targets.*

system and the HV cage are being developed and first experiments will be performed soon in early 2018.

Publications | B

During the construction period I participated in numerous campaigns of the laboratory using the existing set-up and treating the interaction of multiply charged ions with clusters of biomolecules, PAHs and fullerenes. The neutral clusters were produced with the aid of a standard gas aggregation source and an oven device. From these studies several articles have been published.

1. Michael Gatchell, Rudy Delaunay, Giovanna D'Angelo, **Arkadiusz Mika**, Kostiantyn Kulyk, Alicja Domaracka,Patrick Rousseau, Henning Zettergren, Bernd A.Huber and Henrik Cederquist *Production of doubly-charged highly reactive species from long-chain amino acids driven by ion collisions* Phys. Chem. Chem. Phys. (2017); dx.doi.org/10.1039/C7CP00903H

We report on studies of collisions between 3 keV Ar^+ projectile ions and neutral targets of isolated 1,3-butadiene (C_4H_6) molecules and cold, loosely bound clusters of these molecules. We identify molecular growth processes within the molecular clusters that appears to be driven by knockout processes and that could result in the formation of (aromatic) ring structures. These types of reactions are not unique to specific projectile ions and target molecules, but will occur whenever atoms or ions with suitable masses and kinetic energies collide with aggregates of matter, such as carbonaceous grains in the interstellar medium or aerosol nanoparticles in the atmosphere.

2. Dariusz Grzegorz Piekarski, Rudy Delaunay, **Arkadiusz Mika**, Sylvain Maclot, Lamri Adoui, Fernando Martin, Manuel Alcami, Bernd A. Huber, Patrick Rousseau, Sergio Diaz-Tendero and Alicja Domaracka *Production of doubly-charged highly reactive species from long-chain amino acids driven by ion collisions* Phys. Chem. Chem. Phys. (2017); dx.doi.org/10.1039/C7CP00903H

We present a combined experimental and theoretical study of the fragmentation of multiply positively charged g-aminobutyric acid molecules ($GABA^{q+}$, q = 2,3) in the gas phase. The combination of ab initio molecular dynamics simulations with multiple-coincidence mass spectrometry techniques allows us to observe and identify doubly-charged fragments in coincidence with another charged moiety. The present results indicate that double and triple electron capture lead to the formation of doubly-charged reactive nitrogen and oxygen species (RNS and ROS) with different probability due to the different charge localisation and fragmentation behaviour of $GABA^{2+}$ and $GABA^{3+}$. The MD simulations unravel the fast formation (femtosecond) of large doubly charged species, observed in the experimental microsecond timescale. The excess

of positive charge (Coulomb repulsion) is stabilized by cyclic X-member (X = 3-5) ring structures. 5-member cyclic molecules can sequentially evaporate neutral moieties, such as H_2, H_2O and CO_2 leading to smaller doubly charged fragments which are observed in the experiments.

3. R. Delaunay, **A. Mika**, A. Domaracka, L. Adoui, M. Gatchell, H. Zettergren, and H. Cederquist, P. Rousseau, and B.A. Huber *Fusion in C60-van der Waals clusters induced by collisions with slow Ar^+ ions* Submitted to Carbon (2017)

Collision experiments where slow Ar^+ ions (3 keV) interact with van der Waals clusters of C60 fullerenes have been performed. We show that molecular growth processes in which new covalent bonds are formed are highly efficient under these conditions. This is evidenced by the observations of doubly and triply charged collision products containing only two (2) and five (5) intact or close to intact C60 molecules, respectively. In contrast, the appearance sizes of doubly and triply charged van der Waals clusters of C60 molecules are known to be much higher with values of five and ten, respectively. We find that the covalent molecular growth products often contain slightly fewer carbon atoms than n intact C60 molecules and that the average number of missing carbon atoms increases with n. Compared to corresponding femtosecond (fs) laser experiments where covalent molecular growth products also are observed [M. Hedén et al, Phys. Rev. A 71, 055201 (2005)], the average number of missing C-atoms (for a given n) is much lower. The reason is that the knockout of individual C-atoms in binary collisions with atoms and ions creates reactive species with much lower internal energies than in the fs laser experiment. In addition, ion collisions create other types of fragments (e.g. knockout of single C-atoms) than photo-absorption, which favors statistical fragmentation and losses of C2-units from the individual C60 molecules in the clusters. The present experimental findings are well reproduced by molecular dynamics simulations of carbon-knockout and molecular growth inside C60 van der Waals clusters. We find that the so formed nanoparticles contain both aromatic and aliphatic structures.

4. **A. Mika**, R. Delaunay, A. Domaracka, M. Gatchell, H. Zettergren, and H. Cederquist, P. Rousseau, B.A. Huber
   Ion induced chemistry in pure and mixed van der Waals clusters of coronene and C60 fullerene molecules to be submitted

Concerning the thesis work directly, several publications are submitted or to be submitted:

5. M.Bolsa, V.Ivŏsev,K. Haume, L. Ellis-Gibbings, A. Traore, V. Thakare, S. Rosa,P. de Vera, V.-L. Tran, **A. Mika**, D. Boscolo, S. Grellet, A. Verkhovtsev, B. A. Huber, K. Butterworth, K. M. Prise, F. J. Currell, N. J. Mason, J. Golding, E. Scifoni, G. Garcia, F. Boschetti, F. Lux, O. Tillement, C. Louis, K. Stokbro, A. V. Solovyov, and S. Lacombe, *Review article in 'Nanoscale Insights into Ion Beam Cancer Therapy'* edited by A.V. Solovyov Springer International Publishing, Cham, 2017, p.379-434.

6. **A. Mika**, P. Rousseau, A. Domaracka and B.A. Huber , *Fragmentation and Multi-Ionization of Large Bi-Clusters by Multiply Charged Ions* To be submitted to Phys. Rev.

A (2017)

We report on collisions of multiply charged ions with large free Bi nanoparticles in the gas phase. Appearance sizes have been determined for charge states up to q=6 which are in good agreement with the predictions of the liquid drop model, underlining the metallic character of the semi metal. By the analysis of the kinetic energies of the small-size fragments specific decay processes like binary fission and sequential and simultaneous emission of monomers and trimer ions are identified.

7. A. Mika, P. Rousseau, A. Domaracka and B.A. Huber, *Sputtering and electron capture by multiply charged ions from large silver nanoparticles (Ag_n)* To be submitted to PCCP (2017)
8. **A.Mika**, P. Rousseau, A. Domaracka and B.A. Huber *New experimental device for studying collisions of highly charged ions with free metallic nbanoparticles* Rev. Sci. Instrum., to be submitted (2017)

Synthèse

Interaction d'ions multichargés lents avec des nanoparticules métalliques radiosensibilisantes

7

7.1 Introduction

L'étude de l'interaction du rayonnement ionisant, sous forme d'ions énergétiques ou des photons, avec la matière est un sujet de grand interêt. Le but ultime est la connaissance des mécanismes fondamentaux et leurs applications en utilisation quotidienne. C'est sans doute que ces études, au début motivées par la curiosité scientifique, ont changé l'économie mondiale moderne.

Les ions énergétiques sont particulièrement intéressants en raison de leur application en radiothérapie - appelé hadronthérapie - pour traiter le cancer. Cette méthode, développée pendant la seconde partie du XXème siècle, est une méthode non-invasive et ultra-précise pour cibler les tissus malades. En combinaison avec d'autres types de traitement, comme la chimiothérapie, ou améliorée par l'introduction d'agents radiosensibilisants, l'hadronthérapie est devenu de plus et plus efficace pour traiter des tumeurs situées profondément.

7.1.1 Motivation et projet européen Marie Curie ARGENT

L'objectif principal de ce travail était le développement d'un dispositif expérimental permettant l'étude de l'interaction entre des petites nanoparticules métalliques (dont le diamètre est inférieur à 10 nm) et des ions multichargés dans le régime d'énergie cinétiques totales de 10 à 100 keV. Ces investigations sont motivées pour deux raisons principales. Premièrement, c'est l'amélioration des protocoles de traitement par hadronthérapie en utilisant des nanoparticules métalliques comme radiosensibilisants, ce qui exige la compréhension de mécanismes de l'interaction et de l'endommagement induit à l'échelle moléculaire.

Deuxièmement, les agrégats métalliques sont les systèmes multicorps et leur description détaillée en terme de stabilité, de transition de phase, de fragmentation ainsi que les propriétés électroniques sont extrêmement difficiles. Les expériences peuvent fonctionner comme l'inspiration et la source d'informations nouvelles pour stimuler le développement de modèles de plus et plus complets, ainsi que les routes pour la confirmation de leur validité.

7.1.1.1 Le projet européen Marie Curie ARGENT

Le projet ARGENT (l'abbreviation ARGENT représente « Advanced Radiotherapy, Generated by Exploiting Nanoprocesses and Technologies », en français Radiothérapie avancée générée par l'exploitation de processus et technologies nanométriques) est une initiative de la Commission Européenne dans la domaine de formation, commencée en 2014 et se terminant au début de l'année 2018.

Dans ce cadre, des équipes de recherche de différents disciplines (physique, chimie, biologie, pharmacie) travaillent ensemble pour former un ensemble de 13 jeunes chercheurs. L'avantage principal vient du caractère multidisciplinaire. Le travail des jeunes chercheurs est regroupés dans trois groupes de travail. Le premier est consacré à la nanodosimétrie pour l'avancement de la compréhension des processus physico-chimiques initiés par l'interaction entre les ions et la matière biologique afin de prévoir et contrôler les effets de nouveaux traitements accompagnés par l'usage de nanoparticules métalliques. Le deuxième, nanoagents thérapeutiques, cible le développement de nouvelles classes de nanodrogues pour combiner les effets des radiations et la diagnostique en parallèle, ce qui s'appelle l'attitude théranostique. Le troisième groupe de travail, évaluation préclinique, a pour but la transition des résultats scientifiques fondamentaux pour améliorer la pratique dans le milieu clinique et faire progresser la validation d'application de modèles précliniques.

7.1.1.2 Physique de l'irradiation, de l'hadronthérapie et concept de radiosensibilisation

Dans la traitement par la radiothérapie conventionnelle, c'est-à-dire avec des photon de quelques MeV, le dépôt d'énergie caractéristique en fonction de la profondeur impose l'irradiation sous différents angles afin de minimiser la dose dans les tissus sains parce que l'intensité maximale du dépôt apparaît juste à l'entrée du corps.

Au contraire, les ions chargés déposent un maximum d'énergie dans une région bien localisée en profondeur et limitent la destruction de cellules saines, du coup l'irradiation sous multiples angles n'est pas nécessaire. L'ion étant une particule chargée, il interagit avec les atomes et molécules et perd son énergie tout au long du chemin parcouru, ça correspond au concept de pouvoir d'arrêt. Le formule de Bethe-Bloch décrit la perte d'énergie d'un ion et le point où la densité des événement d'ionisation est plus haute s'appelle le pic de Bragg.

Sur la figure 7.1, le comparaison entre les deux types de le rayonnements ionisants (la courbe rose pour les photons de 6 MeV et la courbe rouge pour les protons de 250 MeV) est présentée et le pic de Bragg est bien visible dans le cas des protons. Pour l'irradiation d'une tumeur, son volume nécessite des irradiations multiples à différentes énergies ce qui mène a l'apparition d'un pic de Bragg « étalé » (SOPB) et en conséquence a un dépôt de dose augmenté dans le région des tissus sains (la courbe bleue).

Pour cette raison, une question importante peut être posée : est-ce qu'il est possible de

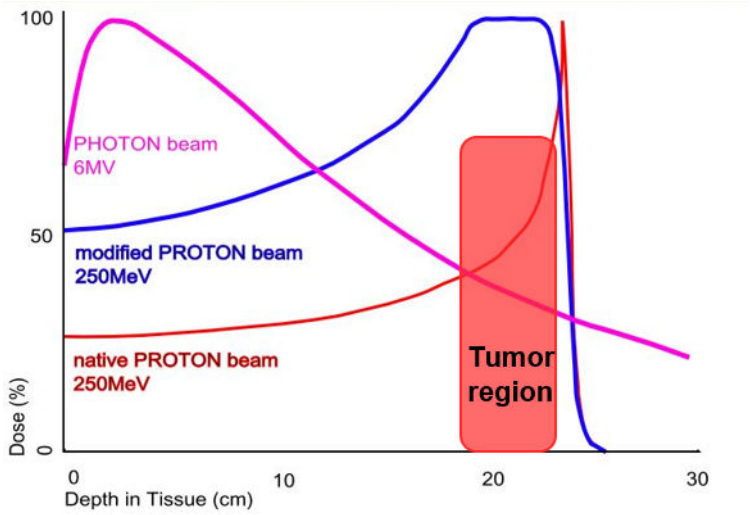

Figure 7.1 *Dose déposée en focntion de la profondeur du tissu pour trois méthodes de traitement différentes : irradiation par un faisceau de photon de 6 MeV (en rose), par un faisceau de protons de 250 MeV natif (en rouge) et modifié (en bleu). Figure adaptée à partir du site internet de University College London (https ://www.hep.ucl.ac.uk/pbt/).*

sensibiliser au rayonnement la région ciblée de la tumeur afin d'obtenir un effet biologique identique tout en réduisant simultanément la dose totale, conséquence du dépôt d'énergie dans la région non-ciblée ? Ce concept est présenté sur la figure 7.2. La réponse est positive et ce type de substances est connu sous le nom de radiosensibilisants.

Les processus d'endommagement à l'échelle nanométrique et cellulaire est très complexe. Les ions qui traversent les cellules, en fait ils traversent un ensemble d'atomes et des molécules dont 70% est constitué d'eau et la partie résiduelle est constituée de biomolécules formant les cellules dont la composition dépend du type de cellule.

Le type de dommage moléculaire le plus important et l'endommagement de l'ADN présent au niveau du noyau cellulaire mais il y a aussi d'autres mécanismes correspondant aux dommages de différentes organelles et de la signalisation inter- et intracellulaire.

À l'échelle moléculaire les mécanismes d'endommagement sont régis par des processus physico-chimiques. Par exemple, l'ionisation de l'ADN est due soit directement par les ions primaires ou par un processus indirect impliquant la présence de radicaux libres. La majorité de la dose est associée aux ionisations et excitations produites par les électrons secondaires et la formation des radicaux produits à l'échelle de temps de 10^{-18}s avec une énergie inférieure à 50 eV. Leur propagation ionise le milieu à l'échelle de temps de 10^{-16}s et détermine l'autre échelle de l'endommagement moleculaire. Avec le processus de couplage électron-phonon, la formation d'ondes de choc a lieu et peut durer quelques centaines de ps.

Pour conclure, pour l'endommagement moléculaire, les processus les plus importants sont les ionisations primaires, la production d'électrons secondaires, de photons, la formation de

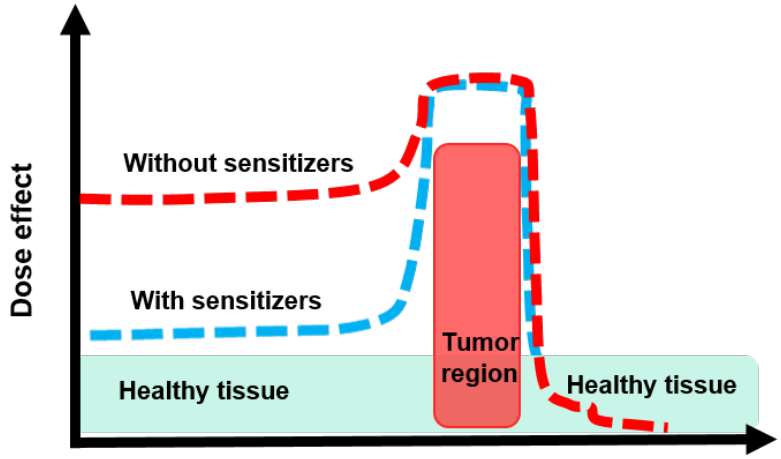

Figure 7.2 *Concept de radiosensibilisation : la ligne pointillée rouge correspond à un effet de dose sans radiosensibilisant alors que la ligne pointillée bleue montre l'effet de la dose avec un agent radiosensibilisant dans le tissu cancéreux.*

radicaux et d'espèces excitées, les fragments moléculaires et les ondes de choc locales. Le caractère multidisciplinaire de l'endommagement est évident, et ceci est aussi multiéchelles les phénomènes ayant lieu entre 10^{-18}s et 10^{-7}s et dans un espace variant de l'Å jusqu'à des centaines de nm.

7.1.1.3 Les nanoparticules métalliques comme radiosensibilisants - le cas de l'argent et du bismuth

Pour appliquer les nanoparticules métalliques comme radiosensibilisants il faut considérer quelques aspects pour leur développement, comme leur forme, la taille, le matériau, la couche de surface, la structure et leur charge nette. Ces aspects influencent la réponse biologique mais le premier intérêt est dans leur interaction avec le rayonnement.

Plusieurs études ont démontré que différents types de nanoparticules peuvent présenter des propriétés radiosensibilisantes [8–12] et un exemple est présenté sur la figure 7.3. Les candidats les plus populaires sont les nanoparticules d'or, en particulier grâce à la biocompatibilité, la facilité de la synthèse et la modification de la surface pour augmenter la sélectivité de cellules cancéreuses, et de manière plus générale, les nanoparticules composées à d'éléments à grand Z. Les deux raisons les plus avancées pour expliquer le rôle radiosensibilisant des nanoparticules métalliques sont l'augmentation de l'émission d'électrons secondaires comparée avec l'eau et l'effet de la surface du métal pour produire les espèces réactives [14, 15]. Le renforcement d'émission électronique dans le cas des petites nanoparticules d'or Au_{32} s'explique par les excitations plasmoniques et par l'excitation de résonance des orbitales 5d [**?**].

Les systèmes modèles choisis dans les expériences de cette thèse sont l'argent et le bis-

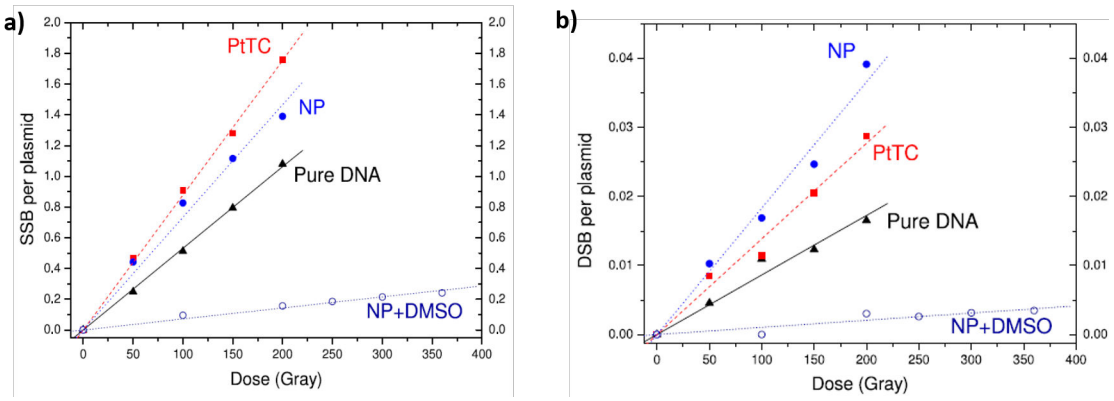

Figure 7.3 *Nombre moyen de a) ruptures simple brin (SSBs) et b) ruptures double brins (DBSs) par plasmide en fonction de la dose. Pour des échantillons d'ADN pur (triangles noirs), d'ADN en présence de PtTC (carrés noirs), d'ADN en présence de nanoparticules de Pt recouvertes de PAA dans une solution avec DMSO (cercles) et sans DMSO (ronds noirs). Les échantillons étaient irradiés par des ions C^{6+} 276 MeV/amu (LET = 13.4 keV/mm), [14].*

muth. L'argent est un métal noble avec une configuration électronique similaire à celle de l'or, connu pour ses propriétés antibactériennes et ayant des spécificités oxydatives à l'échelle nanoscopique. Les nanoparticules de métaux nobles sont connues comme précurseurs de radiosensibilisants pour la nanomédecine, et en particulier pour le traitement du cancer et elles ont différentes propriétés suivant de leur forme (« nanoshells, nanorods, nanodots »), leur taille et leur composition (matériaux du type core/shell). Tous les mécanismes de radiosensiblisation pour l'argent ne sont pas connus, mais l'un d'eux est l'émission d'ions Ag^{+} fonctionnant comme agent oxydant [10].

Le deuxième système étudié avec les ions multichargés sont les agrégats de bismuth. C'est le matériau intéressant à cause de ses propriétés : c'est le métal le plus diamagnétique de tous les métaux avec une conductivité électronique très faible qui subit une transition de phase sémimetal-sémiconducteur si le taille est diminuée à moins que 30 nm. Les raisons pour choisir le bismuth sont aussi sa non-toxicité tout en étant un métal à haut Z et ses applications dans l'industrie biotechnologique pour la bio-imagerie, la bio-détection et récemment les travaux de Hossein et al. ont montré des propriétés radiosensibilisantes plus efficaces que les nanoparticules d'or ou d'argent [18].

7.1.1.4 Les collisions des ions avec les agrégats et les nanoparticules

Les agrégats et les nanoparticules sont devenus les champs de recherche large, partiellement à cause du fait qu'il existe de multiples types d'agrégats. Par exemple, une simple division par le type de liaison donne les agrégats ioniques, covalents, métalliques et van der Walls. Presque toutes les excitations de l'agrégat impliquent des interactions électromagnétiques couplées di-

rectement aux électrons et aux ions et pour le cas des excitations dynamiques, le processus de mesure est destructif ce qui résulte en l'émission de produits comme les photons, les électrons et les fragment neutres et chargés.

Les systèmes les plus examinés dans les expériences de collision avec les ions sont les agrégats de sodium et dès le début il y avait une multitude de questions concernant leur comportement : l'influence des effets électroniques (la structure de couche), la stabilité pour le cas de charge excessive, les similarités et les différences avec les gouttelettes liquides chargées ou les noyaux atomiques. Le dernier concept est très intéressant parce que dans le cas des agrégats métalliques les charges, donc les forces répulsives, et les forces cohésives sont distribuées sur la surface contrairement au cas des forces nucléaires de court distances.

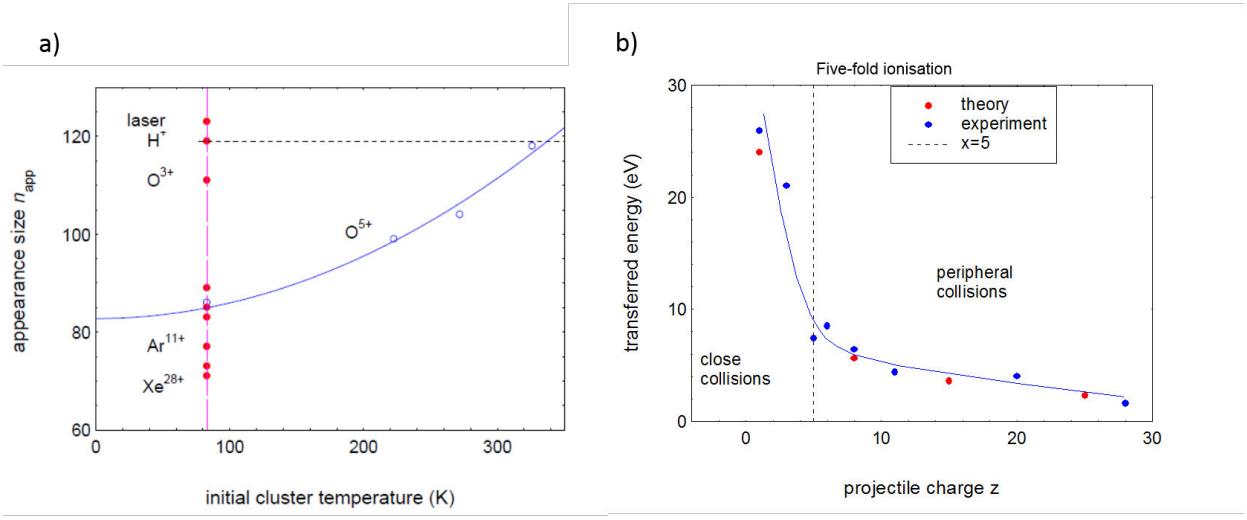

Figure 7.4 *a) Taille d'apparition de l'agrégat de sodium 4 fois chargé en fonction de son énergie interne initiale après collision avec des ions O^{5+} projectile (cercle, ligne bleue) ; la taille d'apparition pour des agrégats ayant une énergie interne initiale de 80 K est donnée dans le cas de collisions avec différents ions projectiles et par photoionisation laser. b) Énergie transférée lors d'une collision avec un ion déterminée à partir de la taille d'apparition des agrégats de sodium 5 fois chargés, Manil B. et al.*

Ainsi les tailles d'apparition pour les agrégats de sodium multi-ionisés ont été déterminées après collision avec des ions ou par photoionisation par impulsion laser []. Dans le cas où la charge finale est égale à 4, la taille d'apparition est n_{app} ∼120 si le projectile est un proton ou par photoionisation laser et elle chute à n_{app} ∼70 pour le projectile de Xe^{28+}. Cela veut dire que l'énergie transférée au système dépend de la charge du projectile. Ainsi, pour ioniser l'agrégat de sodium 5 fois, l'énergie transférée au système est juste de 1.5 eV lors d'une collision avec le Xe^{28+} et dans le cas d'une collision avec le proton cela monte à plus que 25 eV, augmentant fortement l'énergie interne du système. Ces résultats sont présentés sur la figure 7.4.

7.1.1.5 Les collisions entre les ions et les biomolécules

Les scénarios les plus proches de la réalité sont les collisions des ions avec les agrégats de biomolécules et aussi les agrégats de biomolécules entourés d'une « couche » de molécules d'eau. C'est une autre étape pour imiter les conditions dans les tissus. Un exemple sont les agrégats de l'eau $(H_2O)_n$ qui après l'interaction avec les ions produisent les fragments $H^+(H_2O)_{n-1}$ aussi bien que les radicaux OH.

Un autre exemple est les collisions entre des atomes neutres de sodium ou de néon et des agrégats de la molécule AMP (adenosine 5-monophosphate) et de molécules de l'eau afin de comparer la fragmentation de la biomolécule en fonction du degré de solvatation [26]. Une grande stabilité de la biomolécule est observée quand le nombre initial de molécules d'eau est supérieur à 13. L'agrégat dissipant l'énergie par évaporation des molécules d'eau. Par contre, des études de la collision d'ions C^{4+} avec l'uracile hydraté, c'est-à-dire un agrégat contenant une molécule d'uracile entourée d'eau, montrent que les fragments $HCNH^+$ et CO^+ caractéristiques de la molécule isolée sont aussi observés solvatés dans le cas des agrégats, montrant une forte interaction entre l'uracile et les molécules d'eau [27].

7.1.1.6 Les collisions entre les ions et des métaux nobles

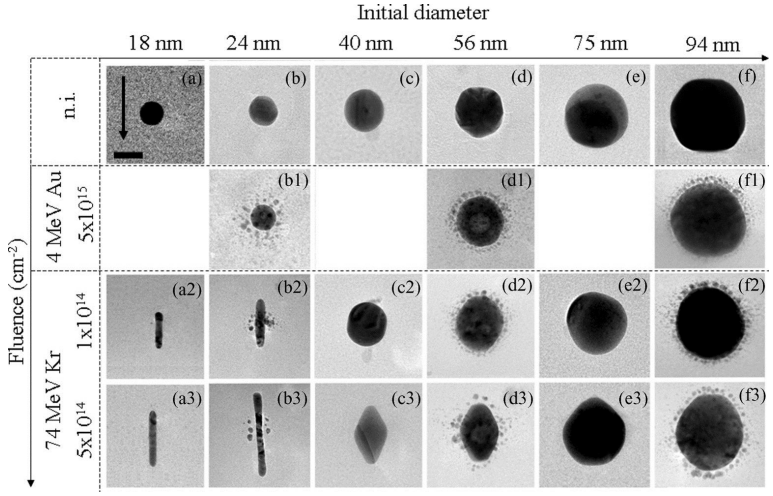

Figure 7.5 *Diagramme montrant les changement morphologiques de nanoparticules d'or. L'axe horizontal représente la taille initiale des NP alors que l'axe vertical représente la fluence. La direction du faisceau d'ions incidents est indiqué par la flèche. Les échantillons (b), (d) et (f) ont été pré-irradiés avec des ions Au de 4 MeV conduisant à un halo de structures satellites autour de la NP centrale (b1), (d1) et (f1). Tous les échantillons ont été irradiés avec des ions Kr de 74 MeV. Figure adaptée à partir de [30].*

Des grandes nanoparticules d'or, ayant un diamètre supérieur de plusieurs dizaines de nm, ont été irradiées par des ions Au à 4 MeV Au et Kr à 74 MeV (le travail effectué au GANIL à

Caen et à ARAMIS à Orsay). Une corrélation entre la forme et la taille des NP a été trouvée - une élongation le long de la trajectoire d'un ion apparait. Pour les nanoparticules plus petites (10-20 nm) la dissolution totale en objets de 2nm ou plus petits est observée [31]. La figure 7.5 présente les images MET avec les distribution de tailles pour différentes doses d'irradiation.

7.2 Dispositif expérimental : COLIMACON DUO

Cette section décrit les principales parties du dispositif expérimental COLIMACON DUO, qui a été développé sur la base du dispositif précédent COLIMACON (COLlision entre les Ions et des Molécules ou des Agrégats COmplexes Neutres). Les modifications essentielles sont l'appareillage pour produire les faisceaux de nanoparticules métalliques, la chambre de purification pour produire les faisceaux neutres et la chambre de dépôt pour leur caractérisation avec des méthodes microscopiques (comme l'AFM ou le TEM).

7.2.1 Description générale

L'expérience est basée sur l'interaction de deux faisceaux (cible : faisceau continu de nanoparticules et d'agrégats et projectile : un faisceau pulsé d'ions) collimatés et se croisant avec un angle de 90 degrés dans la zone d'interaction. Les collisions ont lieu dans des conditions de la pression de base $\leq 10^{-9}$ mbar et augmentant à 10^{-7} mbar en présence du faisceau cible à cause du gaz d'argon, nécessaire pour la pulvérisation, l'agrégation et le transport des nanoparticules.

Sur la figure 7.6 les éléments les plus importantes sont présentés : la source d'agrégats du type agrégation gazeuse et basée sur une décharge magnétron, la chambre de pompage différentiel où les nanoparticules chargées sont éliminées du faisceau cible, la zone de collision (le point de croisement des deux faisceaux), la chambre de dépôt et le système de guidage du faisceau avec l'installation du canon à ions complémentaire.

Les produits de réaction positivement chargés sont extraits par des champs électriques et analysés par le spectromètre à temps de vol de type Wiley-MacLaren en fonction de leur rapport masse/charge. Avec la version précédente du dispositif COLIMACON, plusieurs types d'expériences ont été réalisées sur les agrégats de fullerène, d'hydrocarbures aromatiques polycycliques, de biomolécules (nucléobases, acides aminées ou radiosensibilisants moléculaires), les agrégats métalliques de sodium.

7.2.2 Production des ions multichargés et ligne de transport

L'usage de la source GTS (Grenoble Test Source) de type ECR (en anglais pour « Electron Cyclotron Resonance », résonance cyclotronique électronique) de l'installation ARIBE a permis de générer les faisceaux d'ions multichargés. La conception de source de ce type comprend des parties cruciales : l'injection du gaz et de radio-fréquence, la chambre principale du plasma et

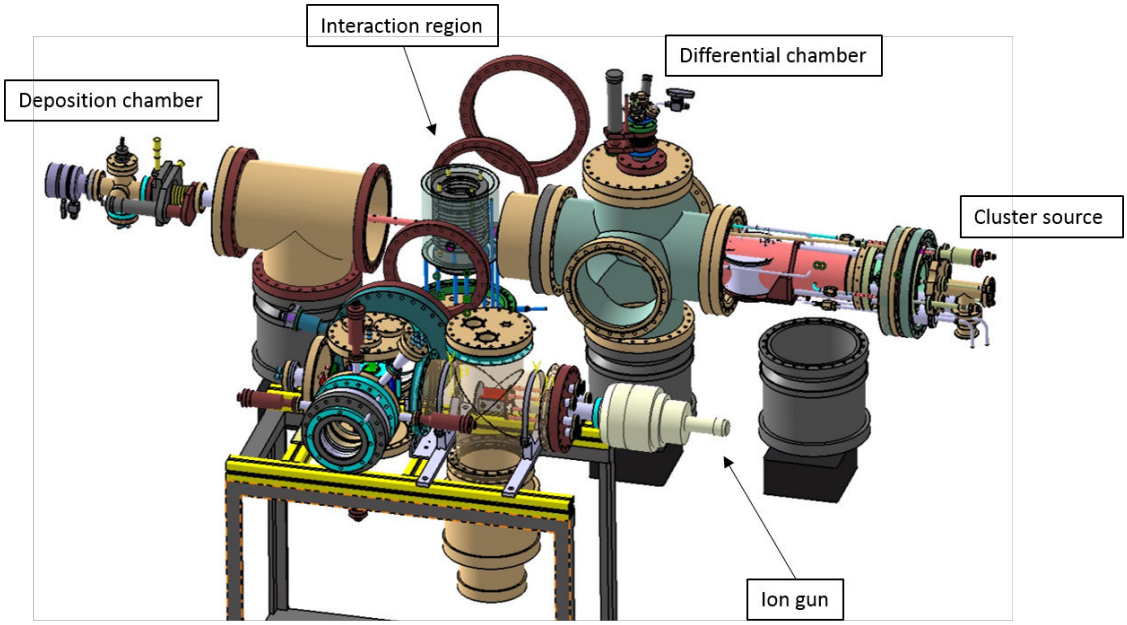

Figure 7.6 *Schéma du dispositif COLIMACON DUO avec les composants principaux : la source d'agrégats basée sur une décharge magnétron, l'étage de pompage différentiel dans lequel le faisceau de nanoparticules neutres est préparé, la zone d'interaction où les deux faisceaux se croisent, la chambre de dépôt. Le spectromètre par temps de vol, monté verticalement au dessus de la zone d'interaction, n'est pas montré. Un canon à ion permet de produire des faisceaux d'ions monochargés pour réaliser des mesures test, le faisceau d'ions produits est dirigé vers la zone d'interaction par un déviateur électrostatique quadripolaire.*

les champs magnétique de confinement composés de bobine pour la composante longitudinale et d'un hexapole pour la composante radiale. Finalement, il y a le système d'électrodes qui permet d'extraire proprement les ions et leur guidage vers le dispositif expérimental.

Le confinement magnétique est nécessaire pour augmenter le chauffage des électrons du plasma et ainsi l'ionisation des ions par l'impact des électrons énergétiques, par exemple le temps caractéristique pour produire les ions dans les états de charge élevés est d'environ 10^{-2}s. La présence des atomes neutres influence la perte des ions et la valeur de la pression est maintenu à un niveau plus bas que 10^{-6} mbar.

Après l'extraction des ions, la mise en forme du faisceau d'ios et son guidage vers la zone d'interaction sont réalisés par la combinaison des multipôles magnétiques (dipôles, quadripôles et hexapôles). En addition, un jeu de deux fentes perpendiculaires situé à l'entrée du dispositif permet d'améliorer la mise en forme du faisceau. Un canon à ions est aussi installé afin d'assurer la production de faisceaux d'ions monochargés pour réaiser des tests sans utiliser les faisceaux de l'installation. La figure 7.7 montre les éléments les plus importants du transport des ions dans le dispositif COLIMACON.

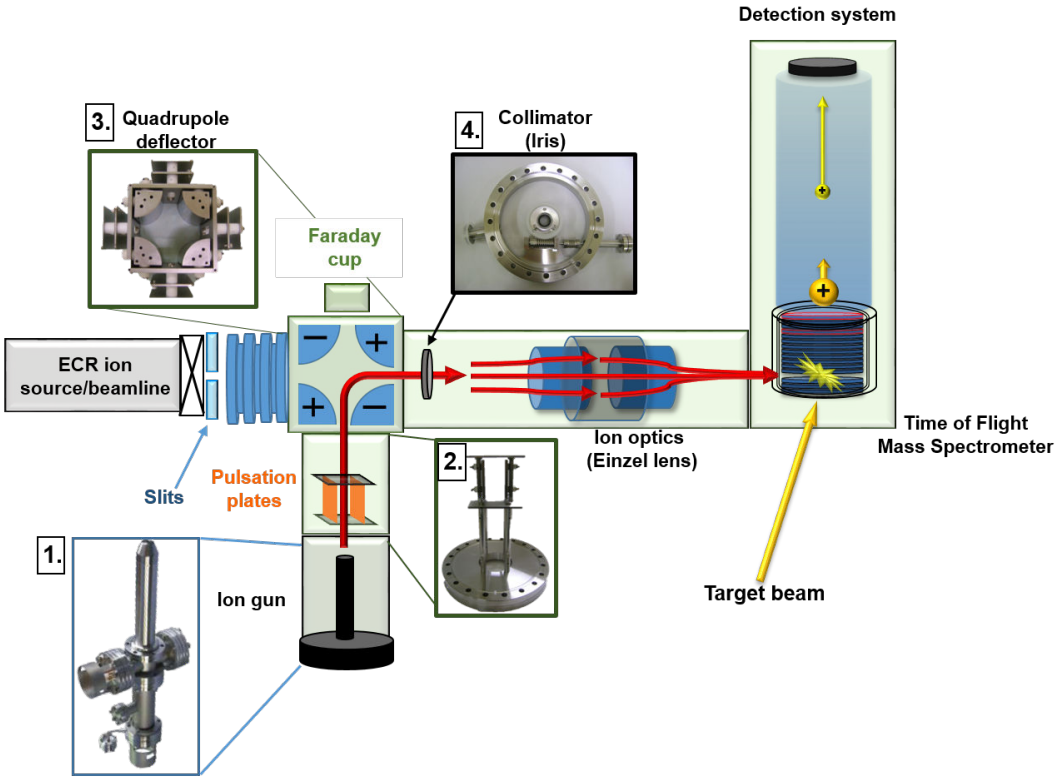

Figure 7.7 *Installation du canon à ion dans le dispositif COLIMACON DUO avec les éléments cruciaux de transport du faisceau projectile vers la zone d'interaction : 1-canon à ion, 2-pulsation du faisceau, 3-déviateur électrostatique quadripolaire, 4-collimateur.*

7.2.3 Production des agrégats et des nanoparticules

La production d'agrégats sous forme de faisceaux moléculaires est déjà une discipline bien établie. La première étape de formation des agrégat est l'obtention d'une pression de vapeur du matériel suffisamment élevée. Dans ce travail les agrégats métalliques sont produits par la méthode de pulvérisation d'un disque métallique par une décharge assistée par un champ magnétique - c'est la méthode de la pulvérisation assisté par décharge magnétron. La construction de la source avec la tête magnétron et la chambre de condensation est présenté sur la figure 7.8.

Les atomes d'un gaz d'argon sont ionisées dans le région du plasma et accélérés à la surface de la cible. La vapeur d'atomes métalliques est transportée dans la région froide, où ils perdent leur énergie cinétique par collision avec le gaz tampon d'argon et commence alors la formation des agrégats.

La distribution en taille des agrégats dépend des conditions thermodynamiques dans la chambre. Après, les agrégats et les nanoparticules sont transportés sous forme d'un faisceau moléculaire formé par le système d'iris et les deux écorcheurs séparant les régions de pompage

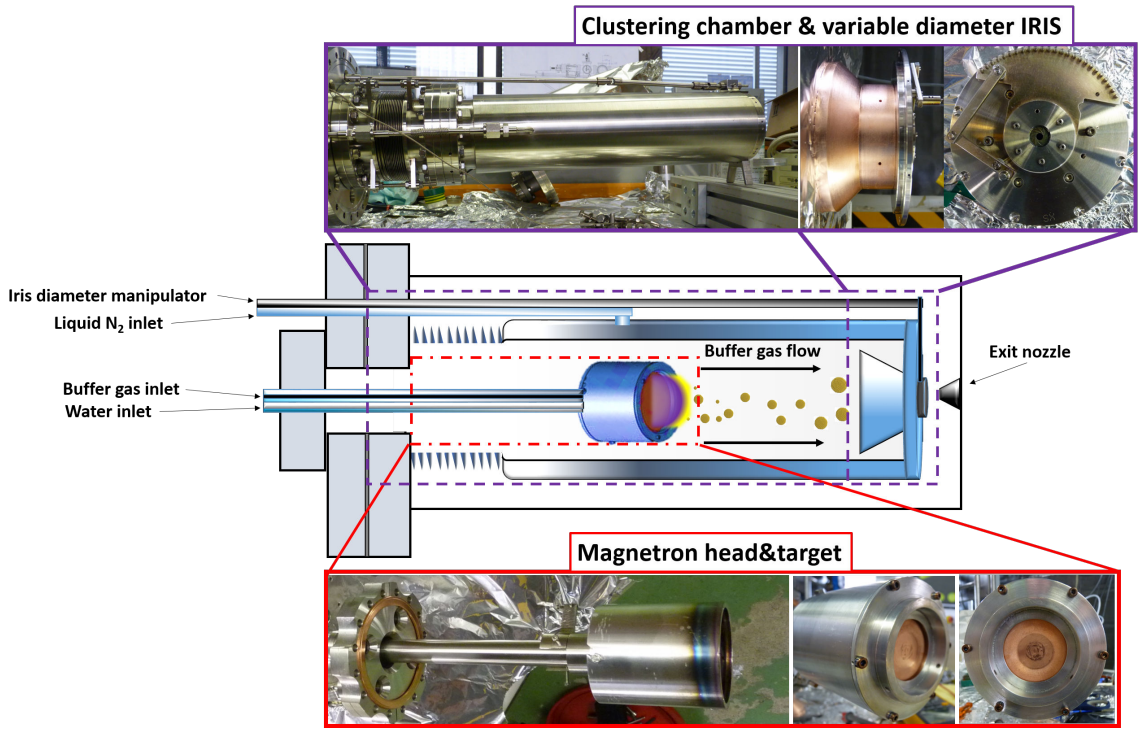

Figure 7.8 *Schéma de la source d'agrégats basée sur une décharge magnétron développée pour le dispositif COLIMACON DUO avec des photographies de éléments les plus importants : la tête magnétron et la chambre de condensation.*

différentiel entre la source d'agrégats et le région d'interaction.

7.2.3.1 Spectrométrie de masse par temps de vol

Le prochaine étape est l'intersection des deux faisceaux de nanoparticules et d'ions au centre de la région d'extraction et leur interaction. Les produits positivement chargés des interactions sont accélérés par un champ électrique pulsé de l'ordre de quelques centaines de volts par cm et ils sont dirigés vers une région d'accélération (de 3 cm) et de vol libre (de 1 m). À la fin de cette zone, ils frappent la surface d'un disque métallique produisant ainsi des électrons secondaires qui guidés par un champ magnétique sont détectés par un détecteur à galettes de micro-canaux.

.

Le temps de vol d'un fragment est dépendant de sa masse et de sa charge suivant la formule :

$$T_{flight} = \frac{L}{v_{particle}} = L\sqrt{\frac{m}{2q \times V}} \tag{1}$$

et c'est pourquoi les différents produits peuvent être distingués sous la forme d'un spectre de masse présenté sur la figure 7.9.

Le système d'acquisition permet d'obtenir les évènement dans le mode multi-stops, signi-

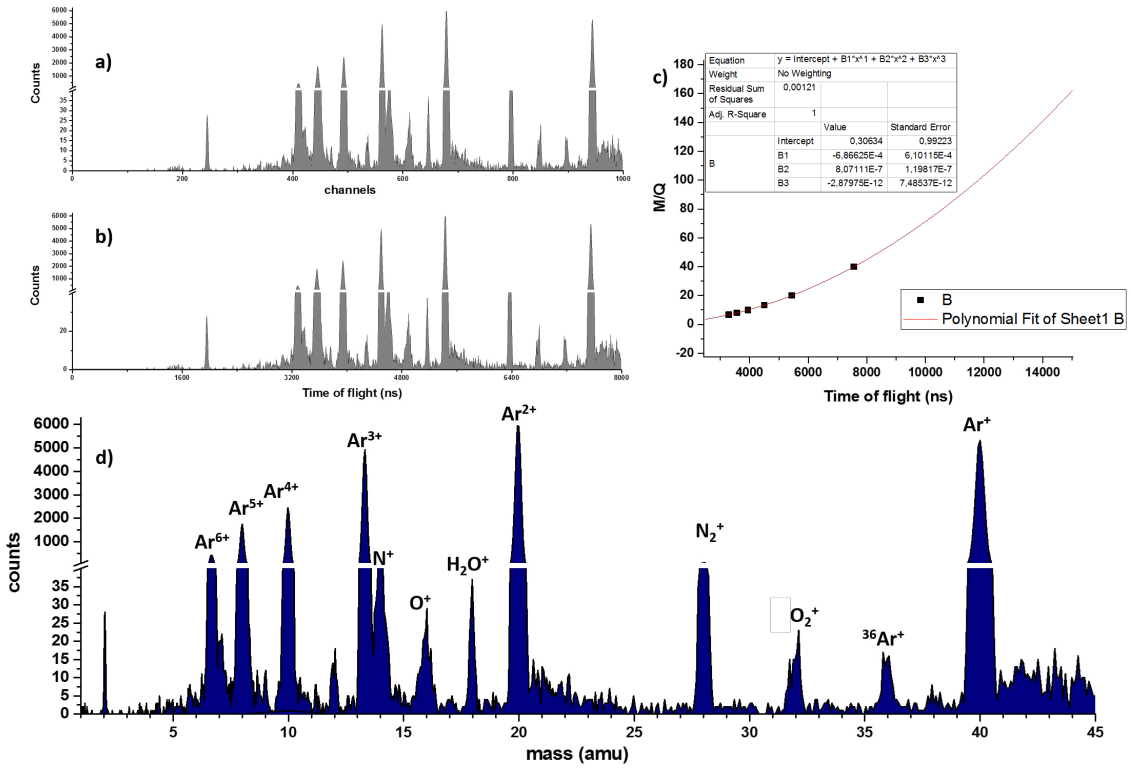

Figure 7.9 *Spectres des produits cationiques obtenus pour la collision d'ions O^{6+} avec des atomes d'argon à une énergie E_{kin}=90keV a) en fonction du canal du système d'acquisition et b) en fonction du temps de vol. c) Courbe de calibration du rapport $\frac{m}{q}$ en fonction du temps de vol. d) Spectre de masse obtenu après calibration suivant le rapport masse sur charge.*

fiant que dans des conditions appropriées il est possible que les ions détectés pour un évènement proviennent d'une collision unique avec un ion projectile et le spectre de multicoïncidence peut être reconstruit.

7.2.3.2 Challenges et difficultés

La conception initiale du dispositif COLIMACON a été adaptée pour les études de petits agrégats, du coup les études de nanoparticules contenants quelques milliers d'atomes implique des difficultés au niveau de leur détection. Premièrement, la densité du gaz tampon est très élevée comparée à la densité de nanoparticules conduisant à un rapport du signaux/bruit réduit. Deuxièmement, pour obtenir une statistique suffisante, une acquisition très longue est nécessaire, mais les conditions thermodynamiques dans la source d'agrégats peuvent changer

légèrement, changeant la distribution de taille considérablement. En addition, l'énergie cinétique des agrégats augmente avec leur masse et pour les grandes nanoparticules, elle peut être trop élevée afin de les extraire proprement vers le spectromètre par temps de vol. Un autre élément est le cas de matériaux ayant plusieurs isotopes parce que la résolution est diminuée. La vitesse finale des ions arrivants à la surface du disque métallique du système de détection doit être suffisante pour initier l'émission des électrons. Enfin, la caractérisation des nanoparticules neutres nécessite d'être réalisée en dehors du dispositif expérimental et cela demande donc leur dépôt et l'accès à des microscopes AFM et MET.

7.3 Théorie

La description de la collision entre un ion et un agrégat métallique adoptée pour cette thèse est fondée sur la division des collisions en deux types : les collisions périphériques et celles pénétrantes. Dans le premier cas, le processus dominant est la capture des électrons d'un objet métallique vers les états électroniques libres du projectile et le modèle classique de la barrière est utilisé pour le décrire. Pour le deuxième cas, le concept de pouvoir d'arrêt dans la matière est utilisé. Nous nous référons alors aux pouvoirs d'arrêt électronique et nucléaire. Enfin le modèle de la goutte liquide permet de traiter le comportement de l'objet métallique après l'interaction avec les ions.

Les processus dominants pour les collisions périphériques sont la capture et la capture multiple d'électrons, la polarisation du nuage électronique à l'échelle de quelques femtosecondes ainsi que les excitations électroniques induites par le champ coulombien (du type plasmonique où les résonances des électrons des orbites d), qui peuvent déexciter par l'émission d'électrons. Pour les collisions pénétrantes, la collision est similaire à celle avec une surface. On peut attendre tous les phénomènes susmentionnées avant la collision, ainsi que le passage à travers l'objet, déposant une quantité d'énergie importante par les pouvoirs d'arrêt électronique et nucleaire dans l'échelle de quelques centaines de femtosecondes, qui peut impliquer l'évaporation, l'ionisation, les cascades de collisions rapides menant à la pulvérisation des atomes.

Dans le modèle classique de la barrière, le potentiel senti par un électron partant de l'agrégat a la forme :

$$V_r = -\frac{q+1}{r} + \frac{R}{2r^2} - \frac{R}{2(r^2-R^2)} - \frac{z}{x-r} - \frac{zR}{xr} + \frac{zR}{xr-R^2} \tag{2}$$

où q est la charge de la nanoparticule, R son rayon, r la distance de l'électron, x la distance entre la nanoparticule et l'ion de charge z. Sur la fig.7.10 la différence de potentiel vu par un électron dans le cas de la présence et de l'absence d'un projectile est montrée pour un agrégat d'argent ayant 5000 atomes.

Le devenir d'un objet ionisé par la capture électronique peut être expliqué par le modèle de la gouttelette liquide. Pour une sphère chargée, deux forces sont responsables par la stabilité : la force répulsive du type Coulomb, menant à la déformation et la force surfacique de cohésion

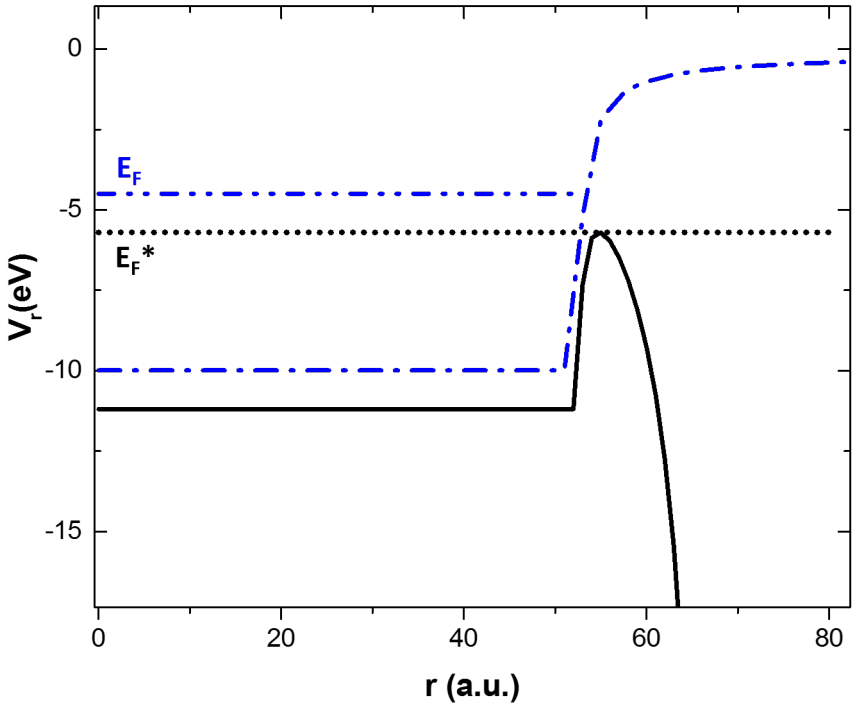

Figure 7.10 *Potentiel V_r vu par un électron avec un projectile (ligne noire continue) et sans projectile (ligne bleue en pointillés). L'ion de charge 3+ est localisé à une distance d=68 u.a. du centre d'un agrégat de 5000 atomes d'argent, c'est à dire à la distance à laquelle la capture électronique se produit. La ligne en points noirs montre le niveau de Fermi abaissé.*

des atomes. La compétition de ces forces se manifeste par la présence d'une barrière, qui diminue quand les forces répulsives sont plus grandes ou identiques aux forces de cohésion et la fragmentation a alors lieu. Le paramètre décrivant la tendance à la fragmentation est la fissilité X. Pour le cas des agrégats métallique la fissilité est donnée par :

$$X = \frac{q^2/n}{(q^2/n)_{critical}} \tag{3}$$

et suivant la valeur de X, différents comportements du processus de fragmentation sont observés comme la fission symétrique (les produits ont des masses finales similaires) ou asymétrique (la masse des produits est différente). Par exemple, pour le cas des gouttelettes de glycol piégées avec X=1, l'émission de jets a été observée comme mécanisme de déexcitation [74].

Dans le cas de collisions centrales, la perte d'énergie par le projectile, son interaction avec les atomes du solide, les effets de diffusion sont normalement traités avec le concept de pouvoir d'arrêt, et parce que le solide est un grand réseau de noyaux et d'électrons, la spécificité de

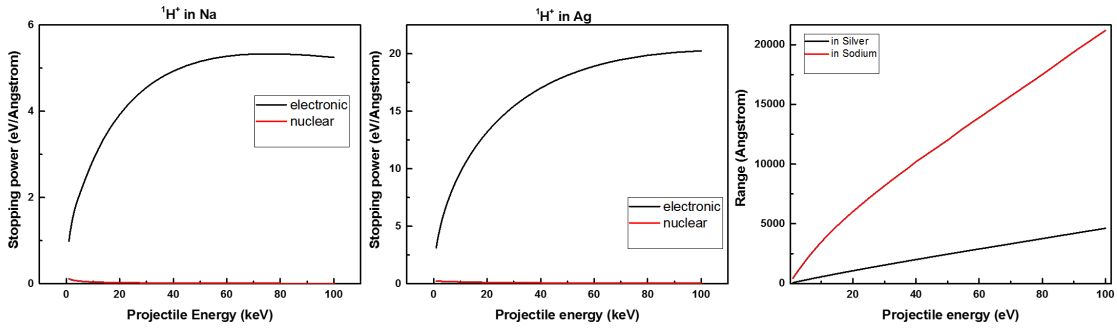

Figure 7.11 *Illustration of the electronic and nuclear stopping power dependencies of protons in sodium and silver as a function of the kinetic energy (left and middle). In figure on the right the penetration depth is shown as a function of the energy. Results are based on SRIM Program calculations with (E=1 to 100 keV).*

l'interaction avec un ion énergétique permet de distinguer les deux parties : l'interaction avec le réseau des noyaux des atomes (la diffusion du projectile, les cascades atomiques) et celui des électrons (la polarisation et l'excitation du système électronique). Il faut donc distinguer le régime de pouvoir d'arrêt électronique et nucléaire. Par exemple pour le cas de proton, la dépendance de pouvoir d'arrêt électronique et nucléaire dans le cas de la pénétration du sodium et de l'argent sont montrées sur la fig.7.11.

7.4 Résultats

7.4.1 Caractérisation du dispositif expérimental développé

Pour cette thèse, il y avait quelques défis expérimentaux : la production de faisceaux de nanoparticules métalliques bien collimatés, la détermination de leur taille, l'investigation de leur interaction avec les ions et l'analyse de produits obtenus. Ces points sont présentés dans les sections suivantes.

7.4.1.1 Système de production des nanoparticules : pulvérisation par décharge magnétron et agrégation gazeuse

Les nanoparticules sont produites par la pulvérisation de disques métalliques de haute pureté ($\geq 99.99\%$). L'observation des spectres positifs était nécessaire pour déterminer les conditions de travail les plus stables. La variation des paramètres expérimentaux montrent qu'il existent quelques conditions essentielles pour produire un faisceau intense et stable : par exemple dans le cas du bismuth, la température doit être plus basse que T_{source}<-150°C ainsi que le flux du gaz doit être au minimum de 80 ml/min.

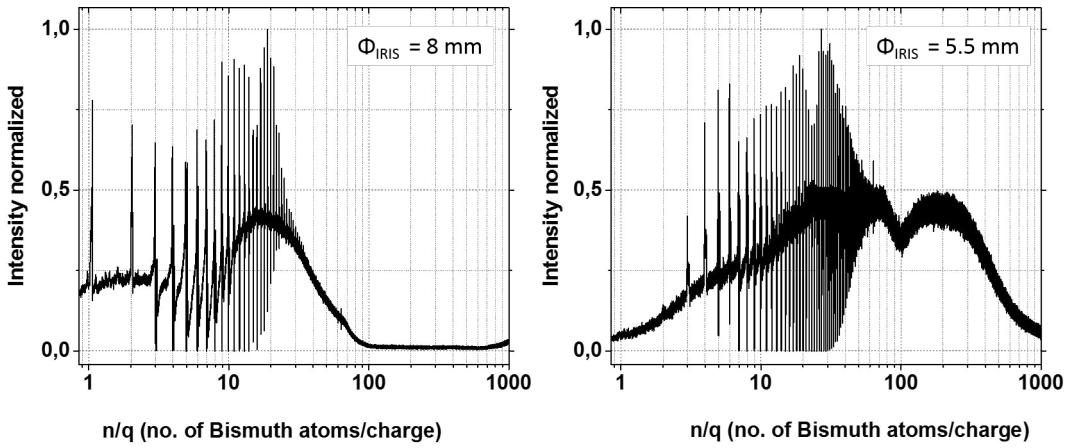

Figure 7.12 *Spectre de masse des agrégats de bismuth positivement chargés produits par la source magnétron avec deux diamètres de l'iris différents : a) Φ_{IRIS}=8mm et b)Φ_{IRIS}=5.5mm.*

Les spectres des agrégats positifs changent si les différents paramètres thermodynamiques sont changés. Par exemple, lorsque la pression interne augmente, un décalage de la distribution de taille est observé vers les agrégats plus massifs. La pression est augmentée par l'augmentation du flux du gaz tampon ou par la diminution du diamètre de l'iris (situé à la sortie de la chambre d'agrégation). Le deuxième cas est présenté sur la fig.7.12. Un autre exemple concerne l'augmentation de la puissance de la décharge, on peut alors observer un décalage de la distribution de masse vers les valeurs plus grandes.

7.4.1.2 Distribution en taille des nanoparticules neutres

Pour mesurer la distribution en taille des agrégats neutres dont l'interaction avec les ions est étudiée dans cette thèse, la construction d'une chambre de dépôt a été nécessaire. Dans cette chambre, le dépôt des nanoparticules neutres est possible dans les conditions de « soft landing », c'est-à-dire pour un impact doux des agrégats lorsque leur énergie cinétique est insuffisante pour les déformer lors de l'impact avec la surface. Pour la microscopie AFM, des échantillons de silicium ont été utilisés pour les dépôts alors que des grilles carbonées étaient montées afin de réaliser la microscopie MET

En générale, les nanoparticules de bismuth ont une taille plus petite que les nanoparticules d'argent. Dans le cas de bismuth, la microscopie MET était alors nécessaire montrant que plus que 97% des agrégats ont un diamètre inférieur à 3 nm. Ceci correspond à des agrégats ayant moins de 700 atomes avec maximum localisé autour de 100 atomes. Il est nécessaire à préciser que la limite de résolution dépend du type du grille utilisé et dans le cas présent elle est de 1.5 nm pour la focalisation utilisée.

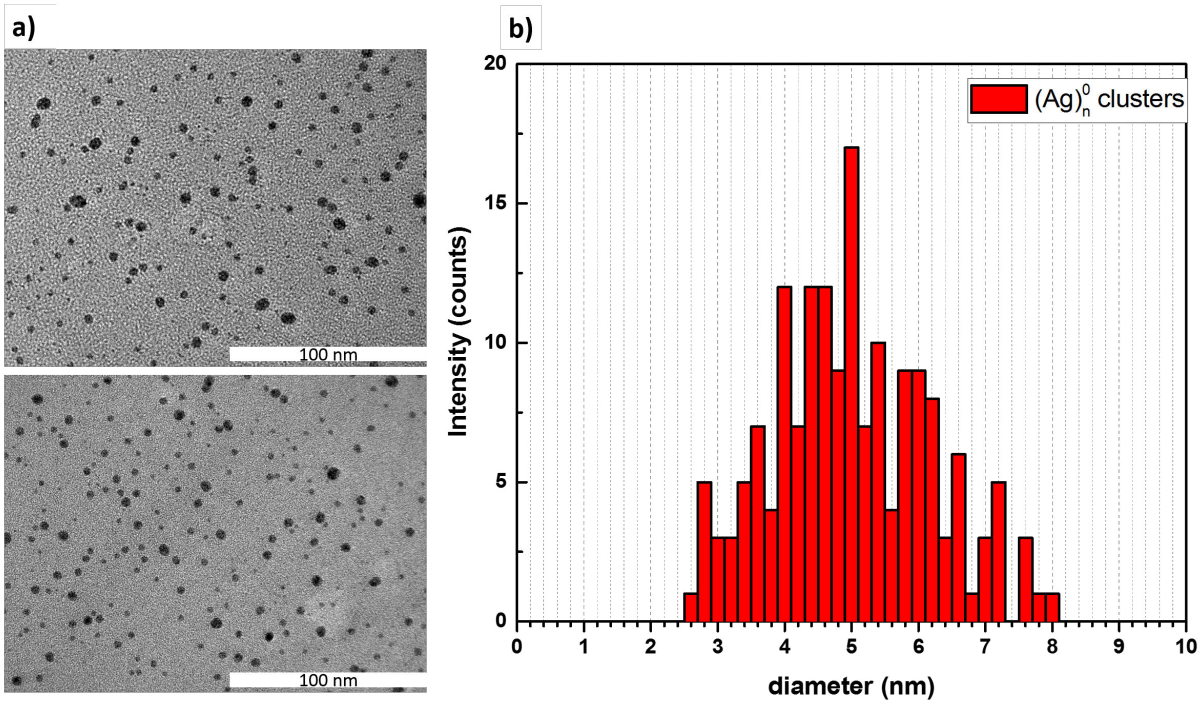

Figure 7.13 *Agrégats déposé sur une substrat de SiO_2 : histogramme montrant la distribution en taille des agrégats d'argent neutres déposés.*

La distribution de taille des nanoparticules d'argent a été obtenue par les microscopies AFM et MET dans les mêmes conditions de production. En général, la distribution commence pour un diamétre de 3 nm et finit à des diamètres plus grands que 10 nm avec une taille moyenne est 5-6 nm. Ceci correspond à un nombre d'atomes qui s'étend de 800 atomes à plus de 15000 atomes. Les résultats de la microscopie MET sont très similaires, donnant des valeurs plus petits de 0.5 nm en moyenne. Un exemple d'image MET avec la distribution de taille pour les nanoparticules d'argent est présenté sur la fig.7.13. Pour certains agrégats plus grands, la focalisation du MET permet de voir aussi une structure montrant des lignes d'atome bien arrangées.

7.4.1.3 Faisceau moléculaire

En utilisant le faisceau d'agrégats positivement chargés produits par la source, l'énergie cinétique des nanoparticules produites a pu être déterminée. En général, la vitesse des atomes d'un gaz dépend de la température du gaz T et de leur masse m et peut être calculée avec l'équation de Maxwell-Boltzmann, montrant que pour le cas du gaz argon à une température de T=100 K la vitesse la plus probable est d'environ 200 m/s. En contrôlant le potentiel appliqué sur l'écorcheur (le petit cône localisé après la sortie de la chambre d'agrégation), il est possible d'arrêter les nanoparticules ayant une énergie inférieure à la valeur du potentiel appliqué. Dans

notre cas, pour l'objet Ag^{+}_{2400}, l'énergie la plus probable était de 3.9 eV, ce qui correspond à une vitesse de 50 m/s.

La connaissance de la vitesse des agrégats et de la zone de couverture permet de détérminer la densité dans un volume de 1 cm^3

$$\rho = \frac{n_{particles}}{V} \approx 2.4 \times 10^6 \, \frac{particles}{cm^3} \tag{4}$$

Pour la pulvérisation de la cible d'argent, le volume pulvérisé après environ 25 jours de travail de la source magnétron est $V_{sputtered} = 1373.5$ mm^3 et le taux de pulvérisation est estimé à $Y_{Ag\,atoms} = 2.03 \times 10^{-5}[g/sec] \sim 10^{17}$ atomes/sec. Ainsi, uniquement une fraction de 10^{-3} à 10^{-4} du matériel sort de la source.

7.4.1.4 Capacités de détection

En utilisant le logiciel SIMION, des calculs de trajectoires pour les différentes conditions d'expérience ont été faits. En particulier, c'est l'effet de la vitesse initiale du faisceau moléculaire qui est important pour la bonne extraction des nanoparticules verticalement dans le spectromètre à temps de vol (et donc leur transmission) aussi bien dans le cas de champ électrique faible (122 V/cm) et plus élevé (244 V/cm). Pour le cas des objets les plus grands, le temps d'extraction n'est pas négligeable afin d'avoir une bonne extraction des produits et maintenir ainsi une bonne trajectoire vers le système de détection.

Dans le cas des champs de 122 V/cm, les simulations montrent que la transmission de 100 % est maintenue pour les énergies plus petites que 4 eV et cela baisse à 0% pour une énergie supérieure à 6 eV. Dans le cas de champs à 244 V/cm, il y a 100% de transmission de 100% pour les énergies plus petites que 6 eV et 0% pour plus grandes que 8 eV.

Une autre élément important, aussi connecté avec l'énergie initiale des produits, est l'énergie cinétique libérée (KER) lors d'une collision. Elle explique la forme du pic avec des contributions de « backward » et « forward » (les fragments émis respectivement vers et en direction opposée du détecteur) par la superposition de formes caractéristiques pour les énergies KER différentes. L'évolution du pic pour les énergies cinétiques de 0 à 10 eV sur un exemple d'un ion Bi^{+} est montré sur la fig.7.14.

L'effet de temps d'extraction est aussi crucial et les simulations de trajectoire ont indiqué que pour l'ion Ag^{+}_{5000} le temps minimal d'application du champ afin qu'il atteigne la surface du détecteur est de 50 μs.

Une dernière chose très importante est la considération de l'efficacité de détection totale. Premièrement, la combinaison de trois grilles réduit la transmission au niveau de 69%. La documentation du détecteur MCP fournit une valeur de 65 % d'efficacité, donc finalement l'efficacité totale est réduite à 45%. Aussi, les produits les plus lourds sont détectées avec une efficacité plus petite. Au total, cette faible valeur d'efficacité entraine un changement dans la statistique des évènements.

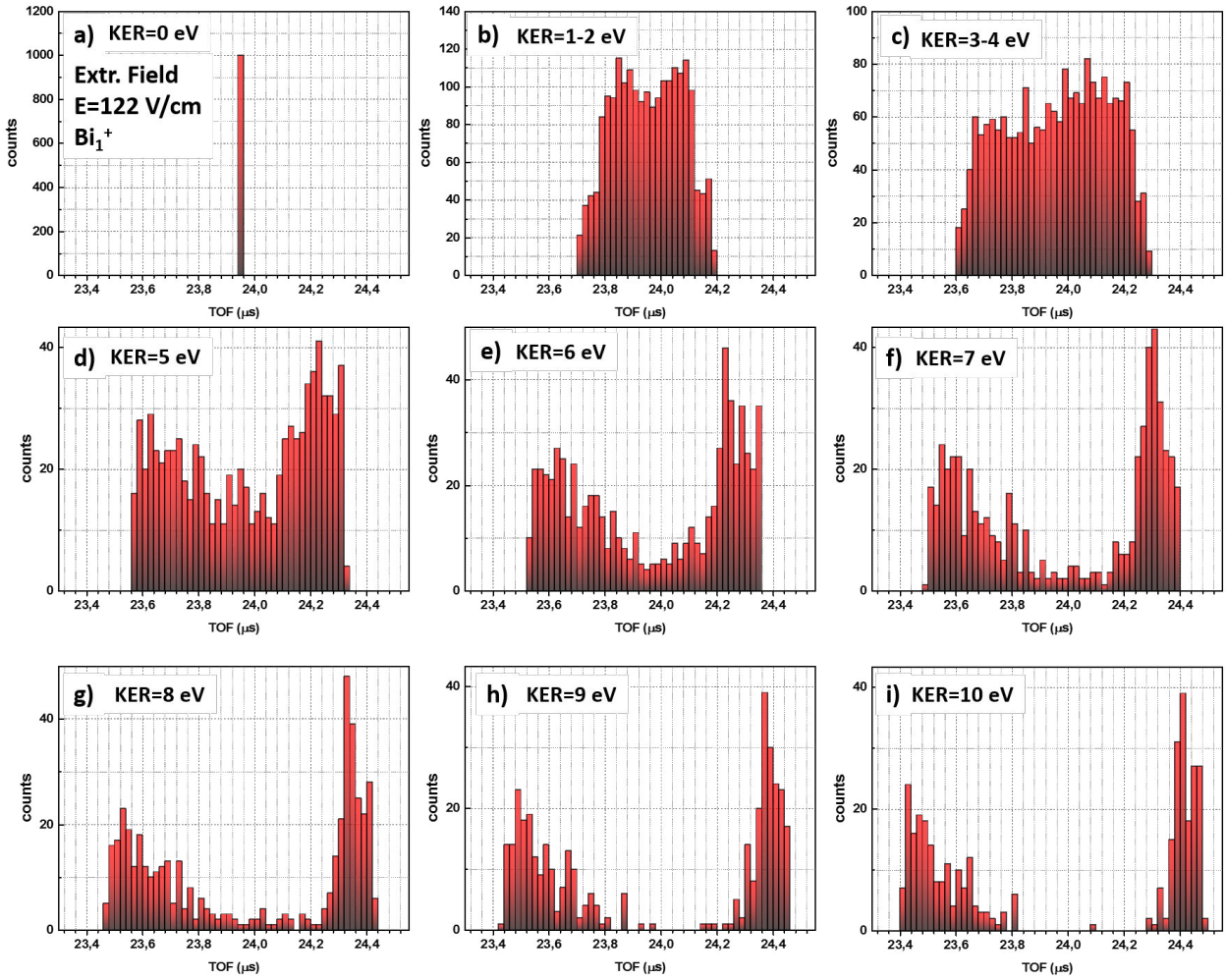

Figure 7.14 *Forme du pic des ions Bi^+ simulé pour un champ d'extraction de 122 V/cm et pour différentes énergies cinétiques lors d'une fragmentation distribuée de manière anisotropique.*

7.4.2 Collisions des ions avec les agrégats métalliques

Les résultats des collisions entre les ions multichargés et les nanoparticules de métaux sont présentés dans cette partie. Pour les systèmes modèles, les métaux de bismuth et d'argent ont été sélectionnés pour les raisons suivantes : l'argent est un metal noble ayant des propriétés thérapeutiques en raison de l'oxydation augmentée par la présence des atomes Ag^+ et pour le bismuth c'est l'intérêt récent comme un métal ayant une petite toxicité qui peut remplacer les métaux nobles pour la théranostique.

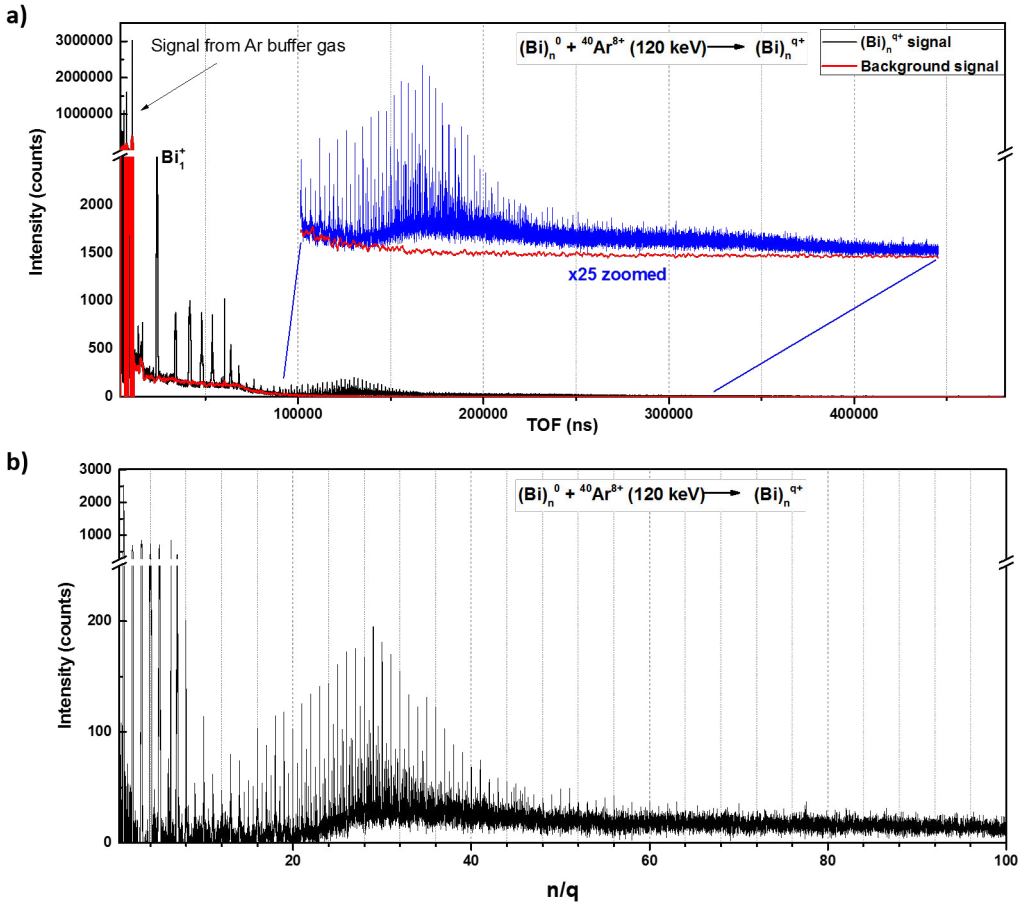

Figure 7.15 *a) Spectre en temps de vol des produits de la collision d'ions Ar^{8+} avec des agrégats neutres de bismuth à une énergie de collision E_{kin}=120 keV. La courbe noire correspond au signal lorsque la cible de nanoparticules est présente alors que le spectre rouge est celui obtenu avec uniquement le gaz porteur. b) Spectre de masse obtenu après soustraction du « bruit » provenant du gaz porteur d'argon.*

7.4.2.1 Collisions des ions avec les petits agrégats libres de bismuth

Le cible d'agrégats de bismuth était une distribution d'agrégats neutres dont le diamètre, déterminé par la microscopie MET, varie entre 1 et 3 nm. La figure 7.15 montre le spectre de masse des produits de la collision d'ions Ar^{8+} avec des agrégats neutres de bismuth à une énergie de collision E_{kin}=120 keV. Deux contributions principales sont visibles : la première est un signe très fort associé à des petits fragments situés dans la gamme de Bi_1^+ jusqu'à Bi_{12}^+ et la deuxième est une distribution large pour des tailles plus grandes que 15 atomes avec le maximum centré sur n/q=30. En outre, une multitude de pics avec un rapport n/q non-entier est visible et démontre la présence d'agrégats multichargés jusqu'à l'état q=6.

Après l'analyse du spectre, il est possible de séparer les contributions venants des différents

q=2	n_{app}=21 ±2	n_{last}=150
q=3	n_{app}=43 ±3	n_{last}=168
q=4	n_{app}=87 ±4	n_{last}=200
q=5	n_{app}=121 ±4	n_{last}=225
q=6	n_{app}=181 ±4	n_{last}=250

Table 1 *Taille d'apparition et taille maximum observées pour les agrégats multichargés de bismuth produits dans la collision avec un ion Ar^{8+} d'énergie 120 keV.*

états de charge et reconstruire les spectres d'abondance, qui démontrent par exemple dans le cas des agrégats doublement chargés une distribution entre n_{app}(q=2)=21 et n_{last}=150. Les résultats pour les charges de q=2 à q=6 sont résumés dans le tableau 1.

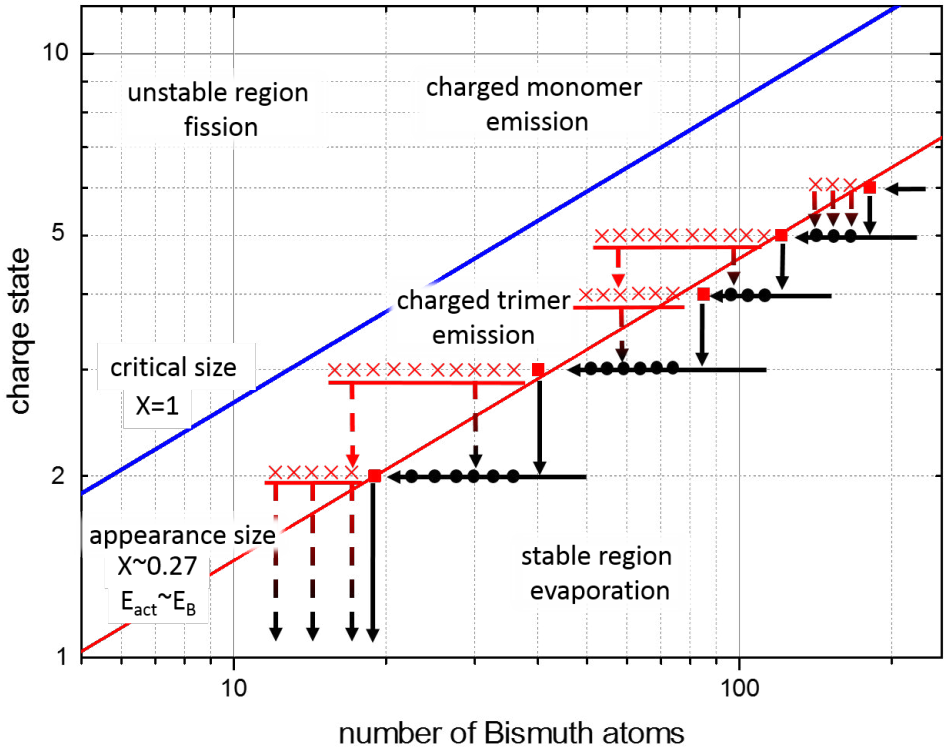

Figure 7.16 *Diagramme de stabilité pour les agrégats de Bi comme montré à la figure 5.5 mais incluant les transitions suivant les processus d'évaporation et de fission.*

Le nombre d'atomes du premier agrégat observé pour une charge q est appelé la taille d'apparition et en déterminant cette valeur pour chaque charge q il est possible d'obtenir le diagramme de stabilité présenté sur la fig.7.16.

Concernant l'évolution des spectres de petits fragments avec le charge du projectile, il a été observé que le signal du monomère de Bi est le plus intense pour tous les cas sauf avec O^{3+}, où

le trimère de Bi est le plus intense. De plus, il a été observé aussi que le rapport d'intensité du monomère et des petits fragments Bi_2^+-Bi_5^+ augmente en augmentant de charge du projectile q. Tous ces observations sont en accord avec le modèle de la goutte liquide pour le cas d'une ionisation par les ions multichargés des agrégats de bismuth neutres.

L'analyse de la forme du pic des petits fragments permet d'obtenir l'information concernant leur énergie cinétique libérée dans le processus de fragmentation. Particulièrement, pour les ions Bi_3^+, Bi_4^+ et Bi_5^+, deux contributions sont bien visibles : une première avec les énergies plus grandes que 4 eV et une deuxième avec des énergies inférieures à 1 eV. Ces observations sont expliquées par le fait que les fragments moins énergétiques viennent préférentiellement d'agrégats doublement chargés plus petits que la taille d'apparition ($n<n_{app}$) ou par processus d'évaporation et les fragments les plus énergétiques sont émis par des agrégats formés dans des états de charge plus hauts.

Pour une analyse plus détaillée, il est intéressant de faire l'étude des coïncidences, cela veut dire de considérer le spectre 2STOP nettoyé des coïncidences avec le gaz tampon. Par cette méthode il est possible d'obtenir des information sur la corrélation entre les petits fragments émis et les agrégats résidus plus grands. La première étape est la reconstruction de la carte à 2D de temps-de-vol TOF1 avec TOF2 (voir fig.7.17) à l'aide du logiciel d'analyse ROOT du CERN. La presence de lignes très visibles sur la carte 2D le long de TOF2 indique que les canaux de fragmentation les plus probables sont l'émission de Bi_1^+-Bi_8^+ (qui est en accord avec les résultats des spectres inclusifs). Nous pouvons aussi trouvé que le fragment de Bi_1^+ est en corrélation avec des agrégats plus petits comparé au fragment Bi_3^+ (même si dans les deux cas la taille du résidu s'étend sur toute la gamme de TOF2). Les fragments plus grands comme Bi_7^+ ou Bi_8^+ viennent en coïncidence avec des agrégats ayant $n/q<90$.

En étudiant la forme du pic pour un fragment en corrélation avec un gamme d'agrégats ayant un rapport n/q, l'énergie cinétique peut être déterminée. Pour les fragments Bi_1^+ et Bi_3^+, l'énergie cinétique du petit fragment augmente en fonction du rapport n/q du second fragment. Dans le cas du trimère, E_{kin}=3.5 eV pour $n/q\approx$11-35 et augmente à la valeur $E_{kin}\approx$5 eV pour $n/q>75$. Un comportement similaire a lieu pour Bi_1^+, mais la valeur initiale pour n/q=11-35 oscille proche de E_{kin}=5.5 eV et monte à E_{kin}=6-6.5 eV pour $n/q>100$.

Différents processus de fragmentation peuvent mener aux résultats obtenus pour le monomère et le trimère. Les calculs de la valeur Q (qui est interprétée comme la différence entre l'énergie totale du système inital - avant la fragmentation et après l'ionisation - et final après la fragmentation) pour l'émission de Bi_1^+ ou Bi_3^+ sont comparés avec l'énergie libérée (KER, donnée surtout au petit fragment) et ils sont en accord avec les valeurs expérimentales pour $n/q\approx>40$, signifiant que la fissilité des agrégats parents doit être $X<1$.

En outre, l'énergie plus grande que 6 eV pour le monomère et le trimère avec $n/q>100$, en supposant que la fissilite est inférieure à 1, indique que les parents doivent être plus grands que quelques milliers d'atomes. Par microscopie MET, il a été montré qu'il n'y a pas de nanoparticules si grandes. La seule possibilité est que la valeur de fissilité excède X=1 et dans ce cas la barrière disparait - dans cette situation l'émission simultanée de la multitude des fragments

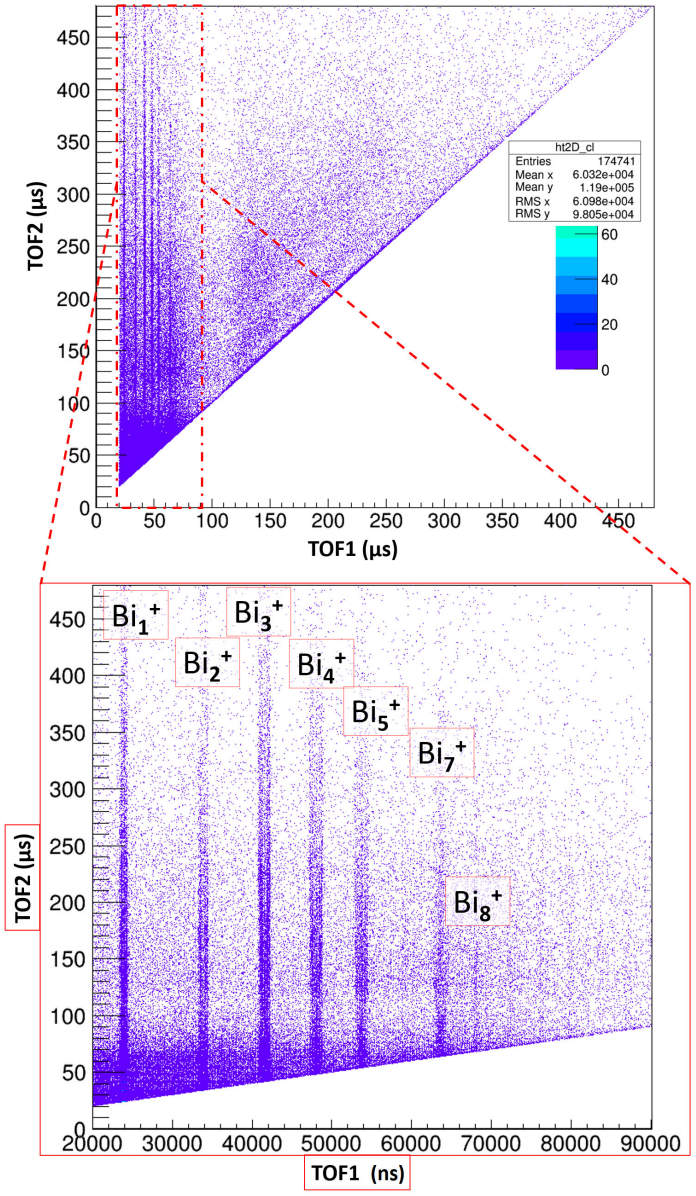

Figure 7.17 *Représentation à deux dimensions des évènements 2STOP après nettoyage des coïncidence avec le gaz tampon dans le cas des collisions entre les nanoparticules de Bi et des ions Ar^{8+} ayant une énergie de 120 keV.*

a lieu et l'explosion coulombienne apparait - toute l'énergie est transformée en mouvement des fragments. Par exemple, si on considère l'agrégat de bismuth ionisé q=12 fois ayant 200 atomes - il a une fissilité X=2.08. En considérant les canaux d'excitation comme l'émission de nombreux des fragments Bi_1^+ et Bi_3^+, on voit que la différence d'énergie Q=60 eV est au final partagée par 8 ou 9 fragments (c'est un minimum local) et emporte 6-7 eV par fragment, qui est en accord avec l'expérience.

Îlots des coincidences

Une dernière partie très intéressante est l'investigation des îlots de coïncidences pour l'arrivée de deux fragments petits apportant des informations importantes concernant la dynamique des processus de fragmentation. La région étudiée correspond à la gamme de 20 à 50 μs, qui est la région de corrélations des paires (Bi_iBi_j) avec i,j=1 à 5. La forme des îlots est différente à cause de différents mécanismes gouvernants le processus de fragmentation. Ils peuvent être décomposés en des sous-îlots plus petits. Il est nécessaire de considérer que la somme des deux fragments analysés en coïncidence est moins que Bi_{10}^+ des agrégats non-observés dans le faisceau primaire et ça indique la fragmentation avec au moins un troisième fragment (chargé ou neutre).

La forme des îlots est différentes pour chaque paire, mais en général ils conservent tous la forme d'un papillon. Il est possible analyser l'évolution d'énergie cinétique d'un fragment dans une paire de corrélation en fonction d'un autre fragment. En général cette énergie du fragment le plus petit baisse en fonction de sa taille et c'est inverse pour l'énergie du fragment plus grand, indiquant que la tendance générale est en accord avec le rapport des masses des fragments pour le système à quasi 2-fragments, même quand les chiffres exactes sont un peu décalés de la situation précise dune fragmentation à deux corps.

Les trois exemples des îlots (Bi_1^+,Bi_5^+), (Bi_1^+,Bi_2^+) et (Bi_3^+,Bi_4^+) ont été analysés profondément pour trouver les différentes contributions des scénario de la fragmentation pour la forme finale observée. Pour le cas de la paire (Bi_1^+,Bi_2^+), la pente moyenne de TOF2/TOF1 (correspondant à le rapport des quantités de mouvement de deux particules) était trouvée à -0.71, qui indique la majorité des évènements ne viennent pas de processus de fission binaire (ou la pente est -1). Les processus doivent impliquer la présence d'une troisième particule (chargée ou neutre) qui va emporter le reste de la quantité de mouvement. La pente est déterminée par la position de maxima d'un îlot, mais il est observé aussi qu'il y a des régions avec un comptage non-négligeable où le pente s'étend par l'angle de $\sim$150°, qui était attribué à la distribution d'énergie et de la quantité de mouvement très large d'une grande distribution des agrégats parents.

Pour le cas de la paire (Bi_1^+,Bi_5^+), il y a deux îlots séparés mais juste en TOF1 (backward et forward pics) de Bi monomère mais pour Bi pentamère c'est une seul pic, impliquant que le monomère est produit avec une grande gamme d'énergies et de directions. La pente est pratiquement $\approx$0.

Le dernier exemple montré sur le Fig.7.18, la paire (Bi_3^+,Bi_4^+) est très intéressante, parce que il est possible de distinguer trois différentes contributions - trois pentes. La première est proche de la valeur $+1$ et ce sont des fragments émis dans la même direction - pour ce cas un troisième objet doit être présent pour conserver la quantité de mouvement. Une explication possible de la fragmentation uni-directionnelle peut venir du caractère semi-métallique/semi-conducteur des petits agrégats. Pendant la capture des électrons, un site d'agrégat positivement chargé apparaît et si les électrons ne peuvent pas équilibrer la charge suffisamment vite, l'émission locale peut avoir lieu. Le deuxième processus avec la pente de -1.1 est proche de la fission binaire (la pente -1) et la petite déviation peut venir d'une émission additionnelle d'un fragment neutre avec la

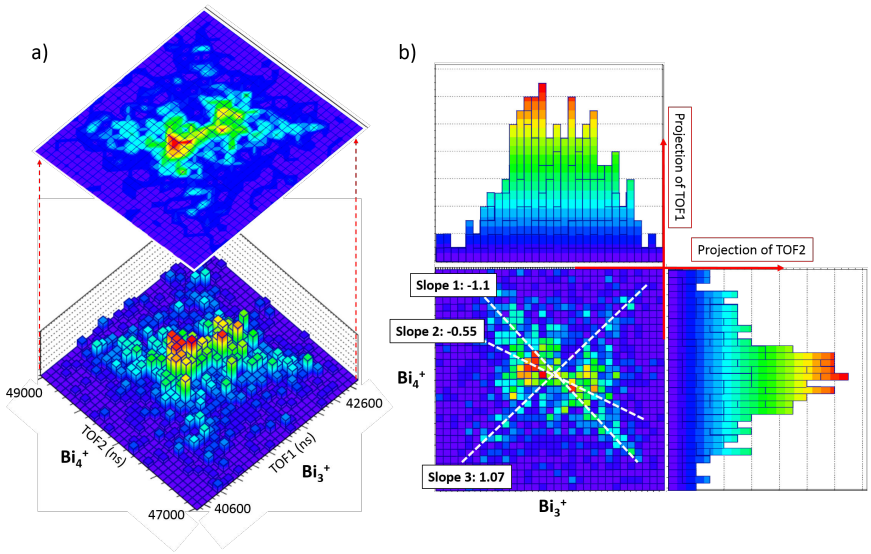

Figure 7.18 *a) Histogramme à 3-dimensions de l'intensité de l'îlot de corrélation (Bi_3^+,Bi_4^+), b) représentation à deux dimensions du même îlot avec des coupes horizontale et verticale.*

petite quantité de moment. La dernière contribution est associée avec la présence de coups sur le ligne caractérisée par la pente de la valeur environ -0.5. La quantité de mouvement pour le tétramère est deux fois plus grande que pour le trimère et ça signifie qu'un troisième fragment prend le reste de la quantité de moment.

7.4.2.2 Collisions des ions avec les grands nanoparticules libres d'argent

Les nanoparticules d'argent sont un autre système examiné, qui est caractérisé par une distribution en taille plus large que le cas du bismuth, avec un diamètre moyen de la nanoparticule de 5.5-6 nm, ayant environ 5000 atomes. Voici, les résultats de leur collision en phase gazeuse avec les ions multichargés.

La première considération importante est que la section efficace géométrique pour un agrégat d'argent de 6 nm est 9 fois plus grande que pour le cas des agrégats de diamètre de 2 nm (comme ceux de bismuth) où les collisions périphériques constituent 85% des collisions pour le charge du projectile q=8. Pour le cas des nanoparticules d'argent, c'est entre 50% (la plus petite charge q du projectile) et 30% (les charges q plus élevées) des collisions qui sont des collisions pénétrantes.

La possibilité d'une émission d'ions Ag^+ d'un agrégat Agn^+ en cas d'ionisation par capture électronique lors d'une collision périphérique est très faible, parce que n est très large (n>2000) et avec les projectiles ayant une charge q petite un agrégat devrait perdre plus de 35 électrons. Du coup la division des collisions en périphériques et pénétrantes est nécessaire.

Le spectre typique pour la collision des nanoparticules d'argent libres en phase gazeuse et

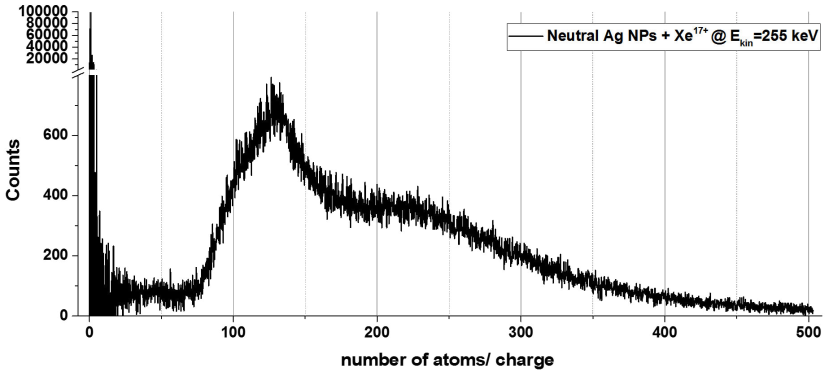

Figure 7.19 *Spectre de masse résultant de la collisions d'ions Xe^{17+} avec un faisceau de nanoparticules neutres Ag_n ayant une distribution en taille comme celle de la Fig.***??**.

le projectile multichargé Xe^{17+} ayant une énergie $E_{kin} = 255$ keV est montré sur la Fig.7.19. En general, le spectre est caractérisé par deux composantes : un premier signal dominé par les petits fragments avec n/q<20 et une deuxième composante avec une distribution très large s'étendant de n/q≈75 à 500 avec un maximum localisé sur n/q=125.

En se concentrant sur les petits fragments (Fig.7.20) et en les comparant avec les spectre pour la pulvérisation de surfaces macroscopiques, on remarque des similitudes. Le pic le plus intense est Ag_1^+ suivi par Ag_2^+ et Ag_3^+ et aussi les oscillations d'intensité avec la parité de n est trouvée en fonction de la taille d'un fragment. De plus, une chute d'intensité après n=3, 9 et 21 correspondant aux effets de fermeture de couche.

Malheureusement, il n'y a pas de calculs pour déterminer l'émission ionique des nanoparticules métalliques libres par collision avec les ions multichargés. Mais quelques groupes de théoriciens (Nordlund, Urbassek) ont fait les simulations concernant le processus de pulvérisation de nanoparticules métalliques d'or par des atomes. Ils ont trouvé qu'il existe une relation entre le rendement de pulvérisation et la taille de l'objet avec une efficacité plus élevée pour un diamètre de 6-7nm. Aussi, la pulvérisation est dominée par la production de trois premiers Ag-mères, même si il y un petit signe de la pulvérisation de fragments plus grands que n=100. Même si les calculs ne concernent pas les agrégats d'argent, une comparisons qualitative est possible car l'argent possède une structure électronique et un rayon de Wigner-Seitz similaires à l'or.

Enfin, la comparaison du rendement de pulvérisation pour les différents projectiles (Xe,Ar,O) et états de charge (q=25,9,6,3,2) normalisé à la valeur de Xe^{25+} est en accord avec la pulvérisation de surface déterminée par une formule empirique en fonction du paramètre $\frac{\sqrt{m}}{v}$ qui est proportionnel au pouvoir d'arrêt nucléaire.

La deuxième composante du spectre est très large et elle est non résolue en raison des contributions isotopiques (107 et 109 amu avec une proportion de 49% et 51%) et la possible contribution des nanoparticules multichargées. Ainsi il est impossible de bien déterminer la

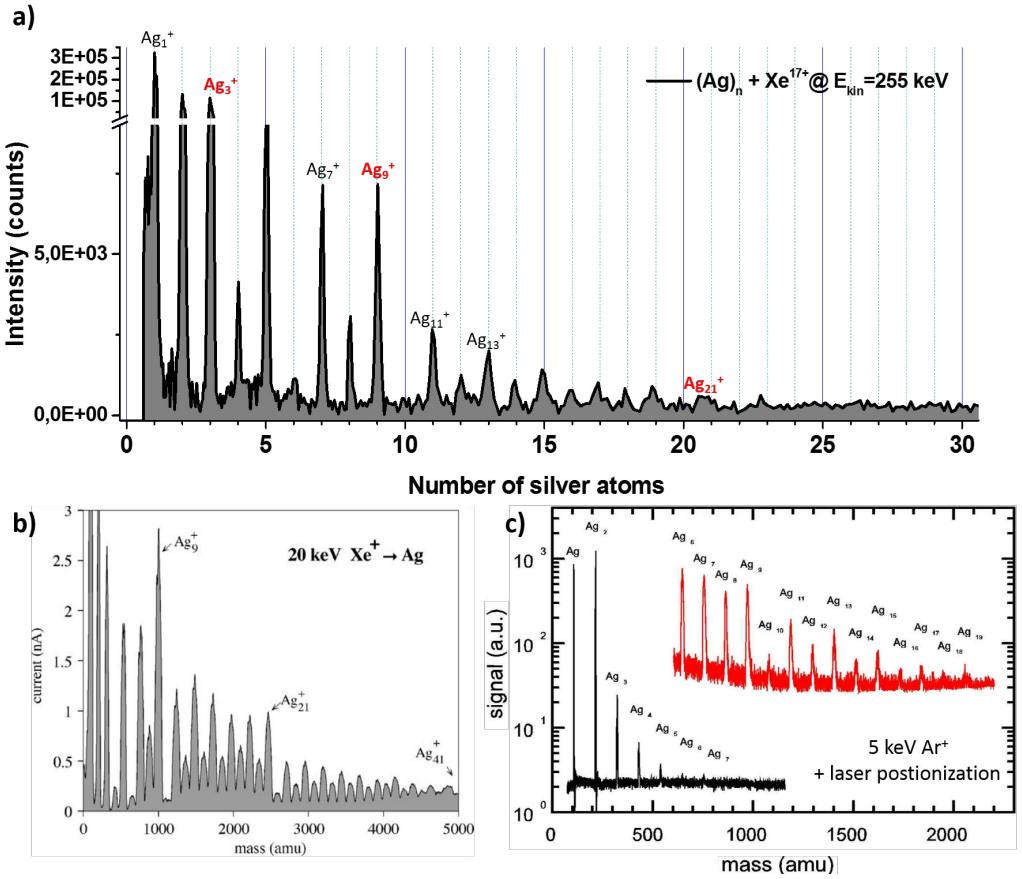

Figure 7.20 *a) Zoom sur la région des petits fragments cationiques ; b) spectre de masse des agrégats cationiques pulvérisés d'une surface polycristalline d'argent par des ions Xe^+ ayant une énergie de 20 keV [89] ; c) spectre de masse des agrégats pulvérisés d'une surface polycristalline d'argent sous forme neutres et post-ionisé par une impulsion laser après impact d'ions Ar^+ de 5 keV [90].*

masse et la charge comme c'était fait pour le cas des agrégats de bismuth. Pour les collisions avec les projectiles comme Ar^{9+} ou Xe^{17+}, on voit que l'évolution du spectre est en accord avec le changement de la distribution de la taille, parce que pour une longueur d'agrégation plus grande le spectre est décalé vers les n/q plus grands. Néanmoins, on n'a pas observé un grand changement de spectre pour les différents états de charge des projectiles sauf dans le cas des ions Xe^{25+}, où la maximum est sur n/q=70 (n/q=100 pour la reste). L'analyse plus détaillée fait la suggestion, que si le maximum sur n/q≈70-150 peut être expliqué par la capture électroniques pour les projectiles hautement chargés, il faut aussi considérer pour les projectiles faiblement chargés que les collision pénétrantes sont responsables de la multi-ionisation des nanoparticules (la collision pénétrante permet de déposer sur le système des électrons et des atomes quelques keV d'énergie), induisant l'émission d'électrons chauds, la deexcitation plasmonique et la pulvérisation. Les expériences faites sur les nanoparticules de

cuivre ont montré des résultats similaires concernant le signal de la distribution large, mais avec n/q s'étendant de 100 à 2400.

7.5 Conclusions et perspectives

Pour étudier les effets d'irradiation des nanoparticules libres d'argent et de bismuth en phase gazeuse avec les ions multichargés, j'ai construit le dispositif expérimental COLIMACON DUO à partir du dispositif précédant permettant de faire des expériences en faisceaux croisés. L'installation et l'adaptation de la source d'agrégats par pulvérisation du type magnetron, d'une chambre de dépôt et d'un canon des ions pour les test ont ainsi été réalisées.

L'application des méthodes microscopiques sur les agrégats neutres déposés sur SiO_2 a permis d'obtenir leur distribution de taille. En addition, pour les expériences plus détaillées en multicoïncidence avec le détecteur des électrons émis et la spectre de masse (avec le système d'acquisition FASTER de LPC Caen), des simulations SIMION et la construction d'un nouveau système d'extraction contenant un détecteur d'électron ont été réalisées.

Pour les agrégats de bismuth, une multitude de résultats a été obtenue :

1. En général, les résultats sont en accord avec le modèle de la gouttelette liquide, même si le Bi a un caractère semi-métallique (et à l'échelle nanoscopique il est semi-conducteur)
2. Le spectre de masse est dominé par des petits fragments énergétiques, mais aussi des agrégats multichargés plus grands sont visibles et la détermination du diagramme de stabilité a été possible pour les charge q=2 à q=6 avec une taille d'apparition suivant la fissilité de X=0.27
3. Les petits fragments sont produits par la fission des agrégats avec une fissilité dans toute la gamme X=0.3 à plus que X=1, ceci est bien observé sur la contribution énergétiques des petits fragments
4. L'analyse des coïncidences 2STOP a aussi été faite et montre que l'émission des monomère vient des agrégats ayants une fissilite plus élévé et les trimer sont émis des agrégats ayants la fissilité moins éléve

Pour les agrégats d'argent, les résultats principaux sont :

1. Les fragments dominants présents sur le spectre de masse sont toujours les monomères, indépendamment de la charge du projectile
2. La production normalisée des trois fragments plus petits est en accord avec la formule empirique décrivant le processus de sputtering avec les ions de differentes énergies cinétiques.
3. Les oscillations d'intensité des pics et la décroissance de l'intensité générale est en accord parfait avec le sputtering des surfaces Ag polycristallines

4. La distribution des fragments plus lourds est détérminée par plusieurs processus : l'ionisations en collisions peripheriques et pénétrantes (le capture électronique et le pouvoir d'arrêt électronique) mais aussi la production des fragments plus grands

Etant donné que les mécanisms principales de radiosensibilisation sont supposés être dus à la production de radicaux et desecond électrons, la présence de particules de métal peut avoir une influence sur la toxicité cellulaire à cause de la production des ions radicaux et les électrons sécondaires, la presence des particules de metaux peut avoir l'influence à la toxicité dans les cellules.

Cette thése met en évidence le fait que l'interaction des ions lents et énergétiques (de 10s à 100s keV) avec les objets nano-metalliques est déstructive et méne à la production d'une'multitude de particules de metaux chargés, d'ions atomiques jusqu'au agregats et fragments larges, par les mécanismes de fission et pulvérisation. En consequence, la concentration de petits particules métalliques est augmentée dans les cellules et les effets de toxicité pouvent être augmentés.

Interaction d'ions multichargés lents avec des nanoparticules métalliques radiosensibilisantes

RÉSUMÉ

Cette thèse est consacrée à l'étude de l'interaction d'ions multichargés avec des particules métalliques de taille nanométrique. Ce travail a eu pour but d'étudier les processus fondamentaux ainsi que d'éclairer leur rôle comme radio-sensibilisants dans le traitement de cancer par hadronthérapie. Le nouveau dispositif développé dans ce cadre consiste en une source d'agrégats de type magnétron, d'une chambre de dépôt afin de permettre la caractérisation de la taille des nanoparticules neutres par analyse microscopique, et d'un spectromètre de masse par temps de vol capable de détecter des systèmes positivement chargés jusqu'à une masse de 50 000 ua. Les études de collisions ont été réalisées avec des agrégats de Bi (2 nm ; 200 atomes) et de Ag (6 nm ; 5000 atomes). Dans le deux cas, le processus de capture multiélectronique crée un système multichargé. Dans le cas du Bi, une grande partie fragmente par la fission asymétrique émettant des petits fragments. Dans le cas des particules plus grandes (Ag), les systèmes multichargés ne fragmentent pas, par contre des petits fragments sont aussi observés mais ils sont le produit de la pulvérisation de la nano-surface lors de collisions pénétrantes. En perspective, des expériences seront réalisées avec des nanoparticules métalliques fonctionnalisées ainsi que le comptage des électrons émis lors de la collision.

Mots-clefs

Nanoparticules métalliques, ions multichargés, spectrometrie de masse à temps de vol, capture multiélectronique, fission asymétrique, pulvérisation, hadronthérapie, radiosensibilisants

Interactions of slow multiply charged ions with large, free radiosensitizing metallic nanoparticles

ABSTRACT

This thesis presents a study of the interaction of multiply charged ions with metallic nano-sized particles both in the context of fundamental processes and possible applications as radiosensitizers in nanoparticle-enhanced hadrontherapy. For this purpose a new experimental set-up has been constructed based on a magnetron-discharge cluster source, a deposition chamber for analyzing the size of neutral nanoparticles with AFM and TEM techniques and a time-of-flight mass spectrometer able to detect positively charged particles with masses up to 50 000 amu. Collision studies were performed with Bi clusters of 2nm in diameter, containing 200 atoms, as well as Ag nanoparticles (6 nm, 5000 atoms). In both cases multi-electron capture leads to the formation of multiply charged systems. In the Bi case a large fraction fragments by asymmetric fission emitting small singly charged fragments. In the case of large Ag nanoparticles multiply charged systems are stable. However, small size fragments are formed due to sputtering of the nano-surface in penetrating collisions. Future experiments will be performed with functionalized metal nanoparticles, aiming to count the number of electrons emitted after ion collisions.

Key-words

Metallic nanoparticles, multiply charged ions, time-of-flight mass spectrometry, multielectron capture, asymmetric fission, sputtering, radiosensitizers, hadrontherapy

Laboratoire

Centre de recherche sur les Ions, les MAtériaux et la Photonique
CIMAP - GANIL
CEA/CNRS/ENSICAEN/Université de Caen Normandie
Boulevard Henri Becquerel, BP5133, 14070 CAEN cedex 5, France